UNIVERSITY OF TWENTE.

Faculty of Engineering Technology

Perturbed Visibility Problem for a Terrestrial and Lunar Orbiter

UT Graduation Number 458
Master of Science Thesis
Mechanical Engineering

David Humphry Ramadhin
s1705814
d.h.ramadhin@student.utwente.nl

20 November 2024

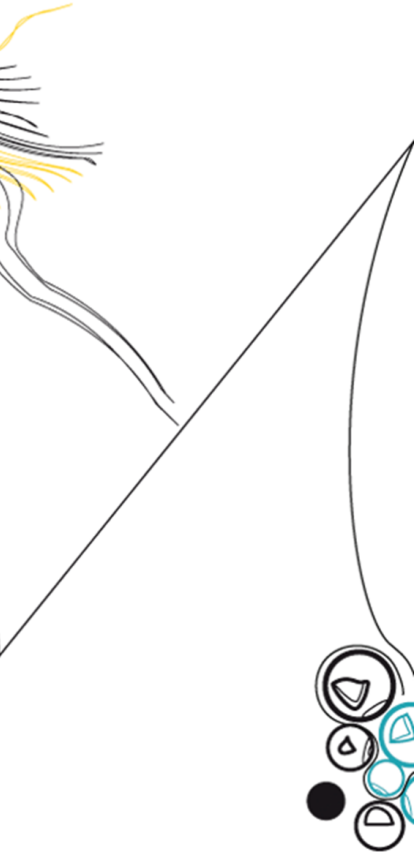

Department:
Engineering Fluid Dynamics

University of Twente
P.O. Box 217
7500 AE Enschede
The Netherlands

A thesis submitted to

University of Twente
Department of Engineering Fluid Dynamics

Instituto Tecnológico de Aeronáutica
Field of Aeronautical Projects, Structures and Aerospace Systems, EAM-1

In partial fulfilment of the requirements for the degrees of
Mechanical Engineering
and
Aeronautical and Mechanical Engineering

by

David Humphry Ramadhin

Committee Members

Prof. Luiz Arthur Gagg Filho	Supervisor
Dr. Ir. Arne van Garrel	Supervisor
Prof. Sandro da Silva Fernandes	Supervisor
Prof. Dr. Ir. Cornelius H. Venner	Chairman
Prof. Willer Gomes dos Santos	Reader
Dr. Ir. Richard Loendersloot	Reader

Foreword and acknowledgments

Even though I arrived in Brazil over a year ago, it still boggles my mind to realise that I am actually here, so far from home. And what a year it has been! I became familiar with a new and, at times, confusing language, wonderful people, a warm and open culture, and tasty food. I feel lucky having been able to enjoy all of this, having the opportunity and freedom to explore a beautiful country the size of a continent.
Besides a journey in Brazil, this past year was also a journey through the field of orbital mechanics. To match the theme of trying new things, supported by six-year-old me who was obsessed with André Kuipers, I chose this topic. At that moment, I had not attended any courses related to astrodynamics, so besides some basics from high school, I was a novice. This, I think, is clearly reflected in my thesis, both by the fundamental start I make in the theoretical background and the final length of the report. To familiarise myself with this subject and its mathematical background, I attempted most of the required derivations, as showcased in the appendices. I had to take small steps, but through it all, I can now confidently say that I have made it my own. That in itself was extremely satisfying, and I am grateful I got the time and chance to discover this fascinating subject.

A guiding star in my process, to whom I am ever so grateful, is my advisor Prof. Gagg. Thank you for all your time, patience, and flexibility. Whatever questions or issues I had, you always made time for me and made sure I remained on the right track. You pushed me to write clearer code and I can now happily say that I wrote my first (somewhat) legible code, something I did not think I would ever manage. Thank you for your support and feedback, and, from time to time, showing how deep the rabbit hole of orbital mechanics goes. I find it an exciting idea that I have only scratched the surface, and that the sky is the limit.
I would also like to thank my second advisor, Prof. da Silva Fernandes. With your course in astrodynamics, you gave me a solid foundation, without which I would not have known where to start. You will see your book cited countless times, as it proved incredibly useful. Your detailed commentary and feedback were helpful and really brought this thesis together.
Being an exchange student came with the perk of having a third advisor, Dr. Ir. van Garrel. Even from far away and in a field that is not your own, you gave me astute advice. From helping me get organised to nudging me in the right direction, shifting my focus where necessary. Thank you for your insights.
I would also like to thank Prof. Dr. Ir. Venner for giving me the possibility to even go on this exchange. It was an amazing experience that I will hold dear for the rest of my life. Thank you for this wonderful opportunity. In that same vein, I would also like to thank Prof. Arbelo, my first contact point in Brazil. When everything was new and confusing, you helped me through and got me started on this exchange.
Gerben, what an adventure this was! From knowing that I was not alone with the struggle of whatever bureaucratic process we had to get through, to travelling with someone that felt the same desire of seeing as much of this stunning country. Thank you for this amazing time, for being a great roommate and an amazing friend. I am so glad that I could share this time with you.
Daniel and Eduardo, you made me realise that working in an office is not nearly as bad as I imagined it to be. Thank you for the laughs, the politics, the hijinks, the pick-me-ups, the nonsense, and the frolics.

Abstract

This report aims to solve the satellite-to-site visibility problem using Escobal's controlling equation, an analytically developed transcendental equation. Once or twice per orbital revolution, this equation is solved numerically to determine the rise and set eccentric anomalies, yielding the visibility windows during which communication between a satellite and ground station is possible.
Accurate modelling of the satellite's motion is essential to solving the visibility problem, and a significant portion of this report addresses this. The satellite's orbit, whether in low Earth or Lunar orbit, is first determined by the two-body problem and then refined by accounting for the dominant perturbations: nonspherical gravity, modelled with zonal harmonics up to the tenth degree, and third-body attraction, considered up to the second degree. These perturbations are averaged to eliminate short-period effects, and the Lagrange equations are used to determine the rate of change of the orbital elements.
To be able to apply the controlling equation, the orbital elements are temporarily held constant within each orbital revolution. Given the short orbital periods and the slow evolution of the orbital elements, this approximation does not cause major inaccuracies. To verify the accuracy of this approach, the visibility problem is also solved using the traditional brute force method, which makes use of a constraint equation. The required ephemeris is generated by numerically integrating the perturbed equations of motion using Cowell's method.
The methodology and implementation is first validated with a Terrestrial orbiter, where the second zonal harmonic dominates. The evolution of the orbital elements aligns well with documented behaviour from literature. Although a first test case regarding visibility does not conform with literature, agreement is found after further investigation and a second test case. The approach is then extended to a Lunar orbiter, where the Moon's gravitational field requires the inclusion of higher-degree harmonics for accurate modelling, as the second zonal harmonic is less prominent. Additionally, the proximity of Earth necessitates modelling its gravitational influence as a third-body perturbation.

Contents

Nomenclature

A	Area	km^2
a	Semi-major axis	km
$\vec{a}$	Acceleration	km/s^2
b	Semi-minor axis	km
$\vec{B}$	Laplace-Runge-Lenz vector	km^3/s^2
c	Constant of integration	–
d	Day	[1, 31]–
E	Eccentric anomaly	[0, 2π] rad
e	Eccentricity, magnitude of eccentricity vector	–
$\hat{E}$	Unit vector representing the y-direction in the topocentric horizon frame	–
$\vec{e}$	Eccentricity vector, apse line	–
F	Focus of an ellipse	–
f	Flatness	–
f	True anomaly	[0, 2π] rad
$\vec{F}$	Force	N
G	Universal gravitational constant	$m^3/(kg\ s^2)$
H	Height above sea level	km
h	Elevation angle	[$-\pi/2$, $\pi/2$] rad
h	Magnitude of specific angular momentum vector	km^2/s
$\vec{h}$	Specific angular momentum	km^2/s
I	Inertia tensor	$kg\ km^2$
i	Inclination	[0, π] rad
$\hat{I}$	Unit vector representing the x-direction in the geocentric equatorial frame	–
J_{2000}	Current epoch	–
$\hat{J}$	Unit vector representing the y-direction in the geocentric equatorial frame	–
$\hat{K}$	Unit vector representing the z-direction in the geocentric equatorial frame	–
L	Mean longitude	rad
L_0	Mean longitude at epoch	rad
l	Mean latitude	rad
M	Mass of primary body	kg
M_e	Mean anomaly	[0, 2π] rad
M_{e_0}	Mean anomaly at epoch	[0, 2π] rad
m	Mass of satellite	kg
m	Month	[1, 12]–
$\vec{N}$	Node line	–
$\vec{n}$	Normal vector	–
P_n	Legendre polynomial of degree n	–
p	Semi-latus rectum	km
$\hat{p}$	Unit vector representing the x-direction in the perifocal frame	–
$\vec{p}$	Momentum	$kg \cdot km/s$
R	Radius primary body	km
R	Distance, magnitude of position vector	km

R_e	Equatorial radius primary body	km
R_p	Polar radius primary body	km
r	Distance, magnitude of position vector	km
r_{SOI}	Radius of the sphere of influence	km
$\vec{R}$	Position vector observer	km
$\vec{R_G}$	Barycentre	km
$\vec{r}$	Position vector	km
$\vec{r}'$	Position vector	km
SD	Mean solar day	h
$\hat{S}$	Unit vector representing the x-direction in the topocentric horizon frame	–
T	Orbital period	s
T_0	Julian centuries with respect to J_{2000}	–
t	Time since periapsis	s
t_{UT}	Universal time	s
U	Gravitational potential	$\mathrm{km}^2/\mathrm{s}^2$
UT	Universal time	hh : mm : ss
V	Potential energy	kJ
v	Speed, magnitude of velocity vector	km/s
$\vec{v}$	Velocity vector	km/s
$\hat{w}$	Unit vector representing the z-direction in the perifocal frame	–
x	Cartesian coordinate x	–
y	Year	[1901, 2099]–
$\hat{Z}$	Unit vector representing the z-direction in the topocentric horizon frame	–
α	Right ascension	[0, 2π] rad
β	Azimuth	[0, 2π] rad
$\vec{\Gamma}$	Perturbing acceleration	km^2/s
γ	Flight path angle	rad
δ	Declination	[-$\pi/2$, $\pi/2$] rad
ε	Specific mechanical energy	$\mathrm{km}^2/\mathrm{s}^2$
ϑ	Arbitrary angle	rad
θ	Local sidereal time	[0, 2π] rad
θ_G	Greenwich sidereal time	[0, 2π] rad
θ_{G_0}	Greenwich sidereal time at 0 UT	[0, 2π] rad
$\dot{\theta}$	Angular velocity	rad/s
λ	Longitude	[0, 2π] rad
μ	Standard gravitational parameter	$\mathrm{km}^3/\mathrm{s}^2$
ρ	Density per unit area	$\mathrm{kg}/\mathrm{km}^2$
ϱ	Slant range, magnitude of slant range vector	km
$\vec{\varrho}$	Slant range vector	km
τ	Time at periapsis	s
φ	Geodetic latitude	[-$\pi/2$, $\pi/2$] rad
φ'	Geocentric latitude	[-$\pi/2$, $\pi/2$] rad
Ω	Right ascension of the ascending node	[0, 2π] rad
ω	Argument of perigee	[0, 2π] rad
ϖ	Longitude of periapsis	rad
$\vec{\Omega}$	Angular velocity	rad/s
$\mathfrak{b}$	Perturbations due to a third body	–

$\mathfrak{C}$	Constraint equation	km
$\mathcal{D}$	Normalised units of distance	distance
$\mathfrak{h}$	Perturbations due to a nonspherical body	km
$\mathfrak{F}$	Controlling equation	km
$\mathfrak{L}$	Lagrangian matrix	km
ℓ_{ij}	Lagrange bracket	km
$\mathscr{R}$	Perturbing force function	$\mathrm{km}^2/\mathrm{s}^2$
$\mathfrak{R}$	Rotation matrix	–
$\mathcal{T}$	Normalised units of time	time
$\mathcal{V}$	Normalised units of velocity	velocity
$(\dot{})$	Derivative with respect to time	–
∇	Nabla operator	–
$(\,^T)$	Transpose	–
$(\vec{})$	Vector	–
$(\hat{})$	Unit vector	–

1 Introduction

Humanity's fascination with space has been prevalent throughout history. From using the Sun and Moon for time keeping to believing that celestial objects were gods [1]. Early navigation efforts relied heavily on the stars, and keeping track of the seasons allowed for successful harvests [2].
Until the early modern time, the motion of planets remained a mystery. Since the time of the old Greeks, the established theory was that the planets move around the Sun in circles with epicycles. This theory was disproven by Johann Kepler, who made use of the meticulous and highly accurate observations of Mars done by Tycho Brahe. Kepler was unable to match these observations with the assumed circular motion. In the search for a correct shape, after years of trial and error, he found that elliptical motion was the correct fit. Based on this, Kepler developed three laws of planetary motion, which were published in 1609 and 1619. Nowadays, they are known as Kepler's laws of planetary motion, and they read as follows [3],

1. The orbit of each planet is an ellipse, with the sun at a focus.
2. The line joining the planet to the sun sweeps out equal areas in equal times
3. The square of the period of a planet is proportional to the cube of its mean distance from the sun.

Through these laws, the orbits of planets could be accurately described. Yet, the reason behind their elliptical shape remained unexplained and lacked a mathematical foundation. This had to wait until Isaac Newton, who came up with his three laws of motion and his law of gravitation, which he published in 1687 [4]. These equations form the basis of the two body problem, from which the orbit of a natural or artificial satellite can be determined.
In modern times, besides observing, humanity has started exploring space as well. Countless satellites orbit the Earth and, aside from scientific purposes, provide us indispensable services like internet, navigation and communication. Generally speaking, three types of orbits exist. Low Earth Orbit (LEO) that has an altitude of 200-2000 km, Medium Earth Orbit (MEO) with altitudes ranging from 2000-35785 km, and Geostationary Earth Orbit (GEO) with an altitude of 35786 km [5]. This specific altitude for a GEO is determined by Kepler's third law, as it results in a satellite having an orbital period that exactly matches a sidereal day, making it appear fixed in the sky for an observer. This is advantageous as an antenna of a ground station must be aimed once and will thereafter always point at the satellite. Besides this, there are many more considerations in choosing a suitable orbit for a satellite, but simply speaking, the higher the orbit, the more costly it is to get the satellite there. A larger distance also means that maintenance is difficult or impossible, and latency is high. On the other side, being further away means a larger coverage area because the satellite can see more of the Earth. This means less satellites are required to provide constant coverage for a specific area [6].

By far, most satellites are in a Low Earth Orbit [7], and due to their lower cost, their share is only expected to rise further in the foreseeable future [8]. These low orbit satellites are precisely the focus of this report. Since coverage of these satellites is limited, services are often provided by a constellation, a group of satellites working in unison. To ensure continuous coverage of a specific region, at least one satellite must be visible at all times [9]. Visibility is necessary because communication between a satellite and a ground station is only possible when there is a direct line of sight [10]. Determining when a satellite is visible is aptly called the satellite-to-site visibility problem, or, in short, the visibility problem. A schematic of this can be seen in figure 1. Here, a satellite is in an elliptical orbit around the Earth, and the ground station or observer is located on the surface of the Earth. The satellite shown here is not in a Low Earth Orbit, which would be much closer to the Earth, but is instead placed further away for illustrative purposes. The points of interest in the visibility problem are the rise and set times of the satellite, the points where the satellite rises above and goes below the horizon of the observer. The time between these two points is called the visibility window. Especially for a satellite in Low Earth Orbit, these windows are brief, both because of the small coverage and the velocity with which the satellite flies by.
Aside from constellations, knowing when communication is possible is relevant for any satellite. A satellite has various different tasks, all of them managed by some scheduling algorithm [11]. Accurately predicting when the visibility window occurs is key, as it determines when certain tasks can, cannot, or should be performed [12]. What is more, this procedure should ideally be efficient and cheap, as computational power of the onboard computer is limited. While technological advancements have increased processing capabilities, they have also enabled the development of nano satellites, which face computational constraints due to their small size [13].

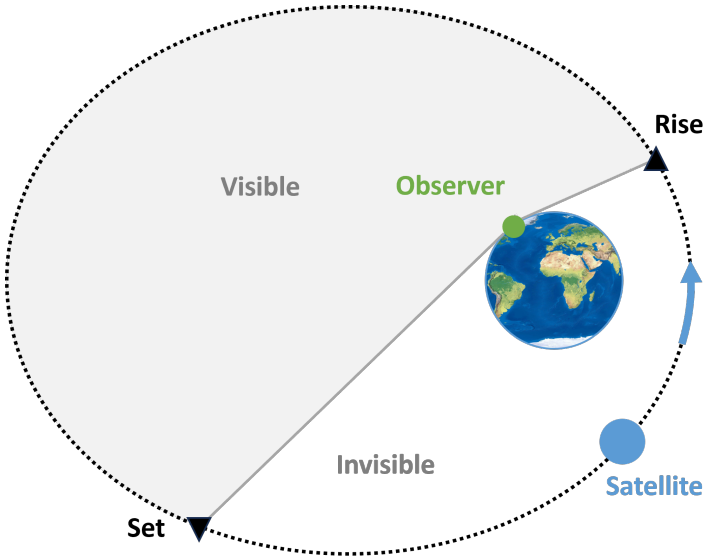

Figure 1: Schematic of the satellite-to-site visibility problem.

Traditionally, the visibility problem is solved using brute force. In a nutshell, a constraint equation is set up to determine whether the satellite is visible. This equation is then solved many times, using the ephemeris (trajectory) of a satellite. In this way, a visibility check is done for each location of the satellite. Looking at figure 1, it can be thought of doing a visibility check at each black dot that constitutes the orbit. Although simple in execution, this method is not very efficient. In order to obtain decent accuracy, a myriad of locations of the satellite must be solved for. In literature, this method serves as a baseline in comparison with other methods [14].

To name a few, Alfano et al. make use of parabolic blending to construct the waveform of the visibility function. The roots of local polynomials are then found to obtain the visibility window [15]. Mai and Palmer employ a coarse-to-fine refinement strategy to determine the closest approach to a ground station [16]. Han et al. utilize self-adaptive Hermite interpolation by approximating the waveform of the visibility function with piecewise cubic curves. The roots of cubic polynomials yield the rise and set times [14].
In addition to these numerical methods, an analytical approach was developed by Escobal [17]. Even though the numerical methods are quite efficient, this method is much cheaper in comparison [18]. Escobal simplifies the visibility problem by transforming the constraint equation, which is used in the brute force method, into a transcendental equation that needs to be solved only once or twice per orbital period. This equation is called the controlling equation and must still be solved for numerically, which can be done with for example Newton-Raphson [19]. All of this sounds ideal, but there is a limitation to this method.
Preliminary calculations in orbital mechanics can be done by considering the two-body problem [20], resulting in the Keplerian orbit. The orbit can be defined by either the state vector, consisting of the position and velocity vector of the satellite, or a set of six constants called the orbital elements. This simple methodology yields a good indication of the orbit, however, many factors like third body attraction or solar radiation pressure are not taken into account, while they do affect the satellite. These forces are much smaller than the primary gravitational attraction, so the Keplerian orbit still serves as a basis, but now these other factors can be added on top as perturbations, resulting in a more accurate model of the orbit [21]. The issue here is that the controlling equation necessitates constant orbital elements found in a Keplerian orbit. In the perturbed orbit, these orbital elements are a function of time, making the application of Escobal's method challenging. Fortuitously, their rate of change is minimal, so it is not that problematic to keep them fixed for a little while, before updating them again. This methodology is assumed to be employed by Escobal, who includes perturbations due to the second zonal harmonic in his analysis [17]. This approach is followed in this report as well, where it must be verified whether this still holds up with the inclusion of more perturbation terms.
In this report, two types of perturbations are considered. First, the perturbations caused by the nonspherical shape of a celestial body are considered. These perturbations are derived from the gravitational potential and described by spherical harmonics, a series expansion that describes the deviations of the celestial body from a sphere [2]. Specifically, zonal harmonics are studied, harmonics that have no dependence on longitude, as opposed to sectoral and tesseral harmonics. The weight given to each zonal harmonic is denoted through the zonal harmonic coefficients J_n, which are a property of a celestial body. For the Earth, the first coefficient J_2 is about 3 orders of magnitude larger than the subsequent zonal harmonic coefficients, meaning that this zonal harmonic is predominant. It corresponds to the oblateness (flattening) of the Earth, which is caused by the Earth's rotation about its axis [22].
The end goal in this report is not to study a satellite in Low Earth Orbit, instead a satellite in a Low Lunar Orbit (LLO) will be studied. As of right now, studying the visibility problem for a Lunar orbiter is not that relevant. Humans have not set foot on the Moon in over 50 years [23], there are only a handful of satellites in a Lunar orbit [24], and there is no permanent Lunar base. Nevertheless, in recent years, interest in the Moon has been renewed [25]. Be it for political, scientific, economic, exploratory, or military reasons, many countries and companies are setting their sights on the Moon [26] [27] [28].

For the Moon, the second zonal harmonic is dominant as well, but to a lesser extent compared with the Earth [29]. Therefore, in accurately modelling a Lunar orbit, adding more zonal harmonics is imperative. Accordingly, the gravitational potential is developed until 10^{th} order [30]. With the focus on the Moon, the second most relevant perturbation for a satellite in LLO is due to the gravitational attraction of the Earth [31]. Because the Earth is both two orders of magnitude heavier than the Moon, and relatively close by, its influence is considerable.
Most of the work in this report lies in accurately modelling the orbit and once this is established, the visibility problem can be solved. Specifically, this will be done for the Brazilian space prober Garatéa-L, a Lunar orbiter to be launched in 2025 [32].
The Lagrange equations will be used to include both of these perturbations and yield a rate of change of the orbital elements. As verification of the implementation of the Lagrange equations, Cowell's method is used by numerically integrating the perturbed equations of motion. This also allows for the application of the brute force method, this time to verify the implementation of Escobal's method.
To summarise, the visibility problem is tackled using Escobal's controlling equation. At first, this is tested for satellites in a Low Earth Orbit, for which plenty of reference material exists. Afterwards, the same methodology is applied to the Lunar orbiter Garatéa-L, a Lunar orbiter. The Keplerian orbit forms the foundation, upon which perturbations, included through the use of the Lagrange equations, are built. The perturbations to be considered are caused by a nonspherical primary body, particularly zonal harmonics, and the attraction of a third body. Both the Lagrange equations and Escobal's method are verified by the application of Cowell's method and the brute force method.
In order to do so, the necessary theoretical background is explored in section 2. This starts with the introduction of the two-body problem and ends with the inclusion of perturbations. Section 3 then describes the procedures that lead to the results presented and discussed in section 4. Finally, conclusions are drawn and recommendations for future research are given in section 5.

2 Theoretical Background

In this section, the required theoretical background, in the form of orbital mechanics, is reviewed. This starts with the introduction of the two-body problem. The corresponding equation of motion is derived and solved, and its applicability to orbital mechanics is discussed. Next, orbits in two dimensions are discussed. Mathematical statements for Kepler's laws are established, after which various other relevant orbital parameters are presented. Then, the switch is made to three-dimensional orbits, which allows for the establishment of the orbital elements. After that, the visibility problem is discussed. A useful frame of reference is introduced, in which the constraint equation for visibility is developed. From this, using Escobal's method, the controlling equation is presented. Lastly, perturbations are introduced. This starts with mathematical techniques that can be used to incorporate perturbations, and is then followed by the development of actual expressions for perturbations caused by a nonspherical primary body.

2.1 Two-body problem

The two-body problem is a problem in classical mechanics, and it studies the motion of two particles that attract each other following Newton's gravitational law. In order to solve this problem, the following simplifying assumptions are made [3].

1. The two attracting bodies are point masses.
2. Aside from the gravitational force of the two point masses, there are no other forces present, neither internal nor external.

The goal is to determine the position and velocity vector, together called the state vector, of both particles at some moment in time, based on an initial state vector [21]. The two-body problem is a specific case of the N-body problem, which, as the name suggests, studies the motion of N interacting particles [3]. Until now, the two-body problem is the only case that can be solved analytically [33].
This section starts with the derivation of the equation of motion of the two-body problem. The obtained differential equation is then applied to orbital mechanics. In order to do that, the underlying assumptions of the two-body problem must be justified. With the switch made to orbital mechanics, constants of motion are explored. With the help of these constants of motion, the equation of motion is solved, resulting in the orbital equation.

2.1.1 Equation of motion

Consider two particles or point masses with mass M and m, as shown in figure 2. Here $\vec{F}_1$ is the force acting on P_1 with mass M due to P_2. $\vec{F}_2$ acts on P_2 and is similar in magnitude, but opposite in direction. The frame of reference in black is placed arbitrarily and should be either at rest or moving with constant velocity in a straight line, without rotating [20].

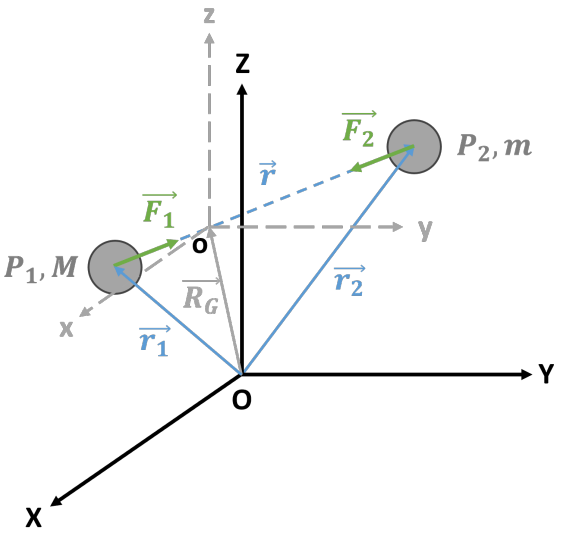

Figure 2: Two point masses in an initial frame of reference XYZ with an arbitrary origin, and a new frame of reference xyz with the barycentre as the origin

Newton's second law, the governing equation, is given as

$$\vec{F} = m\vec{a} = m\ddot{\vec{r}}. \tag{2.1}$$

An expression for the force can be found through Newton's law of universal gravitation [20], which gives

$$\begin{aligned} \vec{F_1} = M\ddot{\vec{r}}_1 &= \ G\frac{Mm}{r^2}\frac{\vec{r}}{r}; \\ \vec{F_2} = m\ddot{\vec{r}}_2 &= -G\frac{Mm}{r^2}\frac{\vec{r}}{r}; \end{aligned} \quad \vec{r} = \vec{r}_2 - \vec{r}_1; \quad r = ||\vec{r}||. \tag{2.2}$$

The position of the barycentre (centre of mass) $\vec{R}_G$ of this system is found through [34]

$$\vec{R_G} = \frac{M\vec{r}_1 + m\vec{r}_2}{M+m}. \tag{2.3}$$

The acceleration of the barycentre, making use of equation (2.2), is given by

$$\ddot{\vec{R}}_G = \frac{M\ddot{\vec{r}}_1 + m\ddot{\vec{r}}_2}{M+m} = \frac{G\frac{Mm}{r^2}\frac{\vec{r}}{r} - G\frac{Mm}{r^2}\frac{\vec{r}}{r}}{M+m} = 0. \tag{2.4}$$

This means that the barycentre can be used as the origin for the frame of reference, more on that in the following section. Subtracting $\vec{F}_1$ from $\vec{F}_2$ gives

$$\ddot{\vec{r}} = -G\frac{M+m}{r^3}\vec{r}. \tag{2.5}$$

This is a linear second order differential vector equation that describes the motion of P_2 relative to P_1. Six constants of integration are required to solve the differential equation.

2.1.2 Orbital mechanics

In orbital mechanics, generally one body is much heavier than the other, think of the Earth orbiting the Sun, or an artificial satellite orbiting the Moon. This means that the gravitational parameter and the barycentre can be simplified to

$$\mu = G(M+m) \approx GM; \quad \vec{R_G} \approx \vec{r_1}; \quad \text{as } M \gg m. \tag{2.6}$$

This simplification means that P_1 is assumed to be fixed in space, so only P_2 is moving. Therefore, the problem has effectively been reduced to a one particle system [34]. Substituting μ in the differential equation gives

$$\ddot{\vec{r}} = -\frac{\mu}{r^3}\vec{r}. \tag{2.7}$$

When applying equation (2.7) to orbital mechanics, the simplifying assumptions of the two-body problem mentioned above must be addressed. At first glance, it seems that they do not match reality. Point masses are an idealisation [35], and space is filled with objects that exert their own gravitational force. However, through a closer examination, both assumptions can be justified.

Point masses Modelling objects as point masses is a simplification often used in physics. In order to show that this simplification is allowed, a look must be taken at the gravitational potential energy V. For two point masses, as described in the two-body problem, the potential energy is given by [21]

$$V = -G\frac{Mm}{r}. \tag{2.8}$$

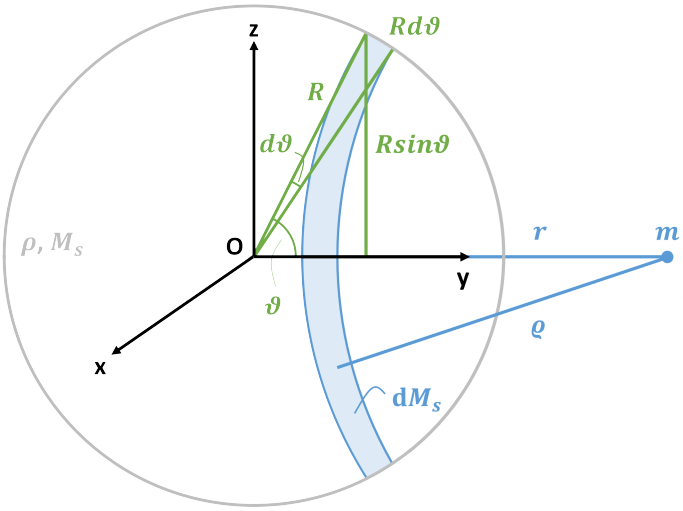

Figure 3: Spherical shell with radius R, constant density per unit area ρ, and mass M_s, and a particle with mass m.

Now consider a spherical shell with constant density per unit area ρ, and a point mass with mass m, as shown in figure 3. The potential energy due to the shell can be calculated by looking at an annulus of infinitesimal width, as shown in blue in figure 3. Throughout the annulus, the distance to the point mass remains constant, denoted by ϱ. Therefore, the gravitational potential energy due to this annulus is

$$dV_s = -\frac{1}{\varrho} Gm\rho \underbrace{2\pi R^2 \sin\vartheta d\vartheta}_{\text{area annulus}}. \tag{2.9}$$

Integrating this over the whole shell gives the gravitational potential energy of the entire shell

$$V_s = -G\frac{4\pi R^2 \rho m}{r} = -G\frac{M_s m}{r}. \tag{2.10}$$

Note that this only holds for points on or outside the shell, so $r \geq R$. To keep the main content of this report concise, more involved derivations are moved to appendix C. The first entry there is a full derivation of equation (2.10), and it can be seen in appendix C.1.1. Note that there is no dependence on ϱ or R left. Now make a solid sphere that is composed of n concentric shells, each with a mass of M_{s_i}. The potential energy due to this solid sphere is given by

$$V = \sum_{i=1}^{n} -G\frac{M_{s_i} m}{r} = -G\frac{Mm}{r}; \quad \sum_{i=1}^{n} M_{s_i} = M. \tag{2.11}$$

This is identical to equation (2.8). Therefore, if the primary body is spherical and has a uniform mass distribution, the gravitational potential energy that is experienced by a satellite outside the radius of the primary body is identical to the gravitational potential energy of a point mass. Accordingly, the force is identical as well, meaning the two-body problem can be applied.

An important side note is that, in reality, the Earth and other celestial bodies do not have a uniform density, nor are they perfectly spherical. The polar radius of for example the Earth is 0.3% smaller than its equatorial radius [22]. The Moon is almost perfectly spherical, but has an uneven mass concentration [36] [37]. Nevertheless, the deviations are relatively minimal, so representing celestial bodies as point masses will suffice for now. The higher order effects of nonspherical gravity are addressed in section 2.6.1.

Forces The second assumption of the two-body problem also needs some explanation, as, in reality, there can be many other forces acting on the system in addition to the gravitational attraction between the two bodies of interest. One example is the gravitational attraction of a third body. A satellite in orbit of the Earth is also attracted by other celestial bodies, such as the Sun or Moon. However, as seen in Newton's law of universal gravitation, equation (2.2), the gravitational force is inversely proportional to the distance squared. Hence, close by the Earth, the magnitude of the Sun's gravitational force should be negligible compared to the attraction of the Earth. The region around the Earth where the attraction of other bodies can be considered by perturbations is called the sphere of influence (SOI) [21]. The size of this region can be determined by looking at the ratio of primary and perturbing accelerations. In figure 4, a schematic of the Sun, the Earth and a satellite in orbit around the Earth called a vehicle is seen [20]. The Earth and the vehicle are drawn much further apart than is the case in reality. This is done solely for illustrative purposes. Keeping this in mind, the position vectors and their magnitudes are related as

$$\vec{r_1} = \vec{r_2} + \vec{r_3}; \quad r_1 \approx r_2. \tag{2.12}$$

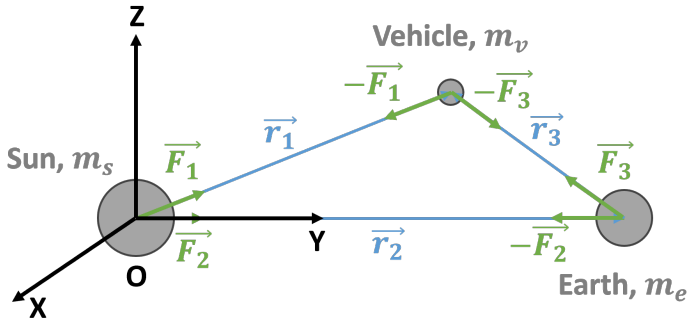

Figure 4: Three body system of the Sun, the Earth, and a vehicle, shown in an inertial frame of reference with its origin at the centre of mass of the Sun.

In the same manner as in section 2.1, the equation of motion of the vehicle relative to the Sun is given by

$$\ddot{\vec{r_1}} = \underbrace{-G\frac{m_s}{r_1^3}\vec{r_1}}_{\vec{a_s}} \underbrace{-G\frac{m_e}{r_3^3}\vec{r_3}}_{\vec{p_e}}. \tag{2.13}$$

Here, the first term $\vec{a_s}$ is the primary acceleration due to the Sun, and the second term $\vec{p_e}$ is the perturbing acceleration due to the Earth.
The equation of motion of the vehicle relative to Earth is given by

$$\ddot{\vec{r_3}} = \underbrace{-G\frac{m_e}{r_3^3}\vec{r_3}}_{\vec{a_e}} \underbrace{-G\frac{m_s}{r_1^3}\vec{r_3}}_{\vec{p_s}}. \tag{2.14}$$

A full derivation is seen in appendix C.1.2. Here, the first term $\vec{a_e}$ is the primary acceleration due to the Earth, and the second term $\vec{p_s}$ is the perturbing acceleration due to the Sun. The magnitudes of the primary and perturbing accelerations, using equation (2.12) to simplify, are given as

$$\begin{aligned} a_s &= G\frac{m_s}{r_2^2}; \qquad a_e = G\frac{m_e}{r_3^2}; \\ p_s &= G\frac{m_s}{r_2^3}; \qquad p_e = G\frac{m_e}{r_3^2}. \end{aligned} \tag{2.15}$$

When choosing which body causes the primary acceleration and which body is responsible for the perturbing acceleration, the correct choice corresponds to the situation that minimises the perturbation ratio p/a. Right at the edge of the sphere of influence, the ratios for both approaches are equal. Solving this for the radius of the sphere of influence r_{SOI} gives

$$\frac{a_s}{p_e} = \frac{a_e}{p_s} \Rightarrow r_{\text{SOI}} = r_2 \left(\frac{m_e}{m_s}\right)^{\frac{2}{5}}. \tag{2.16}$$

Here r_2 corresponds to the semi-major axis of the orbit of the Earth. The actual values of this and r_{SOI} can be seen in appendix A. There it can be seen that the Moon is well within the sphere of influence of the Earth, meaning that the orbit of the Moon is primarily governed by the Earth. In simpler terms, the Moon orbits around the Earth.
With that in mind, the exact same analysis could be done for a satellite that orbits the Moon. In this analysis, the Earth is replaced by the Moon, and the third (perturbing) body is the Earth instead of the Sun. The results of this analysis is the sphere of influence of the Moon, whose value can be found in appendix A as well.
In conclusion, when a satellite is well within the sphere of influence of the primary, which is the case for satellites in LEO or LLO, the gravitational acceleration of the primary body dominates and a two-body approach suffices for now [31]. Third body perturbations will be addressed in section 2.6.2.
Aside from third body attraction, there are other forces that could act on a satellite as well. Think of thrust and drag forces, solar radiation pressure, tidal friction effects [2]. Although these effects, dependent on the situation, could be significant, they fall outside the scope of this report and are therefore neglected. This does diminish accuracy, but the loss is not that substantial. Satellites in LEO are primarily perturbed by drag and nonspherical gravity, [38]. However, drag forces decline heavily with altitude, and above 500 km, they become less and less significant [39] [40]. The Moon does not have a noteworthy atmosphere, so drag perturbations are non-existent. For a satellite in a LLO, nonspherical gravity and third body attraction due to the Earth dominate [31].
Now that both assumptions of the two-body problem are addressed, the switch to orbital mechanics can be made. Therefore, looking back to figure 2, P_2 is now called the satellite, and P_1 the primary body.

2.1.3 Constants of motion

Before working on the solution, it is useful to have a look at two constants of motion, as they aid in solving the equation of motion and are relevant parameters to be used later on.

Specific angular momentum The specific angular momentum $\vec{h}$ of the satellite relative to the primary body is given by

$$\vec{h} = \vec{r} \times \dot{\vec{r}}; \quad h = rv \sin(\vartheta). \tag{2.17}$$

Here ϑ is the angle between the two vectors. Taking the time derivative and using the equation of motion, equation (2.7), gives

$$\dot{\vec{h}} = \dot{\vec{r}} \times \dot{\vec{r}} + \vec{r} \times \ddot{\vec{r}} = -\frac{\mu}{r^3}(\vec{r} \times \vec{r}) = 0. \tag{2.18}$$

This shows that the specific angular momentum remains constant throughout the trajectory. Furthermore, going back to the definition in equation (2.17), it also shows that the position and velocity vector always lie in the same plane. This plane is called the orbital plane, and is further defined in section 2.2.4.

Mechanical energy The specific mechanical energy ε is also conserved along the orbit. This can be found by taking the dot product of the velocity and acceleration vector. Using the equation of motion, equation (2.7), this becomes

$$\dot{\vec{r}} \cdot \ddot{\vec{r}} = \dot{\vec{r}} \cdot -\frac{\mu}{r^3}\vec{r}. \tag{2.19}$$

After some manipulations, which can be seen in appendix C.1.3, this equation can be integrated to yield

$$\frac{d}{dt}\left(\frac{v^2}{2} - \frac{\mu}{r}\right) = 0 \quad \Rightarrow \quad \frac{v^2}{2} - \frac{\mu}{r} = \varepsilon. \tag{2.20}$$

In this equation, a statement of conservation of energy, it can be seen that the relative specific kinetic energy $v^2/2$ together with the specific potential energy $-\mu/r$ gives the specific mechanical energy ε, which is conserved along the trajectory [20]. This is to be expected, as gravity is a conservative force. When the distance between primary body and satellite r is small, the kinetic energy dominates. When the satellite moves further away, kinetic energy is exchanged for potential energy.

2.1.4 Polar orbital equation

Now, to solve the equation of motion (2.7), use can be made of the fact that specific angular momentum is conserved. Take the cross product of equation (2.7) and the specific angular momentum to obtain

$$\ddot{\vec{r}} \times \vec{h} = -\frac{\mu}{r^3}\vec{r} \times \vec{h}. \tag{2.21}$$

After some manipulations, see appendix C.1.4 for the full derivation, this yields

$$\frac{d}{dt}\left(\dot{\vec{r}} \times \vec{h} - \mu\frac{\vec{r}}{r}\right) = 0 \quad \Rightarrow \quad \dot{\vec{r}} \times \vec{h} - \mu\frac{\vec{r}}{r} = \vec{B}. \tag{2.22}$$

Here $\vec{B}$ is a constant of integration, called the Laplace-Runge-Lenz vector. It defines the direction of closest passage of the satellite. To turn this into a scalar equation, take the scalar product with $\vec{r}$, to get

$$\vec{r} \cdot \left(\dot{\vec{r}} \times \vec{h}\right) = \mu\frac{\vec{r} \cdot \vec{r}}{r} + \vec{r} \cdot \vec{B} \Rightarrow r = \frac{h^2}{\mu}\frac{1}{1 + e\cos \mathrm{f}}. \tag{2.23}$$

Again, the full derivation can be seen in appendix C.1.5. The obtained equation is the polar orbital equation, or the orbital equation in short, and it denotes the radial distance between the primary body M and the satellite m. In the equation, the eccentricity e appears, which is the magnitude of the eccentricity vector $\vec{e}$. The eccentricity vector is in the same direction as the Laplace-Runge-Lenz vector, but scaled with μ. It is defined as

$$\vec{e} = \frac{\vec{B}}{\mu}. \tag{2.24}$$

Furthermore, the true anomaly f is the angle between the eccentricity and the position vector, as visualised in figure 6.
The orbital equation, equation (2.23), is the solution of the equation of motion, equation (2.7). Initially, the goal was to solve for the position and velocity as a function of time, but the position is now given by an autonomous system. In section 2.2.3 the relation between true anomaly and time will be addressed.
Dependent on the value of e, equation (2.23) can result in four different trajectories [41]. This can be seen in figure 5. When $e < 1$, the trajectory stays bounded for all true anomalies, which is why they are called orbits.

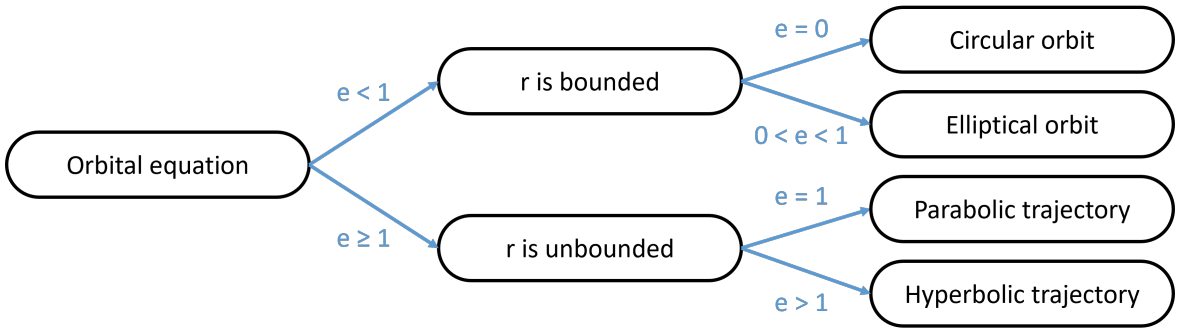

Figure 5: Resulting trajectory or orbit based on the value of eccentricity e in the polar orbital equation.

2.2 Orbits in two dimensions

In this report, interest lies in orbits, and so the eccentricity will be bounded to $e < 1$. Furthermore, the focus lies on elliptical orbits, as a circular orbit is simply an elliptic orbit with no eccentricity [20]. First, mathematical statements for Kepler's laws of planetary motion that were shown in the introduction, section 1, are developed. Next, various relevant variables of the orbit are analysed. Last is the proper introduction of the perifocal reference frame, a frame aligned with the orbital plane.

2.2.1 Kepler's laws of planetary motion

A schematic of an elliptical orbit can be seen in figure 6. An ellipse is defined by its semi-major and its semi-minor axis, denoted with a and, b respectively. These are related through the eccentricity as

$$e = \sqrt{1 - \frac{b^2}{a^2}}. \tag{2.25}$$

The satellite m orbits the primary body M, which is located at the focus F, in counterclockwise direction with increasing true anomaly f.

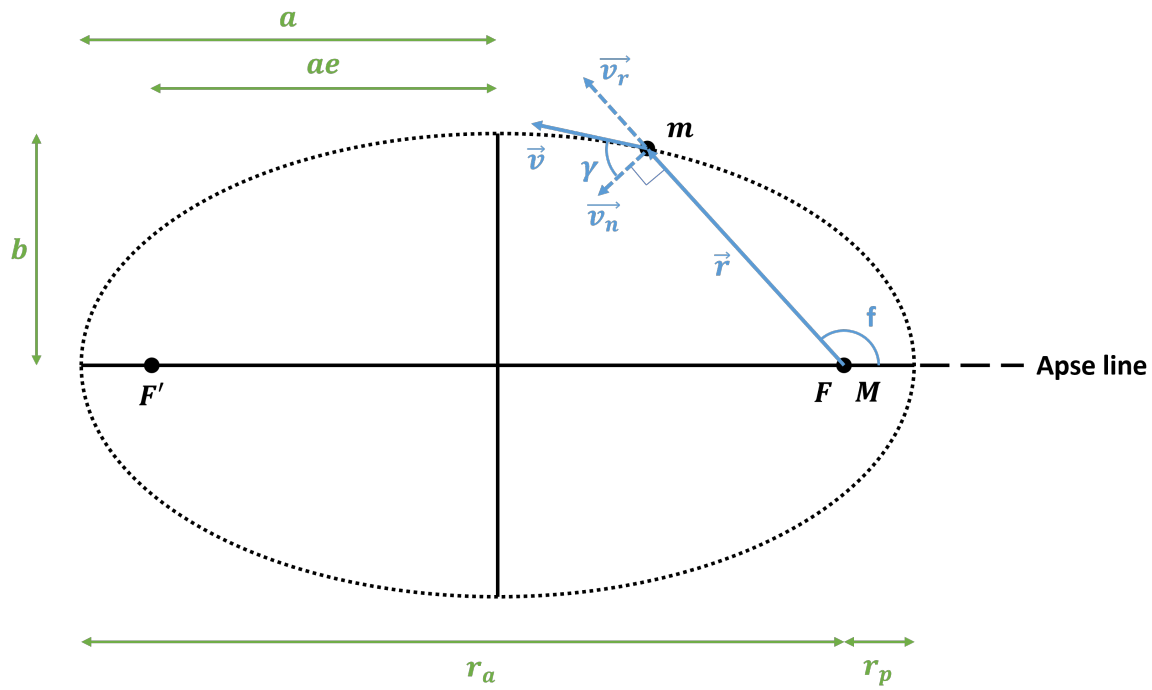

Figure 6: Schematic of an elliptic orbit viewed from above and looking down onto the orbital plane. The primary body M is located at the right focus F, while the focus on the left F' is empty. The apse line connects the closest and furthest passage of the satellite, called the periapsis and apoapsis, respectively.

The minimum and maximum values of r, denoted with r_p for the periapsis, and r_a for the apoapsis, can also be seen in figure 6. These names for the closest and furthest point in an orbit are the general terms. For a Terrestrial satellite, these points are called the perigee and apogee, respectively, while they are named periselene and apselene when a Lunar satellite is considered [42]. With whatever name they are indicated, these points are connected by the apse line, and they can be expressed as

$$\begin{aligned} r\left(\mathrm{f}=0\right) = r_p &= \frac{h^2}{\mu}\frac{1}{1+e}; \\ r\left(\mathrm{f}=\pi\right) = r_a &= \frac{h^2}{\mu}\frac{1}{1-e}. \end{aligned} \tag{2.26}$$

From figure 6 it can be seen that

$$2a = r_p + r_a \quad \Rightarrow \quad a = \frac{h^2}{\mu}\frac{1}{1-e^2}. \tag{2.27}$$

Plugging this in the orbital equation, equation (2.23), gives an alternative form, which can be more convenient in some cases, as will become clear with the introduction of orbital elements in section 2.3.2. It reads as

$$r = a\frac{1-e^2}{1+e\cos\mathrm{f}}. \tag{2.28}$$

This equation is a mathematical statement of Kepler's first law. It describes the elliptical orbits that planets follow around the Sun.
Kepler's second and third law can also be given by mathematical statements. An example of a swept out area ΔA, as is mentioned in Kepler's second law, is shown in figure 7.

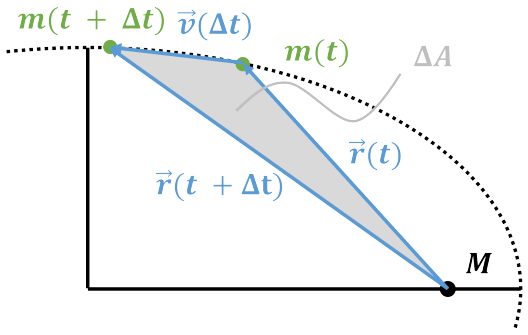

Figure 7: Schematic of a swept out area ΔA in time Δt

Together with the flight path angle, which is defined in figure 6, the swept out area is given by

$$\Delta A = \frac{1}{2}\underbrace{v\Delta t}_{\text{base}}\underbrace{r\sin\left(\frac{1}{2}\pi-\gamma\right)}_{\text{height}}. \tag{2.29}$$

Plugging in the angle $\left(\frac{1}{2}\pi-\gamma\right)$ in equation 2.17 gives an expression for the specific angular momentum and the swept area as

$$h = rv\sin\left(\frac{1}{2}\pi-\gamma\right) \quad \Rightarrow \quad \frac{\Delta A}{\Delta t} = \frac{1}{2}h. \tag{2.30}$$

Since h is constant, the swept out area in a given amount of time Δt is constant as well, which is exactly what Kepler's second law states.

For Kepler's third law, take a full orbital revolution in equation (2.30) to get

$$\frac{A}{T} = \frac{1}{2}h; \quad A = A_{\text{ellipse}} = \pi ab. \tag{2.31}$$

Solving for the period, using equations (2.25) and (2.27), gives

$$T = \frac{2\pi ab}{h} = 2\pi\sqrt{\frac{a^3}{\mu}}. \tag{2.32}$$

This indeed conforms to Kepler's third law, as the mean value that is mentioned is the average of the periapsis and apoapsis, which, following equation (2.28), is the semi-major axis a [3].

2.2.2 Velocity

Looking back to figure 6, where the velocity vector of the satellite is shown, it can be decomposed in a normal v_n and a radial v_r component. This decomposition can be applied to equation (2.17), and with the help of the orbital equation, equation (2.23), the normal velocity is found as

$$h = r\underbrace{v\sin\vartheta}_{v_n} \quad \Rightarrow \quad v_n = \frac{h}{r} = \frac{\mu}{h}\left(1 + e\cos\mathrm{f}\right) = r\dot{\mathrm{f}}. \tag{2.33}$$

The radial velocity can be found by taking the derivative of the orbital equation (2.23) with respect to time, and by making use of the angular velocity in the equation above, giving

$$v_r = \dot{r} = \frac{dr}{d\mathrm{f}}\,\dot{\mathrm{f}} = \frac{\mu}{h}e\sin\mathrm{f}. \tag{2.34}$$

The speed is given by

$$v = \sqrt{v_r^2 + v_n^2} = \frac{\mu}{h}\sqrt{1 + e^2 + 2e\cos\mathrm{f}}. \tag{2.35}$$

Another expression for the speed can be found by making use of the specific mechanical energy, equation (2.20). To determine the value of ε, a point in the orbit must be plugged in. A convenient choice is the perigee, see equation (2.26) for r_p and equation (2.33) for v_p, as there is only a normal velocity component. With that in mind, the apogee could have been chosen as well. Plugging in the expressions gives the following for the specific mechanical energy

$$\varepsilon = -\frac{1}{2}\frac{\mu^2}{h^2}\left(1 - e^2\right). \tag{2.36}$$

An alternative form can be found by using equation (2.28)

$$\varepsilon = -\frac{1}{2}\frac{\mu^2}{\mu a\left(1 - e^2\right)}\left(1 - e^2\right) = -\frac{1}{2}\frac{\mu}{a}. \tag{2.37}$$

This equation shows that the specific mechanical energy only depends on the semi-major axis and not on, for example, the eccentricity. Plugging this back in equation (2.20) and solving for speed gives

$$v = \sqrt{\mu\left(\frac{2}{r} - \frac{1}{a}\right)}. \tag{2.38}$$

This is called the vis-viva equation, and it shows the exchange of kinetic and potential energy, as was explained at the end of section 2.1.3.

2.2.3 Flight time equation

As stated earlier, the time variable does not appear in the orbital equation, where the position of the satellite is a function of true anomaly. The relation between position and time can be found using Kepler's second law and some geometry, for which figure 8 is a useful guide [3] [21]. In this figure, an ellipse with semi-major axis a has been circumscribed with a so-called auxiliary circle with radius a. Equation (2.32) shows that an orbital period is independent of eccentricity, meaning that a hypothetical satellite orbiting in the auxiliary circle would have the same period as the actual satellite in the elliptic orbit. On this auxiliary circle, with the same x-coordinate as the satellite, a point L can be found, a point that defines the eccentric anomaly E.
The y-coordinates of the ellipse and circle can be related through the general definitions of ellipses and circles as

$$\left.\begin{aligned} \frac{x_c^2}{a^2} + \frac{y_c^2}{a^2} &= 1 \\ \frac{x_e^2}{a^2} + \frac{y_e^2}{b^2} &= 1 \end{aligned}\right\} \quad \frac{y_e}{y_c} = \frac{b}{a}. \tag{2.39}$$

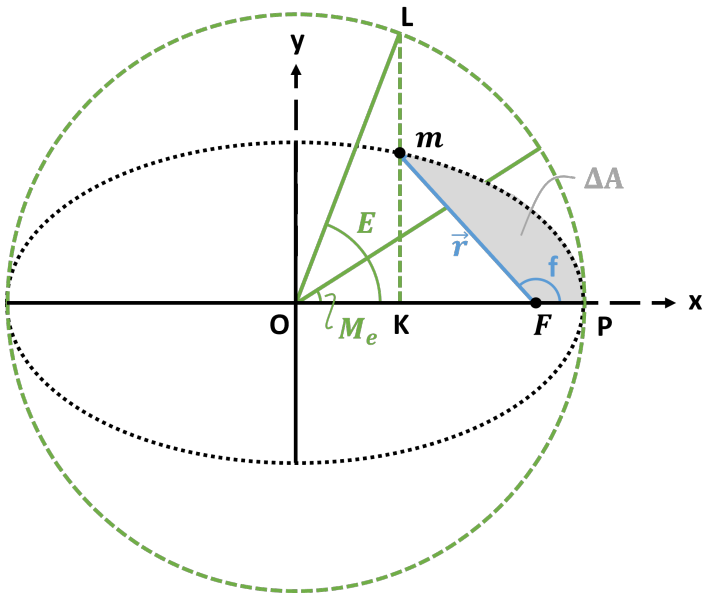

Figure 8: Eccentric anomaly E and mean anomaly M_e defined through an auxiliary circle

With the use of the measurements seen in figure 6 and some geometry, the shaded area ΔA in figure 8 is found to be

$$\Delta A = \frac{1}{2} ab \left(E - e \sin E \right). \tag{2.40}$$

The full derivation can be seen in appendix C.2.1. The time Δt that it took to sweep out the shaded area ΔA, can be found through Kepler's second and third law, equations (2.30) and (2.32), and is found to be

$$\frac{\Delta t}{T} = \frac{\Delta A}{\pi ab} \quad \Rightarrow \quad \Delta t = (E - e \sin E) \sqrt{\frac{a^3}{\mu}}; \quad \Delta t = t - \tau. \tag{2.41}$$

Here τ is the time at periapsis, which is often set to zero for convenience. t is the time since periapsis, but with $\tau = 0$, it is also simply time. Now the mean motion n is introduced, it is the mean angular velocity of the satellite. It can also be thought of the angular velocity of a satellite in a circular orbit, corresponding to the auxiliary circle in figure 8. From equation (2.35) it is seen that the velocity, and therefore the angular velocity, is constant in a circular orbit.

If the mean motion is multiplied with time, an angle called the mean anomaly M_e is found, as

$$n = \frac{2\pi}{T} = \sqrt{\frac{\mu}{a^3}}\,; \quad M_e = n\Delta t = 2\pi\frac{\Delta t}{T}. \tag{2.42}$$

Plugging this in equation (2.41) gives Kepler's equation

$$M_e = E - e\sin E. \tag{2.43}$$

With the help of Kepler's equation, the link between true anomaly and time is almost complete. The final step is to relate eccentric and true anomaly. This can be done by expressing the length of OK in figure 8 in two ways and setting them equal. This gives

$$a\cos E = ae + r\cos \mathrm{f} \quad \Rightarrow \quad E = \arccos\left(\frac{e+\cos \mathrm{f}}{1+e\cos \mathrm{f}}\right). \tag{2.44}$$

Although this is a valid expression, it leads to quadrant ambiguity. By using a trigonometric identity, this can be resolved. The relation becomes

$$E = 2\arctan\left(\sqrt{\frac{1-e}{1+e}}\tan\frac{\mathrm{f}}{2}\right); \quad \tan^2\vartheta = \frac{1-\cos 2\vartheta}{1+\cos 2\vartheta}. \tag{2.45}$$

With these relations, given a true anomaly, the corresponding eccentric anomaly is found through equation (2.45). Then Kepler's equation, equation (2.43) yields the mean anomaly, which relates to the time since periapsis with the help of the mean motion in equation (2.42). The other way around, solving for the true anomaly when time is given, is a bit more complicated. Kepler's equation, equation (2.43), is transcendental and cannot be solved analytically for E. Various solution methods, like Lagrange expansion or Newton-Raphson, can be applied to solve for the eccentric anomaly [43] [44]. True anomaly is then found by rewriting equation (2.45) to

$$\mathrm{f} = 2\arctan\left(\sqrt{\frac{1+e}{1-e}}\tan\frac{E}{2}\right). \tag{2.46}$$

2.2.4 Perifocal frame

So far, quantities like position and velocity have been developed, although no reference frame has yet been mentioned explicitly. So far, this was not strictly necessary, but to facilitate the transition to three dimensions in the next sections, it is useful to do so. Therefore, the perifocal frame is introduced, a frame whose fundamental plane is aligned with the orbital plane, as can be seen in figure 9.

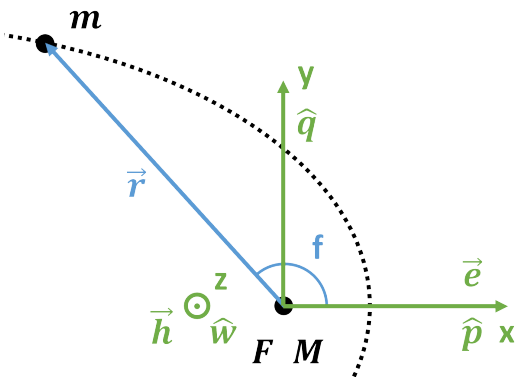

Figure 9: The perifocal reference frame

The origin of the perifocal frame coincides with the primary body that lies in the focus of the orbit. The x-axis is in the direction of the periapsis and is represented by the unit vector $\hat{p}$. This is the same direction as the eccentricity vector $\vec{e}$. The y-axis also lies in the fundamental plane, points in the direction of a true anomaly of $\mathrm{f} = 90°$, and is represented by $\hat{q}$. Lastly, the z-axis is perpendicular to the orbital plane and is represented by $\hat{w}$. It points in the same direction as the angular momentum vector $\vec{h}$, for which it was found that it is perpendicular to both the position and velocity vector in section 2.1.3. Using the orbital equation, equation (2.28), the position vector of the orbiting body can be written as

$$\vec{r} = x\hat{p} + y\hat{q} = \frac{h^2}{\mu}\frac{1}{1 + e\cos\mathrm{f}}\left(\cos\mathrm{f}\hat{p} + \sin\mathrm{f}\hat{q}\right). \tag{2.47}$$

In similar fashion, and using equations (2.33) and (2.34), the velocity vector is given by

$$\vec{v} = \dot{x}\hat{p} + \dot{y}\hat{q} = \frac{\mu}{h}\left(-\sin\mathrm{f}\hat{p} + (e + \cos\mathrm{f})\,\hat{q}\right). \tag{2.48}$$

Using figure 8 and some geometry, the position can also be expressed as a function of eccentric anomaly [19]

$$\vec{r} = a\left(\cos E - e\right)\hat{p} + \left(a\sqrt{1 - e^2}\sin E\right)\hat{q}; \quad r = a\left(1 - e\cos E\right). \tag{2.49}$$

Taking the derivative with respect to time yields the velocity as

$$\vec{v} = -\left(a\dot{E}\sin E\right)\hat{p} + \left(a\dot{E}\sqrt{1 - e^2}\cos E\right)\hat{q}. \tag{2.50}$$

Where the rate of change of the eccentric anomaly can be found from Kepler's equation and the mean motions, equations (2.42) and (2.43)

$$\dot{E} = \frac{n}{1 - e\cos E}. \tag{2.51}$$

2.3 Orbits in three dimensions

Studying orbits in two dimensions is quite convenient in its simplicity, but not all aspects can be studied this way. In this section, the jump to three dimensions is made. To facilitate this, the geocentric-equatorial frame and the geographic coordinate system are introduced. Within this frame, the orbital elements are presented, a convenient set of variables to represent an orbit. Finally, the rotation matrix to transition between the geocentric equatorial frame and the previously established perifocal frame is developed.

2.3.1 Geocentric equatorial frame

In order to study orbits in three-dimensional space, a three-dimensional frame is required. In this report, the geocentric equatorial reference frame is used, as shown schematically in figure 10. The origin of this frame is at the centre of the Earth, and the equator forms the fundamental plane. The x-axis is in the direction of the vernal equinox Υ, pointing towards the Sun at noon on the first day of spring in the Northern Hemisphere [20]. It has the corresponding unit vector $\hat{I}$. The y-direction, which also lies in the fundamental plane, is 90° eastward with respect to the vernal equinox. It is represented by $\hat{J}$. Lastly, the z-direction is normal to the equatorial plane and points northwards. It coincides with the axis of rotation of the Earth and is represented by $\hat{K}$.

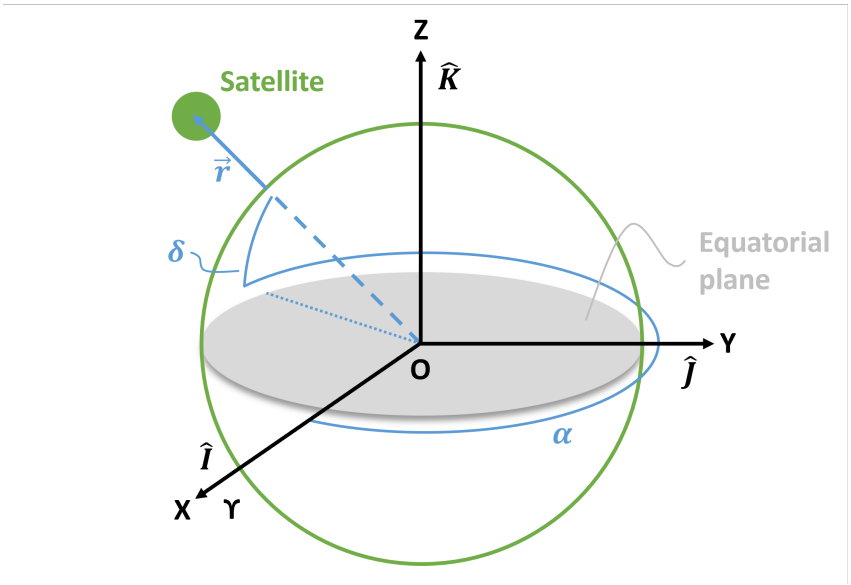

Figure 10: The geocentric equatorial reference frame.

The location of a satellite can be written in either spherical or Cartesian coordinates. The spherical coordinates make use of right ascension α, which measures the degrees eastward of the vernal equinox, and the declination δ, which denotes the degrees north (positive) or south (negative) of the equatorial plane. This gives

$$\vec{r} = r\left(\cos\delta\cos\alpha\hat{I} + \cos\delta\sin\alpha\hat{J} + \sin\delta\hat{K}\right); \quad 0 \leq \alpha < 2\pi; \quad -\frac{\pi}{2} \leq \delta \leq \frac{\pi}{2}. \tag{2.52}$$

Moon As the final objective of this research is to study the visibility of a satellite that orbits the Moon, an appropriate reference frame is desired. This frame is called the Moon-Centered Moon Mean Equator frame and is shown in relation with the geocentric equatorial frame in figure 11 [45]. Just like the geocentric equatorial frame, it is an inertial frame and is generally structured the same way. The equator forms the fundamental plane once more, and the z-axis coincides with the Moon's axis of rotation, pointing northwards. The x-axis is defined to be the IAU-Node of Epoch, which is the cross product of the Earth's z-axis and the Moon's z-axis. This node line is where both Equators cross each other. Lastly, the y-axis is again 90° eastwards in the fundamental plane.
From this point on, whenever the geocentric equatorial frame is mentioned or discussed, it should be kept in mind that the same applies to the corresponding frame of the Moon. The mathematics is identical for either frame.

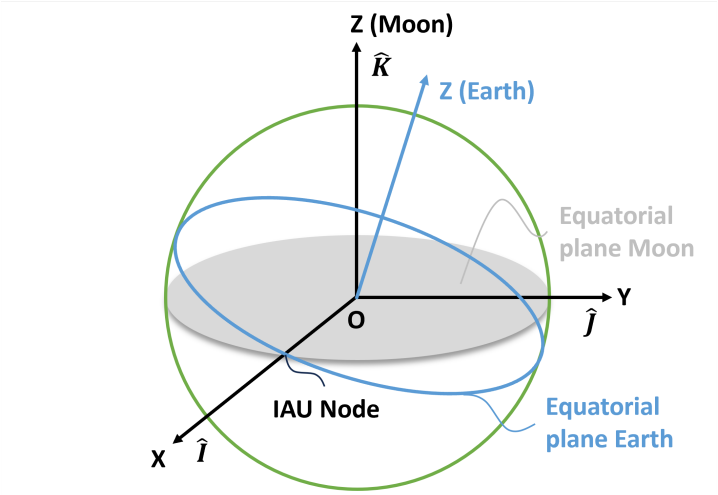

Figure 11: The Moon-Centered Moon Mean Equator reference frame.

2.3.2 Orbital elements

In the polar orbital equation, equation (2.28), the position of the satellite is determined by 3 variables, semi-major axis a, eccentricity e, and true anomaly f. With this, the position within the orbital plane is known. To obtain the position in three dimensions, the orientation of the orbital plane must be defined. The orientation of any rigid object in 3D space can be defined by three angles, also called the Euler angles [46]. These angles are not unique, and several sets exist that can be used interchangeably. In the field of orbital mechanics, the right ascension of the ascending node Ω, inclination i, and argument of perigee ω are employed, as shown in figure 12. Ω is the angle between the vernal equinox and the ascending node. The ascending node lies on the node line, the line where the equatorial and orbital plane intersect. There are two points of intersection, where the ascending node is the specific point in the orbit where the satellite rises above the equatorial plane. Then there is the inclination i, the angle between the equatorial and orbital plane. The inclination is also found as the angle between the axis of rotation of the primary body and the specific angular momentum vector $\vec{h}$. Lastly, the argument of perigee ω is the angle between the node line and the eccentricity vector that points towards the perigee.

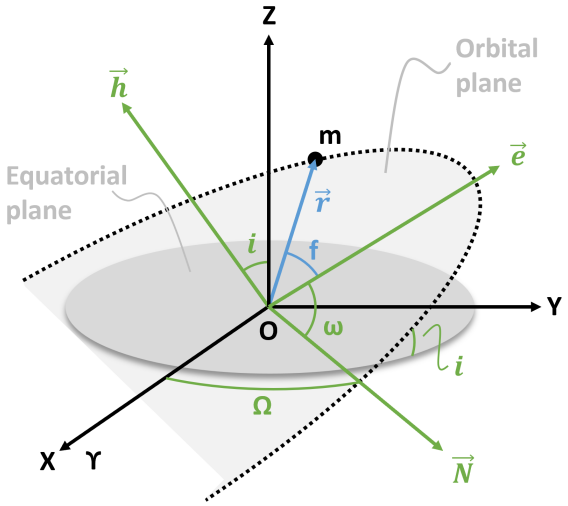

a	semi-major axis
e	eccentricity
i	inclination
Ω	right ascension of the ascending node
ω	argument of perigee
f	true anomaly

Figure 12: Orbital elements in the geocentric equatorial reference frame.

At a given moment in time, the position and velocity vector of a satellite are called the state vector. When the state vector is known, the orbit is fully defined. The same holds for the six variables, together called the orbital elements, shown on the right of figure 12. Either set of six variables suffices, and one set can be transformed in the other. If the state vector is known, the orbital elements can be derived, and vice versa. Transitioning from the orbital elements to the state vector is the topic of the following section, and the process in reverse is described in appendix C.3.1.

As a final note on the orbital elements, the set described here is not unique. True anomaly could, for example, be replaced by eccentric anomaly, mean anomaly, or even time since periapsis. When one variable is known, the others can found using the equations presented in section 2.2. Other elements can also be exchanged for others, as will be done later in section 2.5.

2.3.3 Perifocal to geocentric equatorial frame

In order to transition from the perifocal frame to the geocentric equatorial frame, a rotation is required. This rotation could be done at once in a single, complicated three-dimensional rotation, or it can be achieved by three successive two-dimensional rotations. The second option is both easier to follow and gives more insight in the process, and is therefore the preferred option. Looking at figure 12 once more and focussing on the recently introduced angles in green, the rotations to go from the geocentric equatorial to the perifocal frame are as follows. First rotate around the Z-axis, so around $\hat{K}$, with Ω. This aligns the x-axis with the node line. The second rotation is around the node line $\vec{N}$ with i. Now the z-axis is aligned with the specific angular momentum vector. Finally, rotate around $\vec{h}$ with ω to align the x-axis with the eccentricity vector. Putting these steps in an equation gives the rotation matrix to go from the geocentric equatorial frame to the perifocal frame

$$\begin{aligned}
\mathfrak{R}_{ge\to pf} =& \mathfrak{R}_{\vec{h}}(\omega)\mathfrak{R}_{\vec{N}}(i)\mathfrak{R}_{\hat{K}}(\Omega) \\
=& \begin{bmatrix} \cos\omega & \sin\omega & 0 \\ -\sin\omega & \cos\omega & 0 \\ 0 & 0 & 1 \end{bmatrix} \begin{bmatrix} 1 & 0 & 0 \\ 0 & \cos i & \sin i \\ 0 & -\sin i & \cos i \end{bmatrix} \begin{bmatrix} \cos\Omega & \sin\Omega & 0 \\ -\sin\Omega & \cos\Omega & 0 \\ 0 & 0 & 1 \end{bmatrix} \\
=& \begin{bmatrix} \cos\Omega\cos\omega - \sin\Omega\cos i\sin\omega & \sin\Omega\cos\omega + \cos\Omega\cos i\sin\omega & \sin i\sin\omega \\ -\cos\Omega\sin\omega - \sin\Omega\cos i\cos\omega & -\sin\Omega\sin\omega + \cos\Omega\cos i\cos\omega & \sin i\cos\omega \\ \sin\Omega\sin i & -\cos\Omega\sin i & \cos i \end{bmatrix}.
\end{aligned} \tag{2.53}$$

To execute the rotation in the other direction, as was initially intended, the rotation matrix has to be inverted. Because rotation matrices are orthogonal, taking the inverse is equal to taking the transpose [47]. The position and velocity can thus be expressed in the geocentric equatorial frame as

$$\vec{r}_{ge} = \mathfrak{R}_{pf\to ge}\vec{r}_{pf}; \quad \vec{v}_{ge} = \mathfrak{R}_{pf\to ge}\vec{v}_{pf}; \quad \mathfrak{R}_{pf\to ge} = \mathfrak{R}^T_{ge\to pf}. \tag{2.54}$$

For r_{pf}, equation (2.47) or (2.49), and for v_{pf}, equation (2.48) or (2.50) can be plugged in.

2.4 Visibility problem

With the fundamental orbital mechanics examined, the visibility problem can be explored. The first step is developing an expression for the location of the observer, located on or slightly above the primary body. This is done with the geographic (or selenographic for the Moon) coordinate system. For increased accuracy, the primary body is modelled as an oblate body instead of a spherical one. Therefore, it must be explored how the location of the observer is affected by this. Subsequently, the topocentric horizon frame is introduced, a frame that is centred around the observer and thus well-suited for tackling the visibility problem. In this frame, a constraint equation for visibility is established. This is the equation that is used in the brute force method, as mentioned in the introduction, section 1. Finally, building upon the constraint equation, the controlling equation, as formulated by Escobal, is developed.

2.4.1 Geographic coordinate system

To specify the location of something on (or slightly above) the surface of Earth, the geographic coordinate system is commonly used [48]. The origin of this system is the centre of the Earth, the equator forms the fundamental plane and spherical coordinates are used to specify a position. So far, this system shows many similarities with the geocentric equatorial frame, as shown in section 2.3.1. However, a big difference is that the geographic coordinate system is a moving frame attached to the Earth. The x-direction is pointed at the prime meridian, the meridian that goes through Greenwich, UK. Longitude λ is used to denote the degrees eastward of the prime meridian. Latitude φ denotes the degrees north (positive) or south (negative) of the equatorial plane. The position vector of the observer is therefore given with

$$\vec{R}_{gcs} = (R+H)\left(\cos\varphi\cos\lambda\hat{I} + \cos\varphi\sin\lambda\hat{J} + \sin\varphi\hat{K}\right);. \tag{2.55}$$

$$0 \leq \lambda < 2\pi; \qquad -\frac{\pi}{2} \leq \varphi \leq \frac{\pi}{2}$$

Here R is the radius of the Earth and H the height above sea level. Although ideal when specifying a location on Earth, in the scope of this report, it is advantageous to express the location of the observer in the geocentric equatorial frame, as the position of the satellite can also be given in that frame. Latitude and declination both measure the same quantity, so one can replace the other. In order to link longitude with right ascension, local sidereal time θ is used. The schematic in figure 13 showcases their relation. Longitude plus local sidereal time corresponds to the right ascension α that is right overhead of the observer on the surface.

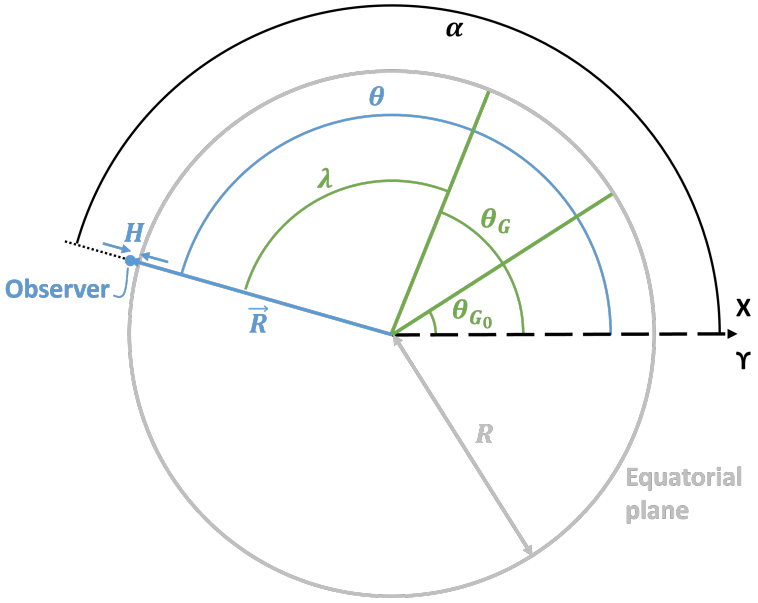

Figure 13: Schematic of the relations between right ascension α, longitude λ, and sidereal time θ.

Figure 13 also shows that the local sidereal time θ is the sum of the longitude of the observer λ and the Greenwich sidereal time θ_G. Since the Earth rotates with a fixed rotational velocity, Greenwich sidereal time is a function of time plus an initial value θ_{G_0}. For the time part, universal time UT is used, a time system that is based around the passage of the Sun across the prime meridian. The procedure of obtaining the Greenwich sidereal time at 0 UT, so the initial condition, involves various standardized calculations based on the time passed since the current Julian epoch $J2000$, which is set at noon on the 1^{st} of January 2000. The exact equations are shown in appendix C.4.1, but in short, it can be written as

$$\begin{aligned} \theta =& \theta_G + \lambda; \\ \theta_G =& \theta_{G_0} + SD\frac{UT}{24} = \theta_{G_0} + \dot{\theta} t_{UT}. \end{aligned} \tag{2.56}$$

Here $\dot{\theta}$ is the rotational velocity of the Earth, UT and t_{UT} are both universal time, written in hours and seconds, respectively. Finally, SD is the mean solar day, which is the time it takes for the Earth to rotate about its axis such that the distant stars appear in the same position. Its value can be found in appendix A. Mean is added because in reality this value is not constant, but varies slightly [20]. Once the local sidereal time is determined, the position vector of an observer can be expressed in the geocentric equatorial frame as

$$\vec{R} = (R+H)\left(\cos\varphi\cos\theta\hat{I} + \cos\varphi\sin\theta\hat{J} + \sin\varphi\hat{K}\right); \quad 0 \leq \theta < 2\pi. \tag{2.57}$$

The Lunar equivalent system to the geographic coordinate system is the selenographic coordinate system [49]. Here, the prime meridian is defined to be approximately the centre of the Moon when it is seen from Earth. Transitioning from the selenographic coordinate system to the Moon-Centered Moon Mean Equator frame is slightly more elaborate due to Lunar librations [50]. Including these phenomena is beyond the scope of this report. Therefore, the problem is simplified, such that as an initial condition it is assumed that the prime meridian of the Moon is aligned with the vernal equinox, such that

$$\theta_{G,\text{Moon}} = SD\frac{UT}{24}. \tag{2.58}$$

2.4.2 Oblate primary body

As stated in section 2.1.2, celestial bodies are not perfectly spherical. One of the more prominent deviations that is also straightforward to implement is oblateness. Due to the rotation of celestial bodies, they slightly bulge at the equator and are slightly flattened at the poles. This shape can be approximated by an ellipse. In this section, only the change in geometry is considered to more accurately specify the position of the observer and its horizon. The gravitational effects will be discussed in section 2.6.1.
Instead of using the eccentricity, as was done for elliptical orbits in section 2.2, it is common to utilize the flatness f. Flatness and eccentricity are related as

$$f = \frac{R_e - R_p}{R_e} = 1 - \sqrt{1 - e^2}; \quad e = \sqrt{2f - f^2}. \tag{2.59}$$

Here R_e and R_p are the equatorial and polar radius respectively, as shown in figure 14. In this figure, both the geodetic and geocentric latitude are shown as well. For a spherical body, these angles are identical, but now they are different except at the poles. The geocentric latitude φ' is the angle between the equator and the position vector of the observer $\vec{R}$. The geodetic latitude φ is the angle between the equator and the normal vector on the surface. The geodetic latitude corresponds to the latitude introduced in section 2.4.1 and is therefore the preferred angle to be used. Using some geometry, as is shown in appendix C.4.2, the position vector of the observer in the geocentric equatorial frame is given by [51][52]

$$\vec{R} = G_1 \left(\cos\varphi \cos\theta \hat{I} + \cos\varphi \sin\theta \hat{J} \right) + G_2 \sin\varphi \hat{K}; \tag{2.60}$$

$$G_1 = \frac{R_e}{\sqrt{1 - (2f - f^2)\sin^2\varphi}} + H; \quad G_2 = \frac{R_e (1 - f)^2}{\sqrt{1 - (2f - f^2)\sin^2\varphi}} + H.$$

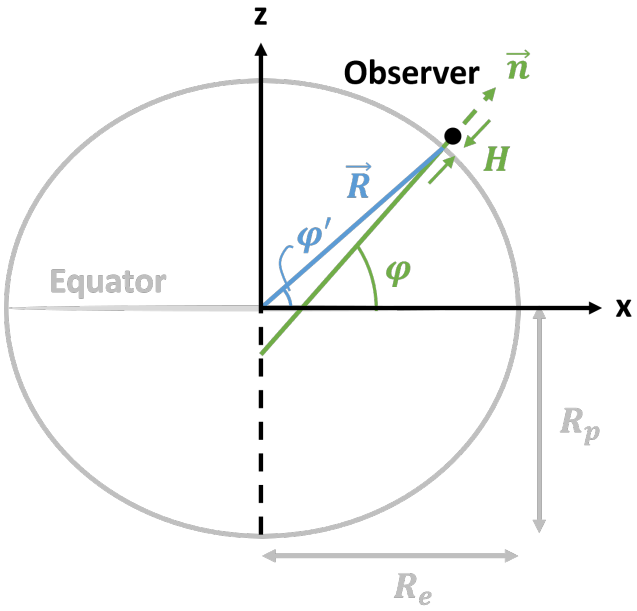

Figure 14: Schematic of an oblate body that shows both the geodetic φ and the geocentric φ' latitude. The oblateness is exaggerated for illustrative purposes.

2.4.3 Topocentric horizon frame

With the position of the observer known, it is convenient to use a suitable reference frame, one that is centred around the observer. This is the topocentric horizon frame, which can be seen in figure 15. It is a moving frame that is attached to the observer, located on or slightly above the surface of the primary body. The fundamental plane is the horizon. In this plane, the x-axis is pointed south and therefore has the corresponding unit vector $\hat{S}$. The y-axis is rotated 90° eastward in the fundamental plane, and points eastwards with unit vector $\hat{E}$. Lastly, the z-axis is normal to the horizon. As this direction points upwards, it is called the zenith, which is denoted with unit vector $\hat{Z}$.
This specific configuration of the topocentric horizon frame is called the SEZ frame. Another common configuration is the ENZ frame, where the x-axis is pointed eastwards and the y-axis points northwards [3].

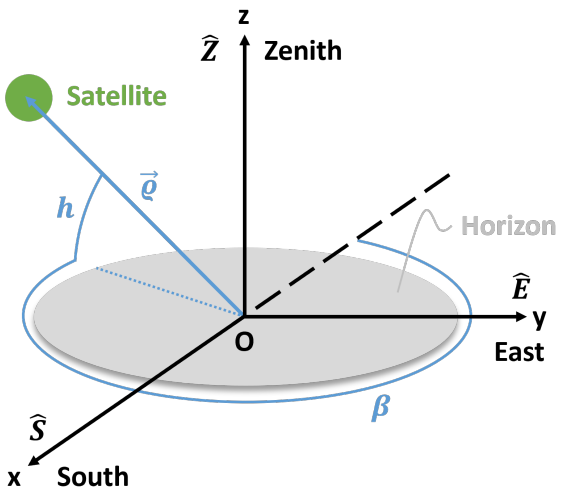

Figure 15: Topocentric horizon frame.

The location of a satellite can be denoted in spherical coordinates with azimuth β, which measures the clockwise degrees from North, and the elevation h, which measures the degrees above or below the fundamental plane. The position vector of the satellite when viewed from the observer is called the slant range vector $\vec{\varrho}$. It is given by [3]

$$\vec{\varrho} = \varrho\left(-\cos h\cos\beta\hat{S} + \cos h\sin\beta\hat{E} + \sin h\hat{Z}\right); \quad 0 \leq \beta < 2\pi; \quad -\frac{\pi}{2} \leq h \leq \frac{\pi}{2}. \tag{2.61}$$

2.4.4 Geocentric equatorial to topocentric horizon frame

To transition from the geocentric equatorial frame to the topocentric horizon frame, a translation and a rotation are required. Both frames are visualised in figure 16. It can be seen that the required translation is equal to the position vector of the observer, equation (2.60), when using an elliptic primary body. Furthermore, the position vectors in the geocentric equatorial frame are related as

$$\vec{\varrho} = \vec{r} - \vec{R}. \tag{2.62}$$

Here $\vec{\varrho}$ has no subscript, as this relation holds in both the geocentric equatorial and the topocentric horizon frame.

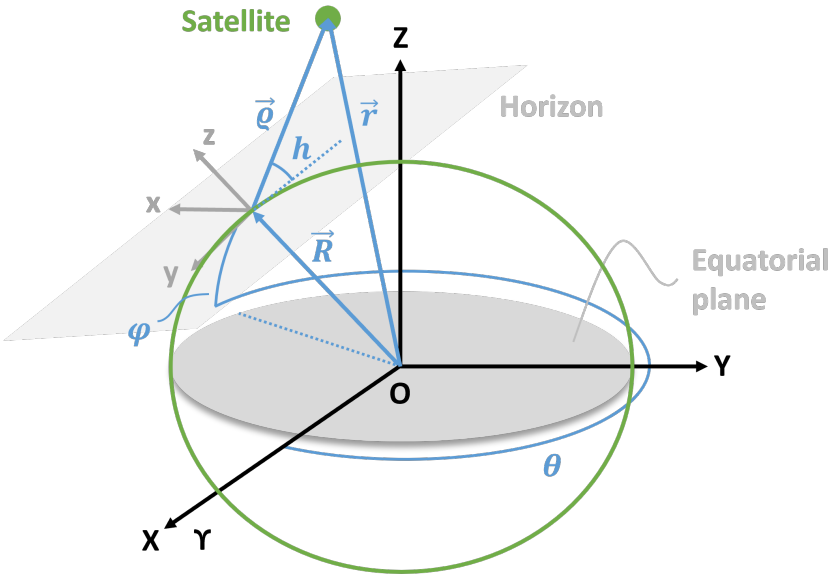

Figure 16: Geocentric equatorial and topocentric horizon frames.

The rotation can be achieved by two subsequent two-dimensional rotations. Using figure 16 as a reference, the topocentric horizon frame is found by first rotating around the Z-axis of the geocentric equatorial frame, so around $\hat{K}$, with the local sidereal time θ. Then around the current orientation of the Y-axis, which is denoted with Y', with $\frac{1}{2}\pi - \varphi$. The rotation matrix looks like

$$\begin{aligned}
\mathfrak{R}_{ge\to th} =& \mathfrak{R}_{Y'}(\frac{1}{2}\pi - \varphi)\mathfrak{R}_{\hat{K}}(\theta) \\
=& \begin{bmatrix} \sin\varphi & 0 & -\cos\varphi \\ 0 & 1 & 0 \\ \cos\varphi & 0 & \sin\varphi \end{bmatrix} \begin{bmatrix} \cos\theta & \sin\theta & 0 \\ -\sin\theta & \cos\theta & 0 \\ 0 & 0 & 1 \end{bmatrix} \\
=& \begin{bmatrix} \sin\varphi\cos\theta & \sin\varphi\sin\theta & -\cos\varphi \\ -\sin\theta & \cos\theta & 0 \\ \cos\varphi\cos\theta & \cos\varphi\sin\theta & \sin\varphi \end{bmatrix}.
\end{aligned} \tag{2.63}$$

With this, the position can be expressed in the topocentric horizon frame as

$$\vec{\varrho}_{th} = \mathfrak{R}_{ge\to th}\vec{\varrho}_{ge}. \tag{2.64}$$

Obtaining the velocity vector is a bit more complicated, since the topocentric horizon frame is a moving frame. However, it is not needed when working on the visibility problem, and will therefore not be discussed.

2.4.5 Constraint equation

In order for a satellite to be visible for an observer, the satellite must at least be above the horizon, meaning a positive elevation angle h. It might be that a larger elevation angle is required before there is visibility, due to for example obstruction of view by a mountain range. This could also work in the other direction, if the observer is located higher than its surroundings, the satellite might be visible below the horizon.
In any case, the elevation angle determines whether the satellite is visible for the observer. Mathematically, this can be described using a constraint equation $\mathfrak{C}$ by taking the dot product of the slant range vector and zenith unit vector [19]

$$\vec{\varrho} \cdot \hat{Z} = \varrho \cos\left(\frac{1}{2}\pi - h\right) \quad \Rightarrow \quad \mathfrak{C} = \left(\vec{r} - \vec{R}\right) \cdot \hat{Z} - \varrho \sin h \geq 0. \tag{2.65}$$

Here, equation (2.62) was used to expand $\vec{\varrho}$. Equation (2.60) gives the position of the observer $\vec{R}$, and the last column of equation (2.63) is used to write the zenith unit vector $\hat{Z}$ in the geocentric equatorial frame. Applying this, the constraint equation can be expanded into components to give

$$\mathfrak{C} = r_x \cos\varphi \cos\theta + r_y \cos\varphi \sin\theta + r_z \sin\varphi - \varrho \sin h - G \geq 0; \tag{2.66}$$

r_x, r_y, and r_z are the components of $\vec{r}$ and these form the ephemeris of a satellite. ϱ and G are given by

$$\varrho = \sqrt{r^2 + G_0^2 - 2r_x G_1 \cos\varphi \cos\theta - 2r_y G_1 \cos\varphi \sin\theta - 2r_z G_2 \sin\varphi}; \tag{2.67}$$
$$G = G_1 \cos^2\varphi + G_2 \sin^2\varphi; \qquad G_0^2 = G_1^2 \cos^2\varphi + G_2^2 \sin^2\varphi.$$

The full derivation of the constraint equation can be seen in appendix C.4.3. With this equation, it can be determined whether there is a line of sight between the observer and the satellite. The brute force method, as mentioned in the introduction, section 1, works by plugging in a myriad of points of the ephemeris and seeing where the constraint equation holds. Through trial and error, the rise and set of the satellite are found. Although this is not a difficult process, the fact that the equation must be solved numerous times makes it a costly method.

2.4.6 Controlling equation

To make this more efficient, [17] developed a so-called controlling equation $\mathfrak{F}$, a transcendental equation that only needs to be solved once or twice per orbital revolution. The constraint equation is modified in a way that leaves only the eccentric anomaly E as a variable. To do so, a couple components in equation (2.66) must be rewritten. First, write the position vector in terms of the perifocal frame and the corresponding rotation matrix. In this frame, the ephemeris can be described by the polar orbital equation. Using equations (2.49) and (2.54), the position vector becomes

$$\vec{r}_{ge} = \mathfrak{R}_{pf \to ge} \vec{r}_{pf} = (a\cos E - e)\,\hat{p} + a\sqrt{1-e^2}\sin E \hat{q}. \tag{2.68}$$

Here, $\hat{p}$ and $\hat{q}$ can be found as the first and second row of the rotation matrix seen in equation (2.53). The slant range, equation (2.67), can be rewritten with the help of equation (2.49) and becomes

$$\varrho = \sqrt{a^2\left(1 - e\cos E\right)^2 + G_0^2 - 2r_x G_1 \cos\varphi \cos\theta - 2r_y G_1 \cos\varphi \sin\theta - 2r_z G_2 \sin\varphi}. \tag{2.69}$$

Lastly, the zenith unit vector can be rewritten, by making use of sidereal time, equation (2.56) and Kepler's equation (2.43)

$$\hat{Z} = \begin{bmatrix} \cos\varphi \cos\left(\lambda + \theta_{G_0} + \dot{\theta}\left(\frac{E - e\sin E}{n} - \tau\right)\right) \\ \cos\varphi \sin\left(\lambda + \theta_{G_0} + \dot{\theta}\left(\frac{E - e\sin E}{n} - \tau\right)\right) \\ \sin\varphi \end{bmatrix}. \tag{2.70}$$

When all of this is plugged in equation (2.65), the controlling equation is found as

$$\mathfrak{F}(E) = (a\cos E - e)\,\hat{p}\cdot\hat{Z}(E) + \left(a\sqrt{1-e^2}\sin E\right)\hat{q}\cdot\hat{Z}(E) - G - \varrho(E)\sin h = 0. \tag{2.71}$$

Here (E) indicates dependence on eccentric anomaly, not multiplication. This relatively simple equation, where the only unknown is the eccentric anomaly E, can be solved to obtain the rise and set time. If the elevation angle for rising and setting are different, the appropriate value must be plugged in, dependent on the case. Then this equation can be solved to obtain the visibility window, which is done once or twice per orbital revolution. This cannot be done analytically, meaning a root-finding algorithm must be employed. This is elaborated upon in section 3.3. Aside from that, the whole procedure is analytical.
Generally speaking, for satellites in a low Earth or Lunar orbit, the controlling function can have six possible shapes for an orbital revolution, all shown in figure 17 [19]. In the first row, the satellite starts out visible, while in the second row, the satellite starts out invisible. The columns show the solutions of two, one, and no roots in an orbital revolution.
Escobal makes use of the fact that these are the only six possible solutions when determining a root estimate that is necessary when solving the controlling equation [17]. This methodology is not applied in this report, as will be elaboration upon in the procedures in section 3.3.

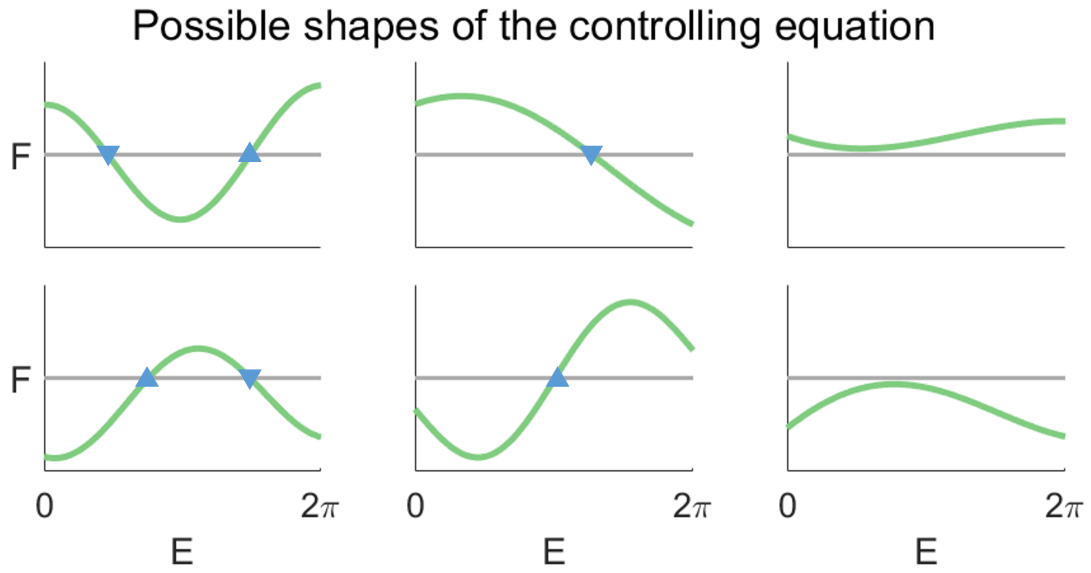

Figure 17: Possible shapes of the controlling equation $\mathfrak{F}$.

2.5 Perturbation techniques

So far, everything that has been discussed is directly based on the two-body problem, which, as mentioned earlier, is not entirely realistic. Although the foundation of the two-body problem remains, there are other phenomena that also play a role. Since these forces are generally small in magnitude, at least relative to the primary gravitational attraction, they are called perturbations. In order to accurately propagate the orbit of a satellite, these perturbations must be addressed [2]. As was indicated in section 2.1.2, there are various causes for perturbations. To recapitulate, they can be caused by gravitational forces, and therefore conservative. Specifically, this could be the attraction of other bodies beside the primary body, or due to a nonspherical primary body. There are also non-gravitational sources, like atmospheric drag or solar-radiation pressure. These perturbations are non-conservative and hence path dependent. No matter what kind of perturbations are included, the equation of motion must be adjusted to [51]

$$\ddot{\vec{r}} + \frac{\mu}{r^3}\vec{r} = \vec{\Gamma}. \tag{2.72}$$

Here $\vec{\Gamma}$ is the sum of all the perturbing accelerations. With this, the original homogeneous equation of motion, equation (2.7) is transformed to an inhomogeneous ordinary differential equation.
This system still has six constants of integration, and the solution can be given by either the state vector or the orbital elements. Various solution methods exist, which can be divided into two main groups: special perturbation techniques and general perturbation techniques [3]. These groups are briefly described before developing the specific methods that will be used in this report.

2.5.1 Special perturbation techniques

Starting with the special perturbation techniques, these methods are aimed at solving for the state vector of the satellite. This is done by numerically integrating the perturbed equation of motion directly, with some time integration scheme. In order to do so, it is often convenient to write the equation of motion, equation (2.72), as a system of first order differential equations [53]

$$\begin{aligned} \dot{\vec{r}} &= \vec{v}; \\ \dot{\vec{v}} &= -\frac{\mu}{r^3}\vec{r} + \vec{\Gamma}. \end{aligned} \tag{2.73}$$

Solving the equations numerically means that an intricate understanding of the perturbing accelerations is not necessarily needed, which can be advantageous. Another advantage is that any and all sorts of perturbations can simply be inserted in the equation of motion. Adversely, the obtained results might not necessarily yield deeper knowledge about the perturbations and their effects. Various methods exist, and in this report Cowell's method is applied.

Cowell's method Cowell's method is very straight forward and works exactly as described above. Directly integrate the perturbed equation of motion numerically [2] using some integration scheme. Aside from its simplicity, another benefit is that this method does not demand that the perturbing accelerations are smaller than the primary acceleration. Although, if this is the case, it might be prudent to review the way in which the system is set up.
A downside of this method is the small time step that is required, especially when the orbit or trajectory is close to a large celestial body. This can be partially mitigated by writing and solving the equation of motion in spherical coordinates instead of Cartesian coordinates, because the state variables will vary slower in this system. However, over longer periods of time, this

remains an expensive method [3]. A slightly more advanced method that partially mitigates the limitation of a small time step is Encke's method, but this goes beyond the scope of this report [54].
Cowell's method will be applied in this study as verification of the forthcoming Lagrange equations. Because the sole goal is validation of the results, the simplicity of Cowell's method is valued highly, while its shortcomings are less relevant.

2.5.2 General perturbation techniques

General perturbation techniques aim to obtain the rate of change of the orbital elements analytically. This process is more involved, and requires some knowledge of orbital mechanics, but it also yields insights into the effects of the perturbations [55]. In the end, depending on the specific method and the type of perturbations, the rates of change of the orbital elements can either be integrated analytically or numerically to obtain their evolution with time. If numerical integration is required, it can be done more efficiently compared to the special perturbation techniques, as the orbital elements change much slower than the state vector [3].
All general perturbation methods are based on variation of parameters, a mathematical technique used to obtain the particular solution of ordinary differential equations once the homogeneous solution is known [53]. Applying variation of parameters to orbital mechanics can be done with various methods. Gauss' method, for example, is a broader method that can handle any type of perturbation, but is therefore also more complex [54]. Lagrange's method can only handle perturbations due to conservative forces, but because of the specialisation, it is simpler in execution. In this report, interest lies in modelling the perturbations caused by a nonspherical primary body and the attraction of a third body. Both perturbations are caused by gravitational attraction, and therefore conservative forces. Thus, Lagrange's method is applicable.

Variation of parameters Variation of parameters, or variation of (the) constants, is a mathematical technique that is used to solve a linear inhomogeneous ordinary differential equation, of which the homogeneous solutions have been found [56]. It can be applied to any order differential equation or system of differential equations, as long as they are linear [57]. The principles of this technique are briefly explored in this section before its application.
For a general system of n first order ordinary differential equations, the solution is based on n constants of integration.

$$\dot{\vec{x}} = \vec{f}\left(\vec{x}, t\right); \quad \vec{x} = \left(x_1, x_2, ..., x_n\right)^T; \quad \vec{f} = \left(f_1, f_2, ..., f_n\right)^T. \tag{2.74}$$

Note that a vector in this case is not defined as a physical vector, as is done in the rest of this report. Instead, it represents an element of $\mathbb{R}^n$ in a more abstract sense. This system is solved by [55]

$$\vec{x} = \vec{\Phi}\left(\vec{c}, t\right); \quad \vec{c} = \left(c_1, c_2, ..., c_n\right)^T. \tag{2.75}$$

Here c_i is a constant of integration. Taking the time derivative and comparing the result to the original system of ordinary differential equations gives

$$\dot{\vec{x}} = \dot{\vec{\Phi}} \quad \Rightarrow \quad \dot{\vec{\Phi}} = \vec{f}. \tag{2.76}$$

Now add a perturbation g to the system, which makes it an inhomogeneous system of ordinary differential equations that reads as

$$\dot{\vec{x}} = \vec{f}\left(\vec{x}, t\right) + \vec{g}\left(\vec{x}, t\right); \quad \vec{g} = \left(g_1, g_2, ..., g_n\right)^T. \tag{2.77}$$

Following variation of parameters, this is solved by

$$\vec{x} = \vec{\Phi}\left(\vec{c}\left(t\right), t\right). \tag{2.78}$$

This is identical to the unperturbed system, however the constants of integration are now a function of time. Taking the derivative of the solution with respect to time once more gives

$$\dot{\vec{x}} = \frac{\partial \vec{\Phi}}{\partial \vec{c}}\dot{\vec{c}} + \dot{\vec{\Phi}} = \frac{\partial \vec{\Phi}}{\partial \vec{c}}\dot{\vec{c}} + \vec{f}. \tag{2.79}$$

Use was made of equation (2.76) to rewrite the equation. $\frac{\partial \vec{\Phi}}{\partial \vec{c}}$ is the Jacobian matrix, which has a non-zero determinant [57]. Comparing this equation to the original system of equations gives the following equation for the constants of integration

$$\frac{\partial \vec{\Phi}}{\partial \vec{c}}\dot{\vec{c}} + \vec{f} = \vec{f}\left(\vec{x}, t\right) + \vec{g}\left(\vec{x}, t\right) \quad \Rightarrow \quad \dot{\vec{c}} = \left(\frac{\partial \vec{\Phi}}{\partial \vec{c}}\right)^{-1}\vec{g}. \tag{2.80}$$

In applying the variation of parameters to orbital mechanics, these constants of integration are the orbital elements. What can be learned from this is that originally, for the unperturbed, homogeneous equation of motion, the constants of integration are constant. The addition of perturbations means an inhomogeneous system must now be solved, where the orbital elements are a function of time.

2.5.3 Lagrange equations

Applying variation of parameters, equation (2.80), to the perturbed equation of motion, equation (2.73), results in [51]

$$\begin{bmatrix} \frac{\partial \vec{r}}{\partial \vec{c}} \\ \frac{\partial \vec{v}}{\partial \vec{c}} \end{bmatrix} \dot{\vec{c}} = \begin{bmatrix} \vec{0} \\ \vec{\Gamma} \end{bmatrix}. \tag{2.81}$$

Apply the following pre-multiplication to obtain the Lagrangian matrix $\mathfrak{L}$ as

$$\begin{bmatrix} -\frac{\partial \vec{v}}{\partial \vec{c}} \\ \frac{\partial \vec{r}}{\partial \vec{c}} \end{bmatrix}^T \begin{bmatrix} \frac{\partial \vec{r}}{\partial \vec{c}} \\ \frac{\partial \vec{v}}{\partial \vec{c}} \end{bmatrix} \dot{\vec{c}} = \begin{bmatrix} -\frac{\partial \vec{v}}{\partial \vec{c}} \\ \frac{\partial \vec{r}}{\partial \vec{c}} \end{bmatrix}^T \begin{bmatrix} \vec{0} \\ \vec{\Gamma} \end{bmatrix}; \quad \Rightarrow \quad \mathfrak{L}\dot{\vec{c}} = \left(\frac{\partial \vec{r}}{\partial \vec{c}}\right)^T \vec{\Gamma}. \tag{2.82}$$

Because gravity is a conservative force, a potential function U exists that can be related to the gravitational acceleration. For the two-body problem, this is given by [21]

$$\ddot{\vec{r}} = -\nabla_{\vec{r}} U_0 \quad \Rightarrow \quad U_0 = -\frac{\mu}{r}. \tag{2.83}$$

The subscript 0 denotes that this corresponds to the zeroth order perturbation, corresponding with the unperturbed case. This will be elaborated upon in section 2.6.1. The subscript $\vec{r}$ is added to denote that the gradient with respect to $\vec{r}$ is meant. In similar fashion, the perturbing acceleration $\vec{\Gamma}$ can be expressed as

$$\vec{\Gamma} = -\nabla_{\vec{r}} U = \nabla_{\vec{r}} \mathscr{R} = \left(\frac{\partial \mathscr{R}}{\partial r}\right)^T. \tag{2.84}$$

$\mathscr{R}$ is called the perturbing force function and is simply the negative of the gravitational potential. With this, the right-hand side of equation (2.82) can be transformed to

$$\mathfrak{L}\dot{\vec{c}} = \left(\frac{\partial \mathscr{R}}{\partial \vec{c}}\right)^T. \tag{2.85}$$

This is the equation that must be solved in order to obtain the rate of change of the orbital elements. Before doing so, the properties of the Lagrangian matrix $\mathfrak{L}$ are explored.

Lagrange brackets The Lagrangian matrix is a 6 by 6 matrix defined as

$$\mathfrak{L} = \left(\frac{\partial \vec{r}}{\partial \vec{c}}\right)^T \frac{\partial \vec{v}}{\partial \vec{c}} - \left(\frac{\partial \vec{v}}{\partial \vec{c}}\right)^T \frac{\partial \vec{r}}{\partial \vec{c}}. \tag{2.86}$$

A single component in this matrix is given by a Lagrange bracket, which is defined as [33]

$$[c_i, c_j] = \ell_{ij} = \left(\frac{\partial \vec{r}}{\partial c_i}\right)^T \frac{\partial \vec{v}}{\partial c_j} - \left(\frac{\partial \vec{v}}{\partial c_i}\right)^T \frac{\partial \vec{r}}{\partial c_j}. \tag{2.87}$$

Lagrange brackets have the following properties

$$[c_i, c_j] = -[c_j, c_i]; \quad [c_i, c_i] = 0; \quad \frac{\partial \ell_{ij}}{\partial t} = 0. \tag{2.88}$$

This means that the Lagrangian matrix $\mathfrak{L}$ is an antisymmetric matrix, containing 15 unique Lagrange brackets $[c_i, c_j]$ that must be determined. The third property of the Lagrange brackets is shown in appendix C.5.1. This means that the partial derivatives in the Lagrange brackets can be evaluated at a conveniently chosen time, which will be done later on [43].
Another point of interest is the behaviour of the Lagrange brackets under a coordinate transformation. This is necessary, because, as will be seen in the following section, plugging in the state vector in the perifocal frame allows for some simplifications. However, the end results are desired in the geocentric equatorial frame.
To do so, apply a rotation of ϑ around the Z-axis to go from an original frame $(OXYZ)$ to a new frame $(OXYZ)'$. Under such a rotation, the Lagrange brackets of the two frames are related as

$$[c_i, c_j] = [c_i, c_j]' + \frac{\partial(\vartheta, S)}{\partial(c_i, c_j)}. \tag{2.89}$$

A full derivation of this is quite lengthy and is therefore moved to appendix C.5.2. In the equation above, the Jacobian is seen, which is defined as

$$\frac{\partial(\vartheta, S)}{\partial(c_i, c_j)} = \frac{\partial \vartheta}{\partial c_i}\frac{\partial S}{\partial c_j} - \frac{\partial \vartheta}{\partial c_j}\frac{\partial S}{\partial c_i}. \tag{2.90}$$

Furthermore, S, see appendix C.5.3 for more detail, is defined as

$$S = \vec{v}^T \left(\frac{\partial \mathfrak{R}(\vartheta)}{\partial \vartheta}\right)^T \mathfrak{R}(\vartheta)\, \vec{r} = \vec{h} \cdot \hat{k} = h_z. \tag{2.91}$$

Here $\hat{k}$ is the unit vector representing the z-direction, which was the axis of rotation. Generalizing this statement to any rotation gives that S is determined by the component of the specific angular momentum $\vec{h}$ about the axis of rotation [51]. With this general statement, the effect of a coordinate transformation on the Lagrangian matrix is found and can be applied to the problem at hand.
In section 2.3.3 it was seen that three rotations are required to transition between the perifocal and geocentric equatorial frame. Using figure 12 and the orbital equations seen in equations (2.23), and (2.28), the parameters are given by

$$S_1(\Omega) = h\cos i = \sqrt{\mu a\,(1-e^2)}\cos i; \quad S_2(i) = 0; \quad S_3(\omega) = h = \sqrt{\mu a\,(1-e^2)}. \tag{2.92}$$

The non-zero derivatives with respect to the orbital elements are given by

$$\begin{aligned}
\frac{\partial S_1}{\partial a} =& \frac{1}{2} na\sqrt{1-e^2}\cos i; & \frac{\partial S_3}{\partial a} =& \frac{1}{2} na\sqrt{1-e^2};\\
\frac{\partial S_1}{\partial e} =& \frac{na^2 e}{\sqrt{1-e^2}}\cos i; & \frac{\partial S_3}{\partial e} =& \frac{na^2 e}{\sqrt{1-e^2}};\\
\frac{\partial S_1}{\partial i} =& -\sqrt{\mu a\left(1-e^2\right)}\sin i.
\end{aligned} \tag{2.93}$$

Therefore, the Lagrange brackets in the geocentric equatorial frame based on inputs in the perifocal frame, with a $'$, are given by

$$[c_i, c_j] = [c_i, c_j]' + \frac{\partial\left(\Omega, S_1\right)}{\partial\left(c_i, c_j\right)} + \frac{\partial\left(\omega, S_3\right)}{\partial\left(c_i, c_j\right)}. \tag{2.94}$$

Whittaker's method With all the necessary properties of the Lagrange brackets explored, they can now be solved for. This is done using Whittaker's method [58][51]. As stated, the analysis is done in the perifocal frame, since this will simplify the expressions. The state vector in the perifocal frame, which is a function of (a, e, E), is once more denoted with a $'$ to make a distinction between frames clear. Equations (2.49) until (2.51) are repeated for convenience

$$\vec{r}' = \begin{bmatrix} a\left(\cos E - e\right) \\ a\sqrt{1-e^2}\sin E \\ 0 \end{bmatrix}; \quad \vec{v}' = \begin{bmatrix} -a\dot{E}\sin E \\ a\dot{E}\sqrt{1-e^2}\cos E \\ 0 \end{bmatrix}; \quad \dot{E} = \frac{n}{1-e\cos E}. \tag{2.95}$$

Whittaker's method utilizes slightly different orbital elements than the Keplerian orbital elements introduced earlier. These orbital elements are formed by the familiar semi-major axis a, eccentricity e, inclination i and, right ascension of the ascending node Ω. Then there is the new longitude of the periapsis ϖ, a compound angle which is given by

$$\varpi = \omega + \Omega. \tag{2.96}$$

The last orbital element is the mean longitude at epoch (reference time) L_0. It is another compound angle and defined as

$$L_0 = \omega + \Omega + M_{e_0} = \varpi + M_{e_0}. \tag{2.97}$$

Here M_{e_0} is the mean anomaly at epoch. These six orbital elements $(a, e, i, \Omega, \varpi, L_0)$ are plugged in for the integration constants $\vec{c}$ in equation (2.85). However, since the analysis starts out in the perifocal frame, a slight adjustment is made. In the perifocal frame, the angles that are used to define the orientation of the orbital plane do not play a role, so this holds for i, Ω, and ϖ. The other three do play a role, however, when splitting L_0 in its components, it is only M_{e_0} that is relevant. In order to obtain the mean anomaly, L_0 and ϖ are combined as

$$\left.\begin{aligned} L =& nt + L_0 = \varpi + M_e \\ M_e =& nt + M_{e_0} \end{aligned}\right\} \left(L_0 - \varpi\right) = M_{e_0}. \tag{2.98}$$

While working in the perifocal frame, $(L_0 - \varpi)$ is used over L_0. Using the mean anomaly at epoch, Kepler's equation, equation (2.43), can be rewritten to

$$nt = \sqrt{\frac{\mu}{a^3}}t + \left(L_0 - \varpi\right) = E - e\sin E. \tag{2.99}$$

In this equation it can be seen that eccentric anomaly, and therefore the state vector, is a function of the same three orbital elements that were mentioned above, so

$$E = E\left(t, a, e, (L_0 - \varpi)\right). \tag{2.100}$$

Using the chain rule, each partial derivative in the Lagrange brackets, equation (2.87), can be written as a sum of other partial derivatives. Keeping equation (2.100) in mind, this looks like [43]

$$\frac{\partial \vec{r}\,'}{\partial c_i} = \frac{\partial \vec{r}\,'}{\partial a}\frac{\partial a}{\partial c_i} + \frac{\partial \vec{r}\,'}{\partial e}\frac{\partial e}{\partial c_i} + \frac{\partial \vec{r}\,'}{\partial (L_0 - \varpi)}\frac{\partial (L_0 - \varpi)}{\partial c_i}. \tag{2.101}$$

To obtain the other derivatives, $\vec{r}\,'$ could be replaced with $\vec{v}\,'$, and c_i could be replaced with c_j. Derivatives of the position or velocity vector with respect to the other three orbital elements i, Ω, and ϖ will be zero and can thus be left out. Plugging equation (2.101) in the Lagrange brackets, equation (2.87), and making use of the Jacobian, equation (2.90), the Lagrange brackets can be rewritten to

$$\begin{aligned}[c_i, c_j]' = &[a, e]' \frac{\partial (a, e)}{\partial (c_i, c_j)} + [e, (L_0 - \varpi)]' \frac{\partial (e, (L_0 - \varpi))}{\partial (c_i, c_j)} \\ &+ [(L_0 - \varpi), a]' \frac{\partial ((L_0 - \varpi), a)}{\partial (c_i, c_j)}.\end{aligned} \tag{2.102}$$

This is quite a lengthy process as the expression itself is large, therefore it is shown in appendix C.5.4. As stated above, Lagrange brackets, and therefore these partial derivatives that form the brackets, are independent of time. This means that they can be evaluated at a convenient time. As the analysis takes place in the perifocal frame, choosing the periapsis significantly simplifies the expressions. The actual process is seen in appendix C.5.5, but as a result, the following is obtained

$$[a, e]' = 0; \quad [e, (L_0 - \varpi)]' = 0; \quad [(L_0 - \varpi), a]' = \frac{1}{2}\sqrt{\frac{\mu}{a}}. \tag{2.103}$$

Equation (2.102) can be simplified with these expressions and, by introducing a new parameter D, even more simplifications are possible. Derivation of D is shown in appendix C.5.6. With all of this, the Lagrange brackets in the perifocal frame are given by

$$[c_i, c_j]' = \frac{\partial ((L_0 - \varpi), D)}{\partial (c_i, c_j)}; \quad D = \sqrt{\mu a}; \quad \frac{\partial D}{\partial a} = \frac{1}{2}na. \tag{2.104}$$

Plugging this in equation (2.94) gives the Lagrange brackets in the geocentric equatorial frame

$$[c_i, c_j] = \frac{\partial ((L_0 - \varpi), D)}{\partial (c_i, c_j)} + \frac{\partial (\Omega, S_1)}{\partial (c_i, c_j)} + \frac{\partial (\omega, S_3)}{\partial (c_i, c_j)}. \tag{2.105}$$

With all of this, the non-zero Lagrange brackets in the geocentric equatorial frame are given by

$$\begin{aligned}
[L_0, a] &= \frac{1}{2}na; & [\varpi, e] &= -\frac{na^2 e}{\sqrt{1 - e^2}}; \\
[\varpi, a] &= -\frac{1}{2}na\left(1 - \sqrt{1 - e^2}\right); & [\Omega, e] &= \frac{na^2 e}{\sqrt{1 - e^2}}(1 - \cos i); \\
[\Omega, a] &= -\frac{1}{2}na\sqrt{1 - e^2}(1 - \cos i); & [\Omega, i] &= -na^2\sqrt{1 - e^2}\sin i.
\end{aligned} \tag{2.106}$$

Reversing the order of the orbital elements means that a minus sign is added to the Lagrange bracket, as was seen in equation (2.88). Therefore, there are 12 non-zero terms in the Lagrangian matrix $\mathfrak{L}$. Plugging this in equation (2.85) gives

$$\begin{bmatrix} 0 & 0 & 0 & [a,\Omega] & [a,\varpi] & [a,L_0] \\ 0 & 0 & 0 & [e,\Omega] & [e,\varpi] & 0 \\ 0 & 0 & 0 & [i,\Omega] & 0 & 0 \\ [\Omega,a] & [\Omega,e] & [\Omega,i] & 0 & 0 & 0 \\ [\varpi,a] & [\varpi,e] & 0 & 0 & 0 & 0 \\ [L_0,a] & 0 & 0 & 0 & 0 & 0 \end{bmatrix} \begin{bmatrix} \dot{a} \\ \dot{e} \\ \dot{i} \\ \dot{\Omega} \\ \dot{\varpi} \\ \dot{L}_0 \end{bmatrix} = \begin{bmatrix} \frac{\partial \mathscr{R}}{\partial a} \\ \frac{\partial \mathscr{R}}{\partial e} \\ \frac{\partial \mathscr{R}}{\partial i} \\ \frac{\partial \mathscr{R}}{\partial \Omega} \\ \frac{\partial \mathscr{R}}{\partial \varpi} \\ \frac{\partial \mathscr{R}}{\partial L_0} \end{bmatrix}. \tag{2.107}$$

Solving for the rates of the orbital elements gives [51]

$$\begin{aligned} \dot{a} =& \frac{2}{na}\frac{\partial \mathscr{R}}{\partial L_0}; \\ \dot{e} =& -\frac{\sqrt{1-e^2}}{na^2 e}\left(\left(1-\sqrt{1-e^2}\right)\frac{\partial \mathscr{R}}{\partial L_0}+\frac{\partial \mathscr{R}}{\partial \varpi}\right); \\ \dot{i} =& -\frac{\tan\left(\frac{1}{2}i\right)}{na^2\sqrt{1-e^2}}\left(\frac{\partial \mathscr{R}}{\partial L_0}+\frac{\partial \mathscr{R}}{\partial \varpi}\right)-\frac{1}{na^2\sqrt{1-e^2}\sin i}\frac{\partial \mathscr{R}}{\partial \Omega}; \\ \dot{L}_0 =& -\frac{2}{na}\frac{\partial \mathscr{R}}{\partial a}+\frac{\sqrt{1-e^2}}{na^2 e}\left(1-\sqrt{1-e^2}\right)\frac{\partial \mathscr{R}}{\partial e}+\frac{\tan(\frac{1}{2}i)}{na^2\sqrt{1-e^2}}\frac{\partial \mathscr{R}}{\partial i}; \\ \dot{\varpi} =& \frac{\sqrt{1-e^2}}{na^2 e}\frac{\partial \mathscr{R}}{\partial e}+\frac{\tan\left(\frac{1}{2}i\right)}{na^2\sqrt{1-e^2}}\frac{\partial \mathscr{R}}{\partial i}; \\ \dot{\Omega} =& \frac{1}{na^2\sqrt{1-e^2}\sin i}\frac{\partial \mathscr{R}}{\partial i}. \end{aligned} \tag{2.108}$$

The perturbing force function will, among others, have a dependency on the semi-major axis a and mean longitude L, which causes an issue in the first term of $\dot{L}_0$ [59]. Applying the chain rule to that derivative while making use of equations (2.42) and (2.98) gives

$$\frac{\partial \mathscr{R}}{\partial a} = \left(\frac{\partial \mathscr{R}}{\partial a}\right)_{\text{explicit}} + \frac{\partial \mathscr{R}}{\partial L}\frac{dn}{da}t. \tag{2.109}$$

The issue that arises comes from time t being explicitly present, which will cause the magnitude of the perturbation to grow with time, meaning perturbation theory is not applicable. This is not desirable, and can be circumvented by the introduction of a new variable L' that incorporates time. After integration, the original variable L_0 could be recovered if so desired [51]. The rate of change of L' is given by

$$\dot{L}' = \dot{L}_0 + tn\dot{n}. \tag{2.110}$$

The expression for $\dot{L}_0$ can now be replaced by [59]

$$\dot{L}' = -\frac{2}{na}\left(\frac{\partial \mathscr{R}}{\partial a}\right)_{\text{explicit}} + \frac{\sqrt{1-e^2}}{na^2 e}\left(1-\sqrt{1-e^2}\right)\frac{\partial \mathscr{R}}{\partial e} + \frac{\tan(\frac{1}{2}i)}{na^2\sqrt{1-e^2}}\frac{\partial \mathscr{R}}{\partial i}. \tag{2.111}$$

The last thing to be done is to transform these orbital elements to the more commonly used Keplerian orbital elements. This can be done with a couple substitutions. In the end, the Lagrange equations that show the rates of change of the Keplerian orbital elements are given by [58]

$$\begin{aligned}
\dot{a} =& \frac{2}{na}\frac{\partial \mathscr{R}}{\partial M_e}; \\
\dot{e} =& -\frac{\sqrt{1-e^2}}{na^2 e}\frac{\partial \mathscr{R}}{\partial \omega} + \frac{1-e^2}{na^2 e}\frac{\partial \mathscr{R}}{\partial M_e}; \\
\dot{i} =& -\frac{1}{na^2\sqrt{1-e^2}\sin i}\frac{\partial \mathscr{R}}{\partial \Omega} + \frac{\cot i}{na^2\sqrt{1-e^2}}\frac{\partial \mathscr{R}}{\partial \omega}; \\
\dot{\Omega} =& \frac{1}{na^2\sqrt{1-e^2}\sin i}\frac{\partial \mathscr{R}}{\partial i}; \\
\dot{\omega} =& \frac{\sqrt{1-e^2}}{na^2 e}\frac{\partial \mathscr{R}}{\partial e} - \frac{\cot i}{na^2\sqrt{1-e^2}}\frac{\partial \mathscr{R}}{\partial i}; \\
\dot{M}_e =& n - \frac{2}{na}\frac{\partial \mathscr{R}}{\partial a} - \frac{1-e^2}{na^2 e}\frac{\partial \mathscr{R}}{\partial e}.
\end{aligned} \tag{2.112}$$

For very small values of either eccentricity or inclination, these equations can become singular, as they appear in some of the denominators. This could be addressed by switching to non-singular elements [51], however this lies outside the scope of this report.

2.6 Perturbation expressions

In this last part of the theoretical background, actual expressions for the perturbations are developed. The goal is to model the perturbations due to both a nonspherical primary body and the attraction of a third body. As mentioned earlier, both are gravitational forces and therefore conservative, such that they can be derived through the gravitational potential U. From this, either be the perturbing force function $\mathscr{R}$ that can be plugged in the Lagrange equations, or the perturbing acceleration $\vec{\Gamma}$ that is required for Cowell's method, can be found. At first, expressions for a nonspherical primary body are developed. Using partially the same methodology, the expressions for the perturbing third body are established.

2.6.1 Nonspherical primary body

In the development of the potential that will follow, use will be made of spherical harmonics, which describe the deviation of the nonspherical primary body in comparison with a perfect sphere [41]. Within spherical harmonics, a distinction can be made between zonal, tesseral, and sectoral harmonics. Zonal harmonics have no dependence on longitude, while the other two are dependent. Only zonal harmonics can cause a secular rate of change in the orbital elements, which will be discussed further later on. Because of this, tesseral and sectoral harmonics are omitted in this report.
A schematic of a nonspherical body is shown in figure 18. It should be kept in mind that the gravitational effects due to a nonspherical primary body can be caused by not only the shape, but by mass distribution as well. Shape is however much easier to visualise, so this is made employed.

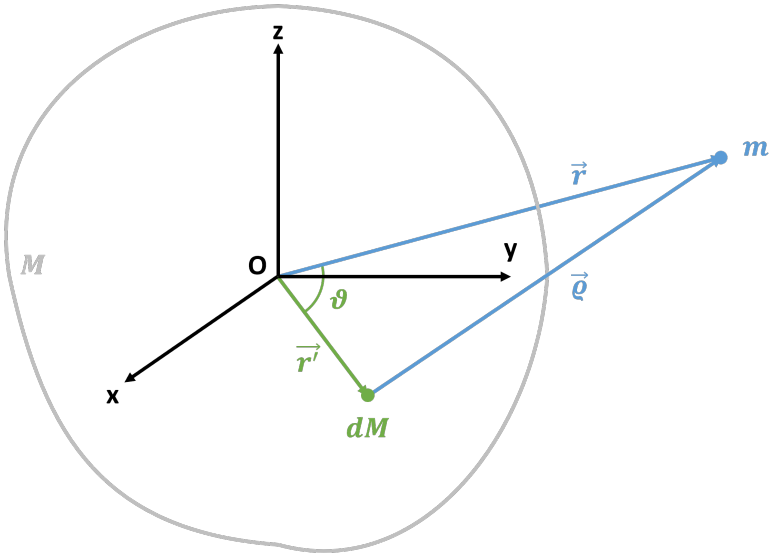

Figure 18: Schematic of a nonspherical body with mass M, an infinitesimal mass dM within the body, and a mass m outside the body.

Here it is seen that the three position vectors are related as

$$\vec{\varrho} = \vec{r} - \vec{r'}; \quad \frac{r'}{r} < 1. \tag{2.113}$$

The gravitational potential of the particle m due to dM is given by [51]

$$dU_\mathfrak{h} = -\frac{G}{\varrho} dM = -\frac{G}{\sqrt{r^2 - 2rr'\cos\vartheta + r'^2}} dM. \tag{2.114}$$

The subscript $_\mathfrak{h}$ stands for 'harmonics' and denotes the gravitational potential related to a nonspherical primary body. In this expression, the law of cosines was used to rewrite ϱ. This expression can be integrated over the body in order to obtain the total potential

$$U_\mathfrak{h} = -\frac{G}{r}\int_V \frac{1}{\sqrt{1-2\frac{r'}{r}\cos\vartheta+\left(\frac{r'}{r}\right)^2}}dM. \tag{2.115}$$

Because $r'/r < 1$, the integrand can be rewritten as a power series [47]

$$\frac{1}{\sqrt{1-2\frac{r'}{r}\cos\vartheta+\left(\frac{r'}{r}\right)^2}} = \sum_{n=0}^{\infty}\left(\frac{r'}{r}\right)^n P_n\left(\cos\vartheta\right). \tag{2.116}$$

Here P_n is the Legendre polynomial of degree n, which can be expressed using Rodrigues' formula that reads as [47]

$$P_n(x) = \frac{1}{2^n n!}\frac{d^n}{dx^n}\left(x^2-1\right)^n. \tag{2.117}$$

A list of the expressions of the first few Legendre polynomials can be seen in appendix A.1. By writing the gravitational potential as an infinite sum.

$$U_\mathfrak{h} = U_{0,\mathfrak{h}} + U_{1,\mathfrak{h}} + U_{2,\mathfrak{h}} + ... + U_{n-1,\mathfrak{h}} + U_{n,\mathfrak{h}} + U_{n+1,\mathfrak{h}} + ..., \tag{2.118}$$

the gravitational potential of degree n is found to be

$$U_{n,\mathfrak{h}} = -\frac{G}{r^{n+1}}\int_V r'^n P_n\left(\cos\vartheta\right)dM. \tag{2.119}$$

Here it can be seen that, due to the r^{n+1} in the denominator, the higher the degree, the smaller the corresponding potential. This is partially cancelled by the r'^n term in the integrand, however because $r > r'$, this does not cancel completely.

Development of gravitational potential In this section, the first few degrees of the gravitational potential are developed such that they can be plugged in the Lagrange equations, equation (2.112). First rewrite $\cos\vartheta$ in equation (2.119) using the definition of the dot product

$$\cos\vartheta = \frac{\vec{r'}\cdot\vec{r}}{r'r} = \frac{r'_x r_x + r'_y r_y + r'_z r_z}{r'r}. \tag{2.120}$$

Now, starting with $n = 0$, following equation (2.119), the gravitational potential becomes

$$U_{0,\mathfrak{h}} = -\frac{G}{r}\int_V P_0\left(\cos\vartheta\right)dM = -\frac{G}{r}\int_V dM = -G\frac{M}{r}. \tag{2.121}$$

This is exactly what was found in equation (2.83). Therefore, this term of the gravitational potential represents a perfect spherical body (or point mass), as was used for the two-body problem. Moving on to the next degree, plugging in $n = 1$ in equation (2.119) gives

$$\begin{aligned} U_{1,\mathfrak{h}} &= -\frac{G}{r^2}\int_V r' P_1\left(\cos\vartheta\right)dM \\ &= -\frac{G}{r^3}\left(r_x\int_V r'_x dM + r_y\int_V r'_y dM + r_z\int_V r'_z dM\right). \end{aligned} \tag{2.122}$$

Looking back to figure 18, the origin was placed at the centre. This is a free choice, and thus a tool to make the mathematics simpler. By placing the origin at the centre of mass $\vec{r'_{cm}}$, the following holds [51]

$$\vec{r'_{cm}} = \frac{1}{M}\int_V \vec{r'} dM = 0 \quad \Rightarrow \quad \int_V \vec{r'} dM = 0. \tag{2.123}$$

This simplifies the potential of first degree to

$$U_{1,\mathfrak{h}} = 0. \tag{2.124}$$

Continuing with the second degree, the gravitational potential is given by

$$\begin{aligned} U_{2,\mathfrak{h}} &= -\frac{G}{r^3}\int_V r'^2 P_2(\cos\vartheta)\, dM \\ &= -\frac{G}{r^3}\int_V \frac{1}{2}\left(\frac{3}{r^2}\left(r'_x r_x + r'_y r_y + r'_z r_z\right)^2 - \left(r'^2_x + r'^2_y + r'^2_z\right)\right) dM. \end{aligned} \tag{2.125}$$

Opposed to the first two degree, the process of rewriting and simplifying this expression is rather lengthy and can be seen in the appendix C.6.1. In this process, the inertia tensor I is used to resolve the integrals. Then it is assumed that the principal axes of inertia are aligned with the coordinate system and that the primary body is axisymmetric about its axis of rotation (the z-axis). Due to the rotational symmetry, the tesseral and sectoral harmonics vanish from the equation. Finally, the position of the satellite is expressed in spherical coordinates through equation (2.57). Instead of the geocentric equatorial frame, with right ascension α and declination δ, the geographic coordinate system, with longitude λ and latitude φ, is used. That is because the gravitational potential is attached to the celestial body and should therefore rotate together with the celestial body. The geographic coordinate system is a co-moving frame and therefore well suited for this. After all these steps and simplifications, the gravitational potential of second degree is given by

$$U_{2,\mathfrak{h}} = -\frac{\mu}{r}\left(\frac{R_e}{r}\right)^2 J_2\left(\frac{1}{2} - \frac{3}{2}\sin^2\varphi\right); \quad J_2 = \frac{I_{zz} - I_{xx}}{MR_e^2}. \tag{2.126}$$

When looking at the last term between brackets, it can be seen that this is exactly the negative expression for the Legendre polynomial of second degree. It turns out that this form can be generalized to give the gravitational potential for degree n [2]

$$U_{n,\mathfrak{h}} = \frac{\mu}{r} J_n \left(\frac{R_e}{r}\right)^n P_n(\sin\varphi); \quad J_n = -\int_V \left(\frac{r'}{R_e}\right)^N \frac{P_n(\sin\varphi')}{M} dM. \tag{2.127}$$

Here J_n is the n^{th} zonal harmonic coefficient, a dimensionless coefficient that is a property of a celestial body. The actual values can be found in the appendix A.2. These coefficients can be seen as weights that quantify the magnitude of the gravitational field corresponding to that degree of spherical harmonic [60]. The spherical harmonics signify the deviation of the gravitational field compared to a perfect sphere. The second spherical harmonic, for example, signifies the oblateness of a celestial body. For the Earth, J_2 is positive, which means that the gravitational force is larger at the equator than at the poles. A visualisation of the first few spherical harmonics is shown in the top of figure 19. They owe this pattern to the Legendre polynomials, as shown in the bottom of figure 19. When $x = -1$ is taken at the bottom of the spheres, each time the Legendre polynomial crosses the x-axis, the corresponding sphere changes colour.

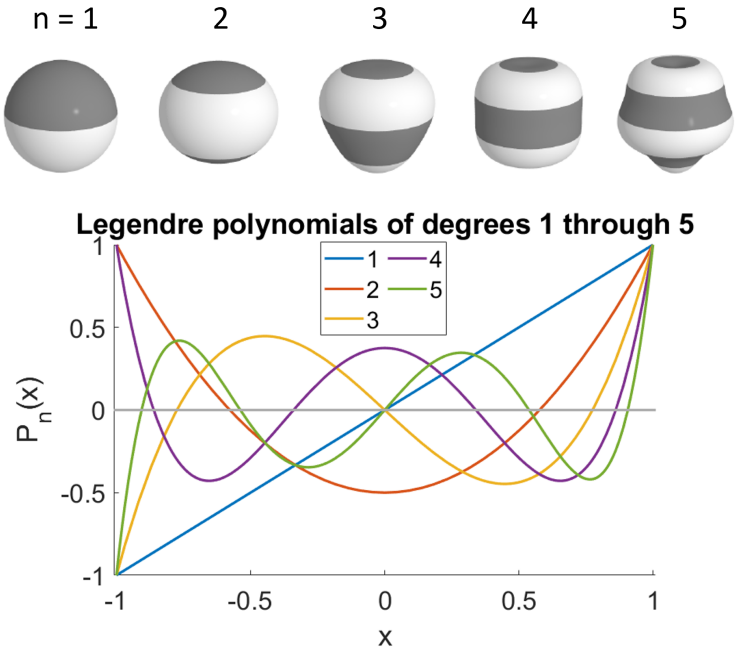

Figure 19: Visualisation of the first five spherical harmonics [60] and the corresponding Legendre polynomials. A colour change in the spheres corresponds to a change of signs, as seen in the Legendre polynomials

Perturbing force function With the potential developed, the perturbing force function is easily obtained as the negative of the potential. However, before plugging this in the Lagrange equations, equation (2.112), a few other things must be addressed. This is illustrated while developing the second degree of the perturbing force function. Following equation (2.126), it is given by

$$\mathscr{R}_{2,\mathfrak{h}} = \frac{\mu}{r}\left(\frac{R_e}{r}\right)^2 J_2 \left(\frac{1}{2} - \frac{3}{2}\sin^2\varphi\right). \tag{2.128}$$

In the Lagrange equations, the perturbing force function appears as a derivative with respect to the orbital elements. With that it mind, it is convenient to change the latitude to orbital elements, which can be done through the spherical law of sines [51]. The spherical triangle is shown in green in figure 20 and the following holds

$$\frac{\sin\varphi}{\sin i} = \frac{\sin(\omega + \mathrm{f})}{\sin\frac{1}{2}\pi}. \tag{2.129}$$

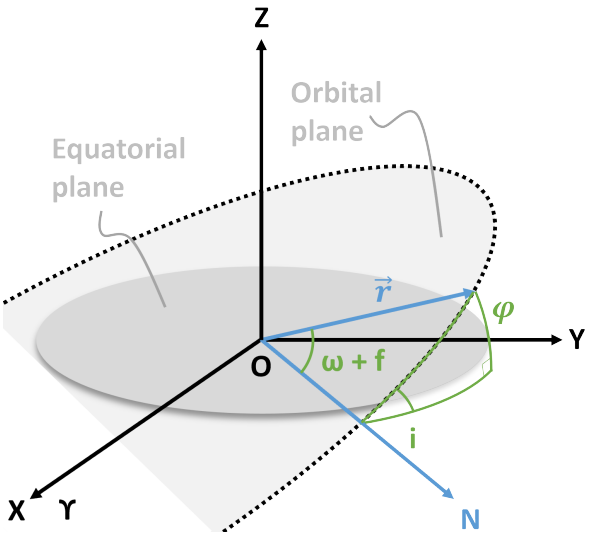

Figure 20: Visualisation of the spherical triangle.

The application of the spherical law of sines is shown in appendix C.6.2 and results in

$$\mathscr{R}_{2,\mathfrak{h}} = \frac{\mu}{a} J_2 \left(\frac{R_e}{a}\right)^2 \left(\left(\frac{1}{2} - \frac{3}{4}\sin^2 i\right)\left(\frac{a}{r}\right)^3 + \frac{3}{4}\sin^2 i \left(\frac{a}{r}\right)^3 \cos\left(2\left(\omega + \mathrm{f}\right)\right)\right). \tag{2.130}$$

This expression fully describes the effects of the perturbation. However, instead of using this immediately, it can be decomposed in three parts, namely secular, long period, and short period [61]. A schematic of this is shown in figure 21. The short period effect is relatively small in magnitude and is caused by a dependence on the true anomaly f [62]. Later on, the Lagrange equations are integrated numerically. With this in mind, getting rid of the short term period effect will save on computational costs, as these rapid fluctuations will require a smaller time step. Since this part causes no permanent change to the orbital elements and the amplitude of these fluctuations is small, no crucial information is lost.
Were tesseral and sectoral harmonics included in the analysis, they would contribute solely with short, medium, and long period effects [41]. As their name suggest, these medium period effects, that are not present with just the zonal harmonics, fall right between the short and medium period effects in both wavelength and amplitude.

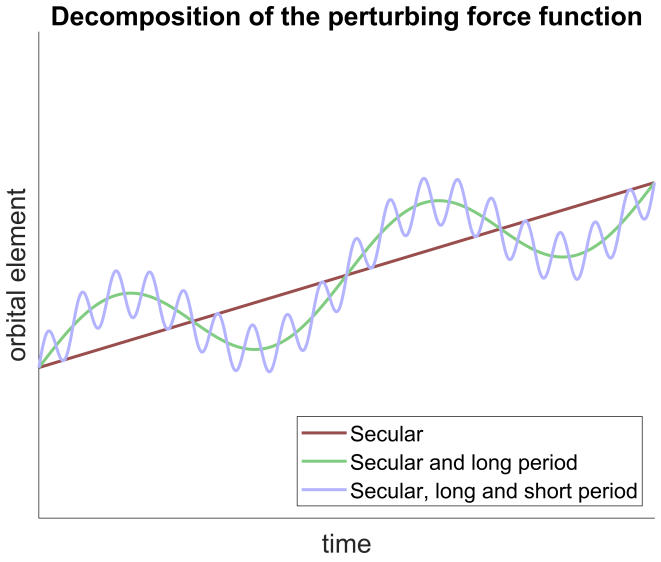

Figure 21: The perturbing force function or gravitational potential can be decomposed in three separate parts.

What is left after the short period part is removed is called the mean part $\langle \mathscr{R}_2 \rangle$. The mean part can be obtained by taking the average of the perturbing force function over a full orbital period [51]. This can be done with

$$\langle \mathscr{R}_{2,\mathfrak{h}} \rangle = \frac{1}{2\pi} \int_0^{2\pi} \mathscr{R}_{2,\mathfrak{h}} dM_e. \tag{2.131}$$

Since $\mathscr{R}_2$ is expressed in terms of true anomaly, it is convenient to change the variable of integration. This can be done by using Kepler's second law and equations (2.43), (2.45), (2.49), & (2.51).

$$\frac{df}{dM_e} = \frac{df}{dE}\dot{E}\frac{dt}{dM_e} = \frac{\sqrt{1-e^2}}{1-e\cos E}\frac{n}{1-e\cos E}\frac{1}{n} = \left(\frac{a}{r}\right)^2 \sqrt{1-e^2}. \tag{2.132}$$

Applying this change of variable and using the orbital equation, equation (2.28), to get rid of r, the mean part is given by

$$\langle \mathscr{R}_{2,\mathfrak{h}} \rangle = \frac{\mu}{a} J_2 \left(\frac{R_e}{a}\right)^2 \frac{1}{(1-e^2)^{\frac{3}{2}}} \left(\frac{1}{2} - \frac{3}{4}\sin^2 i\right). \tag{2.133}$$

The derivation can be seen in appendix C.6.3. Taking the derivatives of the mean part of the perturbing force function with respect to the orbital elements and making use of some trigonometric identities gives

$$\begin{aligned}
\frac{\partial \langle \mathscr{R}_{2,\mathfrak{h}} \rangle}{\partial a} &= -3\frac{\mu}{a^2} J_2 \left(\frac{R_e}{a}\right)^2 \frac{1}{(1-e^2)^{\frac{3}{2}}} \left(\frac{1}{2} - \frac{3}{4}\sin^2 i\right); & \frac{\partial \langle \mathscr{R}_{2,\mathfrak{h}} \rangle}{\partial \Omega} &= 0; \\
\frac{\partial \langle \mathscr{R}_{2,\mathfrak{h}} \rangle}{\partial e} &= 3\frac{\mu}{a} J_2 \left(\frac{R_e}{a}\right)^2 \frac{e}{(1-e^2)^{\frac{5}{2}}} \left(\frac{1}{2} - \frac{3}{4}\sin^2 i\right); & \frac{\partial \langle \mathscr{R}_{2,\mathfrak{h}} \rangle}{\partial \omega} &= 0; \\
\frac{\partial \langle \mathscr{R}_{2,\mathfrak{h}} \rangle}{\partial i} &= -\frac{3}{4}\frac{\mu}{a} J_2 \left(\frac{R_e}{a}\right)^2 \frac{1}{(1-e^2)^{\frac{3}{2}}} \sin 2i; & \frac{\partial \langle \mathscr{R}_{2,\mathfrak{h}} \rangle}{\partial M_e} &= 0.
\end{aligned} \tag{2.134}$$

This can be plugged in the Lagrange equations, equation (2.112), which becomes

$$\begin{aligned}
\dot{a}_{2,\mathfrak{h}} &= 0; & \dot{\Omega}_{2,\mathfrak{h}} &= -\frac{3}{2} n J_2 \left(\frac{R_e}{a}\right)^2 \frac{1}{(1-e^2)^2} \cos i = n_{\Omega,2}; \\
\dot{e}_{2,\mathfrak{h}} &= 0; & \dot{\omega}_{2,\mathfrak{h}} &= -\frac{3}{4} n J_2 \left(\frac{R_e}{a}\right)^2 \frac{1}{(1-e^2)^2} \left(1 - 5\cos^2 i\right) = n_{\omega,2}; \\
\dot{i}_{2,\mathfrak{h}} &= 0; & \dot{M}_{e2,\mathfrak{h}} &= n + \frac{3}{4} n J_2 \left(\frac{R_e}{a}\right)^2 \frac{1}{(1-e^2)^{\frac{3}{2}}} \left(3\cos^2 i - 1\right) = n + n_{M_e,2,\mathfrak{h}}.
\end{aligned} \tag{2.135}$$

With this, the orbital elements can be expressed as a function of time by integrating the Lagrange equations. As stated, this is done with a numerical time integration scheme, which will be discussed in section 3.4.

Looking a bit further in the expressions, the first three elements do not change. When more degrees of the perturbing force function are included, only the semi-major axis will remain constant. In section 2.1.3 it was seen that, for a Keplerian orbit, the specific mechanical energy of a satellite is constant. In this report, only conservative perturbing forces are considered, otherwise the Lagrange equations could not be used. This means that the perturbations will also not add any energy to the system. Using equation (2.37), which relates ε and a, it can be found that the semi-major axis will never exhibit a secular change.

Moving on to Ω, whose rate of change is negative if $i < 90°$, meaning Ω slowly moves in the opposite direction of the motion of the satellite, or westwards. With the node line being defined by Ω, this movement is also called 'regression of the nodes' [20]. If a satellite is placed in a polar orbit, with $i = 90°$, the node line remains fixed, due to the $\cos i = 0$ term in the expression of $\dot{\Omega}$.

In similar fashion, it can be found that the rate of change of ω, named 'apsidal rotation', is positive for $i < 63.43°$ and $i > 116.57°$ [41]. These angles are determined by the roots of the $1 - 5\sin^2 i$ term seen in the equation for $\dot{\omega}$ [2] [63]. If the inclination is exactly equal to these roots, it is named critical inclination, which can be a useful tool when designing a frozen orbit [64]. A frozen orbit aims to keep one or more orbital elements constant, which is done through the selection of the initial orbital elements [65]. A common choice is to keep e and ω (as good as) fixed. The exact orbital elements that lead to a frozen orbit depend, among other factors, on the types of perturbations included and the degree to which they are modelled in the analysis [30].
Since these roots are part of the Lagrange equations, this critical inclination is valid for any celestial body. However, it only holds when there are no other perturbations aside from J_2. If, for example, higher degrees of the perturbing force function are taken into account, the critical inclination shifts [41]. Nonetheless, due to the importance of J_2 for many celestial bodies, this shift is minimal.
The development of higher degrees can be done in the same manner as shown for J_2. It is more mathematically involved because the expressions of the Lagrange polynomials in the gravitational potential become lengthier. With that in mind, only the key steps of the third and fourth degree are shown in appendices C.6.4 and C.6.5 respectively. The subsequent degrees will be derived using the symbolic toolbox of *Matlab*, as addressed in section 3.2.

Perturbing acceleration The perturbing acceleration $\vec{\Gamma}_{\mathfrak{h}}$ is also related to the gravitational potential, as seen in equation (2.84). However, before working on the perturbing acceleration, the potential function is slightly altered. It is beneficial to make use of normalised zonal harmonic coefficients instead of the regular (non-normalised) coefficients in the potential function. This is done because the regular zonal harmonic coefficients get smaller and smaller for higher degrees. When numerical methods are used, this could result in a significant rounding error for the higher degrees [60]. This normalisation is not done for the Lagrange equations, as that process is (mostly) analytical, meaning that these rounding errors are not an issue. Furthermore, for the number of degrees in which the gravitational potential will be expanded in this report, this rounding error is not yet an issue and could therefore be left behind [41]. However, it is good practice, simple to implement, and a good foundation for eventual future work. The normalisation is given by

$$\bar{P}_n = \sqrt{2n+1}P_n; \quad \bar{J}_n = \sqrt{\frac{1}{2n+1}}J_n. \tag{2.136}$$

The values of the normalised zonal harmonic coefficients can be found in appendix A.2. Applying this to equation (2.127) gives

$$U_{n,\mathfrak{h}} = \sqrt{2n+1}\frac{\mu}{r}\bar{J}_n\left(\frac{R_e}{r}\right)^n P_n\left(\frac{z}{r}\right). \tag{2.137}$$

With this, the perturbing acceleration can be determined. As stated in the previous section, the gravitational potential is attached to the celestial body and is therefore most easily expressed in the geographic coordinate system. In this system, spherical coordinates are used, which means that the perturbing acceleration is given by

$$\vec{\Gamma}^S_{n,\mathfrak{h}} = -\nabla_{\vec{r}} U_{n,\mathfrak{h}} = -\begin{bmatrix} \frac{\partial U_{n,\mathfrak{h}}}{\partial r} \\ \frac{1}{r\cos\varphi}\frac{\partial U_{n,\mathfrak{h}}}{\partial \lambda} \\ \frac{1}{r}\frac{\partial U_{n,\mathfrak{h}}}{\partial \varphi} \end{bmatrix} = \sqrt{2n+1}\frac{\mu}{r^2}J_n\left(\frac{R_e}{r}\right)^n \begin{bmatrix} (n+1)\,P_n(\sin\varphi) \\ 0 \\ -\cos\varphi P'_n(\sin\varphi) \end{bmatrix}. \tag{2.138}$$

Here, the S denotes spherical coordinates and P_n' denotes the derivative of the Legendre polynomial of degree n with respect to its argument. It can be calculated manually, but it is also given by the following recurrence relation [66]

$$P_n'(x) = n\frac{xP_n(x) - P_{n-1}(x)}{x^2 - 1}. \tag{2.139}$$

Plugging in $n = 2$ for the second degree gives

$$\vec{\Gamma}^S_{2,\mathfrak{h}} = \sqrt{5}\frac{\mu}{r^2}\bar{J}_2\left(\frac{R_e}{r}\right)^2 \begin{bmatrix} \frac{3}{2}\left(3\sin^2\varphi - 1\right) \\ 0 \\ -\frac{3}{2}\sin 2\varphi \end{bmatrix}. \tag{2.140}$$

As with the perturbing force function, although to a lesser extent, the expressions become longer and longer for higher degrees. The third and fourth degree can be seen in appendix C.6.6. Higher degrees are developed using the symbolic toolbox in *Matlab*.
The goal is to solve equation (2.72) in Cartesian coordinates, therefore the perturbing acceleration should be transformed. Using figure 22 as a guide, to go from Cartesian to spherical coordinates, two rotations are needed. The first rotation is around the z-axis with λ, and the second one is around the current y-axis with $-\varphi$. The second rotation is clockwise, so a minus sign is added to the angle.
The corresponding rotation matrix is given by [60]

$$\begin{aligned} \mathfrak{R}_{C\to S} =& \mathfrak{R}_{y'}(-\varphi)\mathfrak{R}_{\hat{k}}(\lambda) \\ =& \begin{bmatrix} \cos\varphi & 0 & \sin\varphi \\ 0 & 1 & 0 \\ -\sin\varphi & 0 & \cos\varphi \end{bmatrix}\begin{bmatrix} \cos\lambda & \sin\lambda & 0 \\ -\sin\lambda & \cos\lambda & 0 \\ 0 & 0 & 1 \end{bmatrix} \\ =& \begin{bmatrix} \cos\varphi\cos\lambda & \cos\varphi\sin\lambda & \sin\varphi \\ -\sin\lambda & \cos\lambda & 0 \\ -\sin\varphi\cos\lambda & -\sin\varphi\sin\lambda & \cos\varphi \end{bmatrix}. \end{aligned} \tag{2.141}$$

Using some trigonometry, these terms can be expressed with Cartesian coordinates as [67]

$$\begin{aligned} \sin\varphi &= \frac{r_z}{r}; & \cos\varphi &= \frac{\sqrt{r_x^2 + r_y^2}}{r}; \\ \sin\lambda &= \frac{r_y}{\sqrt{r_x^2 + r_y^2}}; & \cos\lambda &= \frac{r_x}{\sqrt{r_x^2 + r_y^2}}. \end{aligned} \tag{2.142}$$

Applying this to equation (2.140) gives

$$\vec{\Gamma}^C_{2,\mathfrak{h}} = \mathfrak{R}_{S\to C}\vec{\Gamma}^S_{2,\mathfrak{h}} = \frac{3\sqrt{5}}{2}\frac{\mu}{r^2}\bar{J}_2\left(\frac{R_e}{r}\right)^2 \begin{bmatrix} \frac{r_x}{r}\left(5\left(\frac{r_z}{r}\right)^2 - 1\right) \\ \frac{r_y}{r}\left(5\left(\frac{r_z}{r}\right)^2 - 1\right) \\ \frac{r_z}{r}\left(5\left(\frac{r_z}{r}\right)^2 - 3\right) \end{bmatrix}; \quad \mathfrak{R}_{S\to C} = \mathfrak{R}^T_{C\to S}. \tag{2.143}$$

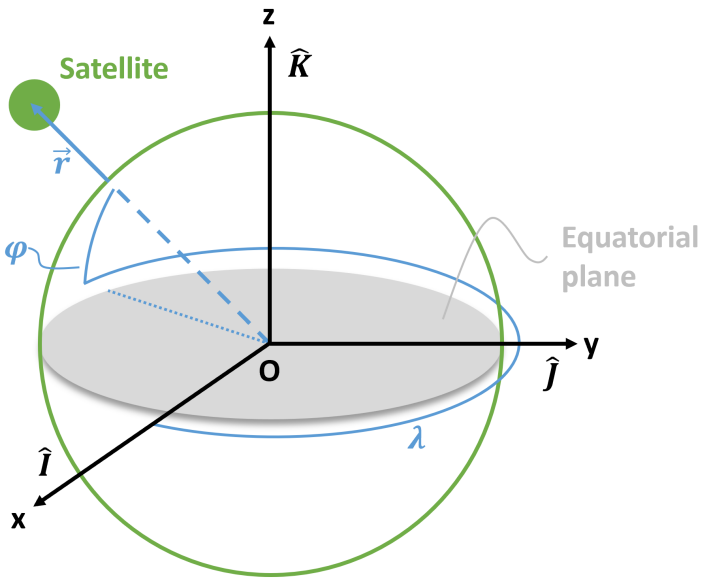

Figure 22: Spherical and Cartesian coordinates.

It should be mentioned that the x, y, and z components of r in the equations above are expressed in the co-moving geographic coordinate system frame. Therefore, as a final step, the perturbing acceleration must be expressed in the inertial geocentric equatorial frame. As was explored in section 2.4.1, this corresponds to a rotation around the z-axis with θ_G. The rotation matrix looks like

$$\mathfrak{R}_{ge\rightarrow gcs} = \begin{bmatrix} \cos\theta_G & \sin\theta_G & 0 \\ -\sin\theta_G & \cos\theta_G & 0 \\ 0 & 0 & 1 \end{bmatrix}. \tag{2.144}$$

Applying this to equation (2.143), while using equation (2.56) for θ_G gives

$$\vec{\Gamma}_{2,\mathfrak{h}}^{C,ge} = \frac{3\sqrt{5}}{2}\frac{\mu}{r^2}\bar{J}_2\left(\frac{R_e}{r}\right)^2 \begin{bmatrix} \left(\frac{r_x}{r}\cos\left(\theta_{G_0}+\dot{\theta}t\right) - \frac{r_y}{r}\sin\left(\theta_{G_0}+\dot{\theta}t\right)\right)\left(5\left(\frac{r_z}{r}\right)^2-1\right) \\ \left(\frac{r_x}{r}\sin\left(\theta_{G_0}+\dot{\theta}t\right) + \frac{r_y}{r}\cos\left(\theta_{G_0}+\dot{\theta}t\right)\right)\left(5\left(\frac{r_z}{r}\right)^2-1\right) \\ \frac{r_z}{r}\left(5\left(\frac{r_z}{r}\right)^2-3\right) \end{bmatrix}. \tag{2.145}$$

With this, $\vec{\Gamma}_{\mathfrak{h}}$ can be plugged in equation (2.73), which is then solved with Cowell's method. As a side note, the perturbing acceleration is not split in a periodic and a mean part, as was done for the perturbing force function. Not doing so means that all effects, secular, long period, and short period, are included in the perturbations, so a more accurate picture is obtained this way. The goal of Cowell's method is, with the minimal amount of work, obtain a result with which to validate Lagrange's method. When graphing, the mean part should be easily distinguishable and if desired can be isolated.

2.6.2 Gravitational attraction of third body

A schematic of the third body perturbation is seen in figure 23. Looking back to figure 18, the figures are strikingly similar, and this will also be seen in the development of the potential. Before working on a mathematical expression, a couple of simplifying assumptions are made in modelling the third body attraction [51] [68]. They read as follows

- The third body has a circular orbit. This means that the distance between the primary and third body, the magnitude of $\vec{r_3}$ seen in figure 23, is constant. This report considers the interaction between the Earth and Moon, meaning that the eccentricity of the Moon's orbit is set from its real value of 0.0549 to 0.
- Only central body potential of the third body is considered, conforming to a two-body problem approach. Zonal harmonics of the third body are not considered. Due to the large distance between the satellite and third body, the loss in accuracy is negligible.
- The inclination of the orbit of the third body is zero, which results in the alignment of the axis of rotation of the primary body with the orbital plane of the third body. This means that the inclination of the Moon is set from 6.68° to 0°.

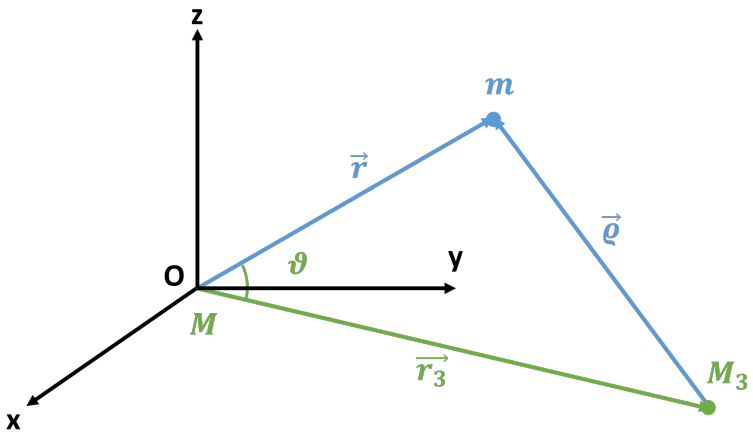

Figure 23: Schematic of the gravitational attraction of a third body. The primary body with mass M is located at the origin, the satellite with negligible mass m is in orbit around the primary body, and the third body with mass M_3 is in a circular orbit around the primary body (or vice versa). The distances are not to scale.

The position vectors are related as

$$\vec{\varrho} = \vec{r} - \vec{r}_3; \quad \frac{r}{r_3} < 1. \tag{2.146}$$

Here $\vec{r_3}$ is the position vector of the third body with respect to the primary body, located at the origin. The subscript $_3$ signifies that it is a parameter of the third body. The perturbing acceleration, following the methodology shown in section 2.1, is given by [69]

$$\vec{\Gamma}_\mathfrak{b} = -\mu_3 \left(\frac{1}{\varrho^3} \vec{\varrho} + \frac{1}{r_3^3} \vec{r_3} \right). \tag{2.147}$$

Here, the subscript $_\mathfrak{b}$ corresponds to the potential of the third body. The number 3 is not used here, as that will become confusing with the expansion of the gravitational potential coming up. Within the brackets, the first term corresponds to the gravitational attraction of the third body on the satellite, and the second term resembles the gravitational attraction of the third body on the primary body [51]. The gravitational potential of the satellite due to the perturbing third body, which relates to the perturbing acceleration following equation (2.84), reads as [70]

$$U_\mathfrak{b} = -\mu_3 \left(\frac{1}{\varrho} - \frac{\vec{r} \cdot \vec{r_3}}{r_3^3} \right). \tag{2.148}$$

Just as in section 2.6.1, the law of cosines can be used to rewrite ϱ and an expansion in Legendre polynomials is applied to give [71]

$$U_\mathfrak{b} = -\frac{\mu_3}{r_3} \left(\sum_{n=0}^{\infty} \left(\frac{r}{r_3} \right)^n P_n \left(\cos \vartheta \right) - \frac{r}{r_3} \cos \vartheta \right). \tag{2.149}$$

There are a few steps in obtaining this expression, as shown in appendix C.6.7. The potential can be simplified by filling in the expressions for the first two Legendre polynomials, see appendix A.1. This gives [51]

$$\begin{aligned} U_\mathfrak{b} &= -\frac{\mu_3}{r_3} \left(1 + \frac{r}{r_3} \cos \vartheta + \sum_{n=2}^{\infty} \left(\frac{r}{r_3} \right)^n P_n \left(\cos \vartheta \right) - \frac{r}{r_3} \cos \vartheta \right) \\ &= -\frac{\mu_3}{r_3} \sum_{n=2}^{\infty} \left(\frac{r}{r_3} \right)^n P_n \left(\cos \vartheta \right). \end{aligned} \tag{2.150}$$

Here the 1, the first term between the brackets, can be taken out. Following equation 2.84, the gradient of the potential results in an acceleration, meaning that there must be dependence on r in the potential for it to matter. As with the zonal harmonics, the higher the degree, the smaller the contribution due to the $(r/r_3)^n$ term. This contribution goes down even faster, since $r_3 \gg r$. [71]

Perturbing force function Once more, the perturbing force function can be found as the negative of the potential, following equation (2.84). Before going to the Lagrange equations, a few things must be addressed. This is illustrated by developing the perturbing force function of second degree, that is given by

$$\mathscr{R}_{2,\mathfrak{b}} = \frac{\mu_3}{r_3} \left(\frac{r}{r_3} \right)^2 \left(\frac{3}{2} \cos^2 \vartheta - \frac{1}{2} \right). \tag{2.151}$$

The cosine term can be rewritten by using the definition of the dot product once more

$$\cos \vartheta = \frac{\vec{r} \cdot \vec{r_3}}{r r_3}. \tag{2.152}$$

The position vector can be rewritten in terms of orbital elements by using equations (2.23), (2.47), and (2.54) [19], which yields

$$\begin{aligned} \vec{r} = r \Big(&\left(\cos \Omega \cos(\omega + \mathrm{f}) - \sin \Omega \sin(\omega + \mathrm{f}) \cos i \right) \hat{I} \\ &+ \left(\sin \Omega \cos(\omega + \mathrm{f}) + \cos \Omega \sin(\omega + \mathrm{f}) \cos i \right) \hat{J} + \left(\sin(\omega + \mathrm{f}) \sin i \right) \hat{K} \Big). \end{aligned} \tag{2.153}$$

The same can be done for the position vector of the third body, however, because of the first and third assumptions made in the modelling of the third body perturbation, the geometry simplifies. For a circular orbit, true, eccentric, and mean anomaly are all equal. This can be visualised when looking back at figure 8. The green auxiliary circle has now become the orbit, setting E and M_e equal. The focus of a circle is its origin, so true anomaly will also be measured from the centre, making it equal to the other anomalies. For a circular orbit, the argument of perigee is undefined, as there is no point of closest passage. This could be solved by introducing the mean latitude l is, which is defined as the angle between the node line and the position vector, but due to the third assumption this does not work. For an orbit with zero inclination, the right ascension of the ascending node, and therefore the node line, is undefined. As a solution, the mean longitude L, which was also seen in Whittaker's method in equation (2.98), is used. Due to the degeneration of the geometry, it is not a compound angle, but instead measures the angle between the position vector of the satellite and the vernal equinox Υ and is given by [51]

$$L_3 = n_3 t. \tag{2.154}$$

This report specifically looks at the Earth and Moon, so, because the Moon is tidally locked, T_3 is equal to the sidereal month of the Moon [72]. After the simplifications, the position vector of the third body is simply the equation for a circle and reads as

$$\vec{r_3} = a_3 \left(\cos n_3 t \hat{I} + \sin n_3 t \hat{J} \right). \tag{2.155}$$

Note that r_3 and a_3 are equivalent, since a circular orbit is assumed. Their value can be found in appendix A. Plugging both expressions back in equation (2.152) gives

$$\cos\vartheta = \cos(\omega + \mathrm{f}) \cos u + \sin(\omega + \mathrm{f}) \sin u \cos i; \quad u = \Omega - n_3 t. \tag{2.156}$$

This is developed in appendix C.6.8. Plugging this in the perturbing force function, equation (2.151), gives

$$\mathscr{R}_{2,\mathfrak{b}} = \frac{1}{2} \frac{\mu_3}{r_3} \left(\frac{a}{r_3} \right)^2 \left(\frac{r}{a} \right)^2 \left(3 \left(\cos(\omega + \mathrm{f}) \cos u + \sin(\omega + \mathrm{f}) \sin u \cos i \right)^2 - 1 \right). \tag{2.157}$$

This equation describes the full perturbing effects. Just as for the nonspherical primary body, the mean part is extracted by taking the average of the perturbing force function over a full orbital revolution, which removes the short period effects. The average can be taken by applying equation (2.131) to the perturbing force function, equation (2.157)

$$\langle \mathscr{R}_{2,\mathfrak{b}} \rangle = \frac{1}{2\pi} \int_0^{2\pi} \frac{1}{2} \frac{\mu_3}{r_3} \left(\frac{a}{r_3} \right)^2 \left(\frac{r}{a} \right)^2 \left(3 \left(\cos(\omega + \mathrm{f}) \cos u + \sin(\omega + \mathrm{f}) \sin u \cos i \right)^2 - 1 \right) dM_e. \tag{2.158}$$

Rather than transforming the variable of integration to true anomaly, eccentric anomaly is used, as that simplifies the mathematics. The following substitutions are made [73]

$$\begin{aligned} \sin \mathrm{f} &= \frac{\sqrt{1-e^2}}{1 - e\cos E} \sin E; \quad \cos \mathrm{f} = \frac{\cos E - e}{1 - e\cos E}; \\ \frac{r}{a} &= 1 - e\cos E; \quad dM_e = (1 - e\cos E)\, dE. \end{aligned} \tag{2.159}$$

This is quite an arduous process that shares many similarities with the steps taken to derive $\langle \mathscr{R}_{2,\mathfrak{b}} \rangle$, as was done in appendix C.6.3. Therefore, to prevent repetition, the expression is given as [30]

$$\begin{aligned}\langle \mathscr{R}_{2,\mathfrak{b}} \rangle = &- \frac{\mu_3 a^2}{2r_3^3} \left(\frac{1}{8} \left(2+3e^2\right) \left(1-3\cos^2 i\right) \right. \\ &-\frac{3}{8} \sin^2 i \left(\left(2+3e^2\right) \cos\left(2u\right) + 5e^2 \cos\left(2\omega\right) \right) \\ &\left. -\frac{15}{16} e^2 \left(\left(1-\cos i\right)^2 \cos\left(2\left(u-\omega\right)\right) + \left(1+\cos i\right)^2 \cos\left(2\left(u+\omega\right)\right) \right) \right).\end{aligned} \tag{2.160}$$

Occasionally, in literature, another average is taken. This time with respect to the motion of the third body L_3 [74] [51] [71]. With this average, medium period effects are removed, effects that were not present in $\mathscr{R}_{n,\mathfrak{b}}$. This is not done in this report, because these medium period effects are, due to the relatively long period of the orbit of the Moon, not that fast and therefore do not impose significant computational demands like the short period effects do.
Equation (2.160) is therefore the final expression, and the derivatives with respect to the orbital elements can be taken. The non-zero derivates are

$$\begin{aligned}\frac{\partial \langle \mathscr{R}_{2,\mathfrak{b}} \rangle}{\partial a} = &- \frac{1}{16} \frac{\mu_3 a}{r_3^3} \left(2\left(2+3e^2\right) \left(1-3\cos^2 i\right) \right. \\ &-6 \sin^2 i \left(\left(2+3e^2\right) \cos\left(2u\right) + 5e^2 \cos\left(2\omega\right) \right) \\ &\left. -15e^2 \left(1-\cos i\right)^2 \cos\left(2\left(u-\omega\right)\right) + \left(1+\cos i\right)^2 \cos\left(2\left(u+\omega\right)\right) \right); \\ \frac{\partial \langle \mathscr{R}_{2,\mathfrak{b}} \rangle}{\partial e} = &- \frac{3}{16} \frac{\mu_3 a^2}{r_3^3} \left(2e \left(1-3\cos^2 i\right) \right. \\ &-2 \sin^2 i \left(3e\cos\left(2u\right) + 5e\cos\left(2\omega\right)\right) \\ &\left. -5e \left(\left(1-\cos i\right)^2 \cos\left(2\left(u-\omega\right)\right) + \left(1+\cos i\right)^2 \cos\left(2\left(u+\omega\right)\right) \right) \right); \\ \frac{\partial \langle \mathscr{R}_{2,\mathfrak{b}} \rangle}{\partial i} = &- \frac{3}{16} \frac{\mu_3 a^2}{r_3^3} \sin i \left(2\left(2+3e^2\right) \cos i \right. \\ &-2 \cos i \left(\left(2+3e^2\right) \cos\left(2u\right) + 5e^2 \cos\left(2\omega\right) \right) \\ &\left. -5e^2 \left(\left(1-\cos i\right) \cos\left(2\left(u-\omega\right)\right) - \left(1+\cos i\right) \cos\left(2\left(u+\omega\right)\right) \right) \right); \\ \frac{\partial \langle \mathscr{R}_{2,\mathfrak{b}} \rangle}{\partial \Omega} = &- \frac{3}{16} \frac{\mu_3 a^2}{r_3^3} \left(2\sin^2 i \left(2+3e^2\right) \sin\left(2u\right) \right. \\ &\left. +5e^2 \left(\left(1-\cos i\right)^2 \sin\left(2\left(u-\omega\right)\right) + \left(1+\cos i\right)^2 \sin\left(2\left(u+\omega\right)\right) \right) \right); \\ \frac{\partial \langle \mathscr{R}_{2,\mathfrak{b}} \rangle}{\partial \omega} = &- \frac{15}{16} \frac{\mu_3 a^2 e^2}{r_3^3} \left(2\sin^2 i \sin\left(2\omega\right) \right. \\ &\left. - \left(\left(1-\cos i\right)^2 \sin\left(2\left(u-\omega\right)\right) + \left(1+\cos i\right)^2 \sin\left(2\left(u+\omega\right)\right) \right) \right).\end{aligned} \tag{2.161}$$

These expressions can now be plugged in the Lagrange equations, equation (2.112).

In this report, the perturbing force function of a third body is truncated after the second term, significantly earlier than for the zonal harmonics. The distance between the Moon and Earth is a couple of orders of magnitude larger than that of a satellite in a LEO, causing the $({}^{r}/_{r_3})^n$ term to decline rapidly. This means that the subsequent degrees barely contribute, which is true for the zonal harmonics as well, but to a lesser degree. What is more, the odd degrees of $U_{n,\mathfrak{b}}$ have no secular rate of change, they only contribute with medium and short period effects. This effectively means that the fourth degree is the first new relevant term, which has a drastically lower magnitude. It is in the order of [74]

$$\langle\langle \mathscr{R}_{4,\mathfrak{b}} \rangle\rangle \sim \frac{\langle\langle \mathscr{R}_{2,\mathfrak{b}} \rangle\rangle}{4096} \left(\frac{a}{r_3} \right)^2 . \tag{2.162}$$

Here, the double chevrons indicate the secular rate of change, which would be obtained if the second averaging step mentioned earlier would be taken.

Perturbing acceleration The perturbing acceleration is given in equation (2.147) and can be written in components with the help of equation (2.146) [70]

$$\vec{\Gamma}_{\mathfrak{b}} = -\mu_3 \begin{bmatrix} \frac{r_x - r_{3,x}}{(r-r_3)^3} + \frac{r_{3,x}}{r_3^3} \\ \frac{r_y - r_{3,y}}{(r-r_3)^3} + \frac{r_{3,y}}{r_3^3} \\ \frac{r_z - r_{3,z}}{(r-r_3)^3} + \frac{r_{3,z}}{r_3^3} \end{bmatrix} . \tag{2.163}$$

Where the position of the third body is found in equation (2.155). An important difference in comparison with the perturbing force function in the previous section is that no series expansion is required. This means that equation (2.163) fully describes the perturbing acceleration due to a third body, while infinite terms of expansion would be necessary in equation (2.149) to achieve the same accuracy with the analytical approach. This is an advantage of using a special perturbation technique over a general perturbation technique.

3 Procedures

In this study, the visibility problem and everything leading up to its solution is solved using *Matlab*. The code consists of a main part and various functions. The only function that requires adjustments is the configurations function, where the initial conditions and settings that are required to run the code are specified. These are described in table 1, and once these inputs are given, the main code can be run.
This starts with the analysis of the Keplerian orbit, for which the controlling equation is solved. Then the perturbations are introduced, by resolving them with the Lagrange equations. The controlling equation is solved once more, to obtain the visibility window. Finally, the verification steps are carried out. Cowell's method is applied to resolve the orbit propagation. This is followed up by the brute force method for the reference visibility. A few key steps in this process are expanded upon in the following sections.

Input	**Options**
Primary body	Earth, Moon
Unit system	Regular, normalised units
Initial condition type satellite	State vector, orbital elements
Initial condition satellite	Initial condition based on the previous setting, either $[\vec{r}^T, \vec{v}^T]$, or $[a, e, i, \Omega, \omega, \text{f}]$
Initial condition type ground station	Local sidereal time, longitude and universal time
Universal time	Universal time if needed based on previous setting YYYY-MM-DD hh:mm:ss
Initial condition ground station	Initial condition based on the previous setting, either $[\theta, \phi, H]$, $[\lambda, \phi, H]$
Rise and set angle	Minimum elevation angle for visibility $[h_{\text{rise}}, h_{\text{set}}]$
Analysis period	Number of orbital periods that are analysed
Zonal harmonic	Highest included zonal harmonic
Time steps per day	k

Table 1: Required inputs for the Matlab code, distance is either in km or $\mathcal{D}$, angles are in degrees.

3.1 Normalised units

Beside SI-units, some literature adopts the use of normalized units. These are employed as the use of, for example, metres or kilometres, is not always convenient at celestial scales [19]. The normalisation depends on the specific problem that is being tackled. In the context of the visibility problem, the preferred choice is setting both the equatorial radius R_e and the gravitational parameter μ of the primary body to unity. Using this, the normalised units of distance $\mathcal{D}$, time $\mathcal{T}$, and velocity $\mathcal{V}$ are given by

$$\mathcal{D} = R_e; \qquad \mathcal{T} = \sqrt{\frac{\mathcal{D}}{\mu}}; \qquad \mathcal{V} = \frac{\mathcal{D}}{\mathcal{T}}. \tag{3.1}$$

3.2 Symbolic toolbox

If perturbations are to be considered, a check is done to see whether the required expressions for the perturbing force function $\mathscr{R}_n$ is present in a dedicated file. These expressions become lengthy for higher degrees and are therefore generated with *Matlab's* symbolic toolbox. The perturbing force function uses equation (2.127) as a starting point, after which equation (2.131) is used to obtain the mean part. Since this part of the code takes relatively long, it is only run when necessary. Once executed, the expressions are saved and can be used in subsequent simulations. This is possible, because the symbolic expressions are universal. When the actual code is run, specific values of both the celestial body and satellite are substituted in. As of right now, the expressions until the 10^{th} degree have been determined. However, this could be higher if so desired by simply increasing the value in the configurations function. The only extra input that would be needed is the values of the (normalised) zonal harmonic coefficients J_n or $\overline{J_n}$.

3.3 fsolve

To solve the visibility problem with Escobal's method, the transcendental controlling equation, equation (2.71) must be solved. To do so, the *Matlab* function *fsolve* is used, a root finding function. It is capable of using various algorithms like the Trust-Region-Dogleg algorithm [75] and the Levenberg-Marquardt algorithm [76]. In order to find a root, an estimate needs to be provided. In Escobal's paper, a method for root estimation is provided [17], but this methodology was found to be not entirely foolproof during the implementation. At times, a root estimation was skipped, which could cause the satellite to rise twice in a row.
Rather than solving the controlling function analytically, it is discretized, allowing an accurate root estimate to be found by identifying where a sign change occurs. While this may initially seem counterintuitive, since the controlling equation was chosen to avoid the need for discretization, the approach remains advantageous. Although discretizing the system introduces an added layer of complexity, the key difference is that only a rough root estimate is required. Unlike the fine discretization needed for the constraint equation, this method demands far less precision, making it computationally inexpensive. While not an ideal solution, as discussed in section 5.2, this approach is sufficient for the current purpose.
fsolve is also used to solve Kepler's equation, equation (2.43) for the eccentric anomaly. In this case, the estimate is given by the mean anomaly [21]. This works best for orbits with a small eccentricity, but even for larger values, convergence is found quickly.

3.4 ode45

Both the Lagrange equations, equation (2.112) and the (perturbed) equation of motion, equations (2.7) and (2.72) must be integrated in time. This is done with *ode45*, a *Matlab* function that is based on the Runge-Kutta method. Specifically, it uses the Dormand-Prince method [77]. This method calculates both the fourth and fifth order accurate solutions at the same time. This allows it to estimate the error at each step and adjust the time step such that the estimated error stays below a certain tolerance. Both the relative and absolute tolerances can be defined, and they are both set to a low value of $1 \cdot 10^{-12}$. Such a low value comes at more computational cost, but is needed in order to obtain accurate results over a longer period of analysis.
Although *ode45* is capable of setting its own variable time step, one is still provided as the last entry in table 1. *Matlab* is then required to show, and thus calculate, the solution at these time steps. It might be that a smaller time step is taken in order to still fulfil the error tolerances, but it will not take larger time steps. The input is specified as the number of steps per day instead of per period, since the length of a period depends on the specific orbit. The reason that this is specified is because of the constraint equation that is applied to the discretised results of Cowell's method. The accuracy of the found rise and set times is dependent on the number of points of the ephemeris, and therefore dependent on the taken time step. Therefore, the time step taken in the coming results is $\Delta t = 1s \Rightarrow k = 86400$. This is already small for Cowell's method, but even more so for the Lagrange equations, where the short period effects have been filtered out. However, to make various comparisons easier, the same time step is taken for both methods.
With this small time step imposed for other reasons than accuracy, Cowell's method is applied in Cartesian coordinates. Using spherical coordinates would allow a larger time step while achieving a similar truncation error, but these considerations are not relevant in this context [3].
It should be noted that *ode45*, which is based on the Runge-Kutta method, is not energy-conserving [78]. This lack of energy conservation can pose an issue, especially when analysing longer time periods, as small numerical errors may accumulate and lead to deviations from the true orbit. To assess the impact of these errors, Cowell's method will also be applied to the Keplerian orbit, where the orbital elements should remain constant. By comparing the results, an estimate of the numerical error introduced by *ode45* can be established. This is not foolproof, as different equations of motion are solved for the Keplerian and perturbed orbit, but it will give some baseline information about the performance. Next to that, literature can provide reference values with which to compare the obtained results of the perturbed system.

3.5 Cowell's method

In figure 24 two flow charts are shown that schematically show how Cowell's method is applied. The left flowchart corresponds to the steps shown in the theoretical background, section 2.6.1. At the start, the position vector in the geocentric equatorial frame is transformed to the position vector in the geographic coordinate system using Greenwich sidereal time. In this system, the perturbing acceleration is derived, which is then transformed from spherical coordinates to Cartesian coordinates through latitude and longitude, both a function of the position vector in the geographic coordinate system. The perturbing acceleration is then transformed to the geocentric equatorial frame using the Greenwich sidereal time once more, but now the rotation matrix is inverted. That leads to the equation of motion to be solved, resulting in the inertial position vector at the following time step.
In the scope of this report, where no sectoral or tesseral harmonics are considered, this process can be shortened, as shown on the right of figure 24. Zonal harmonics have no dependence on longitude, so it need not be addressed separately. Instead, the perturbing acceleration can be transformed to Cartesian coordinates in the geocentric equatorial frame by using Greenwich sidereal time instead of longitude.
In the end, the slightly more elaborate method is still used. With an eye on eventual future research where tesseral harmonics could be included, working this way should prevent issues there. This possibility is simply mentioned for the sake of completeness.

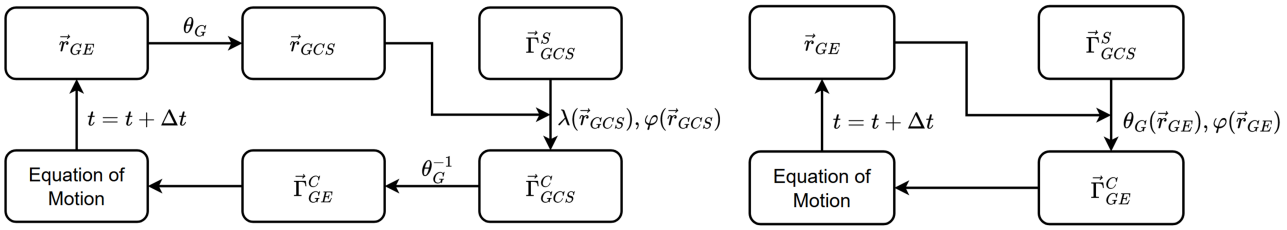

Figure 24: Visualisation of the application of the perturbing acceleration in Cowell's method. Left: process described in theoretical background. Right: shorter version that is possible, since no sectoral or tesseral harmonics are considered.

3.6 Perturbed visibility

Escobal's method is made for a Keplerian orbit where the orbital elements are fixed. This is an issue for the varying orbital elements in the perturbed orbit. The saving grace is that both the orbital period for a satellite in low Earth or Moon orbit is short, and the rate of change of orbital elements is slow. Together, this means that the orbital elements barely change within an orbital revolution. As an example, the roots of the controlling equation for a perturbed orbit where the orbital elements are taken at the start and end of the orbital revolution are as follows

$$\begin{aligned} E_{\text{rise}} &= 67.28°; \quad E_{\text{set}} = 121.70°; \quad \text{(start)} \\ E_{\text{rise}} &= 67.13°; \quad E_{\text{set}} = 121.76°. \quad \text{(end)} \end{aligned}$$

With such minimal differences, assuming that the orbital elements are fixed within an orbital revolution, causes no harm. To obtain specific values, the initial conditions of case II of the Earth, see table 4 in the results, have been used. Although this example is no rigorous proof, it is a showcase of the small scale that is being considered.
With this in mind, the correct selection of orbital elements within an orbital revolution is not that significant. The method adopted here is therefore one that barely requires any extra effort and should give a decent approximation. It is outlined in figure 25. The root estimation is done

with the orbital elements at the start of an orbital revolution. The found estimates can then be linked to a time, at which the orbital elements are known from the Lagrange equations. The orbital elements at this time instance are then used in the controlling equation to solve for the actual roots. This ensures that the roots are found with orbital elements that closely correspond to that root.

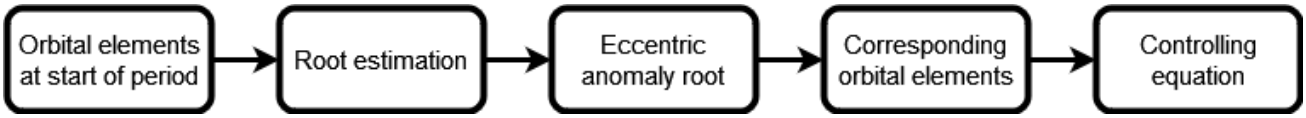

Figure 25: Methodology with which the orbital elements of a perturbed orbit are selected for the controlling equation $\mathfrak{F}$.

Finally, in whatever way the orbital elements are picked, they are taken fixed for a certain amount of time before being updated. The 'jump' in orbital elements causes a discontinuity in the controlling equation. Generally, due to the slow change of the orbital elements, the discontinuity is tiny and therefore causes no issues. However, if the discontinuity happens to jump over a root, this root will not be found through the controlling equation. This is illustrated in figure 26, where the controlling equation is shown for two subsequent periods. Once more, this graph is created with the initial conditions of case II of the Earth, see table 4. For each period, the graph is constructed with the orbital elements at the start of that orbital revolution. When looking at the zoomed in area, it can be seen that the discontinuity jumps over $\mathfrak{F} = 0$. Because both rise and set elevation angles are set at zero, this is where the satellite sets, however it is not found by the controlling equation. To circumvent this issue, the value of the controlling equation at the end of each orbital revolution is compared with the first value of the controlling equation in the consecutive orbital revolution. Mathematically, if there is a sign change in the following expression, a root is skipped, which gives

$$\text{sign}\left(\left[F^p(\text{end}), F^{p+1}(1)\right] - \varrho \sin h\right). \tag{3.2}$$

Here, the proper constraint elevation angle (rise or set) must be plugged in, which can be based on whether the most recent root was a rise or set. If a sign difference occurs, a root is added manually at $E = 0$ of the second orbital revolution, in the case of the example it is added to period 23.

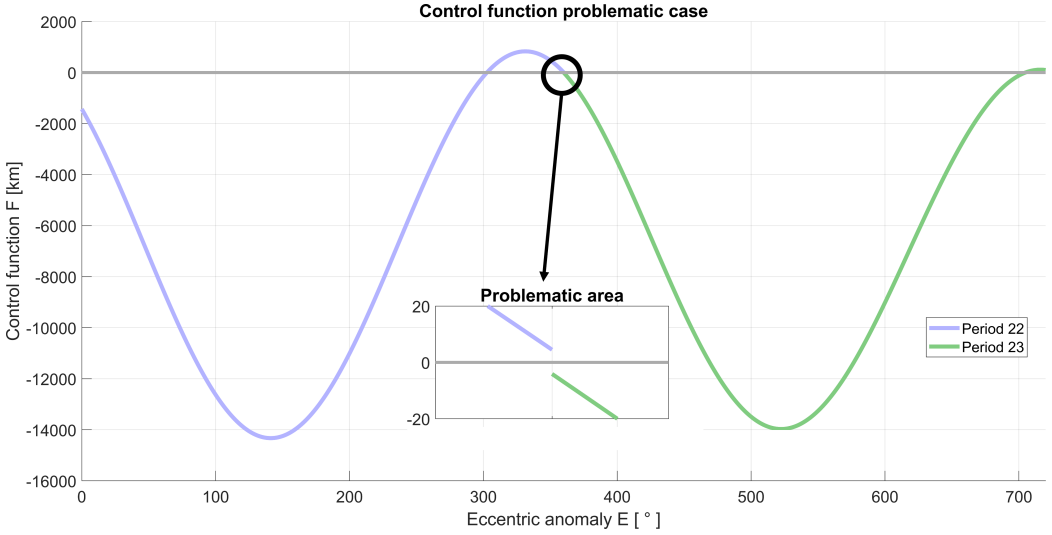

Figure 26: Example of a problematic discontinuity.

4 Results

The generated results are presented and discussed in this section. To start, a satellite in an orbit around the Earth is analysed in terms of its visibility and the behaviour of the orbital elements under higher and higher degrees of zonal harmonics. This serves as a verification of all the implemented mathematics when compared with literature. Subsequently, a Lunar orbiter, the Garatéa-L, is analysed in similar fashion, to facilitate comparison with the Earth. Once all zonal harmonics are included, third body perturbations are added to the analysis as well. Their combined effects are examined in a final analysis over a longer duration of two months. A summary of which perturbations are considered for each case is shown in the table below.

Test cases		**Earth**		**Moon**
		Case I	**Case II**	
Keplerian orbit		✓	✓	✓
Zonal harmonics	J_2		✓	✓
	J_4		✓	✓
	J_{10}		✓	✓
Third body				✓
Zonal harmonics & third body				✓

Table 2: Overview of the cases that are analysed in this report. The zonal harmonic coefficients signify the highest degree that is included in the analysis.

4.1 Earth

In this section, two Terrestrial orbiters are analysed. The initial conditions of both cases are sourced from Escobal.

4.1.1 Case I

For the first case, the example given by Escobal in his article is used. The following initial conditions, in normalised units, are given

Orbital elements		**Ground station**	
$a =$	$1.6\ \mathcal{D}$	$\theta =$	0°
$e =$	0.05	$\varphi =$	45°
$i =$	45°	$H =$	$0\ \mathcal{D}$
$\Omega =$	10°	$h_{\text{rise}} =$	0°
$\omega =$	10°	$h_{\text{set}} =$	0°
f $=$	0°		

Table 3: Initial conditions for case I, using normalised units [17].

As a side note, this orbit cannot be classified as a LEO, but is instead a MEO, since the altitude of the satellite varies between 3300–4400 km. The general approach remains the same, so it can be followed nonetheless. A visualisation of the Keplerian orbit can be seen in figure 27. Here the Earth is placed at the origin and the focus of the orbital ellipse. Since the position of the ground station is defined using local sidereal time instead of latitude and universal time, no Greenwich sidereal time is defined. Therefore, it is set at 0. When the orbit is compared with figure 12, the two angles that define the orientation of the orbital plane i and Ω, and the angle that defines the orientation of the orbit within the orbital plane ω can all be easily recognised. The node line forms the intersection between the equatorial plane and the point where the satellite rises above the equatorial plane (ascending node). The apse line points in the direction of periapsis, the point of closest passage, which is where the satellite is located at the start, since the initial true anomaly is 0.

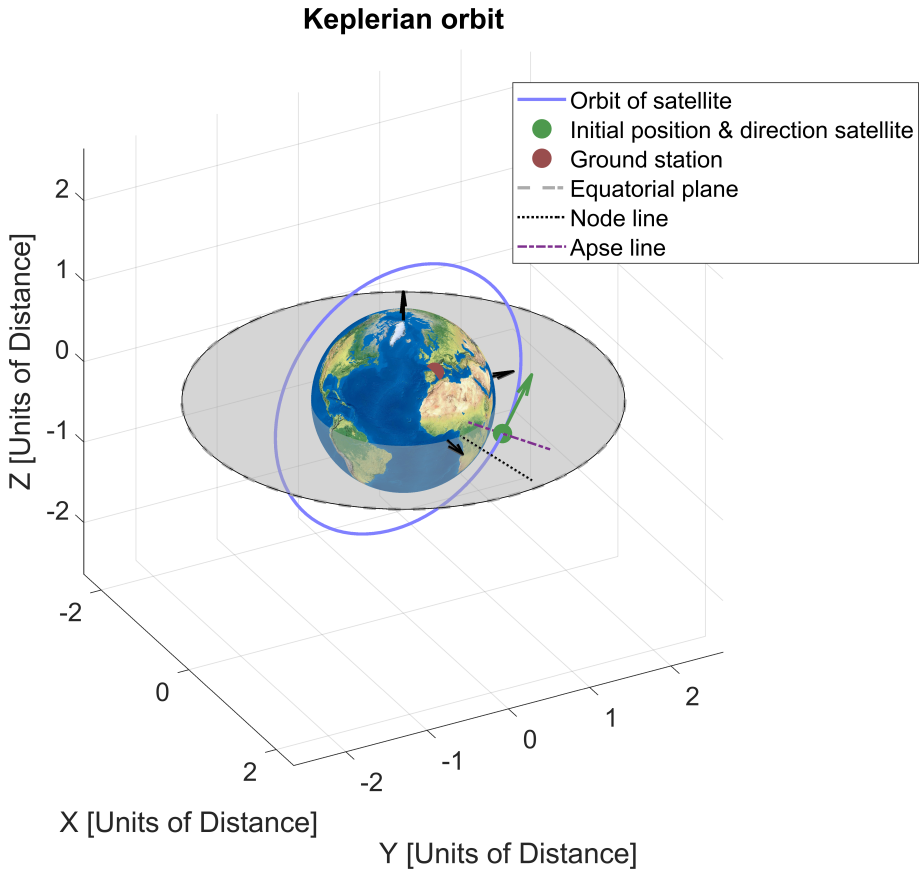

Figure 27: Visualisation of the Keplerian orbit with an orbital period of $T = 2^h 51^{min}$.

As a first test of the implementation, Cowell's method is applied to the unperturbed system, which is illustrated in figure 51 in the appendices. The figure shows that, aside from a few straight lines, no significant changes occur, which aligns with expectations since the orbital elements should remain constant. Although slight variations are present, the rates of change are negligible, confirming that Cowell's method was implemented correctly.
Next up is the visibility problem, for which the controlling equation of the first orbital revolution is shown on the right side of figure 28. On the left side, the controlling equation as presented by Escobal is shown. The rise and set eccentric anomalies are given by

$$\begin{aligned} E_{\text{set}} &= 62.76^\circ; \quad E_{\text{rise}} = 354.80^\circ; \\ E_{\text{set}} &\approx 75^\circ; \quad E_{\text{rise}} \approx 275^\circ. \quad \text{(Escobal)} \end{aligned} \tag{4.1}$$

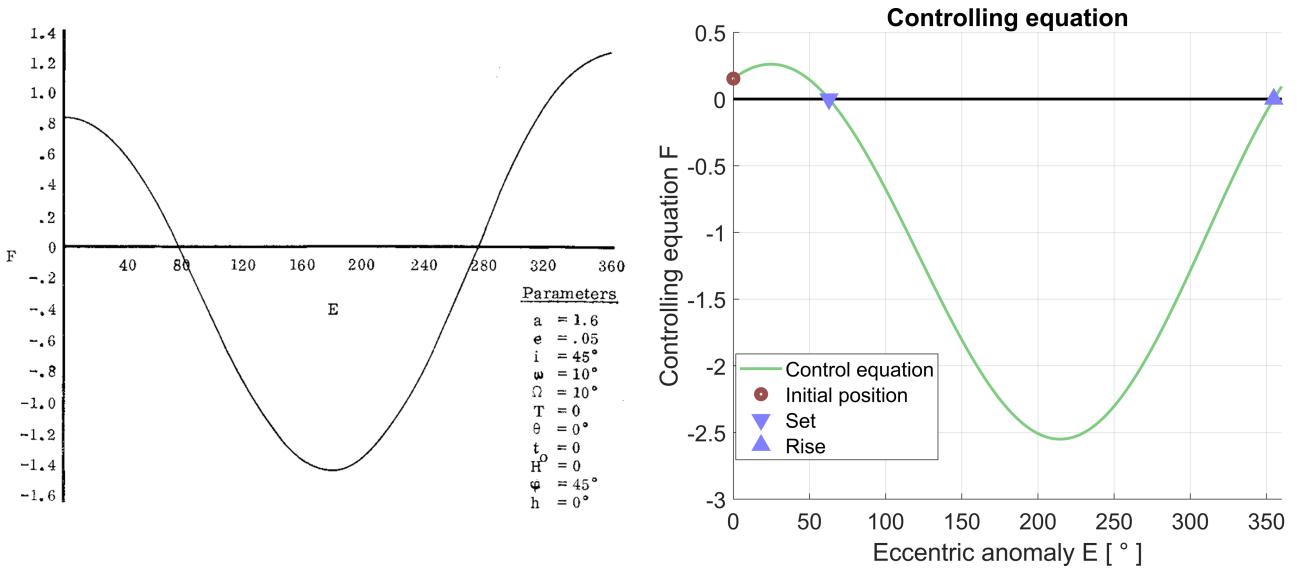

Figure 28: Controlling equation for the first orbital revolution as presented by Escobal [17] on the left, and results generated in the present study on the right.

Although these two figures and roots should be identical, this is clearly not the case. In order to figure out if there is an issue with the implementation, a couple checks of can be done. First of all, the starting point of the controlling function $\mathfrak{F}(E = 0)$ can be checked. Here the controlling equation, equation (2.71), simplifies significantly, and is now given by

$$\mathfrak{F}(E = 0) = a\,(1 - e)\,\hat{p} \cdot \hat{Z} - G = 0.15\,\mathcal{D}. \tag{4.2}$$

The unit zenith vector $\hat{Z}$ is given by equation (2.70). Local sidereal time θ is a function of eccentric anomaly and now reduces to its initial value θ_0. The unit vector in x-direction in the perifocal frame $\hat{p}$ does not simplify further, and is found as the first row of the rotation matrix in equation (2.53). Lastly, the effective radius G is given by equation (2.66) and using normalised units, its value is close to unity due to the minimal flattening of the Earth. Plugging in the initial conditions results in a value far below the starting point of about 0.9 $\mathcal{D}$ as shown by Escobal, indicating that there might be an error here.
As a second check, the slant range at the moment of rise and set can be checked. At these instances, since the rise and set constraint elevation angles are set at zero, both the observer and the satellite should be points in a line tangential to the Earth. This could be checked mathematically, however a visualisation is also insightful, see figure 29. On the right, the slant ranges corresponding to the rise (purple) and set (red) eccentric anomalies are shown to be tangential to the Earth as expected. On the left, the eccentric anomalies provided by Escobal are used. The slant range when the satellite is setting does look close to being tangential, although it passes through the Earth slightly. However, when the satellite rises again, the slant range goes directly through the Earth, meaning that the satellite is far below the horizon of the observer.

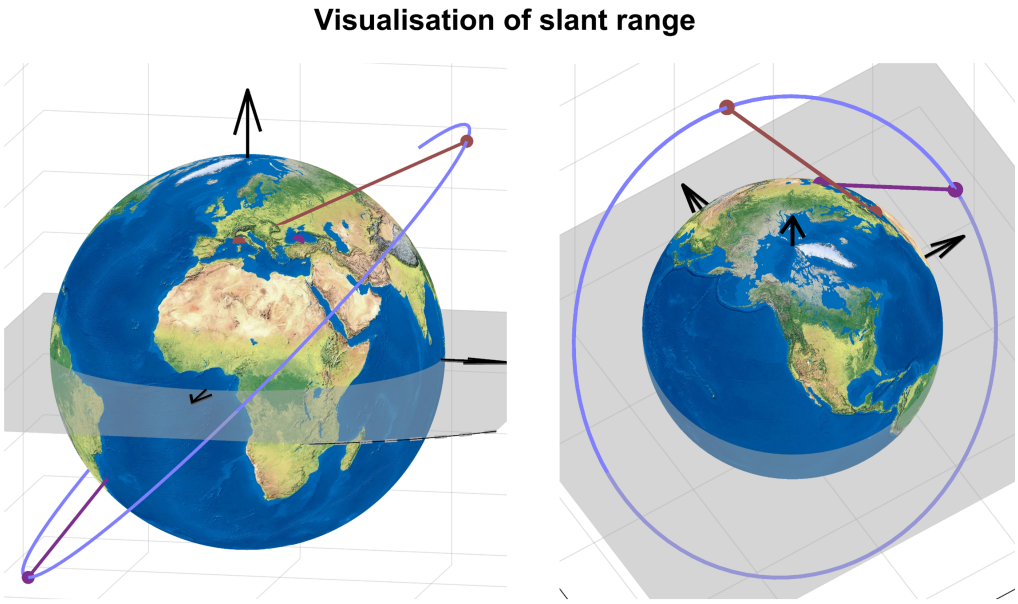

Figure 29: Slant ranges at the moment of rise in purple and set in red, based on Escobal on the left and on results generated in the present study on the right.

As a final check, the visibility problem is solved using the ephemeris found through Cowell's method and application of the constraint equation. The roots are found to be

$$E_{\text{set}} = 62.80°; \qquad E_{\text{rise}} = 354.24°. \tag{4.3}$$

The rise and set angles are not exactly identical to the ones obtained with the controlling equation. As mentioned in the procedures, section 3, this is caused by the fact that the constraint equation is based on a discretised solution. The rise and set angles are then obtained at the angle where the elevation angle crosses 0.
All three checks, the initial value of the controlling equation, the visualisation of the slant ranges at rise and set, and the constraint equation point in the direction that the obtained result is trustworthy. Nevertheless, a lack of correspondence with the creator of this methodology is problematic. Fortunately, Escobal presents another example in his book [19], which is tackled in the second case.

4.1.2 Case II

The initial conditions for the second case, this time in regular units, are as follows

Orbital elements		**Ground station** (*Addis Ababa*)	
$a =$	7658 km	$\lambda =$	38.75°
$e =$	0.05	$\varphi =$	45°
$i =$	45°	$H =$	2.33 km
$\Omega =$	45°	$h_{\text{rise}} =$	0°
$\omega =$	45°	$h_{\text{set}} =$	0°
f =	0°	Date time =	1962-01-04 02:00:00

Table 4: Initial conditions for case II [19].

Keplerian orbit As visual support, the orbit is shown in figure 30. In this case, the initial location of the observer is defined with latitude and universal time, meaning the Earth can be rotated about the Z-axis with the Greenwich sidereal time θ_G.

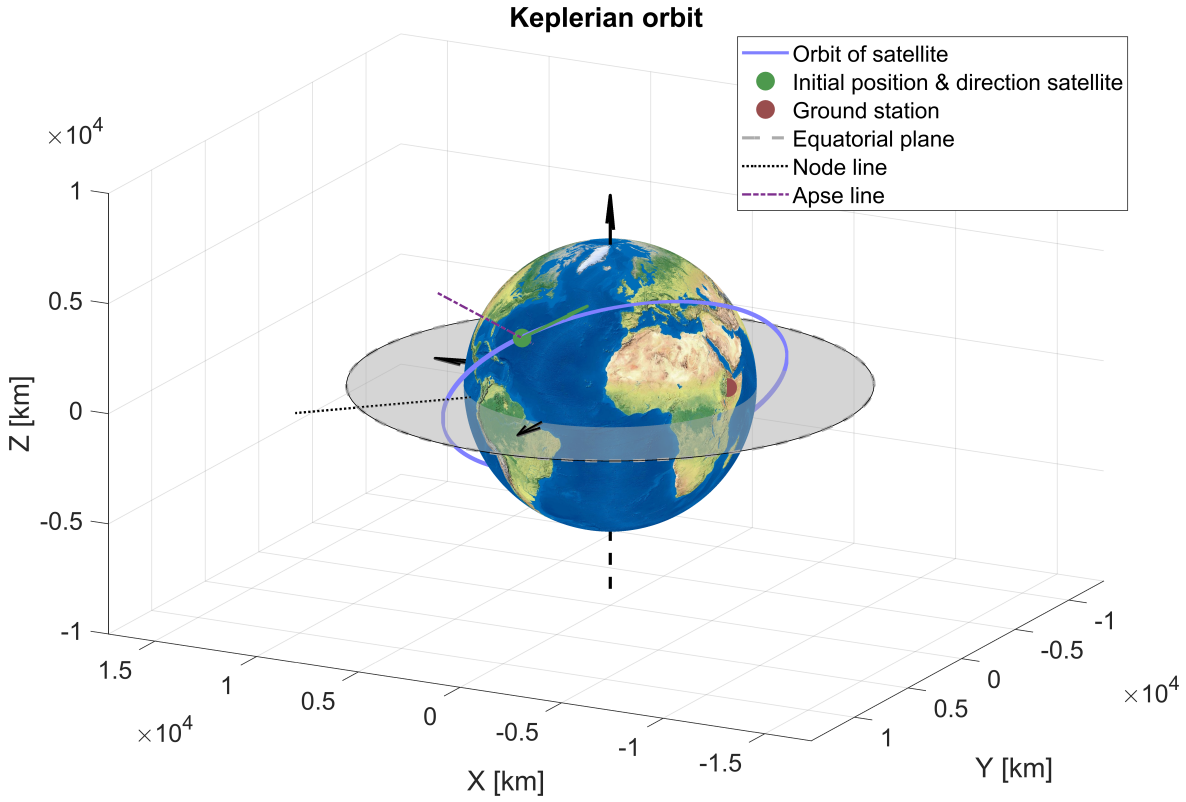

Figure 30: Visualisation of the Keplerian orbit with an orbital period of $T = 1^h 51^{min}$.

The controlling equation for five orbital revolutions is shown in figure 31. Escobal does not provide a graph of the controlling function for this case, only the rise and set eccentric anomaly for the first revolution. These, and the roots obtained from the developed controlling equation, are shown in table 5. In this case, both the results match, giving further confidence in the implementation of the controlling equation. For completeness, the results of the constraint equation are shown as well. There it is seen that the constraint equation applied to the results of Cowell's method matches the result of the controlling equation almost exactly. The row of the fifth period remains empty, as throughout the revolution, the satellite is never visible. The verification steps taken for case I, namely a visualisation of the slant range at rise and set in the first orbital revolution, and the elevation angle throughout five orbital revolutions, can be seen in figure 52 in the appendices.

Period		**Controlling**	**Escobal**	**Constraint**
1	Rise	67.28	67.24	67.35
	Set	121.68	121.68	121.70
2	Rise	79.98		80.01
	Set	155.08		155.09
3	Rise	101.14		101.17
	Set	173.15		173.18
4	Rise	147.20		147.23
	Set	171.48		171.48
5				

Table 5: Rise and set eccentric anomalies in degrees based on the Keplerian orbit

Looking at the graph of the controlling equation in figure 31 once more, slight periodic behaviour is seen. This is broken by the delay of both the rise and set eccentric anomaly and the shift of the maxima and minima, both caused by the rotation of the Earth. If the rotational velocity of the Earth were set to zero, the controlling function would be completely periodic. In this specific case, both the satellite and the observer move eastward, though the observer more slowly, which results in a progressively delayed rise and set with each orbital revolution. The observer, located near the equator, also moves in the direction of the descending node, the point where the satellite dips under the equatorial plane. This initially means that the satellite appears higher above the horizon, resulting in a higher maximum of the controlling function. In the same manner, once the satellite is on the other side of the Earth, it is even further below the horizon, resulting in a lower minimum. After the second revolution, this maximum is reached and the observer moves further away from the path of the satellite. The visibility windows start shrinking, and eventually the satellite is invisible for the entire fifth orbital revolution. The same pattern is seen for the elevation angle, figure 52 in the appendices.

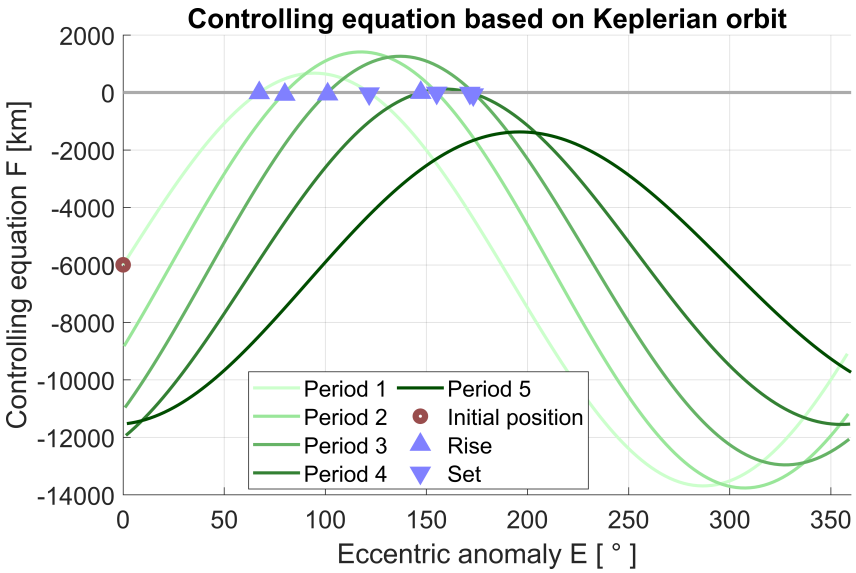

Figure 31: Controlling equation for five orbital revolutions.

Perturbed orbit With the basic model analysed and established, perturbations can be added to the orbit. The first perturbation to consider is the one associated with J_2, the most dominant zonal harmonic. Its influence is not easily visible in the actual orbital, so instead the evolution of the orbital elements is graphed in figure 32. In this figure, the results of both the Lagrange equations and Cowell's method are shown, of which the former is analysed first.
The semi-major axis, eccentricity, and inclination behave as expected following equation (2.135), and remain (as good as) constant. The longitude of the ascending node and the argument of perigee exhibit a linear secular change (mean and long periodic), which is also expected. Since $\dot{\Omega}$ and $\dot{\omega}$ depend only on the three previously mentioned orbital elements that remain constant, these rates of change are constant as well. Their exact rate of change is given by Koiti [60]

$$\begin{aligned} \dot{\Omega} &= -\ 9.97 \left(\sqrt{\frac{R_e}{a}}\right)^7 \frac{1}{1-e^2} \cos i &&= -\ 3.74°/\text{day}; \\ \dot{\omega} &=\ \ 4.98 \left(\sqrt{\frac{R_e}{a}}\right)^7 \frac{1}{1-e^2} \left(5\cos^2 i - 1\right) &&=\ \ 3.97°/\text{day}, \end{aligned} \tag{4.4}$$

which matches exactly with the rates of change seen in the legends of figure 32. Those rates of change around found through linear regression. Finally, while the mean anomaly should exhibit a linear variation, this is obscured by the mean motion, which is also why no rate of change is shown in the legend. By subtracting the mean motion, as done in figure 33, the expected rate of change becomes visible.
Shifting focus to the orbital elements obtained through Cowell's method, the short periodic effects that were filtered out of the perturbing force function immediately stand out. This was not done for the perturbing acceleration, which causes a clear difference. These short period effects are caused by some linear combination of sinusoidal functions of the orbital elements [79] [62] [80]

$$\text{short period effect} = \cos\left(k\omega + l\text{f}\right) + \sin\left(k\omega + l\text{f}\right); \quad k, l = 1, 2, 3. \tag{4.5}$$

Since this depends on ω, which has a secular part, an increasing phase shift is applied to the short period part [51]. This is sufficiently small that it is not yet visible after five orbital revolutions, but should appear in forthcoming longer analyses. Due to the short period effects, the rates of change of the orbital elements that should stay constant (a, e, & i) are appreciably larger

compared to those obtained through the Lagrange equations, as seen in the legends of figure 32. This should also be remedied by a longer analysis period. For Ω, ω, and $M_e - nt$, the secular rates of change are clearly present in both the graph and legend.

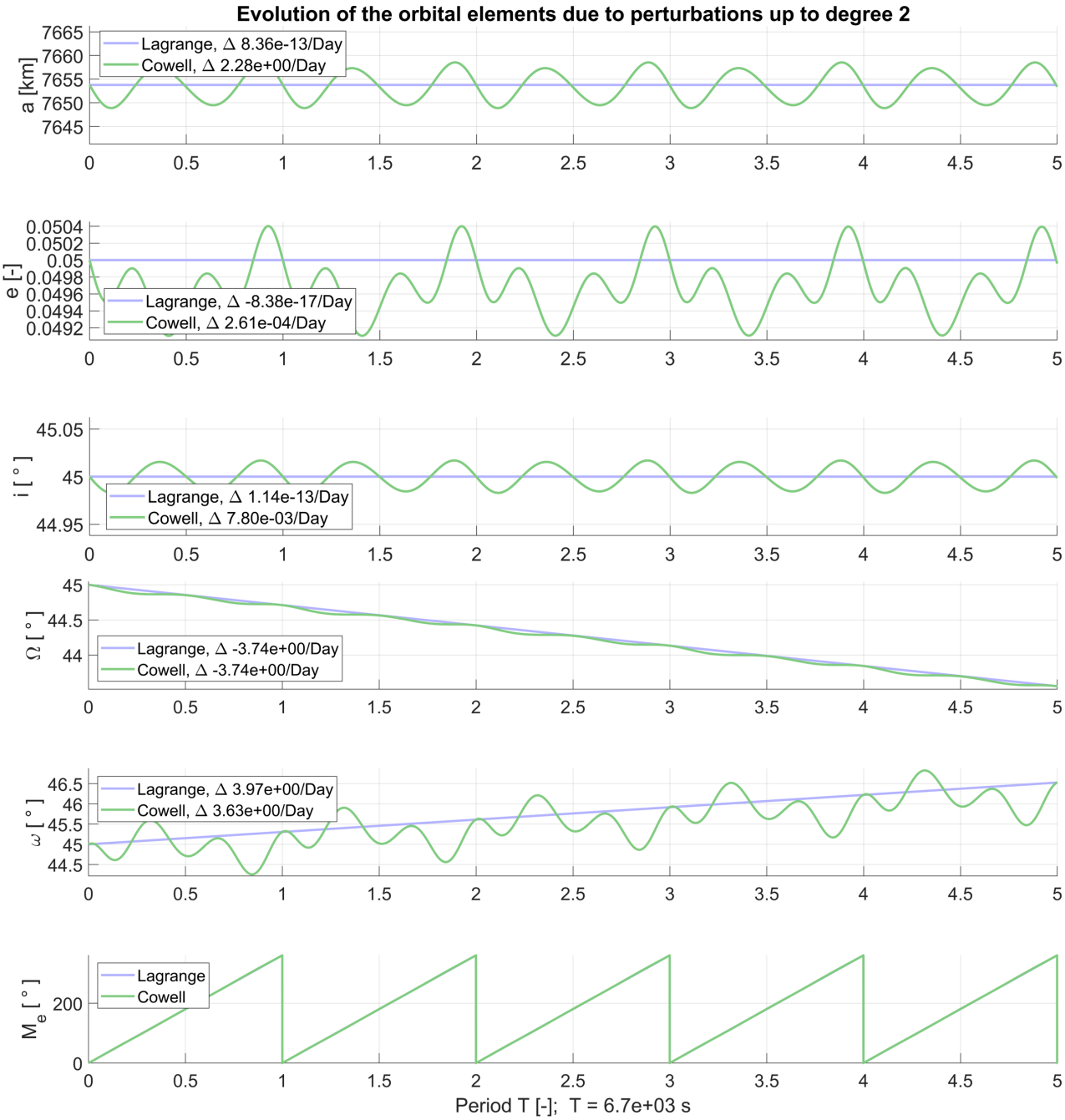

Figure 32: Evolution of the orbital elements due to J_2 over five orbital revolutions. In the legend of each orbital element, the daily rate of change derived from linear regression can be found. This is omitted for the mean anomaly due to the mean motion n.

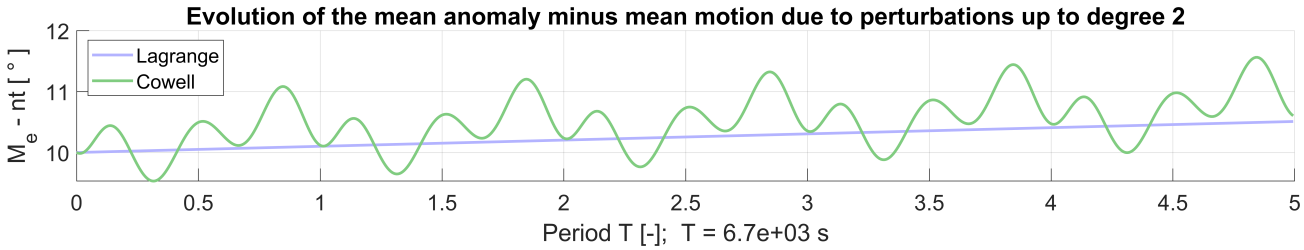

Figure 33: Evolution of mean anomaly minus mean motion due to J_2 over five orbital revolutions.

For the visibility, the controlling equation and elevation angle based on the perturbed orbit can be found in figure 53 in the appendices. However, due to the small differences, a table with the roots, as presented in table 6, is more insightful. For the sake of completeness, the roots of the Keplerian orbit obtained with the controlling equation are presented once more. First, studying the two perturbed results, a slightly larger difference between the two is seen compared to the Keplerian controlling and constraint equation in table 5. This is likely due to the short period effects that result in a little extra deviation.
With time, the perturbed roots start lagging slightly behind their Keplerian counterpart. The difference is minimal, until the fourth period, where the difference is relatively large. An explanation can be found more clearly from the graph of the controlling function, figure 31, where it is seen that the satellite barely rises above the horizon and the controlling function has a low slope around the roots. Due to the secular change of some of the orbital elements, the perturbed controlling equation is moved slightly downwards. With such a minimal slope, this downward shift has a relatively large effect on the visibility window.

Period		**Kepler**	**Perturbed**	
		Controlling	Controlling	Constraint
1	Rise	67.28	67.32	67.61
	Set	121.68	121.70	121.28
2	Rise	79.98	79.83	79.98
	Set	155.08	154.94	155.05
3	Rise	101.14	101.10	100.82
	Set	173.15	172.62	173.00
4	Rise	147.20	149.92	150.11
	Set	171.48	168.34	168.52
5				

Table 6: Rise and set eccentric anomalies in degrees for the Keplerian orbit and the perturbed orbit based on J_2

Next, the subsequent two zonal harmonics are added, as the third and fourth degrees are the most dominant after J_2 [81]. The analysis is extended to 50 orbital revolutions to mitigate some of the shortcomings of the previous analysis, and the evolution of the orbital elements is shown in figure 34.

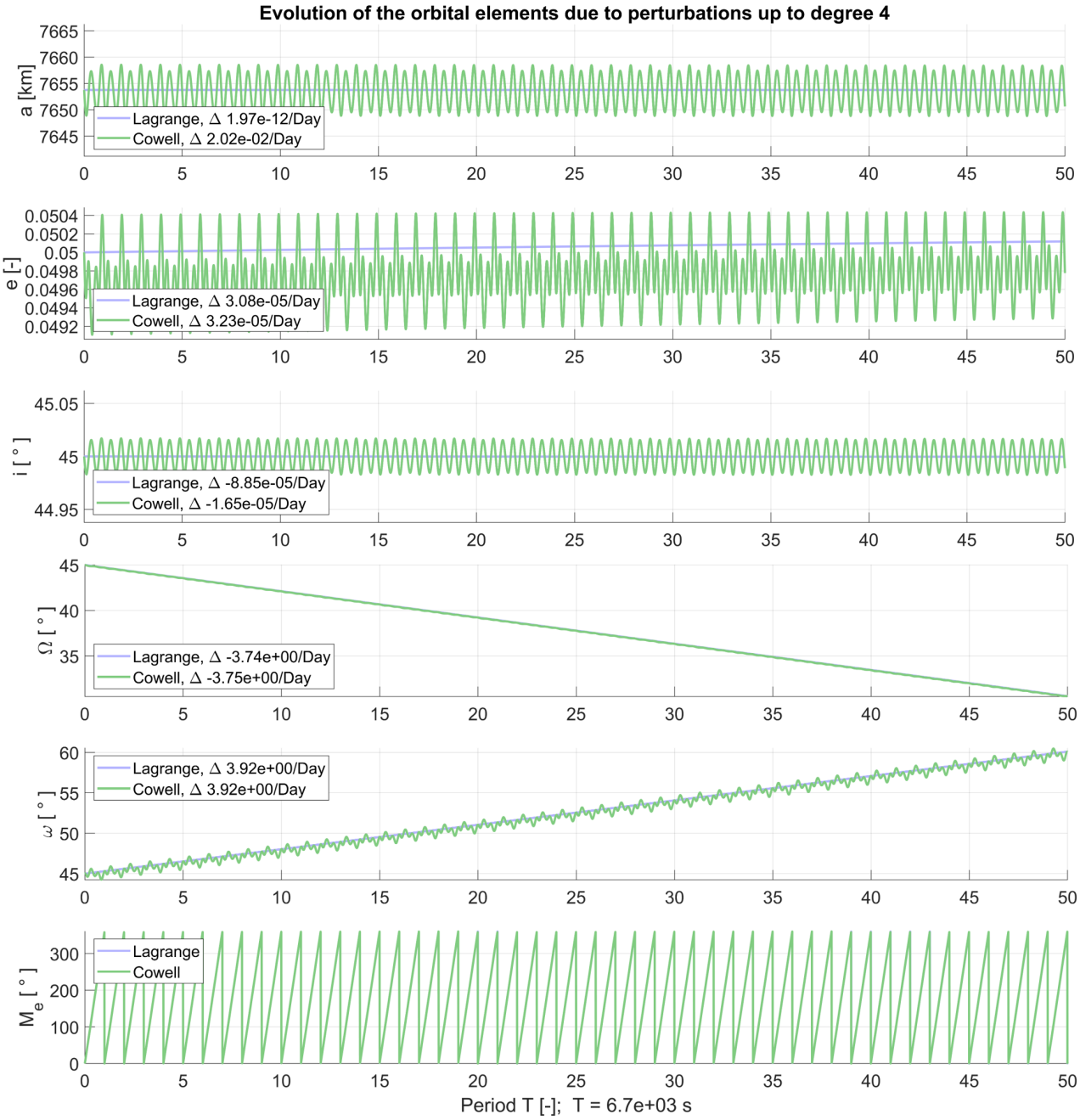

Figure 34: Evolution of the orbital elements due to perturbations up to J_4 over 50 orbital revolutions

The semi-major axis is now the only orbital element that remains constant. The eccentricity and inclination should now be changing, but this is only barely visible for the eccentricity and not at all for the inclination. Comparing the rates of change of these elements obtained from the Lagrange equations with those seen in figure 32, they have increased significantly, showcasing that they are indeed changing with time. Another indication that they are no longer constant is that the rates of changes from both Lagrange and Cowell are now in the same order of magnitude, which was not the case when only J_2 was analysed. Finally, when looking at the endpoints of Cowell's method for the first three orbital elements, the slight phase shift due to the change in the argument of perigree is visible, corresponding to what was expected based on equation (4.5). For the Earth, both J_3 and J_4 are negative, compared to a positive J_2. This means that J_3 and J_4 cause a negative secular opposed to the positive rate of change due to J_2. Due to the large difference in magnitude of the coefficients, this is only noticeable for ω in the rate of change per

day. The rate of change of Ω remains the same as what was seen in figure 32. Since a longer period is analysed, the short periodic parts are less relevant, resulting in (almost) identical rates of change from both the Lagrange equations and Cowell's method.
The inclusion of additional zonal harmonics has not led to significant changes in the orbital elements, which aligns well with findings in the literature. The effects of J_3 and J_4 on a satellite in LEO are both about two to three orders of magnitude weaker than J_2 [82].
As a final addition, the zonal harmonics up to the 10^{th} degree are included. Because these additions are even weaker than J_3 and J_4 [83], the evolution of the orbital elements is practically identical to what was seen above, and therefore only shown in figure 54 in the appendices. More interesting is a visualisation of the orbit, as presented in figure 35. Due to the longer period of analysis, the changes in the orbit are actually visible. On the left side, by the node line, the regression of nodes is clearly seen. From this point of view the apsidal rotation of ω, a rotation of the orbit within the orbital plane, is not readily discernable.
Right above the South of France, a fixed point in the orbit can be seen. Each orbital revolution, it looks like the satellite passes through the same location. Such a point is present on the other side of the Earth as well, and they are caused by the fact that Ω changes, while i does not. This causes successive orbits to cross path when seen from above, and with the slow change of Ω, those crossing points appear to be constant. If a larger difference is applied, the crossing points clearly move. This is illustrated in figure 36, where a small part of the initial and various subsequent orbits are shown from the side. The lines in blue represent the initial and subsequent orbits, with only a small shift in Ω. For these orbits, the crossing point seems to be fixed. This is not the case any more when the green line that represents an orbit further in the future, corresponding to a larger shift in Ω, is included. This figure does not even include the shift in ω, which disrupts this process even further by altering the altitude of the satellite. From above, zoomed out, and over a relatively short period of analysis, like in figure 35, it might look like there is a fixed crossing point for all orbits, but this is not the case.

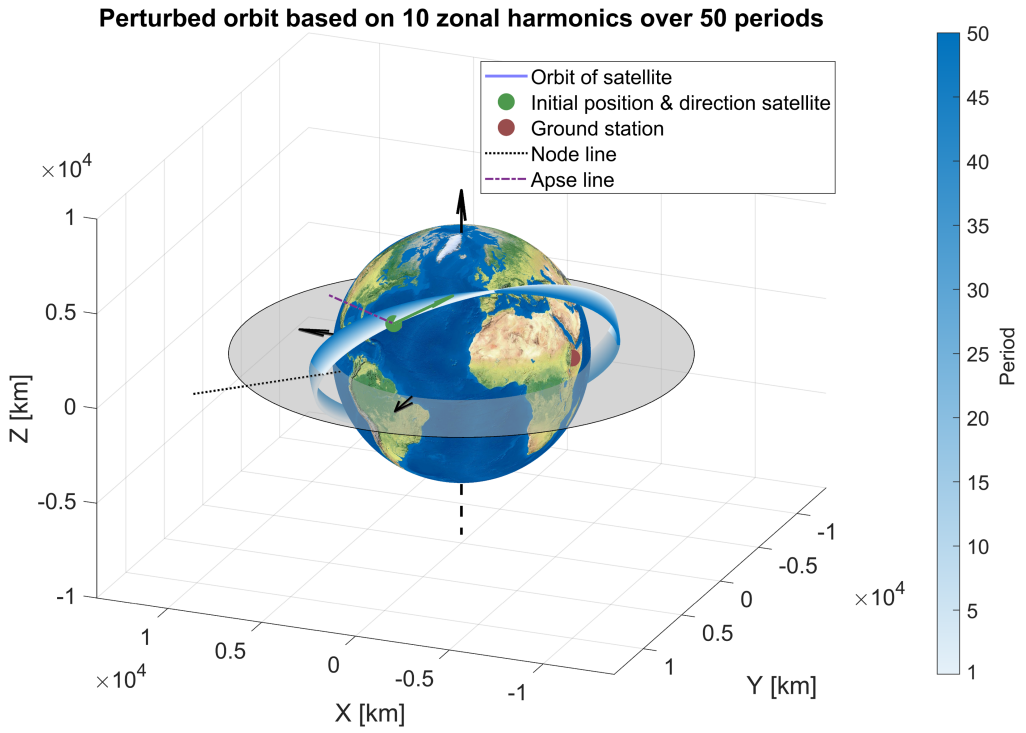

Figure 35: Visualisation of the perturbed orbit due to perturbations up to J_{10} over 50 orbital revolutions.

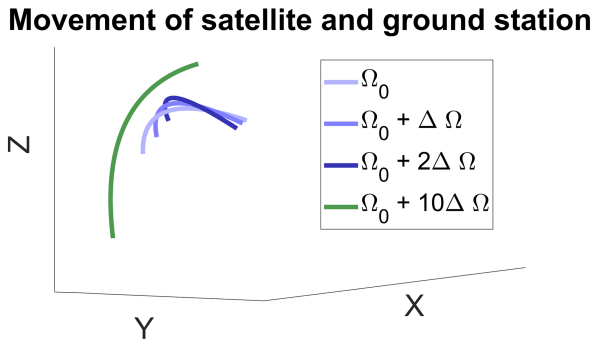

Figure 36: Illustration of the crossing of orbits. As time passes, Ω drifts more and more, causing the crossing point to slowly shift.

With the evolution of the orbital elements properly analysed, the visibility can be discussed. Rather than presenting the rise and set eccentric anomalies, as was done earlier, the roots are transformed to time, as that is the more useful end result. The visibility windows of both the Keplerian and perturbed orbit are shown in green in figure 37. For this figure, the period of analysis is extended from 50 to 52 orbital revolutions to completely finish the fourth day. The first thing that stands out are the large blocks of invisibility. The ground station and satellite can communicate for only 7.7% of the total time in the Keplerian orbit and 8.0% in the perturbed orbit. Figure 37 also shows an almost periodic effect over the days, which is caused by the movement of the ground station. In approximately a day, the ground station returns to its original position and since the orbit remains truly constant for the Keplerian case and roughly constant for the perturbed case, almost identical rise and set times are observed on each day. Because the orbital period is not an integer divisor of a sidereal day of the Earth, the result is not exactly periodic.
The visibility windows of the Keplerian and perturbed orbit have much in common, but there are a few instances where the perturbed case has a visibility window more or less. As time passes, the differences between the two become larger, as the perturbed orbit drifts away from the Keplerian orbit.

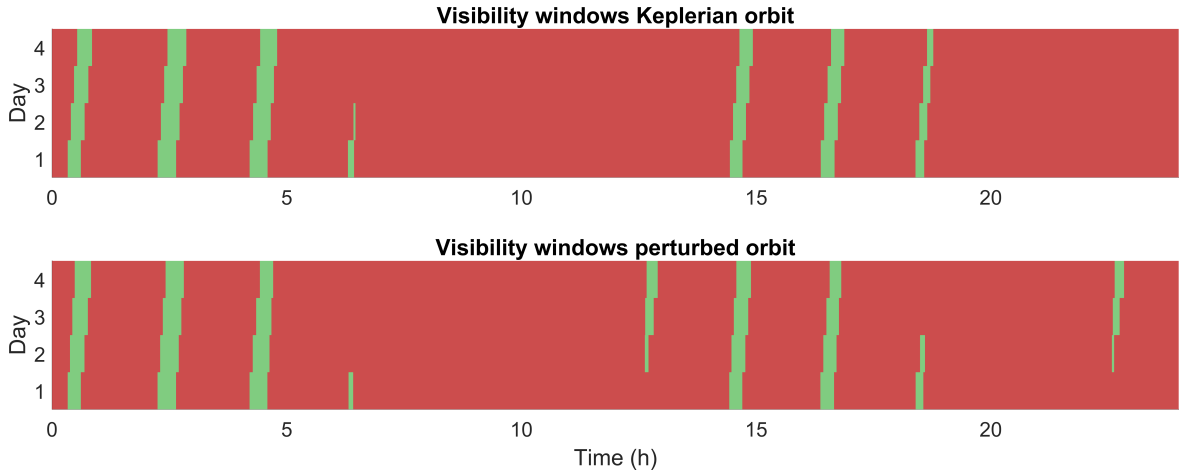

Figure 37: Visibility windows of both the Keplerian and perturbed orbits, with perturbations up to J_{10}, observed over four days. Green means the satellite is visible, red invisible. The y-axis shows the days since the start, and the x-axis shows the hours of the current day.

For the complete picture, the visibility windows from Cowell's method and the constraint equation are shown in figure 55 in the appendices. However, at this scale, the differences are so small that this figure is nearly identical to figure 37.
That is a good first sign, but to explore the differences between the controlling and constraint equation, the actual rise and set times are needed. All the rise and set times are presented in the appendices in table 13 for the Keplerian orbit and table 14 for the perturbed orbit. Since this is quite some data, a summary is presented in table 7. For the Keplerian orbit, great correspondence is found. The differences are no more than a second and seem to be mostly constant throughout the days. The differences for the perturbed orbit are, although still in the order of seconds, noticeably larger. This can be attributed to the inclusion of the short period effects in Cowell's method. Although small, the modelled orbits are marginally different and that clearly shows up in the rise and set times. In the last column, it can be seen that the actual lengths of the visibility windows differ by a greater amount. This indicates that if the controlling equation finds a rise time before the constraint equation, it is likely that it will find a set time after the constraint equation, or vice versa.

	Kepler		**Perturbed**		
	Rise	Set	Rise	Set	Δt windows
Average day 1	00.49	00.49	07.99	05.66	10.29
Average day 2	00.50	00.35	11.93	04.39	15.88
Average day 3	00.48	00.57	10.35	06.61	15.14
Average day 4	00.43	00.68	09.65	07.37	15.57
Average total	00.46	00.50	09.91	06.29	14.28
Maximum	00.95	00.99	26.50	24.27	30.43

Table 7: The average and maximum absolute differences between the roots found through the controlling and constraint equation, given in seconds and centiseconds. The final column showcases the absolute difference between the lengths of the visibility windows.

With this, the results for Terrestrial orbiters are concluded. Within this case, correspondence with literature was found and the verification steps, Cowell's method and the constraint equation, both agree with the obtained results. Therefore, the switch can be made to a Lunar orbiter.
Third body perturbations stemming from the Moon have not been included in this analysis, as their influence would be marginal. For satellites in LEO, the force the Moon exerts is roughly two orders of magnitude smaller than that caused by J_4 [39] [83].

4.2 Moon

The planned orbit of Garatéa-L, a Brazilian space probe to be launched in 2025, is analysed in this section [30]. One of its objectives is to take pictures of the South Pole-Aitken basin [84], an enormous impact crater close to the South Pole of the Moon [85]. With this in mind, the (imaginary) ground station is placed in this basin. The initial conditions for this case can be seen in table 8. The orbital elements are chosen such that both eccentricity and argument of perigee are frozen when nonspherical gravity up to the 12^{th} degree and third body attraction up to the 2^{nd} degree is taken into consideration [30]. Although only the first ten zonal harmonics are included in the final analysis in this report, these elements should showcase a slow rate of change.

Orbital elements		**Ground station**	
$a =$	$1903\ km$	$\lambda =$	191°
$e =$	0.070941	$\varphi =$	-53°
$i =$	63.182°	$H =$	$0\ km$
$\Omega =$	270°	$h_{\text{rise}} =$	0°
$\omega =$	270°	$h_{\text{set}} =$	0°
f $=$	0°		

Table 8: Initial conditions for Garatéa-L [30].

4.2.1 Keplerian orbit

The satellite in its Keplerian orbit and the ground station are shown in figure 38. In this figure, the x-axis, which points towards the Earth, is not visible. The 'camera' looks at the dark side of the Moon, which is where the South Pole-Aitken basin is located. For clarity, the negative z-axis is added as a dashed line.

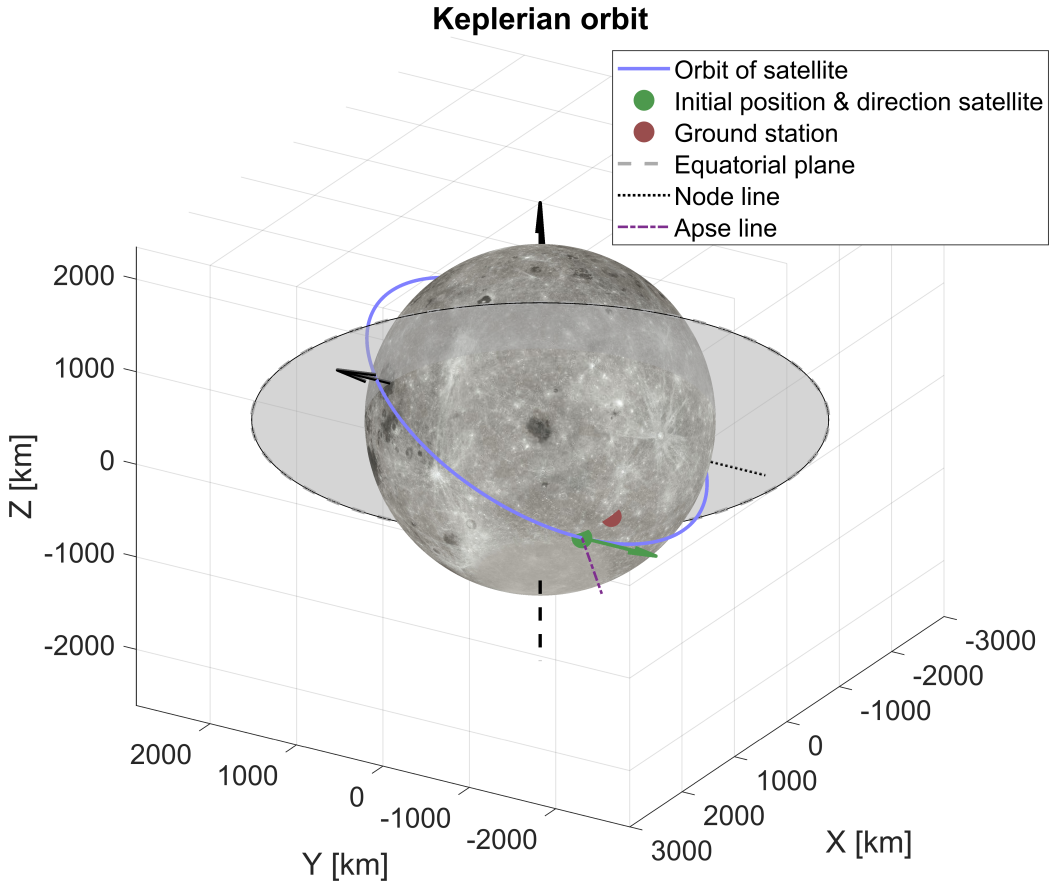

Figure 38: Visualisation of the Keplerian orbit of Garatéa-L with an orbital period of 2^h04^m.

The satellite is in a relatively low orbit, where the periselene is located closely to the basin. Ideal for taking detailed pictures, but due to the low altitude the satellite does not cover a large area, meaning the window for taking these pictures is small. This is exactly what is seen in figure 39, that shows the controlling equation for five orbital revolutions. The meagre visibility windows occur at the start of each orbital revolution, where the satellite barely rises above the horizon. The periodicity of the controlling function also stands out in figure 39. As discussed for the Earth, this periodicity is disturbed by the rotation of the primary body. Comparing this case to case II of the Earth, the disturbance is reduced by both the rotational velocity of the Moon being more than 25 times slower than that of the Earth and by the observer being located relatively close to the South Pole. The combined effect is a slowly moving observer and thus a slow shift of the visibility window over time. This can be seen with more detail in table 9, where the roots of the constraint equation are also given. The results of both methods again match closely, so even though there is no reference case available in literature, this self-verification validates the results.

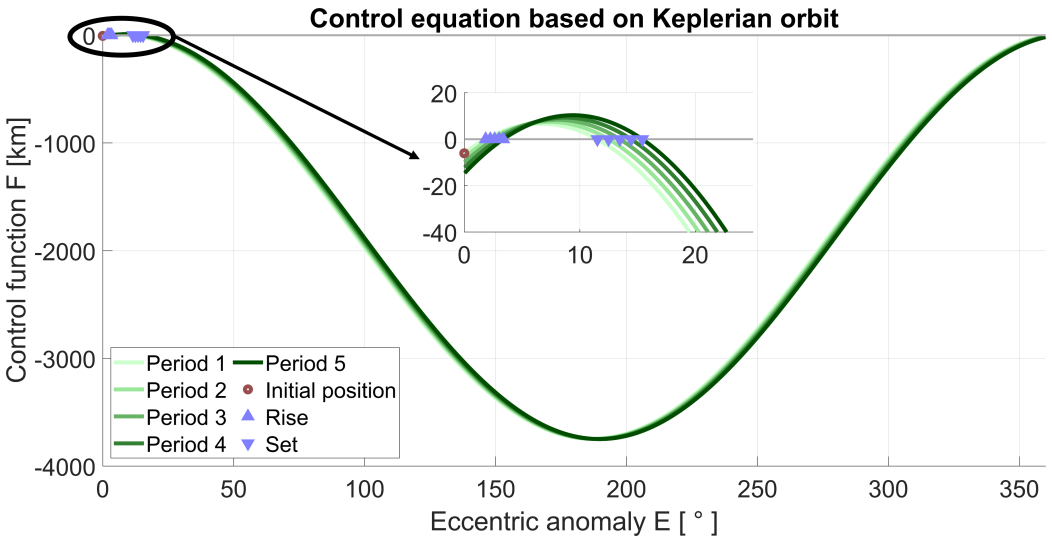

Figure 39: Controlling equation of the Keplerian orbit for five orbital revolutions.

From table 9 it can be found that, on average, the rise eccentric anomaly shifts by about 0.3° with each revolution, which corresponds to about 6 seconds. The set times shift with about 15 seconds, meaning the visibility window gets minimally larger with time. This process can be visualized by imagining the Moon rotating counterclockwise around the z-axis, when looking at figure 38. As the Moon rotates, the ground station moves to the right and downward, approaching the satellite's path and moving farther from the periselene. This motion accounts for the delayed rise time and the even greater delay in the set time.

Period		Controlling	Constraint
1	Rise	1.85	1.87
	Set	11.52	11.54
2	Rise	2.25	2.29
	Set	12.49	12.53
3	Rise	2.63	2.65
	Set	13.47	13.51
4	Rise	3.01	3.02
	Set	14.44	14.45
5	Rise	3.38	3.38
	Set	15.42	15.43

Table 9: Rise and set eccentric anomalies in degrees based on the Keplerian orbit.

4.2.2 Perturbed orbit

Once more, the foundation is laid and the model can be expanded to include perturbations. Roughly the same steps as for the Earth are followed to facilitate comparisons, with some cases slightly shortened to avoid repetition. Once the zonal harmonics are included, third body perturbations are studied as well.

Zonal harmonics For the Moon, the perturbations associated with J_2 are still the dominant term for a satellite in LLO, though to a lesser extent in comparison with the Earth. The evolution of the orbital elements is showcased in figure 41. The Lagrange equations show, conforming to expectations, that the first three orbital elements, a, e, and i, remain constant, as the short period effects have been filtered out. Ω exhibits the anticipated linear variation, although much less than what was seen for the Earth in figure 32. The same holds for ω, although here it must be addressed that the satellite is placed in an almost critical inclination when just J_2 is considered, as was found in equation (2.135). This means that for this analysis, the rate of change is minimal. Using this equation, the rate of change of both Ω and ω should be equal to [20]

$$\begin{aligned}
\dot{\Omega} = & -\frac{3}{2}\left(\frac{\sqrt{\mu}J_2R_e^2}{\sqrt{a^7}\left(1-e^2\right)^2}\right)\cos i && = - \quad 9.77\cdot 10^{-8}\ \text{rad}/s = \quad -0.484^\circ/\text{day};\\
\dot{\omega} = & -\frac{3}{2}\left(\frac{\sqrt{\mu}J_2R_e^2}{\sqrt{a^7}\left(1-e^2\right)^2}\right)\left(\frac{5}{2}\sin^2 i - 2\right) && = \quad 1.92\cdot 10^{-9}\ \text{rad}/s = \quad 0.00950^\circ/\text{day},
\end{aligned}$$

which matches the rates of change seen in figure 41. The results of Cowell's method, aside from the short periodic effects, match the results of the Lagrange equations. Interesting to see is that, for the first three orbital elements, the short periodic effects stand on top of the constant value obtained through the Lagrange equations. Taking the average of Cowell's method would result in a different value than the one given by the Lagrange equations. This effect was already partially seen with the evolution of eccentricity in figure 34, where the mean value of Cowell's method is slightly below the value obtained from the Lagrange equations.
A possible explanation lies in the difference between mean and osculating orbital elements, a field of study beyond the scope of this report. To quickly summarise, mean orbital elements describe an orbit over a longer period where any periodic fluctuations, short, medium, or long, are not taken into account. This is useful for long term analysis in for example orbit propagation [86] [87].
Osculating orbital elements describe the Keplerian orbit of a satellite at an exact moment, which is illustrated in figure 40. All types of perturbations, with all their effects, are taken into account for the true orbit, shown in blue. If then, at a specific time instance t_1, all perturbations were 'turned off', the satellite would continue in a Keplerian orbit. This Keplerian orbit is the osculating orbit, shown in green, corresponding to that instance. If the same is done at a later time t_2, the current osculating orbit is different compared to its predecessor, due to the perturbations in the true orbit. The osculating orbit changes constantly, and it only osculates ("kisses") the real orbit at the current time instant [44]. Osculating orbital elements are mostly used in, for example, real-time satellite tracking [88]. Going back to the results in figure 41, both the Lagrange equation and Cowell's method make use of the same orbital elements, specifically the mean elements. This is correct for the Lagrange equations, where the short periodic effects have been filtered out, but not for Cowell's method, which should use the osculating orbital elements in order to have the same mean value as the Lagrange equations [30]. This conversion is in and of itself an entire field of study [89] and, as stated, not within the scope of this report.

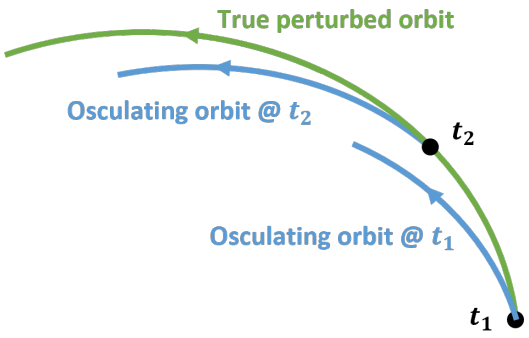

Figure 40: Difference between a true perturbed orbit and osculating orbit at two time steps.

In any case, the magnitude of the fluctuations is minimal and the secular rates of change of both methods match decently, so this should not cause any issues further down the line. The biggest deviation in rate of change is seen for the argument of perigee, but it is expected that for a longer analysis this difference will disappear.

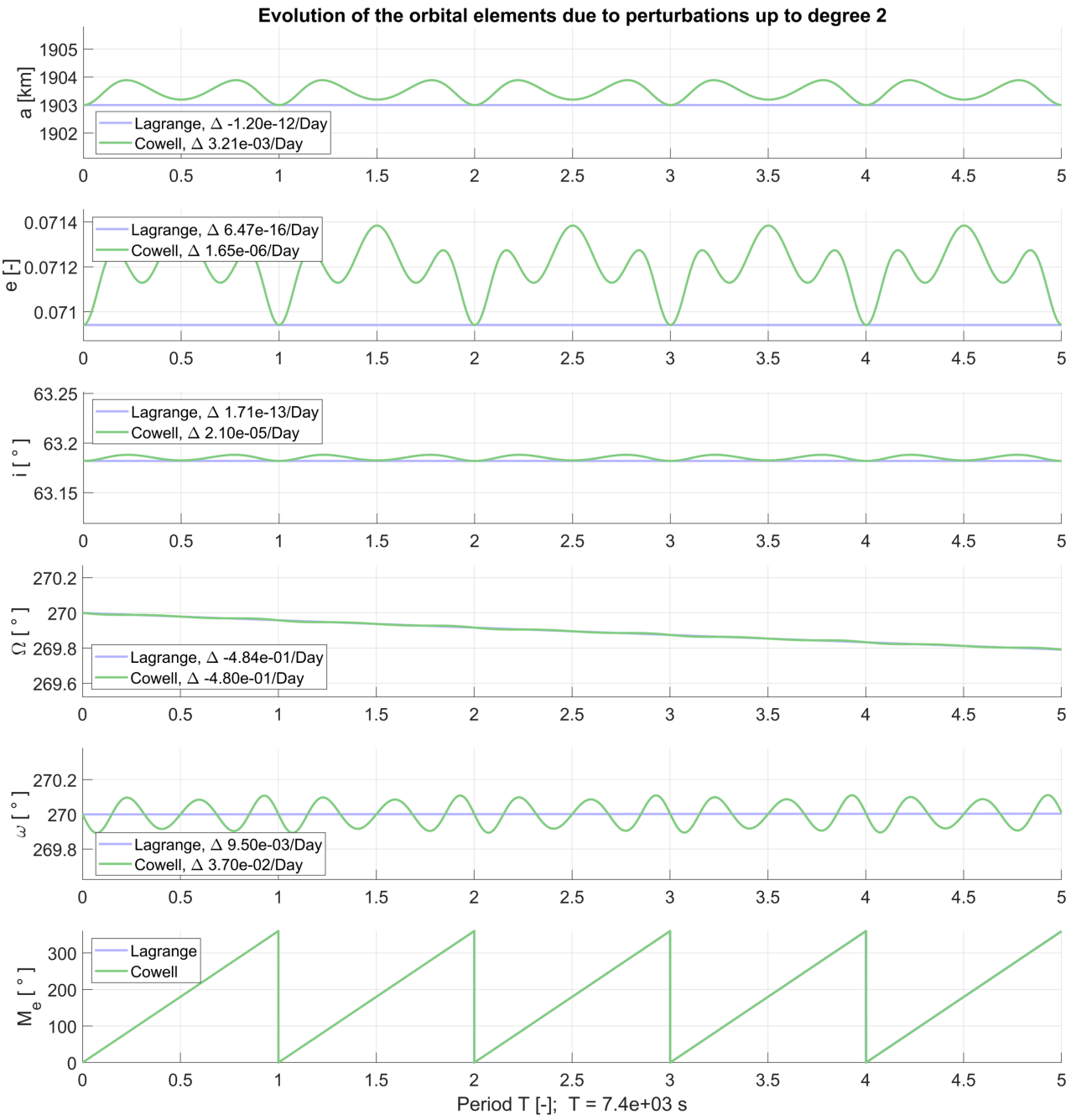

Figure 41: Evolution of the orbital elements due to J_2 over five orbital revolutions.

For now, the visibility analysis is postponed to later. First, the next two zonal harmonics are included, as shown in figure 42. Similar observations apply to the first three orbital elements, as noted earlier for Earth in figure 34. Compared with J_2, the rate of change of Ω has diminished slightly. The first big difference is found for ω, which shows a larger rate of change. Due to the minimal effects of J_2, the effects of the new zonal harmonics are clearly noticeable.
More correspondence between the rates of change between Cowell's method and the Lagrange equations is found now that a longer period is analysed and the importance of the short periodic effects has lessened.

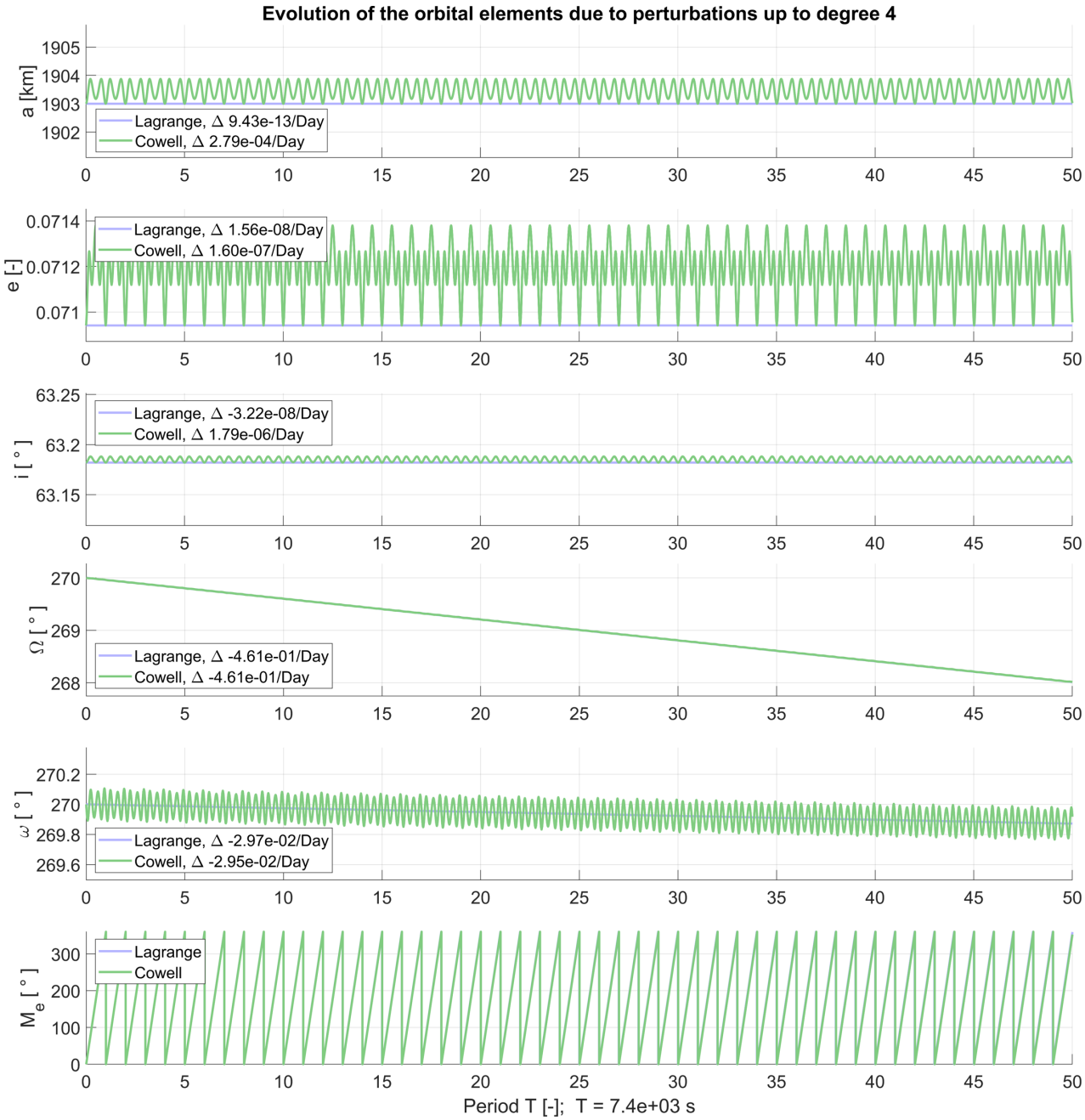

Figure 42: Evolution of the orbital elements due to J_4 over 50 orbital revolutions.

Extending the model further, in figure 43 perturbations up until J_{10} have been included. Albeit still not visible from the graphs, the rate of change of the eccentricity and inclination have increased further when compared to J_4. Ω secular rate of change is slightly less, but the most notable difference comes once again from ω who is now visibly increasing. Although the differences in comparison with only the second zonal harmonic are not that significant, the fact that at least some change is visible showcases that J_2 is less dominant for the Moon than it is for the Earth.

It should be noted that this effect is magnified by both the initial condition for the inclination and the fact that the satellite studied here is much closer to the Moon, compared to the satellite studied for the Earth. Therefore, the $(R_e/a)^n$ terms seen in equations (2.135), (C.81), and (C.85) diminish slower for increasing degrees, giving the higher degrees more relevance.

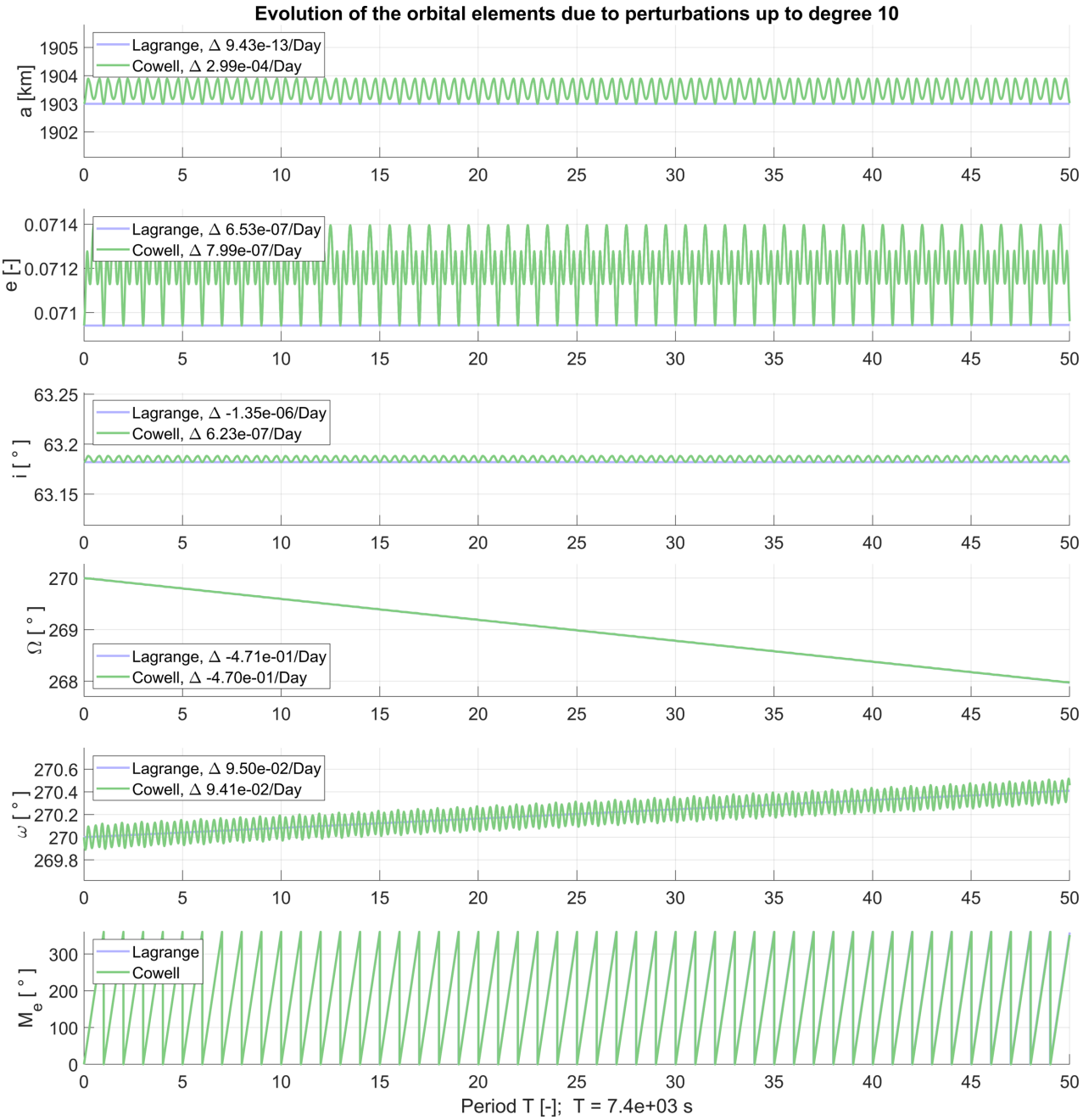

Figure 43: Evolution of the orbital elements due to J_{10} over 50 orbital revolutions.

Third body attraction As a final addition, perturbations due to third body attraction are included. This is first done in isolation, without any zonal harmonics, in order to clearly identify the specific effects caused by a third body. To do so, a longer period of 14 days is analysed, as can be seen in figure 44. The longer analysis is necessary to capture the medium period effects due to the motion of the third body.
As always, the semi-major axis remains constant, besides minimal short period effects for Cowell's method. Besides the medium period effects, eccentricity and inclination remain constant. Right ascension of the ascending node and argument of perigee both display a secular rate of change. Making comparisons with literature is not as straightforward as for the zonal harmonics, because of the non-linear evolution [36] [41]. Nevertheless, with the help of Cowell's method, self-verification is possible.
The results of both methods have excellent correspondence, only differing in the short period effects. Besides the semi-major axis, where these short periodic effects dominate, the rates of change of the orbital elements match closely. This also justifies the exclusion of the higher degrees in the perturbing force function $\mathscr{R}_{n,\mathfrak{b}}$. As discussed in section 2.6.2, there is no truncation of the perturbing acceleration, so all effects are inherently included in Cowell's method. Nonetheless, these higher degrees barely contribute, such that the Lagrange equations still lie exactly on top of Cowell's method.

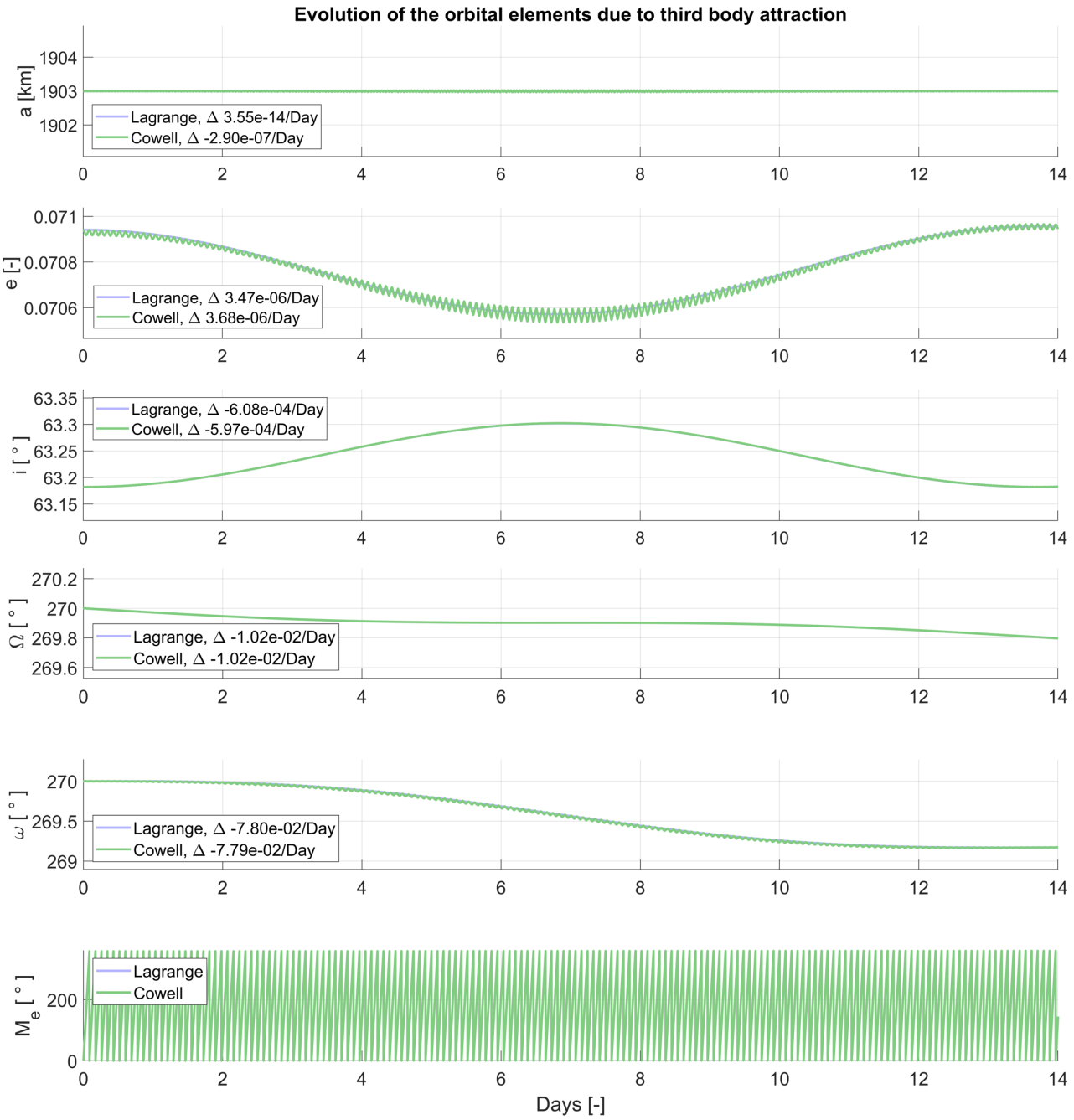

Figure 44: Evolution of the orbital elements due to third body attraction over two weeks or almost 163 orbital revolutions.

Zonal harmonics & third body attraction With each component analysed separately, both the effects of a nonspherical primary body and the third body attraction can be combined and analysed over a period of two months. As a quick check, Cowell's method has been applied to the Keplerian orbit, to see whether this longer analysis causes any issues. The 'evolution' can be seen in figure 56 in the appendices, and shows negligible rates of changes.
A visualisation of the perturbed orbit is shown in figure 45, where the regression of nodes is visible once more. Although a substantially longer period is analysed, the secular rates of change are less in comparison with the Earth, so the apparent fixed crossing points in the orbit are still present.

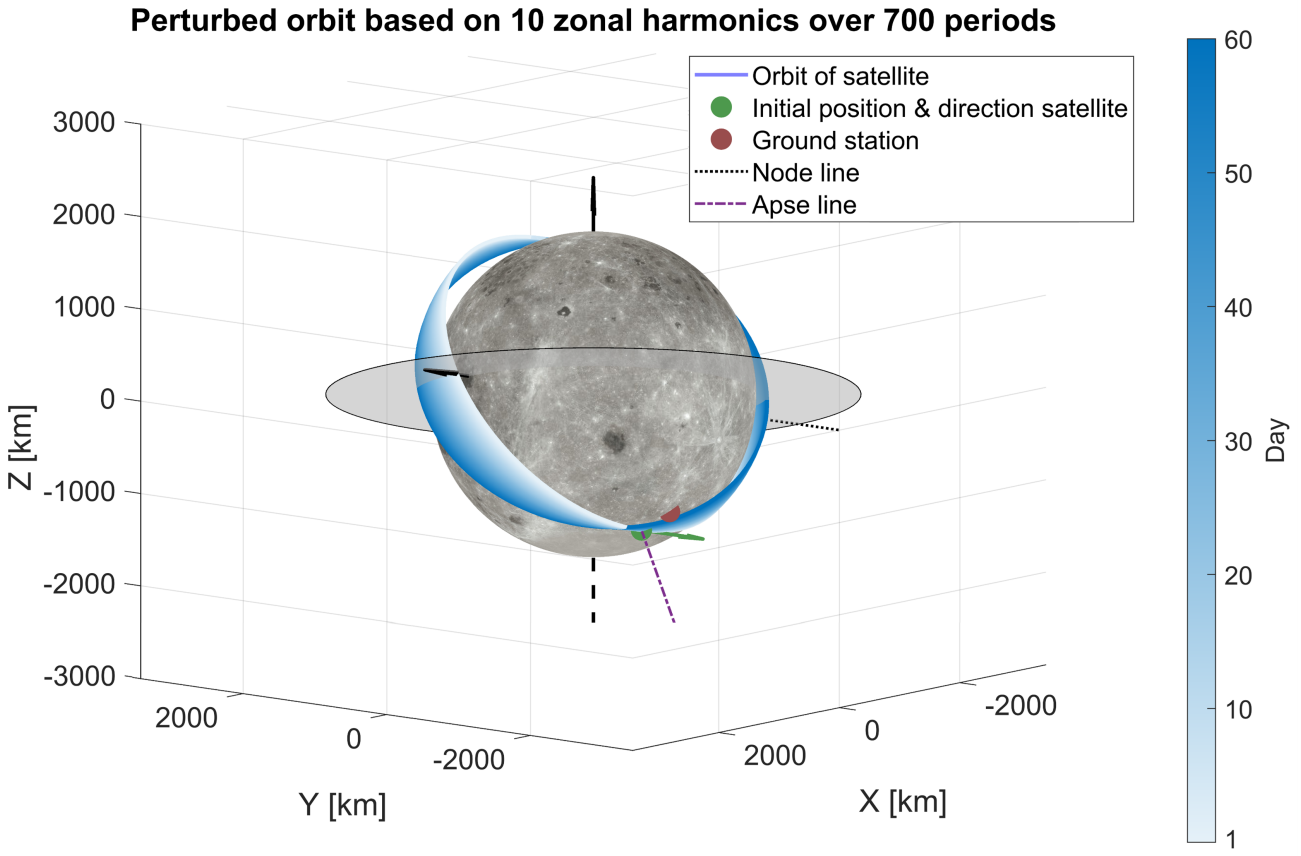

Figure 45: Visualisation of the perturbed orbit due to zonal harmonics up to J_{10} and third body attraction over two months.

Continuing to the evolution of the orbital elements, which is shown in figure 46. As with all previous cases, the semi-major axis remains constant, since no energy is added to the system. For clarity, the blue line has been made slightly wider for some orbital elements, but there are no fluctuations present in the Lagrange equations. The enlargement is especially necessary for the eccentricity, where the results of Cowell's method dominate the view. The solution of the Lagrange equation is visible at the bottom of the green block and clearly displays the medium period effects of the third body attraction. Cowell's method in green combines those medium period effects with the short period effects caused by the zonal harmonics. The same combination is seen for the inclination, although the short period effects are significantly less prominent. The evolution of the right ascension of the ascending node is dominated by the secular rate of change due to the zonal harmonics, which is prominent enough that both the short and medium period effects are not visible any more. Its evolution can be thought of as a summation of the ten zonal harmonics in figure 43 and the third body perturbation in figure 44. This only gives an indication, as the effects are non-linear, so superposition is not possible.
Continue to the argument of perigee, where all effects, short and medium periodic, and secular are clearly visible. A concern, however, is the difference between the two results, as the result of the Lagrange equation slightly outpaces the result of Cowell's method. In the graph, the blue line starts in the middle of the green line, but slowly moves upward. This could indicate an issue somewhere, which will be problematic when a longer stretch of time is analysed and the argument of perigee drifts away further. Looking back to the evolution of the zonal harmonics, figure 43, it is likely that the problem originates here, as there is already a difference between the two methods. The period of analysis is too short to see the difference in the graph, but the rates of change do show a difference.

Possible explanations for this difference could be due to the distinction between osculating and mean orbital elements mentioned earlier. The mean values of inclination obtained from the two methods differ slightly, leading to differences in the rates of change of ω. It could also be due to the different methodologies applied to obtain either result. At least for now, the difference is not significant, approximately 0.9° in 60 days, which about equals the amplitude of the short period effects. It should therefore at most cause minimal issues in the determination of the visibility windows. For now, the analysis will simply continue, but this observation will come back in the recommendations.

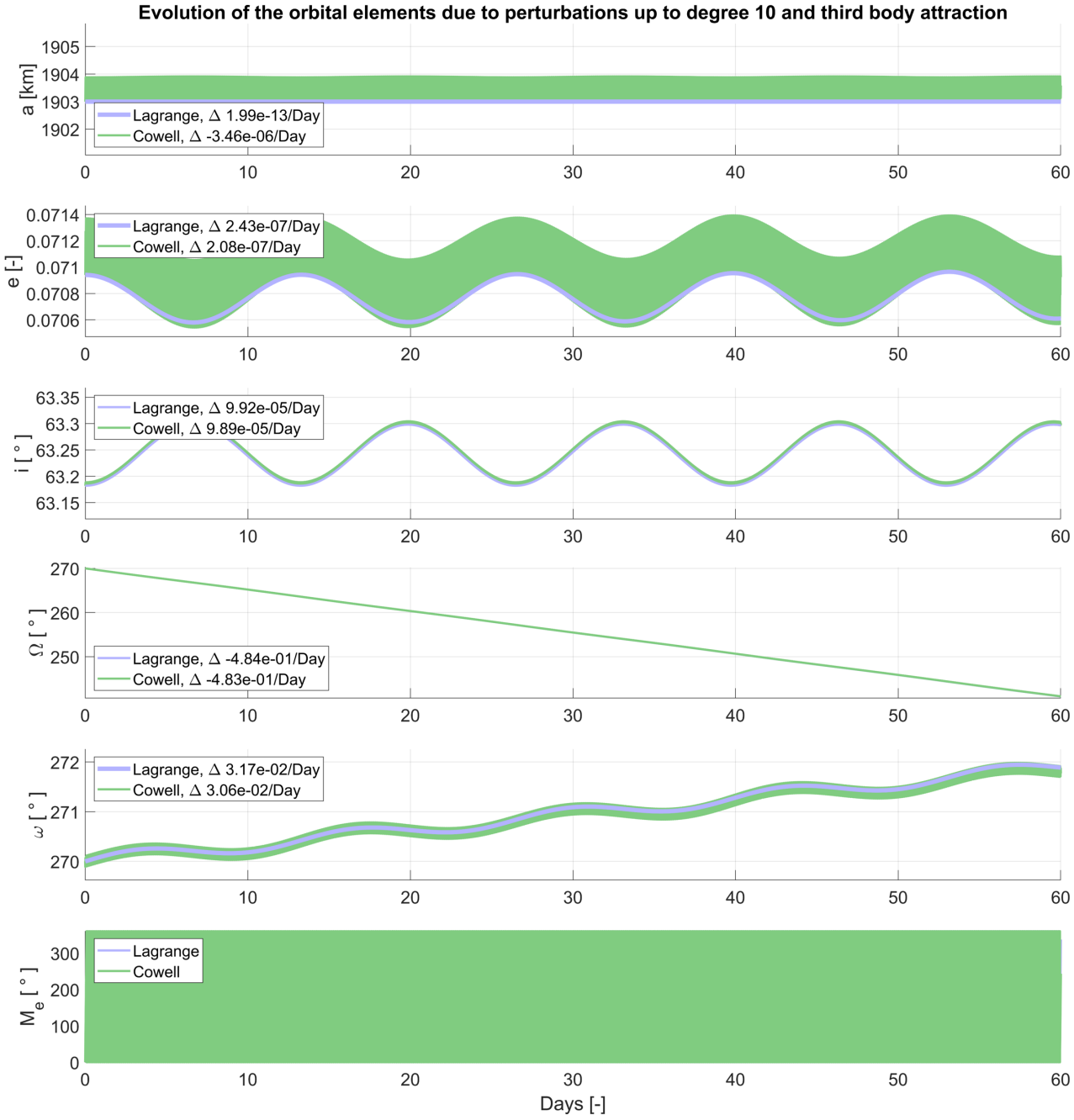

Figure 46: Evolution of the orbital elements due to both zonal harmonics up till the 10^{th} degree and third body attraction over two months or almost 700 orbital revolutions.

With all the perturbations included, the visibility problem can now be tackled. The visibility windows are shown in figures 47 and 48 for the Keplerian and perturbed orbit, respectively. The length of an orbital revolution, a little over 2 hours, can be clearly distinguished as approximately the distance between each rise (or each set). This was also visible in figure 37, but less consistent due to the faster rotational velocity of the Earth.
Starting with the similarities between both figures, the visibility windows follow the same pattern of getting larger and smaller. Both figures also show two bands of continuous invisibility, and three bands of occasional visibility. These observations can be explained by looking at figure 49 which shows the movement of the satellite and ground station viewed from the South Pole of the Moon. Focus, for the moment, only on the Keplerian orbit and imagine the ground station, due to the rotation of the Moon, slowly moving clockwise. With this motion, the ground station moves from its initial position in the direction of the orbit, resulting in larger visibility windows. As the ground station moves further, away from the orbit, the windows get smaller and smaller until the ground station reaches about 11 o'clock and there is no visibility left. This remains the case until the ground station reaches approximately 7 o'clock, which takes a little more than two weeks. Around this position, there is visibility once more. The windows first grow larger as the ground station moves further in the path of the satellite, then shrink when it moves past the path, and slowly starts growing once it reaches the next intersection of ground path and orbit. By now, the initial position has been reached, and the whole cycle, that took a bit longer than 27 days, starts anew. The length of the cycle is determined by the sidereal month of the Moon, marked by black squares in figures 47 and 48. This is similar to the periodicity seen for the Earth in figure 37, which corresponded to a sidereal day.
Shifting to the perturbed orbit, the gist of the story remains the same, but the orbit now changes over time. In figure 49, it can be seen that the perturbations cause the orbit to rotate counterclockwise, which shortens the cycle. Due to the lower magnitude of the perturbations, it takes a while before any discernable difference between the Keplerian and perturbed orbit is seen. However, clear divergence is seen in the final band of visibility windows in figures 47 and 48. The final band starts at the end of day 48 and ends on day 60 for the Keplerian orbit. For the perturbed orbit, the first visibility window of the last band occurs at the start of day 47 and already ends halfway day 58.

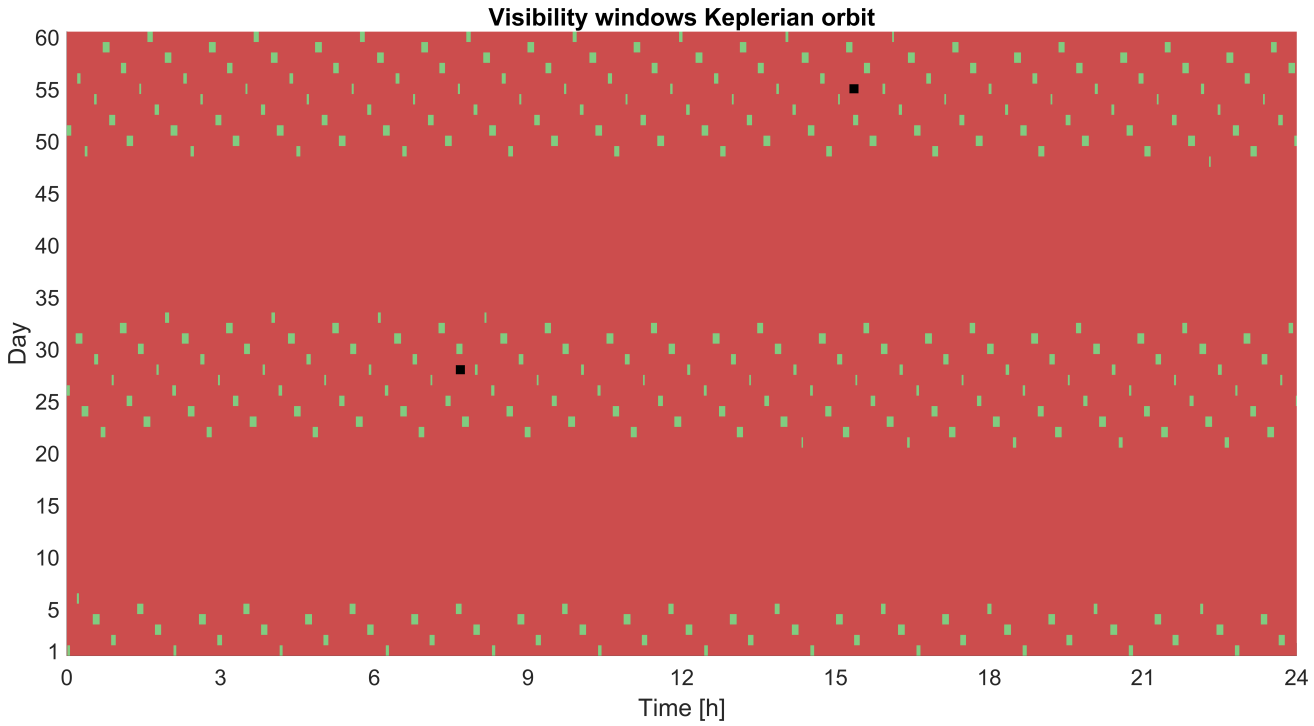

Figure 47: Visibility windows of the Keplerian orbit over two months. Green means the satellite is visible, red invisible, and the black square marks the passing of a sidereal month. Ground station and satellite can communicate for 2.24% of the total time.

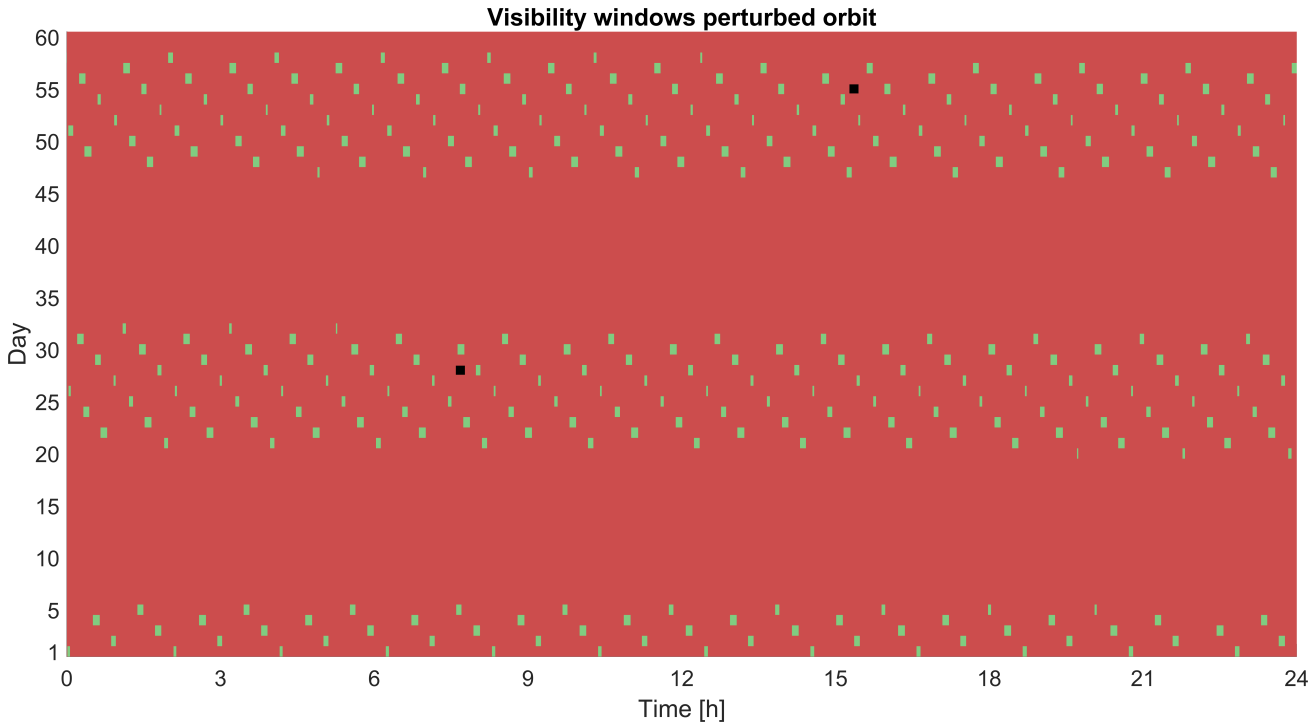

Figure 48: Visibility windows of the perturbed orbit with perturbations up till J_{10} and third body attraction over two months. Green means the satellite is visible, red invisible, and the black square marks the passing of a sidereal month. Ground station and satellite can communicate for 2.17% of the total time.

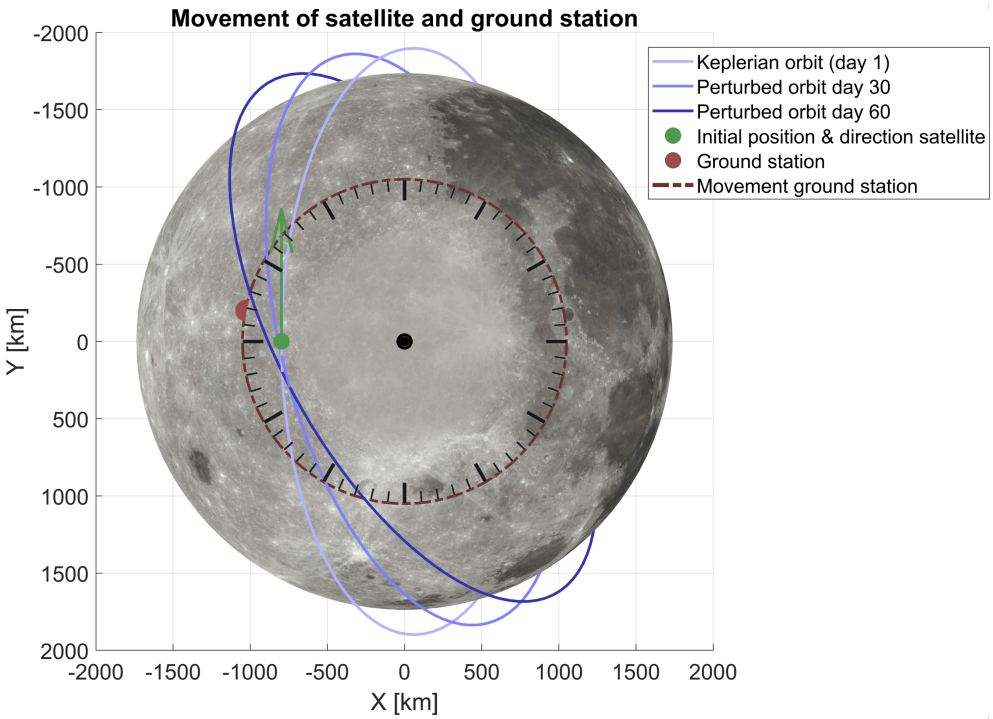

Figure 49: Orbit and ground station as seen from the South Pole, indicated with a black dot. Due to the rotation of the Moon, the ground station rotates clockwise. The position of the ground station is indicated with the help of the clock face.

The large scale of the visibility windows does not allow for precise comparison between the controlling and constraint equation. Instead, the absolute differences between the two methods are plotted in figure 50, and some additional information is provided in table 10. A full list of all the rise and set times is too much to show, instead only the first few orbital evolution are shown in table 15 in the appendices.
The graph for at the Keplerian orbit does not show much relevant information, aside from the fact that there is great correspondence between both methods. The table confirms this, showcasing that the average difference is less than half a second. The three groups in this table correspond to the three bands of visibility and are separated by the two weeks of invisibility.
The graph of the perturbed orbit, right in figure 50 displays more cohesion instead of the chaotic mess of the Keplerian orbit. For the first group, the differences are minimal. Within this time frame, the relatively weak perturbations do not have a significant effect on the orbit yet, which shows in the low average. The first group also does not cover a full band of visibility and instead only covers the last part, where, following the next two groups, the differences are smaller.

The second and third groups, who show the same general behaviour, have significantly higher differences in comparison with the first group. These differences are the largest for the first few windows of each group. This comes back to the same situation as was explored for the fourth of case II of the Earth in table 6. When there is only a small visibility window, which is the case for the first few windows after a long time of invisibility, the controlling equation or elevation angle barely rise above 0 and the slope around the roots is low. Therefore, a tiny translation up or downwards, caused by the slightly different orbital elements of the two methods, causes a large shift in the roots. Similar behaviour, although to a lesser extent, is seen for the last few windows of these groups.
What is also interesting to see is the opposite movement of the rise and set differences in group two and three. If one is decreasing, the other one is increasing and vice versa. This indicates that both methodologies both provide a somewhat different time when these windows occur and a slightly different length of the visibility windows. This observation is reflected in the last column of table 10.
Finally, there is a small increase in the average difference between group two and three. This could be caused by the divergence of ω, as found in figure 46.

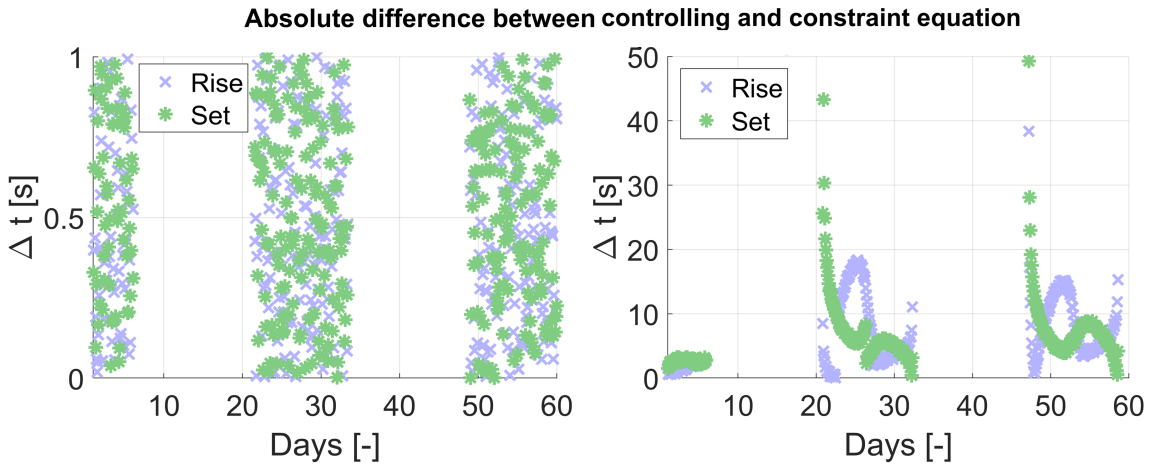

Figure 50: Absolute difference of rise and set times between the controlling and constraint equation, left: Keplerian orbit, right: Perturbed orbit.

	Kepler		**Perturbed**		
	Rise	Set	Rise	Set	Δt windows
Average group 1	00.43	00.54	01.82	02.63	00.89
Average group 2	00.47	00.49	07.69	07.26	07.39
Average group 3	00.45	00.50	08.29	07.47	07.84
Average total	00.46	00.50	06.90	06.53	6.43
Maximum	01.00	01.00	38.38	49.29	88.00

Table 10: The average and maximum absolute difference between the roots found through the controlling and constraint equation, given in seconds and centiseconds. Groups 1, 2, and 3 refer to the bands of visibility seen in figure 50. The final column showcases the absolute difference between the lengths of the visibility windows.

5 Conclusions

In this section, conclusions are drawn from the obtained results. This is followed by various recommendations for future research.

5.1 Conclusions

The goal of this work was to model the orbit of a satellite while solving the visibility problem using Escobal's controlling equation. The model aimed to account for nonspherical gravity and third body attraction, the most significant perturbations for a satellite in low Earth or Lunar orbit. This was done through the perturbing force function, based on the gravitational potential. Before plugging the perturbing force function in the Lagrange equations, an average was taken to get rid of the short period effects. The generated results were subsequently verified by Cowell's method and the constraint equation.

At first, to assess the implementation of the model, the Earth was taken as the primary body, for which there are plenty of references available in literature. While an initial attempt did not yield agreement, further investigation and a second test case led to consensus. The dominant J_2 zonal harmonic was implemented, causing the orbital elements to evolve as expected. The visibility windows determined with the controlling equation were found with good correspondence between both literature and the brute force method. The model was then expanded by including zonal harmonics up to the 10^{th} degree, although their effect on the orbital elements and visibility was minimal.

For the Moon, the same steps were taken to facilitate easy comparison with the Earth. At the core, both systems showcase similar behaviour, but there are some key differences. J_2 is less dominant, meaning that the effects of higher degrees have significant impact. Additionally, both the low magnitude of the zonal harmonic coefficients and the slow rotational velocity of the Moon caused the analysis to be less dynamic. Each visibility window is nearly identical to its predecessor found in an earlier orbital revolution.

As a final addition, third body attraction due to the Earth was introduced, first in isolation, and subsequently in addition to the model with the zonal harmonics. In a longer analysis of two months, most orbital elements show great correspondence between the Lagrange equations and Cowell's method. Only the argument of perigee showed a slight disparity, which grew to about 0.9° over the duration of the analysis. This difference was small enough that it did not cause any significant issues in the determination of the visibility windows, although its effect was noticeable. The discrepancy may stem from the distinction between mean and osculating orbital elements, a topic not addressed in this report.

The Lunar orbit analysed in this report has a low altitude, with its periselene is almost directly overhead of the ground station. This combination resulted in short visibility windows that, at most, lasts around 8 minutes. The rise and set times determined by both the controlling and constraint equation are furthest apart after a long period of invisibility. Those first few visibility windows are short and most susceptible to the small differences between both methodologies, like the averaging out of the short period effects in the perturbing force function. Besides a couple outliers, Escobal's method and the brute force method show great congruity, with an average difference in rise times and set times between the two methods of approximately seven seconds. With time, the difference becomes marginally larger, likely due to the divergence of the argument of perigee.

All in all, the application of Escobal's controlling equation appears to be viable for a satellite in low orbit. The orbital elements had to be kept temporarily fixed when plugging them in the controlling equation, but this caused minimal deterioration in accuracy compared with the brute force method.

5.2 Recommendations

In this report, many validation steps were taken, both in the form of self-verification by using different methodologies and by consulting literature. Although this is crucial to invoke trust in the results presented, numerically integrating both the Lagrange equations and the perturbed equation of motion in Cowell's method comes at a computational cost. This is a drawback that has not been considered in the making of this report, but should be a focus in future research. No attempt has been made to quantify the current computational cost, as the current implementation is far from optimal.

Reducing the computational requirements could be achieved in various ways. Should Escobal's method be deemed sufficiently accurate based on this report, the verification steps using Cowell's method and the constraint equation could be entirely eliminated. A less drastic measure could employ the use of separate time steps when differential equations are numerically integrated. In this report, the time step is equal whether the Lagrange equations or the system perturbed equations of motion are solved. Especially for the Lagrange equations, where the short period effects have been filtered out of the perturbing force function, a larger time step could be taken without encountering accuracy concerns. What is more, analytical solutions of the Lagrange equations exist, which could be used to skip the numerical integration as a whole [79] [62]. The time step could also be increased for Cowell's method, although to a lesser extent due to the short period effects. As was explained in the procedures, section 3.4, the imposed time step for Cowell's method is not caused by accuracy concerns, but instead necessary for the constraint equation. A possible solution is to start out with a larger time step for which the constraint equation can be solved. This would result in a rough estimate of a root, around which Cowell's method could be applied once more, solving for ephemeris with more points around the root. Solving the constraint equation a second time with this input should result in an accurate root determination. A basic root finding algorithm like the bisection method would prove useful in this approach [90].

Then there is the improvement in the determination of the root estimates for the controlling equation. As discussed in the procedures, section 3.3, this is now done by discretising the controlling equation, which diminishes the benefits of the controlling equation. The methodology presented by Escobal [17] was found to have some limitations, which could be due to an issue with implementation, or be a limitation of the methodology itself. If it is the latter, the method could be augmented by making use of the roots found in previous orbital revolution. This would especially yield accurate root estimates for the Moon, due to its low rotational velocity.

Once these improvements are addressed, a proper comparison in computational cost could be made between the controlling equation and the brute force approach. As Escobal's method is almost completely analytical, it should offer a significant advantage in computational cost. But whether that is the case, and how much cheaper it actually is, should be investigated.

In whatever way the computational cost would be reduced, doing so would open the door to longer analyses, which are less feasible at the moment. Studying the behaviour of the orbital elements over a longer period can reveal slight inaccuracies that build over time. Besides accuracy checks, studying the behaviour of a satellite over a long period is essential because elements like long period effects, which were not observed in this report, can be included. This also holds for the medium period effects caused by a third body, which were only barely captured in the current analysis. These effects were observed for half a period in isolation and a little over two periods in combination with the zonal harmonics. Although this gave an indication of the behaviour of the orbital elements, a more complete picture would be obtained in an extended analysis.

Concerning inaccuracies, the divergence observed for the argument of perigee between the Lagrange equations and Cowell's method in figure 46 should be investigated. Whether this is caused by the difference between mean and osculating orbital elements, an issue with the implementation, or simply a result of applying different methodologies to obtain the orbit, a definitive answer is essential.

As a final point, the inclusion of more perturbations could be considered for a more accurate model. A constraint in the methodology used in this report is the use of the Lagrange equations, which are only applicable to conservative forces. Perturbations like drag or solar radiation pressure can therefore not be incorporated. If their inclusion is desired, a switch must be made to for example Gauss' method, that allows for any type of perturbing force [3]. Within the Lagrange equations, slight accuracy improvements could be made. Tesseral and sectoral harmonics do not contribute with a secular rate of change. They only cause short and medium period effects, although the magnitude of these effects is minimal, even in comparison with the short period effects caused by zonal harmonics [41]. A larger improvement could be made by more accurately modelling third body perturbations. This could be done by, for example, including the inclination of the orbit of the Moon instead of setting it to 0. Furthermore, the attraction of the Sun could be included in the model with relative ease, as the same methodology applies as is used for the Earth as a third body. For both cases, initialising and keeping track of the correct relative position of all celestial bodies would become more involved, but nothing that would require drastic changes to the model.

References

[1] E.C. Krupp. *Echoes of the Ancient Skies: The Astronomy of Lost Civilizations*. Oxford paperbacks : Mythology, astronomy. Oxford University Press, 1994. ISBN: 9780195088014.

[2] V.A. Chobotov. *Orbital Mechanics*. AIAA Education Series. American Institute of Aeronautics & Astronautics, 2002. ISBN: 9781600860973.

[3] R.R. Bate, D.D. Mueller and J.E. White. *Fundamentals of Astrodynamics*. Dover Books on Aeronautical Engineering Series. Mineola, NY: Dover Publications, 1971. ISBN: 9780486600611.

[4] I. Newton, I.B. Cohen and A. Whitman. *The Principia: Mathematical Principles of Natural Philosophy*. The Principia: Mathematical Principles of Natural Philosophy. University of California Press, 1999. ISBN: 9780520088160.

[5] Arthur C. Clarke. "Extra-terrestrial relays: Can rocket stations give world-wide radio coverage". In: *Wireless World* (Oct. 1945), pp. 305–308.

[6] Ruth Pritchard-Kelly and John Costa. "Low Earth Orbit Satellite Systems: Comparisons with Geostationary and Other Satellite Systems, and their Significant Advantages". In: *Journal of Telecommunications and the Digital Economy* 10.1 (Mar. 2022), pp. 1–22. ISSN: 2203-1693. DOI: 10.18080/jtde.v10n1.552.

[7] ESA. *ESA'S ANNUAL SPACE ENVIRONMENT REPORT*. July 2024.

[8] Ryan Brukardt, Jesse Klempner and Brooke Stokes. *Space: Investment shifts from GEO to LEO and now beyond*. Available at: https://www.mckinsey.com/industries/aerospace-and-defense/our-insights/space-investment-shifts-from-geo-to-leo-and-now-beyond. Accessed on: 2024-09-15. Chicago, IL, 2022.

[9] Miaoyan Zhang and Jun Zhang. "A Fast Satellite Selection Algorithm: Beyond Four Satellites". In: *IEEE Journal of Selected Topics in Signal Processing* 3.5 (Oct. 2009), pp. 740–747. ISSN: 1932-4553. DOI: 10.1109/jstsp.2009.2028381.

[10] Yuri Ulybyshev. "Geometric Analysis of Low-Earth-Orbit Satellite Communication Systems: Covering Functions". In: *Journal of Spacecraft and Rockets* 37.3 (May 2000), pp. 385–391. ISSN: 1533-6794. DOI: 10.2514/2.3572.

[11] Joseph C Pemberton and Flavius Galiber. "A constraint-based approach to satellite scheduling". In: *DIMACS Series in Discrete Mathematics and Theoretical Computer Science* 57 (2001), pp. 101–114.

[12] Xiaowan Li, Fang Cheng, Pengli Shen and Dongliang Liu. "Fast Determination of Satellite-to-Moon Visibility Using an Adaptive Interpolation Method Based on Vertex Protection". In: *Sensors* 22.12 (June 2022), p. 4451. ISSN: 1424-8220. DOI: 10.3390/s22124451.

[13] J. Douglas Liddle, Antony P. Holt, Susan J. Jason, Kathryn A. O'Donnell and Edward J. Stevens. "Space science with CubeSats and nanosatellites". In: *Nature Astronomy* 4.11 (Nov. 2020), pp. 1026–1030. ISSN: 2397-3366. DOI: 10.1038/s41550-020-01247-2.

[14] Chao Han, XiaoJie Gao and XiuCong Sun. "Rapid satellite-to-site visibility determination based on self-adaptive interpolation technique". In: *Science China Technological Sciences* 60.2 (Dec. 2016), pp. 264–270. ISSN: 1869-1900. DOI: 10.1007/s11431-016-0513-8.

[15] Salvatore Alfano, DAVID NEGRON and Jennifer L Moore. "Rapid determination of satellite visibility periods". In: *Journal of the Astronautical Sciences* 40.2 (1992), pp. 281–296.

[16] Yan Mai and Philip Palmer. "Fast algorithm for prediction of satellite imaging and communication opportunities". In: *Journal of Guidance, Control, and Dynamics* 24.6 (2001), pp. 1118–1124.

[17] P. R. ESCOBAL. “RISE AND SET TIME OF A SATELLITE ABOUT AN OBLATE PLANET”. In: *AIAA Journal* 1.10 (Oct. 1963), pp. 2306–2310. ISSN: 1533-385X. DOI: 10.2514/3.2057.

[18] Manuel A Sánchez, Beatriz Jilete, Srinivas J Setty and Tim Flohrer. “Employing Fast Orbit Prediction for Optimisation of Satellite Visibility Computation”. In: *1st NEO and Debris Detection Conference*. 2019.

[19] P.R. Escobal. *Methods of Orbit Determination*. Krieger Publishing Company, 1976. ISBN: 9780882753195.

[20] H.D. Curtis. *Orbital Mechanics for Engineering Students*. Aerospace Engineering. Elsevier Science, 2013. ISBN: 9780080977485.

[21] J.E. Prussing and B.A. Conway. *Orbital Mechanics*. Oxford University Press, 2013. ISBN: 9780199837700.

[22] W. Torge. *Geodesy*. W. de Gruyter, 2001. ISBN: 9783110170726.

[23] Michael J. Neufeld. *Why Has It Been 50 Years Since Humans Went to the Moon? | National Air and Space Museum*. Dec. 2022. URL: https://airandspace.si.edu/stories/editorial/why-50-years-since-humans-went-moon.

[24] Emily Furfaro. *Does Anything Orbit the Moon? We Asked a NASA Technologist: Episode 24 - NASA*. Nov. 2022. URL: https://www.nasa.gov/general/does-anything-orbit-the-moon-we-asked-a-nasa-technologist/.

[25] Magdalena Petrova. *Why there is a new global race to the moon*. Jan. 2024. URL: https://www.cnbc.com/2024/01/20/why-there-is-a-new-global-race-to-the-moon-.html.

[26] I.A. Crawford. “The scientific case for renewed human activities on the Moon”. In: *Space Policy* 20.2 (May 2004), pp. 91–97. ISSN: 0265-9646. DOI: 10.1016/j.spacepol.2004.02.007.

[27] Clive R. Neal. “The Moon 35 years after Apollo: What’s left to learn?” In: *Geochemistry* 69.1 (Feb. 2009), pp. 3–43. ISSN: 0009-2819. DOI: 10.1016/j.chemer.2008.07.002.

[28] Robert Bruce Pittman, Lynn D. Harper, Mark E. Newfield and Daniel J. Rasky. “Lunar Station: The Next Logical Step in Space Development”. In: *New Space* 4.1 (Mar. 2016), pp. 7–14. ISSN: 2168-0264. DOI: 10.1089/space.2015.0031.

[29] Tao Nie and Pini Gurfil. “Lunar frozen orbits revisited”. In: *Celestial Mechanics and Dynamical Astronomy* 130 (Sept. 2018), p. 61. DOI: 10.1007/s10569-018-9858-0.

[30] L. A. Gagg Filho and S da Silva Fernandes. “A semi analytic theory for preliminary analysis of GARATéA-L Brazilian lunar mission”. unpublished. 2024.

[31] Sergey Trofimov, Maksim Shirobokov and Michael Ovchinnikov. “Design and Study of Satellite Constellations in Frozen Low Lunar Orbits”. In: *73rd International Astronautical Congress*. Sept. 2022.

[32] A. Gouveia. *Conheça a Garatéa-L, missão que pretende levar o Brasil à Lua em 2025*. Jan. 2023. URL: https://www.correiobraziliense.com.br/ciencia-e-saude/2022/08/5028275-conheca-a-garatea-l-missao-que-pretende-levar-o-brasil-a-lua-em-2025.html.

[33] E.T. Whittaker. *A Treatise on the Analytical Dynamics of Particles and Rigid Bodies*. Cambridge Mathematical Library. Cambridge University Press, 1988. ISBN: 9780521358835.

[34] Keith Fratus. *Lecture notes The two-body problem*. 2015.

[35] Wilhelm H. Westphal. “Mechanics of Point Masses and Rigid Bodies”. In: *A Short Textbook of Physics: Not Involving the Use of Higher Mathematics*. Berlin, Heidelberg: Springer Berlin Heidelberg, 1968, pp. 6–57. ISBN: 978-3-642-85476-7. DOI: 10.1007/978-3-642-85476-7_2.

[36] David Folta and David Quinn. “Lunar Frozen Orbits”. In: *AIAA/AAS Astrodynamics Specialist Conference and Exhibit*. American Institute of Aeronautics and Astronautics, June 2006. DOI: 10.2514/6.2006-6749.

[37] Sean C. Solomon and M.Nafi Toksöz. “On the density distribution in the moon”. In: *Physics of the Earth and Planetary Interiors* 1.7 (1968), pp. 475–484. ISSN: 0031-9201. DOI: https://doi.org/10.1016/0031-9201(68)90016-2.

[38] U. Walter. *Astronautics: The Physics of Space Flight*. Springer International Publishing, 2019. ISBN: 9783319743738.

[39] J Virgili Llop, PC Roberts, Zhou Hao, L Ramio Tomas and Valentin Beauplet. “Very low earth orbit mission concepts for earth observation: Benefits and challenges”. In: *Reinventing Space Conference*. 2014, pp. 18–21.

[40] Lance McCreary. “A satellite mission concept for high drag environments”. In: *Aerospace Science and Technology* 92 (2019), pp. 972–989. ISSN: 1270-9638. DOI: https://doi.org/10.1016/j.ast.2019.06.033.

[41] D.A. Vallado. *Fundamentals of Astrodynamics and Applications*. Space technology library. Microcosm Press, 2022. ISBN: 9781881883227.

[42] Dave Doody. *Basics of Spaceflight: Glossary - NASA Science*. 2024. URL: https://science.nasa.gov/learn/basics-of-space-flight/glossary/.

[43] G.W. Collins. *The Foundations of Celestial Mechanics*. Astronomy and astrophysics series. Pachart Publishing House, 1989. ISBN: 9780881260090.

[44] F.R. Moulton. *An Introduction to Celestial Mechanics*. Alcester, England: Read Books, 2008. ISBN: 9781408674185.

[45] Ralph B. Roncoli. *Lunar Constants and Models Document*. Tech. rep. Jet Propulsion Laboratory California Institute of Technology, 2005.

[46] J.W. Cornelisse, H.F.R. Schöyer and K.F. Wakker. *Rocket Propulsion and Spaceflight Dynamics*. Aerospace Engineering Series dl. 1. Pitman, 1979. ISBN: 9780273011415.

[47] George B Arfken, Hans J Weber and Frank E Harris. *Mathematical methods for physicists: a comprehensive guide*. Cambridge, MA: Academic press, 2011.

[48] University of Twente ITC. *Living Textbook | Geographic coordinate system*. 2024. URL: https://ltb.itc.utwente.nl/page/498/concept/81589.

[49] Ann D Hartung. *Lunar Ephemeris Selenograhpic Coordinates of the Earth and Sun for 1971 and 1972*. Tech. rep. NATIONAL AERONAUTICS and SPACE ADMINISTRATION, 1972.

[50] Donald H. Eckhardt. “Theory of the libration of the moon”. In: *The Moon and the Planets* 25.1 (Aug. 1981), pp. 3–49. ISSN: 1573-0794. DOI: 10.1007/bf00911807.

[51] S. S. Fernandes and M. C. F. P. S. Zanardi. *Fundamentos de Astronáutica e suas Aplicações*. Editora UFABC, 2018. ISBN: 9788568576762.

[52] P.K. Seidelmann, United States Naval Observatory. Nautical Almanac Office and Great Britain. Nautical Almanac Office. *Explanatory Supplement to the Astronomical Almanac*. Explanatory Supplement to the Astronomical Almanac. University Science Books, 1992. ISBN: 9781891389450.

[53] J.C. Robinson. *An Introduction to Ordinary Differential Equations*. Cambridge University Press, 2004. ISBN: 9780521533911.

[54] D.L. Boulet. *Methods of Orbit Determination for the Microcomputer*. Richmond, VA: Willmann-Bell, Incorporated, 1991. ISBN: 9780943396347.

[55] V.R. Bond and M.C. Allman. *Modern Astrodynamics: Fundamentals and Perturbation Methods*. Princetion, NJ: Princeton University Press, 2021. ISBN: 9780691223902.

[56] M. Braun. *Differential Equations and Their Applications: An Introduction to Applied Mathematics*. Texts in Applied Mathematics. Springer New York, 1992. ISBN: 9780387978949.

[57] William F. Trench. *Elementary Differential Equations with Boundary Value Problems*. Brooks/Cole Thomson Learning, 2013. ISBN: 9780534368418.

[58] D. Brouwer and G.M. Clemence. *Methods of Celestial Mechanics*. New York, NY: Elsevier Science, 2013. ISBN: 9781483225784.

[59] P.M. Fitzpatrick. *Principles of Celestial Mechanics*. Academic Press, 1970. ISBN: 9780122579509.

[60] Hélio Koiti, Kuga Valdemir, Carrara Kondapalli and Rama Rao. *Satélites Artificiais - Movimento Orbital*. 2011.

[61] Min Hu, Yongjing Ruan, Huifeng Zhou, Jiahui Xu and Wen Xue. "Long-Term Orbit Prediction and Deorbit Disposal Investigation of MEO Navigation Satellites". In: *Aerospace* 9.5 (May 2022), p. 266. ISSN: 2226-4310. DOI: 10.3390/aerospace9050266.

[62] Yoshihide Kozai. "The motion of a close earth satellite". In: *Astronomical Journal, Vol. 64, p. 367 (1959)* 64 (1959), p. 367.

[63] Maria Lívia G T X da Costa, Rodolpho Vilhena de Moraes, Jean Paulo S Carvalho and Antônio Fernando B A Prado. "Artificial satellites orbiting planetary satellites: critical inclination and sun-synchronous orbits". In: *Journal of Physics: Conference Series* 911.1 (2017), p. 012018. DOI: 10.1088/1742-6596/911/1/012018.

[64] Stanley Q. Kidder and Thomas H. Vonder Haar. "On the Use of Satellites in Molniya Orbits for Meteorological Observation of Middle and High Latitudes". In: *Journal of Atmospheric and Oceanic Technology* 7.3 (June 1990), pp. 517–522. ISSN: 1520-0426. DOI: 10.1175/1520-0426(1990)007<0517:otuosi>2.0.co;2.

[65] Shannon L. Coffey, André Deprit and Bruce R. Miller. "The critical inclination in artificial satellite theory". In: *Celestial Mechanics* 39.4 (Dec. 1986), pp. 365–406. ISSN: 1572-9478. DOI: 10.1007/bf01230483.

[66] F.B. Hildebrand. *Introduction to Numerical Analysis*. Dover books on advanced mathematics. Dover Publications, 1987. ISBN: 9780486653631.

[67] Randy A Eckman, Aaron J Brown, Daniel R Adamo and Robert G Gottlieb. *Normalization and implementation of three gravitational acceleration models*. Tech. rep. NASA, 2016.

[68] Giorgio E. O. Giacaglia, James P. Murphy and Theodore L. Felsentreger. "A semi-analytic theory for the motion of a lunar satellite". In: *Celestial Mechanics* 3.1 (Mar. 1970), pp. 3–66. ISSN: 1572-9478. DOI: 10.1007/bf01230432.

[69] Matthew M. Berry and Vincent T. Coppola. "Correct Modeling of the Indirect Term for Third-Body Perturbation". In: *Astrodynamics Specialist Conference*. (AAS 07–417). Mackinac Island, Michigan: AIAA, 2007.

[70] G. E. Cook. "Luni-Solar Perturbations of the Orbit of an Earth Satellite". In: *Geophysical Journal International* 6.3 (Apr. 1962), pp. 271–291. ISSN: 0956-540X. DOI: 10.1111/j.1365-246X.1962.tb00351.x.

[71] Antonio Fernando Bertachini de Almeida Prado. “Third-Body Perturbation in Orbits Around Natural Satellites”. In: *Journal of Guidance, Control, and Dynamics* 26.1 (2003), pp. 33–40. DOI: 10.2514/2.5042.

[72] Christopher Clouse, Andrea Ferroglia and Miguel C N Fiolhais. “Spin–orbit gravitational locking—an effective potential approach”. In: *European Journal of Physics* 43.3 (Mar. 2022), p. 035602. DOI: 10.1088/1361-6404/ac5638.

[73] Carlos Renato Huaura SolÓrzano. “Perturbação de Terceiro Corpo com Modelos de Média Simples”. MA thesis. INPE, São José dos Campos, 2002.

[74] I. da Costa, Antônio Fernando and Bertachini de Almeida Prado. “ORBITAL EVOLUTION OF A SATELLITE PERTURBED BY A THIRD-BODY”. In: *Advances in Space Dynamics*. 2000.

[75] M. J.D. Powell. *A Fortran subroutine for solving systems of nonlinear algebraic equations*. Tech. rep. Atomic Energy Research Establishment, Nov. 1968.

[76] Kenneth Levenberg. “A METHOD FOR THE SOLUTION OF CERTAIN NON-LINEAR PROBLEMS IN LEAST SQUARES”. In: *Quarterly of Applied Mathematics* 2.2 (1944), pp. 164–168. ISSN: 0033569X, 15524485.

[77] J.R. Dormand and P.J. Prince. “A family of embedded Runge-Kutta formulae”. In: *Journal of Computational and Applied Mathematics* 6.1 (Mar. 1980), pp. 19–26. ISSN: 0377-0427. DOI: 10.1016/0771-050x(80)90013-3.

[78] F. Capuano, G. Coppola, L. RÁndez and L. de Luca. “Explicit Runge–Kutta schemes for incompressible flow with improved energy-conservation properties”. In: *Journal of Computational Physics* 328 (2017), pp. 86–94. ISSN: 0021-9991. DOI: https://doi.org/10.1016/j.jcp.2016.10.040.

[79] Dirk Brouwer. “Solution of the problem of artificial satellite theory without drag”. In: *Astronomical Journal* 64 (1959), p. 378.

[80] James A. Ward. *Variations in orbital elements*. Aug. 1971.

[81] Sandro da Silva Fernandes and Francisco das Chagas Carvalho. “Effects of the main zonal harmonics on optimal low-thrust limited-power transfers”. In: *Journal of the Brazilian Society of Mechanical Sciences and Engineering* 43.12 (Nov. 2021). ISSN: 1806-3691. DOI: 10.1007/s40430-021-03229-5.

[82] P. Fortescue, G. Swinerd and J. Stark. *Spacecraft Systems Engineering*. Wiley, 2011. ISBN: 9781119978367.

[83] Tyler Reid, Todd Walter and Per Enge. “L1/L5 SBAS MOPS Ephemeris Message to Support Multiple Orbit Classes”. In: *Proceedings of the 2013 International Technical Meeting of The Institute of Navigation*. Jan. 2013, pp. 78–92.

[84] M. A. Ivanov, H. Hiesinger, C. H. van der Bogert, C. Orgel, J. H. Pasckert and J. W. Head. “Geologic History of the Northern Portion of the South Pole-Aitken Basin on the Moon”. In: *Journal of Geophysical Research: Planets* 123.10 (Oct. 2018), pp. 2585–2612. ISSN: 2169-9100. DOI: 10.1029/2018je005590.

[85] Noah E. Petro and Carlé M. Pieters. “Surviving the heavy bombardment: Ancient material at the surface of South Pole-Aitken Basin”. In: *Journal of Geophysical Research: Planets* 109.E6 (June 2004). ISSN: 0148-0227. DOI: 10.1029/2003je002182.

[86] Roberto Flores, Burhani Makame Burhani and Elena Fantino. “A method for accurate and efficient propagation of satellite orbits: A case study for a Molniya orbit”. In: *Alexandria Engineering Journal* 60.2 (2021), pp. 2661–2676. ISSN: 1110-0168.

[87] Martin Lara, Juan F. San-Juan and Denis Hautesserres. "HEOSAT: a mean elements orbit propagator program for highly elliptical orbits". In: *CEAS Space Journal* 10.1 (2018), pp. 3–23. DOI: 10.1007/s12567-017-0152-x.

[88] Gabriella Gaias, Camilla Colombo and Martin Lara. "Accurate Osculating/Mean Orbital Elements Conversions for Spaceborne Formation Flying". In: *27th International Symposium on Space Flight Dynamics (ISSFD)*. Feb. 2018.

[89] H. G. Walter. "Conversion of osculating orbital elements into mean elements". In: *The Astronomical Journal* 72 (1967), p. 994. ISSN: 0004-6256. DOI: 10.1086/110374.

[90] John P.T. Mo, Sherman C.P. Cheung and Raj Das. "Chapter 2 - Basic Numerical Techniques". In: *Demystifying Numerical Models*. Ed. by John P.T. Mo, Sherman C.P. Cheung and Raj Das. Butterworth-Heinemann, 2019, pp. 5–31. ISBN: 978-0-08-100975-8. DOI: https://doi.org/10.1016/B978-0-08-100975-8.00002-3.

[91] William M Mularie. *World Geodetic System 1984 Its Definition and Relationships with Local Geodetic Systems*. Jan. 2000.

A Physical Parameters

In this appendix, various relevant parameters are presented. The physical parameters of the Earth, Moon, and Sun shown in the table below have been sourced from Curtis and Roncoli [20] [45].

Celestial body	**Earth**	**Moon**	**Sun**
Mass M $[km]$	$5.974 \cdot 10^{24}$	$73.48 \cdot 10^{21}$	$1.989 \cdot 10^{30}$
Equatorial radius R_e $[km]$	6 378.14	1737.4	696000
Flatness f $[-]$	0.00335364228	0.0	-
Gravitational parameter μ $[km^3/s^2]$	398 600.4356	4 902.801076	$13.2712 \cdot 10^{10}$
Sidereal day or month SD $[h]$	23.9345	655.68	609.12
Sphere of influence SOI $[km]$	$9.25 \cdot 10^5$	$6.6 \cdot 10^4$	-
Semi-major axis orbit a $[km]$	$149.6 \cdot 10^6$	$384.4 \cdot 10^3$	-
Eccentricity orbit e $[-]$	0.0167	0.0549	-
Inclination orbit i $[^\circ]$	23.45	6.68	7.25

The universal gravitational constant G is defined as

$$G = 6.67259 \cdot 10^{-11} \mathrm{m}^3/(\mathrm{kg\ s}^2).$$

A.1 Legendre polynomials

The first ten Legendre polynomials can be seen in the table below. In general, they can be expressed with Rodrigues' formula as [47]

$$P_n(x) = \frac{1}{2^n n!} \frac{d^n}{dx^n} \left(x^2 - 1\right)^n. \tag{A.1}$$

Degree n	**Legendre polynomial** $P_n(x)$
0	1
1	x
2	$\frac{1}{2}(3x^2 - 1)$
3	$\frac{1}{2}(5x^3 - 3x)$
4	$\frac{1}{8}(35x^4 - 30x^2 + 3)$
5	$\frac{1}{8}(63x^5 - 70x^3 + 15x)$
6	$\frac{1}{16}(231x^6 - 315x^4 + 105x^2 - 5)$
7	$\frac{1}{16}(429x^7 - 693x^5 + 315x^3 - 35x)$
8	$\frac{1}{128}(6435x^8 - 12012x^6 + 6930x^4 - 1260x^2 + 35)$
9	$\frac{1}{128}(12155x^9 - 25740x^7 + 18018x^5 - 4620x^3 + 315x)$
10	$\frac{1}{256}(46189x^{10} - 109395x^8 + 90090x^6 - 30030x^4 + 3465x^2 - 63)$

A.2 Zonal harmonics

The first ten normalised zonal harmonic coefficients for the Earth and Moon are listed in table 11. With these, the regular zonal harmonic coefficients are found through

$$J_n = \overline{J_n}\sqrt{2n+1} \tag{A.2}$$

For completeness, these are presented in table 12.

Degree	**Earth** [91]	**Moon** [45]
2	$4.84165371736 \cdot 10^{-4}$	$0.90901094948 \cdot 10^{-4}$
3	$-9.57254173792 \cdot 10^{-7}$	$0.32030716796 \cdot 10^{-5}$
4	$-5.39873863789 \cdot 10^{-7}$	$-0.32140954503 \cdot 10^{-5}$
5	$-6.85323475630 \cdot 10^{-8}$	$0.22100987639 \cdot 10^{-6}$
6	$1.49957994714 \cdot 10^{-7}$	$-0.37647906448 \cdot 10^{-5}$
7	$-9.09789371450 \cdot 10^{-8}$	$-0.56133065640 \cdot 10^{-5}$
8	$-4.96711667324 \cdot 10^{-8}$	$-0.23195390552 \cdot 10^{-5}$
9	$-2.76714300853 \cdot 10^{-8}$	$0.35424158214 \cdot 10^{-5}$
10	$-5.26222488569 \cdot 10^{-8}$	$0.93303628588 \cdot 10^{-6}$

Table 11: Normalised zonal harmonic coefficients $\overline{J_n}$

Degree	**Earth**	**Moon**
2	$1.08262668355 \cdot 10^{-3}$	$2.03261027533 \cdot 10^{-4}$
3	$-2.53265648533 \cdot 10^{-6}$	$8.47453109571 \cdot 10^{-6}$
4	$-1.61962159137 \cdot 10^{-6}$	$-9.64228635084 \cdot 10^{-6}$
5	$-2.27296082869 \cdot 10^{-7}$	$7.33006834958 \cdot 10^{-7}$
6	$5.40681239107 \cdot 10^{-7}$	$-1.35741457110 \cdot 10^{-5}$
7	$-3.52359908418 \cdot 10^{-7}$	$-2.17402428396 \cdot 10^{-5}$
8	$-2.04799466985 \cdot 10^{-7}$	$-9.56370452733 \cdot 10^{-6}$
9	$-1.20616967365 \cdot 10^{-7}$	$1.54410325813 \cdot 10^{-5}$
10	$-2.41145438626 \cdot 10^{-7}$	$4.27570940617 \cdot 10^{-6}$

Table 12: Zonal harmonic coefficients J_n

B Additional Results

In this section, additional results are shown. They are not essential for the main story told in the results of the main report in section 4, but they do provide some additional details.

B.1 Case I

Figure 51 shows the orbital elements of the Keplerian orbit over one orbital revolution. It can be seen that the orbital elements obtained from Cowell's method stay (as good as) constant, meaning that this method has been implemented correctly.

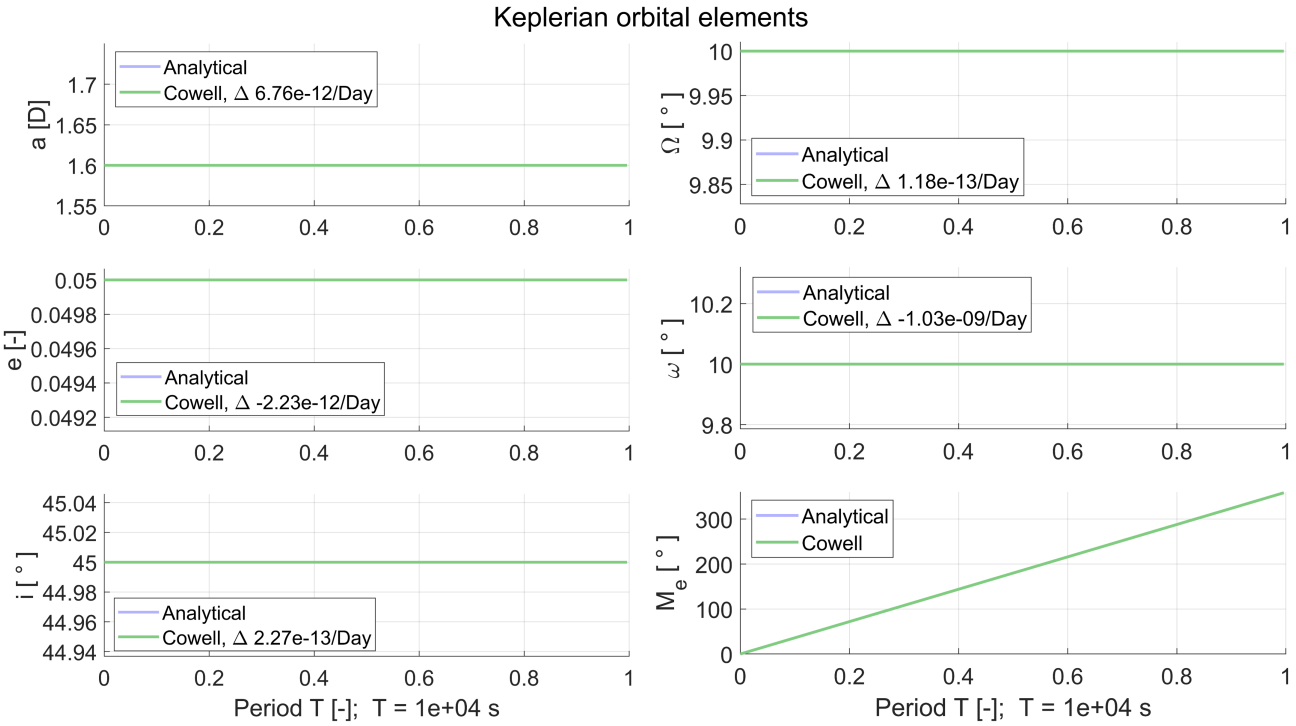

Figure 51: 'Evolution' of the orbital elements of a Keplerian orbit using Cowell's method. The legend shows the rate of change of the orbital elements extrapolated to a day.

B.2 Case II

Figure 52 shows the same verification steps that were taken for case I, as a final validation. On the left, the elevation angle of the Keplerian orbit over five orbital revolutions is shown. Although this is a different variable than the controlling equation, both are a measure of visibility, so similar behaviour is observed compared to figure 31. The maxima and minima shift in the same manner, and the roots match as well. The right of figure 52 shows the slant range of the rise and set in the first orbital revolution. As expected, the slant ranges are tangential to the Earth.

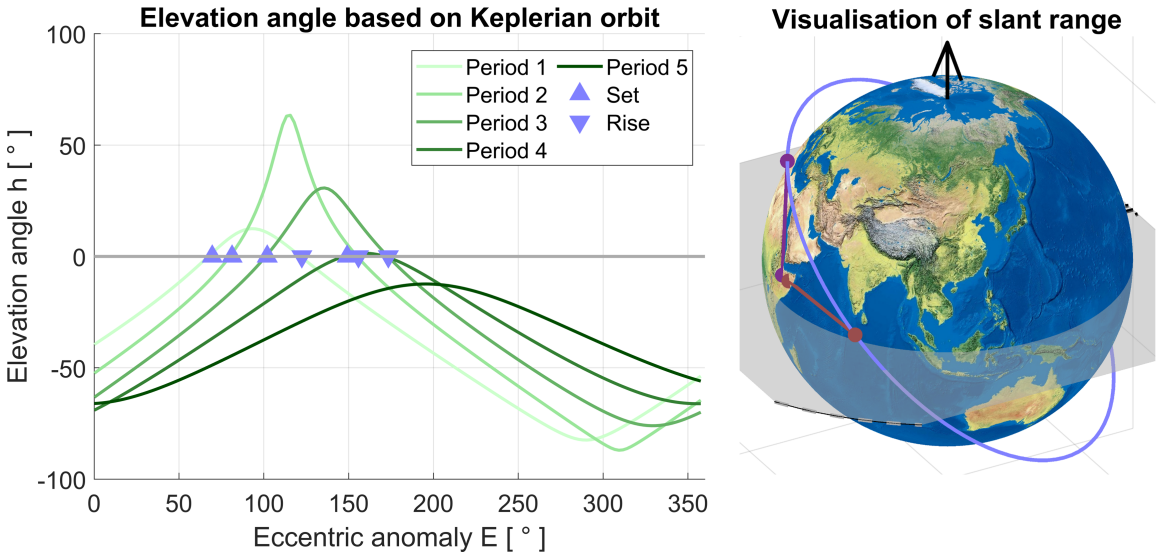

Figure 52: Verification of visibility window. Left: Elevation angle for five orbital revolutions. Right: Slant range at rise (purple) and set (red) for the first orbital revolution.

Figure 53 show both the controlling function and the elevation angle of the perturbed orbit based on J_2. These figures are look-alikes of their Keplerian counterparts, figures 31 and 52. Due to the short analysis period, the effect of the perturbations is not noticeable yet.

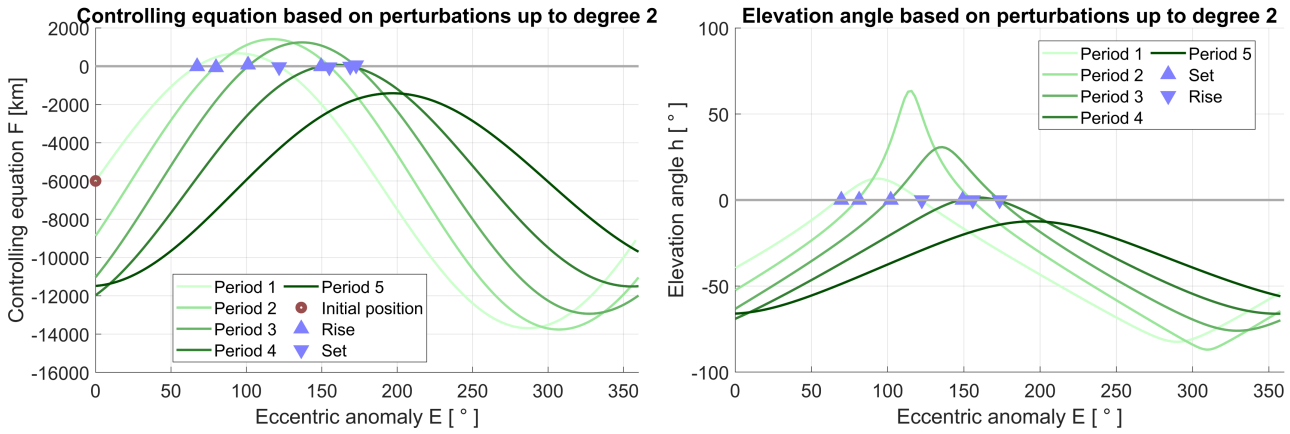

Figure 53: Left: Controlling equation based on the orbital elements at the start of the period. Right: Elevation angle. Both are shown for five orbital revolutions based on perturbations associated with J_2.

Figure 54 shows the evolution of the orbital elements of a perturbed orbit, including perturbations up till J_{10} over 50 orbital revolutions. Although more degrees are included in comparison with figure 34, the contribution of these degree are so meagre that no difference is observed.

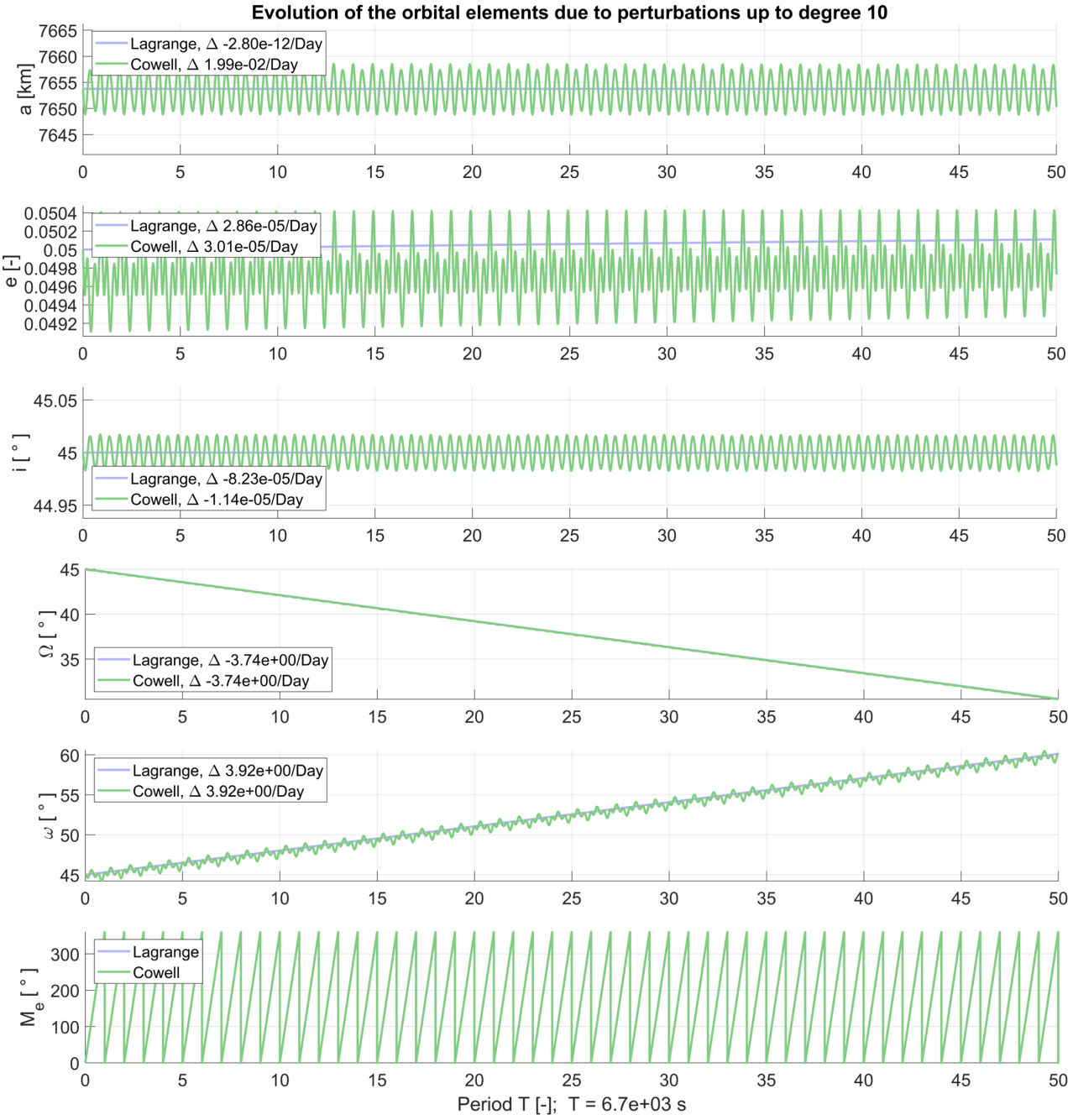

Figure 54: Evolution of orbital elements due to perturbations up to J_{10} over 50 orbital revolutions.

Figure 55 shows the visibility windows that are obtained from the constraint equation applied to the results of Cowell's method. These windows closely match those found from the controlling equation showcased in figure 37.

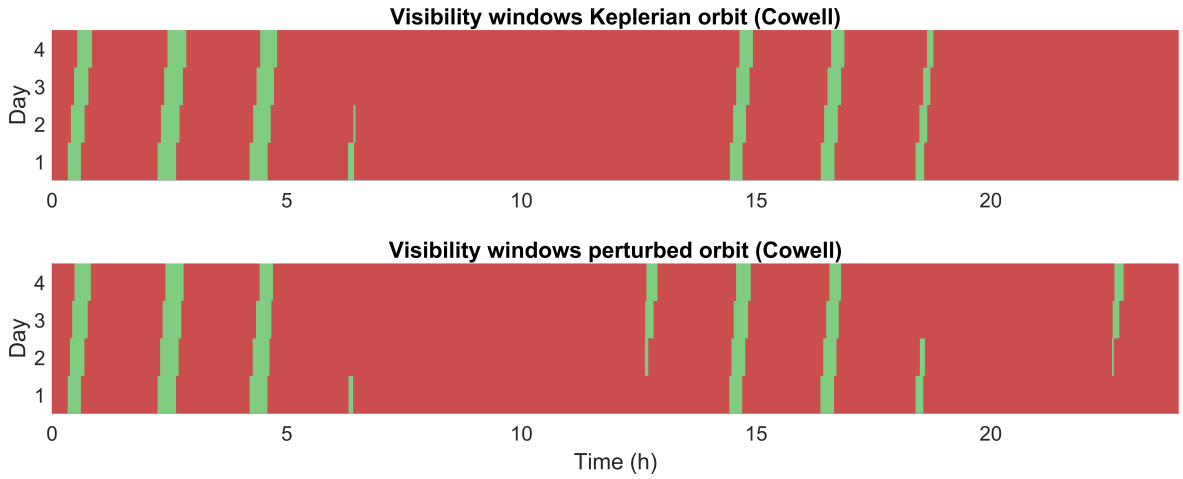

Figure 55: Visibility windows of both the Keplerian and perturbed orbit with perturbations up till J_{10} over 4 days obtained from Cowell's method and the constraint equation. Green means the satellite is visible, red invisible

Tables 13 and 14 showcase the exact rise and set times of the Keplerian and perturbed orbit over 52 orbital revolutions (approximately 4 days), respectively. Both the results from the controlling and the constraint equation are shown, followed by the absolute difference between the two.

Keplerian orbit

Rise			Set		
Controlling	**Constraint**	**Difference**	**Controlling**	**Constraint**	**Difference**
00:19:57	00:19:57	0.61	00:36:47	00:36:47	0.41
02:14:52	02:14:52	0.52	02:38:32	02:38:32	0.24
04:12:27	04:12:28	0.46	04:35:26	04:35:27	0.57
06:18:07	06:18:08	0.41	06:25:57	06:25:57	0.17
14:26:19	14:26:19	0.46	14:42:28	14:42:28	0.56
16:22:29	16:22:30	0.93	16:40:08	16:40:09	0.76
18:23:35	18:23:35	0.02	18:34:43	18:34:44	0.70
24:23:58	24:23:58	0.33	24:41:35	24:41:35	0.10
26:19:03	26:19:03	0.26	26:42:54	26:42:55	0.81
28:16:54	28:16:55	0.45	28:39:31	28:39:31	0.10
30:25:09	30:25:10	0.95	30:27:46	30:27:46	0.00
38:30:21	38:30:22	0.74	38:46:54	38:46:55	0.81
40:26:50	40:26:50	0.02	40:44:18	40:44:19	0.59
42:28:25	42:28:26	0.78	42:38:38	42:38:39	0.06
48:28:00	48:28:00	0.13	48:46:20	48:46:21	0.31
50:23:14	50:23:15	0.26	50:47:15	50:47:15	0.67
52:21:23	52:21:23	0.59	52:43:35	52:43:36	0.99
62:34:25	62:34:26	0.49	62:51:19	62:51:20	0.91
64:31:12	64:31:13	0.77	64:48:27	64:48:28	0.18
66:33:19	66:33:19	0.28	66:42:31	66:42:31	0.10
72:32:03	72:32:03	0.10	72:51:04	72:51:04	0.87
74:27:27	74:27:27	0.51	74:51:34	74:51:35	0.77
76:25:54	76:25:54	0.69	76:47:38	76:47:38	0.30
86:38:31	86:38:32	0.82	86:55:42	86:55:43	0.70
88:35:35	88:35:36	0.12	88:52:36	88:52:36	0.50
90:38:19	90:38:19	0.34	90:46:20	90:46:21	0.95

Table 13: Rise and set times of the Keplerian orbit obtained from the controlling and constraint equation, given in $hh:mm:ss$, and the (absolute) difference given in seconds and centiseconds

Perturbed orbit up till J_{10}

Rise			Set		
Controlling	**Constraint**	**Difference**	**Controlling**	**Constraint**	**Difference**
00:19:56	00:20:02	06.21	00:36:47	00:36:40	07.47
02:14:49	02:14:52	02.87	02:38:29	02:38:31	02.55
04:12:27	04:12:22	05.01	04:35:16	04:35:23	07.24
06:19:00	06:19:04	04.09	06:24:57	06:25:00	03.52
14:25:46	14:26:01	15.23	14:42:29	14:42:34	05.09
16:22:16	16:22:34	18.15	16:39:47	16:39:34	13.29
18:24:04	18:24:09	04.38	18:33:57	18:33:58	00.49
24:23:16	24:23:22	05.51	24:41:48	24:41:38	10.23
26:18:33	26:18:33	00.03	26:42:22	26:42:24	01.57
28:16:57	28:16:47	09.62	28:38:23	28:38:29	06.04
36:38:16	36:38:42	26.50	36:42:58	36:43:02	04.05
38:29:01	38:29:16	14.69	38:46:47	38:46:48	01.52
40:26:26	40:26:41	15.24	40:43:24	40:43:21	02.93
42:30:07	42:30:02	05.12	42:36:28	42:36:31	02.74
46:35:23	46:35:38	14.69	46:38:17	46:38:01	15.74
48:26:41	48:26:45	03.95	48:46:33	48:46:21	12.07
50:22:23	50:22:20	03.74	50:46:07	50:46:07	00.50
52:21:44	52:21:29	14.33	52:41:17	52:41:23	06.14
60:39:07	60:39:24	17.02	60:50:03	60:50:10	06.49
62:32:28	62:32:42	13.51	62:50:53	62:50:52	01.13
64:30:48	64:31:01	12.46	64:46:52	64:46:50	02.01
70:37:00	70:37:08	07.47	70:45:46	70:45:28	17.90
72:30:10	72:30:12	01.92	72:51:03	72:50:51	12.35
74:26:20	74:26:13	07.35	74:49:43	74:49:42	01.04
76:26:56	76:26:37	19.02	76:43:54	76:43:59	05.48
84:41:23	84:41:37	13.59	84:55:34	84:55:38	04.16
86:36:05	86:36:17	12.54	86:54:50	86:54:48	02.30
88:35:25	88:35:33	07.73	88:50:15	88:50:13	01.98
94:39:47	94:39:53	05.39	94:51:51	94:51:26	24.27

Table 14: Rise and set times of the perturbed orbit obtained from the controlling and constraint equation, given in $hh:mm:ss$, and the (absolute) difference given in seconds and centiseconds

B.3 Moon

Figure 56 shows the 'evolution' of the orbital elements of the Keplerian orbit over 60 days. Even over this longer period of analysis, the results of Cowell's method stay (as good as) constant.

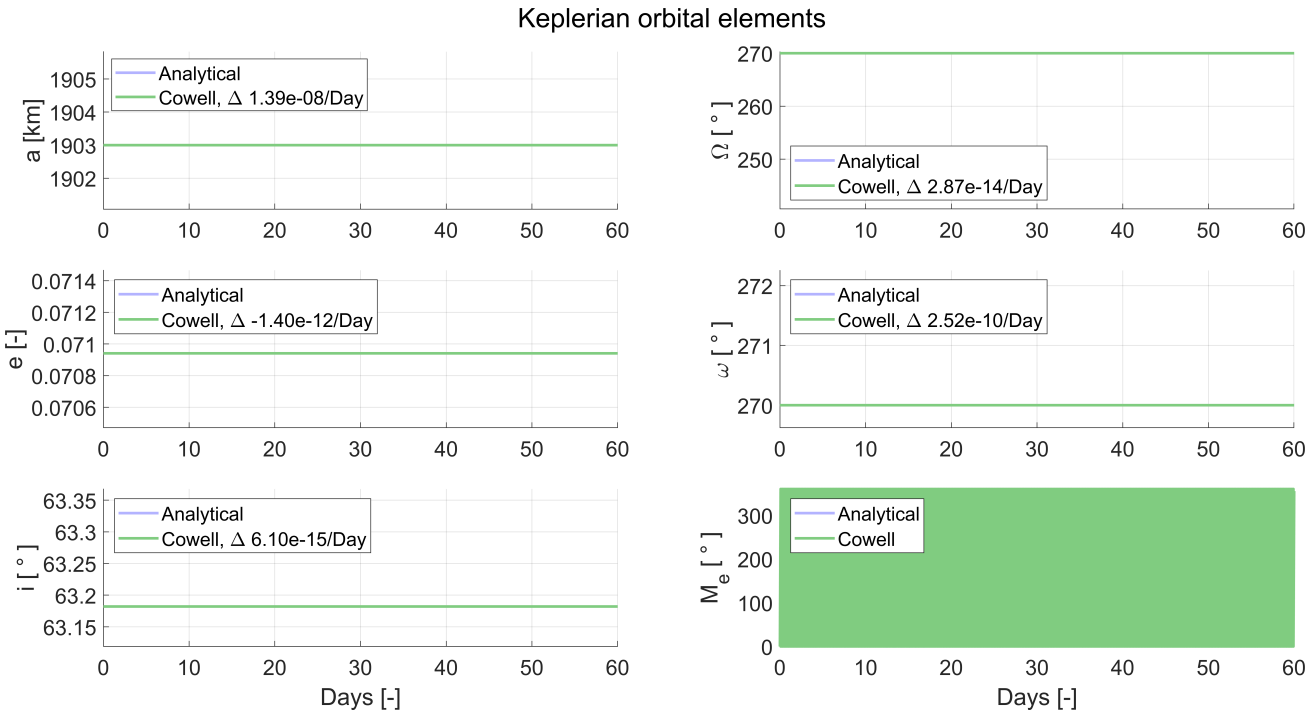

Figure 56: 'Evolution' of the orbital elements of a Keplerian orbit using Cowell's method over two months.

Table 15 showcases the exact rise and set times of the perturbed orbit over 29 orbital revolutions. The same number of entries are shown as in table 14. The rest is left out, as that would result in a considerable amount of pages being filled with data. Both the results from the controlling and the constraint equation are shown, followed by the absolute difference between the two.

Perturbed orbit up to J_{10} & third body attraction

Rise			Set		
Controlling	**Constraint**	**Difference**	**Controlling**	**Constraint**	**Difference**
00:00:35	00:00:36	0.61	00:03:41	00:03:43	1.52
02:04:52	02:04:53	0.61	02:08:10	02:08:12	2.06
04:09:09	04:09:10	0.80	04:12:38	04:12:41	2.51
06:13:26	06:13:27	1.14	06:17:07	06:17:09	1.90
08:17:42	08:17:43	0.60	08:21:36	08:21:38	2.30
10:21:59	10:22:00	1.15	10:26:04	10:26:07	2.72
12:26:15	12:26:16	0.78	12:30:33	12:30:35	2.21
14:30:31	14:30:33	1.46	14:35:01	14:35:04	2.78
16:34:48	16:34:49	1.17	16:39:29	16:39:32	2.46
18:39:04	18:39:05	0.91	18:43:58	18:44:00	2.27
20:43:20	20:43:21	0.66	20:48:26	20:48:28	2.24
22:47:36	22:47:38	1.42	22:52:54	22:52:56	2.38
24:51:53	24:51:54	1.16	24:57:21	24:57:24	2.70
26:56:09	26:56:10	0.88	27:01:49	27:01:52	3.23
29:00:25	29:00:27	1.58	29:06:16	29:06:19	2.99
31:04:42	31:04:43	1.24	31:10:43	31:10:46	2.97
33:08:58	33:09:00	1.87	33:15:10	33:15:13	3.21
35:13:14	35:13:16	1.44	35:19:36	35:19:39	2.71
37:17:31	37:17:33	1.97	37:24:02	37:24:05	2.48
39:21:47	39:21:49	1.42	39:28:28	39:28:31	2.54
41:26:04	41:26:06	1.81	41:32:54	41:32:57	2.91
43:30:21	43:30:22	1.12	43:37:19	43:37:22	2.59
45:34:38	45:34:39	1.36	45:41:44	45:41:47	2.60
47:38:54	47:38:56	1.50	47:46:09	47:46:11	2.95
49:43:11	49:43:13	1.55	49:50:33	49:50:35	2.65
51:47:28	51:47:30	1.49	51:54:57	51:54:59	2.72
53:51:46	53:51:47	1.32	53:59:20	53:59:23	3.17
55:56:03	55:56:05	2.03	56:03:43	56:03:46	3.00
58:00:20	58:00:22	1.61	58:08:06	58:08:09	3.24

Table 15: Rise and set times of the perturbed orbit obtained from the controlling and constraint equation, given in $hh:mm:ss$, and the (absolute) difference given in seconds and centiseconds

C Derivations & Procedures

In this appendix, step by step derivations and standardised procedures are shown for the referenced equations or sections in the theoretical background, section 2. The subsections in this appendix match to those seen in the theoretical background

C.1 Two body problem

C.1.1 Potential energy of a spherical shell

Derivation of equation (2.10). The area of the annulus in figure 3 is given by

$$A_{\text{annulus}} = \underbrace{2\pi R \sin\vartheta}_{\text{circumference}} \underbrace{R d\vartheta}_{\text{height}}. \tag{C.1}$$

Integrate the potential energy of the annulus over the whole surface

$$V_s = -Gm\rho 2\pi R^2 \int_0^\pi \frac{\sin\vartheta}{\varrho} d\vartheta. \tag{C.2}$$

Use the law of cosines

$$\varrho^2 = R^2 + r^2 - 2Rr\cos\vartheta. \tag{C.3}$$

To relate the change of ϱ to the change of ϑ, implicit differentiation can be used. Take the derivative with respect to ϱ, but use $\vartheta = \vartheta(\varrho)$

$$2\varrho = 2Rr\sin\vartheta \frac{d\vartheta}{d\varrho} \quad \Rightarrow \quad \frac{\sin\vartheta}{\varrho} d\vartheta = \frac{1}{Rr} d\varrho. \tag{C.4}$$

With this, the integrand of the potential energy can be transformed. This means that the boundaries of the integral must be transformed as well. Using figure 3 as a reference gives

$$\varrho(\vartheta = 0) = r - R; \quad \varrho(\vartheta = \pi) = r + R. \tag{C.5}$$

In order for the new boundaries to make sense, it is necessary that the point mass lies outside the spherical shell. Solving the integral gives

$$\begin{aligned} V_s &= -\frac{Gm\rho 2\pi R^2}{Rr} \int_{r-R}^{r+R} d\varrho \\ &= -\frac{Gm\rho 2\pi R^2}{Rr} \left[\varrho\right]_{r-R}^{r+R} \\ &= -G\frac{m\rho 4\pi R^2}{r} \\ &= -G\frac{M_s m}{r}. \end{aligned} \tag{C.6}$$

C.1.2 Sphere of influence

Derivation of the equation of motion of a vehicle relative to Earth, equation (2.14). Start by constructing the equation of motion of the Earth relative to the Sun

$$\ddot{\vec{r}}_2 = G\frac{m_v}{r_3^3}\vec{r_3} - G\frac{m_s}{r_2^3}\vec{r_2}. \tag{C.7}$$

Subtract it from the equation of motion of the vehicle relative to the Sun, equation (2.13)

$$\begin{aligned}
\ddot{\vec{r}}_1 - \ddot{\vec{r}}_2 =& -G\frac{m_s}{r_1^3}\vec{r_1} - G\frac{m_e}{r_3^3}\vec{r_3} - G\frac{m_v}{r_3^3}\vec{r_3} + G\frac{m_s}{r_2^3}\vec{r_2} \\
=& -G\frac{1}{r_3^3}\left(m_e - m_v\right)\vec{r_3} - Gm_s\left(\frac{1}{r_1^3}\vec{r_1} - \frac{1}{r_2^3}\vec{r_2}\right) \\
=& -G\frac{m_e}{r_3^3}\left(1 - \frac{m_v}{m_e}\right)\vec{r_3} - G\frac{m_s}{r_1^3}\left(\vec{r_1} - \frac{r_1^3}{r_2^3}\vec{r_2}\right).
\end{aligned} \tag{C.8}$$

Now, using $m_v \ll m_e$ and equation (2.12), the equation of motion is found to be

$$\begin{aligned}
\ddot{\vec{r}}_3 =& -G\frac{m_e}{r_3^3}\left(1 - \frac{m_v}{m_e}\right)\vec{r_3} - G\frac{m_s}{r_1^3}\left(\vec{r_1} - \frac{r_1^3}{r_2^3}\vec{r_2}\right) \\
=& -G\frac{m_e}{r_3^3}\vec{r_3} - G\frac{m_s}{r_1^3}\left(\vec{r_2} + \vec{r_3} - \frac{r_1^3}{r_2^3}\vec{r_2}\right) \\
=& -G\frac{m_e}{r_3^3}\vec{r_3} - G\frac{m_s}{r_1^3}\vec{r_3} - G\frac{m_s}{r_1^3}\left(1 - \frac{r_1^3}{r_2^3}\right)\vec{r_2} \\
=& -G\frac{m_e}{r_3^3}\vec{r_3} - G\frac{m_s}{r_1^3}\vec{r_3}.
\end{aligned} \tag{C.9}$$

C.1.3 Specific mechanical energy

Derivation of equation (2.20). Take the dot product of the velocity and acceleration vector and substitute the orbital equation of motion, equation (2.7), in to get

$$\begin{aligned}
\dot{\vec{r}}\cdot\ddot{\vec{r}} =& \dot{\vec{r}}\cdot -\frac{\mu}{r^3}\vec{r} \\
\frac{1}{2}\frac{d}{dt}\left(\dot{\vec{r}}\cdot\dot{\vec{r}}\right) =& -\mu\frac{r\dot{r}}{r^3} \\
\frac{1}{2}\frac{d}{dt}\left(\dot{\vec{r}}\cdot\dot{\vec{r}}\right) =& -\mu\frac{\dot{r}}{r^2} \\
\frac{1}{2}\frac{d}{dt}\left(\dot{r}^2\right) =& \frac{d}{dt}\left(\frac{\mu}{r}\right) \\
\frac{d}{dt}\left(\frac{v^2}{2} - \frac{\mu}{r}\right) =& 0 \quad \Rightarrow \quad \frac{v^2}{2} - \frac{\mu}{r} = \varepsilon.
\end{aligned} \tag{C.10}$$

C.1.4 Laplace-Runge-Lenz vector

Derivation of the Laplace-Runge-Lenz vector, equation (2.22). Use the following vector identity

$$\vec{A} \times (\vec{B} \times \vec{C}) = \vec{B}(\vec{A} \cdot \vec{C}) - \vec{C}(\vec{A} \cdot \vec{B}). \tag{C.11}$$

Furthermore, equations (2.17) and (2.18) for the specific angular momentum are used. Apply all of this to equation (2.21) to obtain the following

$$\begin{aligned}
\ddot{\vec{r}} \times \vec{h} &= -\frac{\mu}{r^3}\vec{r} \times \vec{h} \\
\ddot{\vec{r}} \times \vec{h} &= -\frac{\mu}{r^3}\vec{r} \times \left(\vec{r} \times \dot{\vec{r}}\right) \\
\frac{d}{dt}\left(\dot{\vec{r}} \times \vec{h}\right) - \dot{\vec{r}} \times \dot{\vec{h}} &= \frac{\mu}{r^3}\left[\dot{\vec{r}}(\vec{r} \cdot \vec{r}) - \vec{r}\left(\vec{r} \cdot \dot{\vec{r}}\right)\right] \\
\frac{d}{dt}\left(\dot{\vec{r}} \times \vec{h}\right) &= \frac{\mu}{r^3}\left[\dot{\vec{r}}r^2 - \vec{r}r\dot{r}\right] \\
&= \mu\left[\frac{\dot{\vec{r}}r - \vec{r}\dot{r}}{r^2}\right] \\
&= \mu\frac{d}{dt}\left(\frac{\vec{r}}{r}\right) \\
\frac{d}{dt}\left(\dot{\vec{r}} \times \vec{h} - \mu\frac{\vec{r}}{r}\right) &= 0 \quad \Rightarrow \quad \dot{\vec{r}} \times \vec{h} - \mu\frac{\vec{r}}{r} = \vec{B}.
\end{aligned} \tag{C.12}$$

C.1.5 Polar orbital equation

Derivation of the polar orbital equation, equation (2.23). Use the following vector identity

$$\vec{K} \cdot (\vec{L} \times \vec{M}) = \vec{L} \cdot (\vec{M} \times \vec{K}) = \vec{M} \cdot (\vec{K} \times \vec{L}). \tag{C.13}$$

Furthermore, equation (2.17) for the specific angular momentum is used to obtain

$$\begin{aligned}
\dot{r} \cdot \left(\dot{\vec{r}} \times \vec{h} = \mu\frac{\vec{r}}{r} + \vec{B}\right) \\
\vec{r} \cdot \left(\dot{\vec{r}} \times \vec{h}\right) &= \mu\frac{\vec{r} \cdot \vec{r}}{r} + \vec{r} \cdot \vec{B} \\
\left(\vec{r} \times \dot{\vec{r}}\right) \cdot \vec{h} &= \mu r + rB\cos\mathrm{f} \\
\vec{h} \cdot \vec{h} &= r\left(\mu + B\cos\mathrm{f}\right) \\
h^2 &= r\mu\left(1 + \frac{B}{\mu}\cos\mathrm{f}\right) \\
&\Rightarrow r = \frac{h^2}{\mu}\frac{1}{1 + e\cos\mathrm{f}}; \quad \vec{e} = \frac{\vec{B}}{\mu}.
\end{aligned} \tag{C.14}$$

C.2 Orbits in two dimensions

C.2.1 Swept area

Derivation of equation (2.40). Makes use of figures 6 and 8, and the relation between circles and ellipses, equation (2.39). Plugging that in and using some geometry gives

$$\begin{aligned}
\Delta A =& A_{KmP} - A_{FKm} \\
=& \frac{y_e}{y_c} A_{KLP} - \frac{1}{2}\left(ae - a\cos E\right)\frac{y_e}{y_c} a \sin E \\
=& \frac{b}{a}\left(A_{LOP} - A_{KLO}\right) - \frac{1}{2}\left(ae - a\cos E\right)\frac{b}{a} a \sin E \\
=& \frac{b}{a}\left(\pi a^2 \frac{E}{2\pi} - \frac{1}{2} a\cos E\; a \sin E\right) - \frac{1}{2}\left(ae - a\cos E\right)\frac{b}{a} a \sin E \\
=& \frac{1}{2} ab\left(E - e\sin E\right).
\end{aligned} \tag{C.15}$$

C.3 Orbits in three dimensions

C.3.1 State vector to orbital elements

The procedure to go from the state vector to the orbital elements is as follows [20]

$$\vec{r}, \vec{v} \quad \Rightarrow \quad a, e, i, \Omega, \omega, \text{f}. \tag{C.16}$$

1. Specific angular momentum $\vec{h}$

$$\vec{h} = \vec{r} \times \vec{v}; \quad h = \sqrt{h_x^2 + h_y^2 + h_z^2}. \tag{C.17}$$

2. Inclination i

$$i = \arccos\left(\frac{h_z}{h}\right). \tag{C.18}$$

3. Node line $\vec{N}$

$$\vec{N} = \hat{K} \times \vec{h}; \quad N = \sqrt{N_x^2 + N_y^2 + N_z^2}. \tag{C.19}$$

4. Right ascension of the ascending node Ω

$$\Omega = \begin{cases} \arccos\left(\frac{N_x}{N}\right) & (N_y \geq 0)\,; \\ 2\pi - \arccos\left(\frac{N_x}{N}\right) & (N_y < 0)\,. \end{cases} \tag{C.20}$$

5. Eccentricity e, making use of radial velocity v_r

$$\vec{e} = \frac{1}{\mu}\left(\left(v^2 - \frac{\mu}{r}\right)\vec{r} - r v_r \vec{v}\right); \quad e = \sqrt{e_x^2 + e_y^2 + e_z^2}; \quad v_r = \frac{\vec{r} \cdot \vec{v}}{r}. \tag{C.21}$$

6. Semi-major axis a

$$a = \frac{h^2}{\mu}\frac{1}{1 - e^2}. \tag{C.22}$$

7. Argument of perigee ω

$$\omega = \begin{cases} \arccos\left(\frac{\vec{N} \cdot \vec{e}}{Ne}\right) & (e_z \geq 0)\,; \\ 2\pi - \arccos\left(\frac{\vec{N} \cdot \vec{e}}{Ne}\right) & (e_z < 0)\,. \end{cases} \tag{C.23}$$

8. True anomaly f

$$\text{f} = \begin{cases} \arccos\left(\frac{\vec{e} \cdot \vec{r}}{er}\right) & (v_r \geq 0)\,; \\ 2\pi - \arccos\left(\frac{\vec{e} \cdot \vec{r}}{er}\right) & (v_r < 0)\,. \end{cases} \tag{C.24}$$

C.4 Visibility problem

C.4.1 Sidereal time

For the Earth, local sidereal time θ, based on universal time, is determined using the following equations [20] [52]

$$\begin{aligned}
&\theta = \theta_G + \lambda;\\
&\theta_G = \theta_{G_0} + SD\frac{UT}{24};\\
&\theta_{G_0} = 100.4606184 + 36000.77004T_0 + 0.000387933T_0^2 - 2.583\left(10^{-8}\right)T_0^3;\\
&T_0 = \frac{J_0 - 2451545}{36525};\\
&J_0 = 367y - \text{INT}\left\{\frac{7\left[y + \text{INT}\left(\frac{\text{m}+9}{12}\right)\right]}{4}\right\} + \text{INT}\left(\frac{275\text{m}}{9}\right) + d + 1721013.5.
\end{aligned} \tag{C.25}$$

Note that this only holds for the years 1901–2091. INT signifies that only the integer part is retained.

C.4.2 Oblate primary body

Derivation of equation (2.60). Following figure 14, the x and z coordinates in terms of the geocentric latitude are given by

$$x = R_e\cos\varphi'; \quad z = R_e\sqrt{1-e^2}\sin\varphi'. \tag{C.26}$$

For z, equation (2.25) is used to relate the semi-major and semi-minor axis of an ellipse. With this, the slope of a line tangent to the primary body can be calculated as

$$\frac{dz}{dx} = \frac{dz}{d\varphi}\left(\frac{dx}{d\varphi}\right)^{-1} = -\frac{R_e\sqrt{1-e^2}\cos\varphi'}{R_e\sin\varphi'} = -\frac{\sqrt{1-e^2}}{\tan\varphi'}. \tag{C.27}$$

The slope of a line normal to the oblate primary body can be obtained by taking the negative reciprocal of the slope of the tangent line

$$\frac{dx}{dz} = \frac{\tan\varphi'}{\sqrt{1-e^2}}. \tag{C.28}$$

This slope is exactly equal to the tangent of the geodetic latitude, as that line is normal to the ellipse per definition. This gives

$$\tan\varphi = \frac{\tan\varphi'}{\sqrt{1-e^2}} \quad \Rightarrow \quad \tan\varphi' = \tan\varphi\sqrt{1-e^2}. \tag{C.29}$$

Interest lies in $\sin\varphi'$ and $\cos\varphi'$, since those terms must be replaced in equation (C.26). This can be done with some algebra and trigonometry. $\sin\varphi'$ is found through

$$\begin{aligned}
\frac{\sin\varphi'}{\cos\varphi'} &= \frac{\sin\varphi}{\cos\varphi}\sqrt{1-e^2}\\
\frac{\sin\varphi'}{\sqrt{1-\sin^2\varphi'}} &= \frac{\sin\varphi}{\sqrt{1-\sin^2\varphi}}\sqrt{1-e^2}\\
\sin^2\varphi'\left(1-\sin^2\varphi\right) &= \sin^2\varphi\left(1-e^2\right)\left(1-\sin^2\varphi'\right)\\
\sin^2\varphi' - \sin^2\varphi\sin^2\varphi' &= \sin^2\varphi - e^2\sin^2\varphi - \sin^2\varphi\sin^2\varphi' + e^2\sin^2\varphi\sin^2\varphi'\\
\sin^2\varphi'\left(1-e^2\sin^2\varphi\right) &= \left(1-e^2\right)\sin^2\varphi\\
\sin\varphi' &= \frac{\sqrt{1-e^2}\sin\varphi}{\sqrt{1-e^2\sin^2\varphi}}.
\end{aligned} \tag{C.30}$$

Now $\cos\varphi'$ is found as

$$\cos\varphi' = \frac{\sin\varphi'}{\tan\varphi'} = \frac{\frac{\sqrt{1-e^2}\sin\varphi}{\sqrt{1-e^2\sin^2\varphi}}}{\tan\varphi\sqrt{1-e^2}} = \frac{\cos\varphi}{\sqrt{1-e^2\sin^2\varphi}}. \tag{C.31}$$

So, plugging these expressions back in equation (C.26), the position of the observer in terms of flatness and geodetic latitude becomes

$$x = R_e\frac{\cos\varphi}{\sqrt{1-(2f-f^2)\sin^2\varphi}}; \quad z = R_e\frac{(1-f^2)\sin\varphi}{\sqrt{1-(2f-f^2)\sin^2\varphi}}. \tag{C.32}$$

C.4.3 Constraint equation

The derivation of the constraint equation, equation (2.66) makes use of equations (2.60) for the position of the observer, (2.62) for the slant range, and (2.63) for the zenith unit vector. By expanding the dot product and plugging the appropriate expressions in, the following is obtained

$$\begin{aligned}
\vec{\varrho}\cdot\hat{Z} =& \varrho\sin h \\
\varrho_x Z_x + \varrho_y Z_y + \varrho_z Z_z =& \varrho\sin h \\
(r_x - R_x)\cos\varphi\cos\theta + (r_y - R_y)\cos\varphi\sin\theta + (r_z - R_z)\sin\varphi =& \varrho\sin h \\
(r_x - G_1\cos\varphi\cos\theta)\cos\varphi\cos\theta + (r_y - G_1\cos\varphi\sin\theta)\cos\varphi\sin\theta & \\
+ (r_z - G_2\sin\varphi)\sin\varphi =& \varrho\sin h \\
r_x\cos\varphi\cos\theta + r_y\cos\varphi\sin\theta + r_z\sin\varphi - G_1\cos^2\varphi - G_2\sin^2\varphi =& \varrho\sin h \\
r_x\cos\varphi\cos\theta + r_y\cos\varphi\sin\theta + r_z\sin\varphi =& \varrho\sin h + G.
\end{aligned} \tag{C.33}$$

The slant range is given by

$$\begin{aligned}
\varrho =& \sqrt{(r_x - R_x)^2 + (r_y - R_y)^2 + (r_z - R_z)^2} \\
=& \sqrt{(r_x - G_1\cos\varphi\cos\theta)^2 + (r_y - G_1\cos\varphi\sin\theta)^2 + (r_z - G_2\sin\varphi)^2} \\
=& \big(r_x^2 + r_y^2 + r_z^2 + G_1^2\cos^2\varphi\cos^2\theta + G_1^2\cos^2\varphi\sin^2\theta + G_2^2\sin^2\varphi \\
& -2r_xG_1\cos\varphi\cos\theta - 2r_yG_1\cos\varphi\sin\theta - 2r_zG_2\sin\varphi\big)^{\frac{1}{2}} \\
=& \sqrt{r^2 + G_0^2 - 2r_xG_1\cos\varphi\cos\theta - 2r_yG_1\cos\varphi\sin\theta - 2r_zG_2\sin\varphi}.
\end{aligned} \tag{C.34}$$

C.5 Perturbation techniques

C.5.1 Time invariance of Lagrange brackets

To prove that Lagrange brackets are independent of time, as seen in equation (2.88), start with the definition of the Lagrange bracket [51]

$$\ell_{ij} = \left(\frac{\partial \vec{r}}{\partial c_i}\right)^T \frac{\partial \vec{v}}{\partial c_j} - \left(\frac{\partial \vec{v}}{\partial c_i}\right)^T \frac{\partial \vec{r}}{\partial c_j}. \tag{C.35}$$

Taking the time derivative and applying the properties of the Lagrange brackets stated in equations (2.88) gives

$$\begin{aligned}
\frac{\partial \ell_{ij}}{\partial t} &= \frac{\partial}{\partial t}\left[\left(\frac{\partial \vec{r}}{\partial c_i}\right)^T \frac{\partial \vec{v}}{\partial c_j} - \left(\frac{\partial \vec{v}}{\partial c_i}\right)^T \frac{\partial \vec{r}}{\partial c_j}\right] \\
&= \left(\frac{\partial \vec{v}}{\partial c_i}\right)^T \frac{\partial \vec{v}}{\partial c_j} + \left(\frac{\partial \vec{r}}{\partial c_i}\right)^T \frac{\partial \dot{\vec{v}}}{\partial c_j} - \left(\frac{\partial \dot{\vec{v}}}{\partial c_i}\right)^T \frac{\partial \vec{r}}{\partial c_j} - \left(\frac{\partial \vec{v}}{\partial c_i}\right)^T \frac{\partial \vec{v}}{\partial c_j} \\
&= \left(\frac{\partial \vec{r}}{\partial c_i}\right)^T \frac{\partial \dot{\vec{v}}}{\partial c_j} - \left(\frac{\partial \dot{\vec{v}}}{\partial c_i}\right)^T \frac{\partial \vec{r}}{\partial c_j}.
\end{aligned} \tag{C.36}$$

Following its definition, equation (2.86), it can be seen that the Lagrangian matrix is solely determined using the two-body problem, no perturbations are included. The derivates of the state vector are taken with respect to the constants of integration, but it is irrelevant whether the constants of integration are a function of time or not. That means that equation (2.83) can be used for the acceleration terms. This gives

$$\begin{aligned}
\frac{\partial \ell_{ij}}{\partial t} &= \left(\frac{\partial \vec{r}}{\partial c_i}\right)^T \frac{\partial}{\partial c_j}\left(-\nabla_r U_0\right) - \left(\frac{\partial}{\partial c_i}\left(-\nabla_r U_0\right)\right)^T \frac{\partial \vec{r}}{\partial c_j} \\
&= \left(\frac{\partial \vec{r}}{\partial c_i}\right)^T \frac{\partial}{\partial c_j}\left(-\left(\frac{\partial U_0}{\partial \vec{r}}\right)^T\right) + \frac{\partial}{\partial c_i}\left(\frac{\partial U_0}{\partial \vec{r}}\right)\frac{\partial \vec{r}}{\partial c_j} \\
&= -\left(\frac{\partial}{\partial \vec{r}}\left(\frac{\partial U_0}{\partial c_j}\right)\frac{\partial \vec{r}}{\partial c_i}\right) + \frac{\partial}{\partial \vec{r}}\left(\frac{\partial U_0}{\partial c_i}\right)\frac{\partial \vec{r}}{\partial c_j} \\
&= -\frac{\partial^2 U_0}{\partial c_i \partial c_j} + \frac{\partial^2 U_0}{\partial c_j \partial c_i} \\
&= 0.
\end{aligned} \tag{C.37}$$

This was done for an arbitrary bracket, meaning that the complete Lagrangian matrix $\mathfrak{L}$ is independent of time.

C.5.2 Rotation of Lagrangian matrix

Derivation of equation (2.89) [51]. Take an angle ϑ with which is rotated around the Z-axis. This signifies a change of coordinate system from the original system $(OXYZ)$ to the new system $(OXYZ)'$, as shown in figure 57.

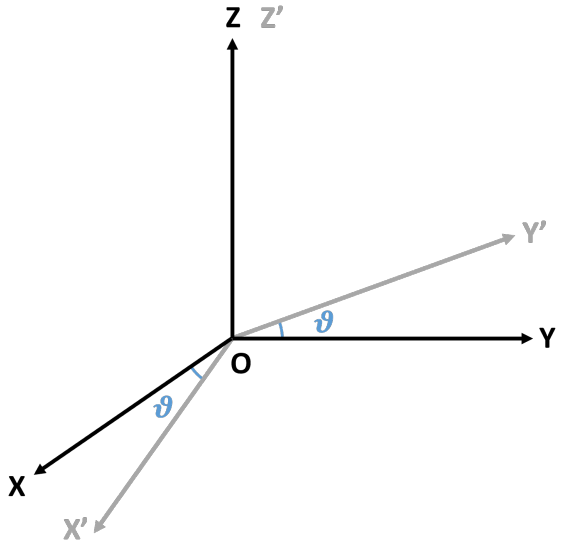

Figure 57: Visualisation of an arbitrary rotation about the Z-axis with ϑ.

This rotation corresponds to a rotation matrix of

$$\mathfrak{R}(\vartheta) = \begin{bmatrix} \cos\vartheta & \sin\vartheta & 0 \\ -\sin\vartheta & \cos\vartheta & 0 \\ 0 & 0 & 1 \end{bmatrix}. \tag{C.38}$$

The position and velocity vector of the two systems are related as

$$\vec{r}' = \mathfrak{R}(\vartheta)\,\vec{r}; \quad \vec{v}' = \mathfrak{R}(\vartheta)\,\vec{v}. \tag{C.39}$$

Taking the partial derivative with respect to the constant of integration $\vec{c}$ gives

$$\begin{aligned} \frac{\partial \vec{r}'}{\partial \vec{c}} &= \frac{\partial \mathfrak{R}(\vartheta)}{\partial \vartheta}\frac{\partial \vartheta}{\partial \vec{c}}\vec{r} + \mathfrak{R}(\vartheta)\frac{\partial \vec{r}}{\partial \vec{c}}; \\ \frac{\partial \vec{v}'}{\partial \vec{c}} &= \frac{\partial \mathfrak{R}(\vartheta)}{\partial \vartheta}\frac{\partial \vartheta}{\partial \vec{c}}\vec{v} + \mathfrak{R}(\vartheta)\frac{\partial \vec{v}}{\partial \vec{c}}. \end{aligned} \tag{C.40}$$

Using this, the Lagrangian in the new system is given by

$$\begin{aligned}
\mathfrak{L}' &= \left(\frac{\partial \vec{r}'}{\partial \vec{c}}\right)^T \frac{\partial \vec{v}'}{\partial \vec{c}} - \left(\frac{\partial \vec{v}'}{\partial \vec{c}}\right)^T \frac{\partial \vec{r}'}{\partial \vec{c}} \\
&= \left(\frac{\partial \mathfrak{R}}{\partial \vartheta}\frac{\partial \vartheta}{\partial \vec{c}}\vec{r} + \mathfrak{R}\frac{\partial \vec{r}}{\partial \vec{c}}\right)^T \left(\frac{\partial \mathfrak{R}}{\partial \vartheta}\frac{\partial \vartheta}{\partial \vec{c}}\vec{v} + \mathfrak{R}\frac{\partial \vec{v}}{\partial \vec{c}}\right) \\
&\quad - \left(\frac{\partial \mathfrak{R}}{\partial \vartheta}\frac{\partial \vartheta}{\partial \vec{c}}\vec{v} + \mathfrak{R}\frac{\partial \vec{v}}{\partial \vec{c}}\right)^T \left(\frac{\partial \mathfrak{R}}{\partial \vartheta}\frac{\partial \vartheta}{\partial \vec{c}}\vec{r} + \mathfrak{R}\frac{\partial \vec{r}}{\partial \vec{c}}\right) \\
&= \left(\frac{\partial \mathfrak{R}}{\partial \vartheta}\frac{\partial \vartheta}{\partial \vec{c}}\vec{r}\right)^T \left(\frac{\partial \mathfrak{R}}{\partial \vartheta}\frac{\partial \vartheta}{\partial \vec{c}}\vec{v}\right) + B\left(\frac{\partial \vartheta}{\partial \vec{c}}\vec{r}\right)^T \frac{\partial \vec{v}}{\partial \vec{c}} + B^T \left(\frac{\partial \vec{r}}{\partial \vec{c}}\right)^T \left(\frac{\partial \vartheta}{\partial \vec{c}}\vec{v}\right) \\
&\quad + \left(\mathfrak{R}\frac{\partial \vec{r}}{\partial \vec{c}}\right)^T \left(\mathfrak{R}\frac{\partial \vec{v}}{\partial \vec{c}}\right) - \left(\frac{\partial \mathfrak{R}}{\partial \vartheta}\frac{\partial \vartheta}{\partial \vec{c}}\vec{v}\right)^T \left(\frac{\partial \mathfrak{R}}{\partial \vartheta}\frac{\partial \vartheta}{\partial \vec{c}}\vec{r}\right) - B\left(\frac{\partial \vartheta}{\partial \vec{c}}\vec{v}\right)^T \frac{\partial \vec{r}}{\partial \vec{c}} \\
&\quad - B^T \left(\frac{\partial \vec{v}}{\partial \vec{c}}\right)^T \left(\frac{\partial \vartheta}{\partial \vec{c}}\vec{r}\right) - \left(\mathfrak{R}\frac{\partial \vec{v}}{\partial \vec{c}}\right)^T \left(\mathfrak{R}\frac{\partial \vec{r}}{\partial \vec{c}}\right).
\end{aligned} \tag{C.41}$$

Where B is defined as

$$B = \left(\frac{\partial \mathfrak{R}(\vartheta)}{\partial \vartheta}\right)^T \mathfrak{R}(\vartheta); \quad B = -B^T. \tag{C.42}$$

Now the goal is to isolate the original Lagrangian matrix, which can be found from the last terms in each line. Note that the transpose of the rotation matrix is equal to the inverse. This gives

$$\begin{aligned}
\mathfrak{L}' &= \left(\frac{\partial \vec{r}}{\partial \vec{c}}\right)^T \frac{\partial \vec{v}}{\partial \vec{c}} - \left(\frac{\partial \vec{v}}{\partial \vec{c}}\right)^T \frac{\partial \vec{r}}{\partial \vec{c}} \\
&\quad + \left(\frac{\partial \vartheta}{\partial \vec{c}}\right)^T \left[r^T \left(\frac{\partial \mathfrak{R}}{\partial \vartheta}\right)^T \frac{\partial \mathfrak{R}}{\partial \vartheta} v - v^T \left(\frac{\partial \mathfrak{R}}{\partial \vartheta}\right)^T \frac{\partial \mathfrak{R}}{\partial \vartheta} r\right] \frac{\partial \vartheta}{\partial \vec{c}} \\
&\quad + \left(\frac{\partial \vartheta}{\partial \vec{c}}\right)^T \left[\vec{r}^T B \frac{\partial \vec{v}}{\partial \vec{c}} - \vec{v}^T B \frac{\partial \vec{r}}{\partial \vec{c}}\right] + \left[\left(\frac{\partial \vec{r}}{\partial \vec{c}}\right)^T B^T \vec{v} - \left(\frac{\partial \vec{v}}{\partial \vec{c}}\right)^T B^T \vec{r}\right] \frac{\partial \vartheta}{\partial \vec{c}} \\
&= \mathfrak{L} + \left(\frac{\partial \vartheta}{\partial \vec{c}}\right)^T \left[\vec{r}^T B B^T \vec{v} - \vec{v}^T B B^T \vec{r}\right] \frac{\partial \vartheta}{\partial \vec{c}} \\
&\quad + \left(\frac{\partial \vartheta}{\partial \vec{c}}\right)^T \left[\vec{r}^T B \frac{\partial \vec{v}}{\partial \vec{c}} - \vec{v}^T B \frac{\partial \vec{r}}{\partial \vec{c}}\right] + \left[\left(\frac{\partial \vec{r}}{\partial \vec{c}}\right)^T B^T \vec{v} - \left(\frac{\partial \vec{v}}{\partial \vec{c}}\right)^T B^T \vec{r}\right] \frac{\partial \vartheta}{\partial \vec{c}}.
\end{aligned} \tag{C.43}$$

In the second term, the part between square brackets falls away because it can be seen as taking the dot product. This looks like

$$\vec{r}^T B B^T \vec{v} = \left(B^T \vec{r}\right) \cdot \left(B^T \vec{v}\right) = \left(B^T \vec{v}\right) \cdot \left(B^T \vec{r}\right) = \vec{v}^T B B^T \vec{r}. \tag{C.44}$$

This gives

$$\mathfrak{L} = \mathfrak{L}' - \left(\frac{\partial \vartheta}{\partial \vec{c}}\right)^T \left[\vec{r}^T B \frac{\partial \vec{v}}{\partial \vec{c}} - \vec{v}^T B \frac{\partial \vec{r}}{\partial \vec{c}}\right] - \left[\left(\frac{\partial \vec{r}}{\partial \vec{c}}\right)^T B^T \vec{v} - \left(\frac{\partial \vec{v}}{\partial \vec{c}}\right)^T B^T \vec{r}\right] \frac{\partial \vartheta}{\partial \vec{c}}. \tag{C.45}$$

Make the following substitution to simplify the expression further

$$S = \vec{v}^T B \vec{r}. \tag{C.46}$$

Now take the derivative of S with respect to $\vec{c}$ and make use of the fact that B is antisymmetric

$$\frac{\partial S}{\partial \vec{c}} = \left(\frac{\partial \vec{v}}{\partial \vec{c}}\right)^T B\vec{r} + \vec{v}^T B\frac{\partial \vec{r}}{\partial \vec{c}} = -\vec{r}^T B\frac{\partial \vec{v}}{\partial \vec{c}} + \vec{v}^T B\frac{\partial \vec{r}}{\partial \vec{c}}. \tag{C.47}$$

The same thing can be done for the transpose of the derivative. Applying this gives

$$\mathfrak{L} = \mathfrak{L}' + \left(\frac{\partial \vartheta}{\partial \vec{c}}\right)^T \frac{\partial S}{\partial \vec{c}} - \left(\frac{\partial S}{\partial \vec{c}}\right)^T \frac{\partial \vartheta}{\partial \vec{c}}. \tag{C.48}$$

With this, the Lagrange brackets in the different frames are related as

$$[c_i, c_j] = [c_i, c_j]' + \frac{\partial(\vartheta, S)}{\partial(c_i, c_j)}. \tag{C.49}$$

Here the Jacobian is used, which is defined as

$$\frac{\partial(\vartheta, S)}{\partial(c_i, c_j)} = \frac{\partial \vartheta}{\partial c_i}\frac{\partial S}{\partial c_j} - \frac{\partial \vartheta}{\partial c_j}\frac{\partial S}{\partial c_i}. \tag{C.50}$$

C.5.3 Definition of S

Derivation of equation (2.91) [51]. First, work out the definition of B

$$B = \left(\frac{\partial}{\partial \vartheta}\begin{bmatrix} \cos\vartheta & \sin\vartheta & 0 \\ -\sin\vartheta & \cos\vartheta & 0 \\ 0 & 0 & 1 \end{bmatrix}\right)^T \begin{bmatrix} \cos\vartheta & \sin\vartheta & 0 \\ -\sin\vartheta & \cos\vartheta & 0 \\ 0 & 0 & 1 \end{bmatrix} = \begin{bmatrix} 0 & -1 & 0 \\ 1 & 0 & 0 \\ 0 & 0 & 0 \end{bmatrix}. \tag{C.51}$$

Plug this in the definition of S

$$S = \begin{bmatrix} v_x & v_y & v_z \end{bmatrix} \begin{bmatrix} 0 & -1 & 0 \\ 1 & 0 & 0 \\ 0 & 0 & 0 \end{bmatrix} \begin{bmatrix} r_x \\ r_y \\ r_x \end{bmatrix} = r_x v_y - r_y v_x = h_z. \tag{C.52}$$

Here h_z signifies the z or 3^{rd} component of the specific angular momentum vector.

C.5.4 Rewrite Lagrange brackets

To derive equation (2.102), start with the definition of the Lagrange bracket, equation (2.87), and substitute the derivatives of the state vector with respect to the orbital elements, equation (2.101), in. The mathematics mainly comes down to expanding the brackets and regrouping terms. Although not complicated, the sheer size of the expression can make it difficult to keep an overview. First the brackets are worked away to give

$$
\begin{aligned}
\ell'_{ij} &= \left(\frac{\partial \vec{r}'}{\partial c_i}\right)^T \frac{\partial \vec{v}'}{\partial c_j} - \left(\frac{\partial \vec{v}'}{\partial c_i}\right)^T \frac{\partial \vec{r}'}{\partial c_j} \\
&= \left(\frac{\partial \vec{r}'}{\partial a}\frac{\partial a}{\partial c_i} + \frac{\partial \vec{r}'}{\partial e}\frac{\partial e}{\partial c_i} + \frac{\partial \vec{r}'}{\partial (L_0-\varpi)}\frac{\partial (L_0-\varpi)}{\partial c_i}\right)^T \\
&\quad \cdot \left(\frac{\partial \vec{v}'}{\partial a}\frac{\partial a}{\partial c_j} + \frac{\partial \vec{v}'}{\partial e}\frac{\partial e}{\partial c_j} + \frac{\partial \vec{v}'}{\partial (L_0-\varpi)}\frac{\partial (L_0-\varpi)}{\partial c_j}\right) \\
&\quad - \left(\frac{\partial \vec{v}'}{\partial a}\frac{\partial a}{\partial c_i} + \frac{\partial \vec{v}'}{\partial e}\frac{\partial e}{\partial c_i} + \frac{\partial \vec{v}'}{\partial (L_0-\varpi)}\frac{\partial (L_0-\varpi)}{\partial c_i}\right)^T \\
&\quad \cdot \left(\frac{\partial \vec{r}'}{\partial a}\frac{\partial a}{\partial c_j} + \frac{\partial \vec{r}'}{\partial e}\frac{\partial e}{\partial c_j} + \frac{\partial \vec{r}'}{\partial (L_0-\varpi)}\frac{\partial (L_0-\varpi)}{\partial c_j}\right) \\
&= \left(\frac{\partial \vec{r}'}{\partial a}\frac{\partial a}{\partial c_i}\right)^T \left(\frac{\partial \vec{v}'}{\partial a}\frac{\partial a}{\partial c_j}\right) + \left(\frac{\partial \vec{r}'}{\partial a}\frac{\partial a}{\partial c_i}\right)^T \left(\frac{\partial \vec{v}'}{\partial e}\frac{\partial e}{\partial c_j}\right) \\
&\quad + \left(\frac{\partial \vec{r}'}{\partial a}\frac{\partial a}{\partial c_i}\right)^T \left(\frac{\partial \vec{v}'}{\partial (L_0-\varpi)}\frac{\partial (L_0-\varpi)}{\partial c_j}\right) + \left(\frac{\partial \vec{r}'}{\partial e}\frac{\partial e}{\partial c_i}\right)^T \left(\frac{\partial \vec{v}'}{\partial a}\frac{\partial a}{\partial c_j}\right) \\
&\quad + \left(\frac{\partial \vec{r}'}{\partial e}\frac{\partial e}{\partial c_i}\right)^T \left(\frac{\partial \vec{v}'}{\partial e}\frac{\partial e}{\partial c_j}\right) + \left(\frac{\partial \vec{r}'}{\partial e}\frac{\partial e}{\partial c_i}\right)^T \left(\frac{\partial \vec{v}'}{\partial (L_0-\varpi)}\frac{\partial (L_0-\varpi)}{\partial c_j}\right) \\
&\quad + \left(\frac{\partial \vec{r}'}{\partial (L_0-\varpi)}\frac{\partial (L_0-\varpi)}{\partial c_i}\right)^T \left(\frac{\partial \vec{v}'}{\partial a}\frac{\partial a}{\partial c_j}\right) + \left(\frac{\partial \vec{r}'}{\partial (L_0-\varpi)}\frac{\partial (L_0-\varpi)}{\partial c_i}\right)^T \left(\frac{\partial \vec{v}'}{\partial e}\frac{\partial e}{\partial c_j}\right) \\
&\quad + \left(\frac{\partial \vec{r}'}{\partial (L_0-\varpi)}\frac{\partial (L_0-\varpi)}{\partial c_i}\right)^T \left(\frac{\partial \vec{v}'}{\partial (L_0-\varpi)}\frac{\partial (L_0-\varpi)}{\partial c_j}\right) - \left(\frac{\partial \vec{v}'}{\partial a}\frac{\partial a}{\partial c_i}\right)^T \left(\frac{\partial \vec{r}'}{\partial a}\frac{\partial a}{\partial c_j}\right) \\
&\quad - \left(\frac{\partial \vec{v}'}{\partial a}\frac{\partial a}{\partial c_i}\right)^T \left(\frac{\partial \vec{r}'}{\partial e}\frac{\partial e}{\partial c_j}\right) - \left(\frac{\partial \vec{v}'}{\partial a}\frac{\partial a}{\partial c_i}\right)^T \left(\frac{\partial \vec{r}'}{\partial (L_0-\varpi)}\frac{\partial (L_0-\varpi)}{\partial c_j}\right) \\
&\quad - \left(\frac{\partial \vec{v}'}{\partial e}\frac{\partial e}{\partial c_i}\right)^T \left(\frac{\partial \vec{r}'}{\partial a}\frac{\partial a}{\partial c_j}\right) - \left(\frac{\partial \vec{v}'}{\partial e}\frac{\partial e}{\partial c_i}\right)^T \left(\frac{\partial \vec{r}'}{\partial e}\frac{\partial e}{\partial c_j}\right) \\
&\quad - \left(\frac{\partial \vec{v}'}{\partial e}\frac{\partial e}{\partial c_i}\right)^T \left(\frac{\partial \vec{r}'}{\partial (L_0-\varpi)}\frac{\partial (L_0-\varpi)}{\partial c_j}\right) - \left(\frac{\partial \vec{v}'}{\partial (L_0-\varpi)}\frac{\partial (L_0-\varpi)}{\partial c_i}\right)^T \left(\frac{\partial \vec{r}'}{\partial a}\frac{\partial a}{\partial c_j}\right) \\
&\quad - \left(\frac{\partial \vec{v}'}{\partial (L_0-\varpi)}\frac{\partial (L_0-\varpi)}{\partial c_i}\right)^T \left(\frac{\partial \vec{r}'}{\partial e}\frac{\partial e}{\partial c_j}\right) \\
&\quad - \left(\frac{\partial \vec{v}'}{\partial (L_0-\varpi)}\frac{\partial (L_0-\varpi)}{\partial c_i}\right)^T \left(\frac{\partial \vec{r}'}{\partial (L_0-\varpi)}\frac{\partial (L_0-\varpi)}{\partial c_j}\right).
\end{aligned}
\tag{C.53}
$$

Note that " $\cdot$ " do not signify the dot product, instead they represent multiplication and are added for clarification. By using the reverse product rule, terms can be combined. Furthermore, by grouping terms of the same orbital elements together, the general definition of the Lagrange brackets can be recognized, but this time in terms of the orbital elements instead of the arbitrary constants

$$
\begin{aligned}
\ell'_{ij} = &\left(\left(\frac{\partial \vec{r}'}{\partial a}\right)^T \frac{\partial \vec{v}'}{\partial a} - \left(\frac{\partial \vec{v}'}{\partial a}\right)^T \frac{\partial \vec{r}'}{\partial a}\right) \frac{\partial a}{\partial c_i}\frac{\partial a}{\partial c_j} + \left(\left(\frac{\partial \vec{r}'}{\partial a}\right)^T \frac{\partial \vec{v}'}{\partial e} - \left(\frac{\partial \vec{v}'}{\partial a}\right)^T \frac{\partial \vec{r}'}{\partial e}\right) \frac{\partial a}{\partial c_i}\frac{\partial e}{\partial c_j} \\
&+ \left(\left(\frac{\partial \vec{r}'}{\partial a}\right)^T \frac{\partial \vec{v}'}{\partial (L_0-\varpi)} - \left(\frac{\partial \vec{v}'}{\partial a}\right)^T \frac{\partial \vec{r}'}{\partial (L_0-\varpi)}\right) \frac{\partial a}{\partial c_i}\frac{\partial (L_0-\varpi)}{\partial c_j} \\
&+ \left(\left(\frac{\partial \vec{r}'}{\partial e}\right)^T \frac{\partial \vec{v}'}{\partial a} - \left(\frac{\partial \vec{v}'}{\partial e}\right)^T \frac{\partial \vec{r}'}{\partial a}\right) \frac{\partial e}{\partial c_i}\frac{\partial a}{\partial c_j} + \left(\left(\frac{\partial \vec{r}'}{\partial e}\right)^T \frac{\partial \vec{v}'}{\partial e} - \left(\frac{\partial \vec{v}'}{\partial e}\right)^T \frac{\partial \vec{r}'}{\partial e}\right) \frac{\partial e}{\partial c_i}\frac{\partial e}{\partial c_j} \\
&+ \left(\left(\frac{\partial \vec{r}'}{\partial e}\right)^T \frac{\partial \vec{v}'}{\partial (L_0-\varpi)} - \left(\frac{\partial \vec{v}'}{\partial e}\right)^T \frac{\partial \vec{r}'}{\partial (L_0-\varpi)}\right) \frac{\partial e}{\partial c_i}\frac{\partial (L_0-\varpi)}{\partial c_j} \\
&+ \left(\left(\frac{\partial \vec{r}'}{\partial (L_0-\varpi)}\right)^T \frac{\partial \vec{v}'}{\partial a} - \left(\frac{\partial \vec{v}'}{\partial (L_0-\varpi)}\right)^T \frac{\partial \vec{r}'}{\partial a}\right) \frac{\partial (L_0-\varpi)}{\partial c_i}\frac{\partial a}{\partial c_j} \\
&+ \left(\left(\frac{\partial \vec{r}'}{\partial (L_0-\varpi)}\right)^T \frac{\partial \vec{v}'}{\partial e} - \left(\frac{\partial \vec{v}'}{\partial (L_0-\varpi)}\right)^T \frac{\partial \vec{r}'}{\partial e}\right) \frac{\partial (L_0-\varpi)}{\partial c_i}\frac{\partial e}{\partial c_j} \\
&+ \left(\left(\frac{\partial \vec{r}'}{\partial (L_0-\varpi)}\right)^T \frac{\partial \vec{v}'}{\partial (L_0-\varpi)} - \left(\frac{\partial \vec{v}'}{\partial (L_0-\varpi)}\right)^T \frac{\partial \vec{r}'}{\partial (L_0-\varpi)}\right) \frac{\partial (L_0-\varpi)}{\partial c_i}\frac{\partial (L_0-\varpi)}{\partial c_j} \\
= &[a,a]' \frac{\partial a}{\partial c_i}\frac{\partial a}{\partial c_j} + [a,e]' \frac{\partial a}{\partial c_i}\frac{\partial e}{\partial c_j} + [a,(L_0-\varpi)]' \frac{\partial a}{\partial c_i}\frac{\partial (L_0-\varpi)}{\partial c_j} + [e,a]' \frac{\partial e}{\partial c_i}\frac{\partial a}{\partial c_j} \\
&+ [e,e]' \frac{\partial e}{\partial c_i}\frac{\partial e}{\partial c_j} + [e,(L_0-\varpi)]' \frac{\partial e}{\partial c_i}\frac{\partial (L_0-\varpi)}{\partial c_j} + [(L_0-\varpi),a]' \frac{\partial (L_0-\varpi)}{\partial c_i}\frac{\partial a}{\partial c_j} \\
&+ [(L_0-\varpi),e]' \frac{\partial (L_0-\varpi)}{\partial c_i}\frac{\partial e}{\partial c_j} + [(L_0-\varpi),(L_0-\varpi)]' \frac{\partial (L_0-\varpi)}{\partial c_i}\frac{\partial (L_0-\varpi)}{\partial c_j}.
\end{aligned}
\tag{C.54}
$$

Using the properties of the Lagrange brackets, equation (2.88), to get rid of some terms, the equation can already be shortened. As a final step, the Jacobian, equation (2.90), is used and the equation can be rewritten to its final, compact form

$$
\begin{aligned}
\ell'_{ij} = &[a,e]' \frac{\partial a}{\partial c_i}\frac{\partial e}{\partial c_j} - [a,e]' \frac{\partial e}{\partial c_i}\frac{\partial a}{\partial c_j} + [e,(L_0-\varpi)]' \frac{\partial e}{\partial c_i}\frac{\partial (L_0-\varpi)}{\partial c_j} \\
&- [(e,L_0-\varpi)]' \frac{\partial (L_0-\varpi)}{\partial c_i}\frac{\partial e}{\partial c_j} + [(L_0-\varpi),a]' \frac{\partial (L_0-\varpi)}{\partial c_i}\frac{\partial a}{\partial c_j} \\
&- [(L_0-\varpi),a]' \frac{\partial a}{\partial c_i}\frac{\partial (L_0-\varpi)}{\partial c_j} \\
= &[a,e]' \frac{\partial (a,e)}{\partial (c_i,c_j)} + [e,(L_0-\varpi)]' \frac{\partial (e,(L_0-\varpi))}{\partial (c_i,c_j)} \\
&+ [(L_0-\varpi),a]' \frac{\partial ((L_0-\varpi),a)}{\partial (c_i,c_j)}.
\end{aligned}
\tag{C.55}
$$

C.5.5 Partial derivatives of Lagrange brackets

In order to obtain equation (2.103), a couple steps must be taken. First, the partial derivatives of the state vector with respect to the relevant orbital elements are determined as [51]

$$\begin{aligned}
\frac{\partial \vec{r}'}{\partial a} &= \begin{bmatrix} \cos E - a - a\sin E \frac{\partial E}{\partial a} \\ \sqrt{1-e^2}\sin E + a\sqrt{1-e^2}\cos E \frac{\partial E}{\partial a} \\ 0 \end{bmatrix}; \\
\frac{\partial \vec{v}'}{\partial a} &= \begin{bmatrix} -\dot{E}\sin E + a\dot{E}\cos E \frac{\partial E}{\partial a} - a\sin E \frac{\partial \dot{E}}{\partial a} \\ \sqrt{1-e^2}\left(\dot{E}\cos E - a\dot{E}\sin E \frac{\partial E}{\partial a} + a\cos E \frac{\partial \dot{E}}{\partial a}\right) \\ 0 \end{bmatrix}; \\
\frac{\partial \vec{r}'}{\partial e} &= \begin{bmatrix} -a - a\sin E \frac{\partial E}{\partial e} \\ -\frac{ae}{\sqrt{1-e^2}}\sin E + a\sqrt{1-e^2}\cos E \frac{\partial E}{\partial e} \\ 0 \end{bmatrix}; \\
\frac{\partial \vec{v}'}{\partial e} &= \begin{bmatrix} -a\dot{E}\cos E \frac{\partial E}{\partial e} - a\sin E \frac{\partial \dot{E}}{\partial e} \\ -\frac{ae}{\sqrt{1-e^2}}\dot{E}\cos E + a\sqrt{1-e^2}\left(-\dot{E}\sin E \frac{\partial E}{\partial e} + \cos E \frac{\partial \dot{E}}{\partial e}\right) \\ 0 \end{bmatrix}; \\
\frac{\partial \vec{r}'}{\partial (L_0 - \varpi)} &= \begin{bmatrix} -a\sin E \frac{\partial E}{\partial (L_0-\varpi)} \\ a\sqrt{1-e^2}\cos E \frac{\partial E}{\partial (L_0-\varpi)} \\ 0 \end{bmatrix}; \\
\frac{\partial \vec{v}'}{\partial (L_0 - \varpi)} &= \begin{bmatrix} -a\dot{E}\cos E \frac{\partial E}{\partial (L_0-\varpi)} - a\sin E \frac{\partial \dot{E}}{\partial (L_0-\varpi)} \\ a\sqrt{1-e^2}\left(-\dot{E}\sin E \frac{\partial E}{\partial (L_0-\varpi)} + \cos E \frac{\partial \dot{E}}{\partial (L_0-\varpi)}\right) \\ 0 \end{bmatrix}.
\end{aligned} \tag{C.56}$$

Aside from the orbital elements used in Whittaker's method, eccentric anomaly E is also seen, for which expressions are required. The partial derivatives of (the rate of change of) eccentric anomaly are found by differentiating Kepler's equation, equation (2.99), which yields

$$\begin{aligned}
\frac{\partial E}{\partial a} &= -\frac{3nt}{2a\left(1 - e\cos E\right)}; \\
\frac{\partial \dot{E}}{\partial a} &= -\frac{3n}{2a\left(1 - e\cos E\right)} - \frac{ne\sin E}{\left(1 - e\cos E\right)^2}\frac{\partial E}{\partial a}; \\
\frac{\partial E}{\partial e} &= \frac{\sin E}{1 - e\cos E}; \\
\frac{\partial \dot{E}}{\partial e} &= -\frac{n}{(1 - e\cos E)^2}\left(-\cos E + e\sin E \frac{\partial E}{\partial e}\right); \\
\frac{\partial E}{\partial \left(L_0 - \varpi\right)} &= \frac{1}{1 - e\cos E}; \\
\frac{\partial \dot{E}}{\partial \left(L_0 - \varpi\right)} &= -\frac{n\sin E}{(1 - e\cos E)^2}\frac{\partial E}{\partial \left(L_0 - \varpi\right)}.
\end{aligned} \tag{C.57}$$

Now, due to the time invariance of the Lagrange brackets, a convenient point can be chosen. This point is the periapsis, which corresponds to $E = 0$. Plugging this in the derivatives of the state vector with respect to the orbital elements simplify significantly to

$$\begin{aligned}
\left(\frac{\partial \vec{r}'}{\partial a}\right)_{E=0} &= \begin{bmatrix} 1-e \\ 0 \\ 0 \end{bmatrix}; \quad \left(\frac{\partial \vec{v}'}{\partial a}\right)_{E=0} = \begin{bmatrix} 0 \\ -\frac{1}{2}n\sqrt{\frac{1+e}{1-e}} \\ 0 \end{bmatrix}; \\
\left(\frac{\partial \vec{r}'}{\partial e}\right)_{E=0} &= \begin{bmatrix} -a \\ 0 \\ 0 \end{bmatrix}; \quad \left(\frac{\partial \vec{v}'}{\partial e}\right)_{E=0} = \begin{bmatrix} 0 \\ \frac{na}{(1-e)\sqrt{1-e^2}} \\ 0 \end{bmatrix}; \\
\left(\frac{\partial \vec{r}'}{\partial \left(L_0 - \varpi\right)}\right)_{E=0} &= \begin{bmatrix} 0 \\ a\sqrt{\frac{1+e}{1-e}} \\ 0 \end{bmatrix}; \quad \left(\frac{\partial \vec{v}'}{\partial \left(L_0 - \varpi\right)}\right)_{E=0} = \begin{bmatrix} -\frac{na}{(1-e)^2} \\ 0 \\ 0 \end{bmatrix}.
\end{aligned} \tag{C.58}$$

Plugging this back in the Lagrange brackets of equation (2.102), it is found that

$$\begin{aligned}
[a,e]' &= \left(\frac{\partial \vec{r}'}{\partial a}\right)^T \frac{\partial \vec{v}'}{\partial e} - \left(\frac{\partial \vec{v}'}{\partial a}\right)^T \frac{\partial \vec{r}'}{\partial e} \\
&= \begin{bmatrix} 1-e & 0 & 0 \end{bmatrix} \begin{bmatrix} 0 \\ \frac{na}{(1-e)\sqrt{1-e^2}} \\ 0 \end{bmatrix} - \begin{bmatrix} 0 & -\frac{1}{2}n\sqrt{\frac{1+e}{1-e}} & 0 \end{bmatrix} \begin{bmatrix} -a \\ 0 \\ 0 \end{bmatrix} \\
&= 0; \\
[e,(L_0-\varpi)]' &= \left(\frac{\partial \vec{r}'}{\partial e}\right)^T \frac{\partial \vec{v}'}{\partial \left(L_0 - \varpi\right)} - \left(\frac{\partial \vec{v}'}{\partial e}\right)^T \frac{\partial \vec{r}'}{\partial \left(L_0 - \varpi\right)} \\
&= \begin{bmatrix} -a & 0 & 0 \end{bmatrix} \begin{bmatrix} -\frac{na}{(1-e)^2} \\ 0 \\ 0 \end{bmatrix} - \begin{bmatrix} 0 & \frac{na}{(1-e)\sqrt{1-e^2}} & 0 \end{bmatrix} \begin{bmatrix} 0 \\ a\sqrt{\frac{1+e}{1-e}} \\ 0 \end{bmatrix} \\
&= 0; \\
[(L_0-\varpi),a]' &= \left(\frac{\partial \vec{r}'}{\partial \left(L_0 - \varpi\right)}\right)^T \frac{\partial \vec{v}'}{\partial a} - \left(\frac{\partial \vec{v}'}{\partial \left(L_0 - \varpi\right)}\right)^T \frac{\partial \vec{r}'}{\partial a} \\
&= \begin{bmatrix} 0 & a\sqrt{\frac{1+e}{1-e}} & 0 \end{bmatrix} \begin{bmatrix} 0 \\ -\frac{1}{2}n\sqrt{\frac{1+e}{1-e}} \\ 0 \end{bmatrix} - \begin{bmatrix} -\frac{na}{(1-e)^2} & 0 & 0 \end{bmatrix} \begin{bmatrix} 1-e \\ 0 \\ 0 \end{bmatrix} \\
&= -\frac{1}{2}na\frac{1+e}{1-e} + \frac{na}{1-e} \\
&= \frac{1}{2}na = \frac{1}{2}\sqrt{\frac{\mu}{a}}.
\end{aligned} \tag{C.59}$$

C.5.6 Change of parameters

Change of variables from a to D, as seen in equation (2.104), starts with equation (2.103) [51]

$$\begin{aligned}[c_i, c_j]' =& \frac{1}{2}\sqrt{\frac{\mu}{a}}\frac{\partial\left(\left(L_0 - \varpi\right), a\right)}{\partial\left(c_i, c_j\right)} \\ =& \frac{1}{2}\sqrt{\frac{\mu}{a}}\left(\frac{\partial\left(L_0 - \varpi\right)}{\partial c_i}\frac{\partial a}{\partial c_j} - \frac{\partial\left(L_0 - \varpi\right)}{\partial c_j}\frac{\partial a}{\partial c_i}\right).\end{aligned} \tag{C.60}$$

Introducing D as a function of a, using the chain rule gives

$$\frac{\partial D}{\partial c_i} = \frac{\partial D}{\partial a}\frac{\partial a}{\partial c_i} \quad \Rightarrow \quad \frac{\partial a}{\partial c_i} = \frac{\partial a}{\partial D}\frac{\partial D}{\partial c_i}. \tag{C.61}$$

The same holds for c_j. Plugging this in the Lagrange bracket results in

$$\begin{aligned}[c_i, c_j]' =& \frac{1}{2}\sqrt{\frac{\mu}{a}}\left(\frac{\partial\left(L_0 - \varpi\right)}{\partial c_i}\frac{\partial a}{\partial D}\frac{\partial D}{\partial c_j} - \frac{\partial\left(L_0 - \varpi\right)}{\partial c_j}\frac{\partial a}{\partial D}\frac{\partial D}{\partial c_i}\right) \\ =& \frac{1}{2}\sqrt{\frac{\mu}{a}}\frac{\partial a}{\partial D}\left(\frac{\partial\left(L_0 - \varpi\right)}{\partial c_i}\frac{\partial D}{\partial c_j} - \frac{\partial\left(L_0 - \varpi\right)}{\partial c_j}\frac{\partial D}{\partial c_i}\right).\end{aligned} \tag{C.62}$$

Choose D such that the term before the brackets becomes unity

$$\begin{aligned}\frac{1}{2}\sqrt{\frac{\mu}{a}}\frac{\partial a}{\partial D} =& 1 \\ \int \frac{1}{2}\sqrt{\frac{\mu}{a}}\frac{\partial a}{\partial D}dD =& \int 1 dD \\ \int \frac{1}{2}\sqrt{\frac{\mu}{a}}da =& D \\ \Rightarrow D =& \sqrt{\mu a}.\end{aligned} \tag{C.63}$$

C.6 Perturbation expressions

C.6.1 Simplification of $U_{2,\mathfrak{h}}$

In order to go from equation (2.125) to equation (2.126), expand the brackets and move terms outside the integral [51]

$$\begin{aligned}
U_{2,\mathfrak{h}} =& -\frac{G}{r^3}\int_V r'^2 P_2\left(\cos\vartheta\right) dM \\
=& -\frac{G}{r^3}\int_V \frac{1}{2}\left(\frac{3}{r^2}\left(r'_x r_x + r'_y r_y + r'_z r_z\right)^2 - \left(r'^2_x + r'^2_y + r'^2_z\right)\right) dM \\
=& -\frac{G}{r^3}\int_V \frac{1}{2}\left(\frac{3}{r^2}\left(r'^2_x r_x^2 + r'^2_y r_y^2 + r'^2_z r_z^2 + 2r'_x r'_y r_x r_y + 2r'_x r'_z r_x r_z + 2r'_y r'_z r_y r_z\right)\right. \\
& \left. - \left(r'^2_x + r'^2_y + r'^2_z\right)\right) dM \\
=& -\frac{G}{r^3}\left(\left(\frac{3r_x^2}{2r^2} - \frac{1}{2}\right)\int_V r'^2_x dM + \left(\frac{3r_y^2}{2r^2} - \frac{1}{2}\right)\int_V r'^2_y dM + \left(\frac{3r_z^2}{2r^2} - \frac{1}{2}\right)\int_V r'^2_z dM\right) \\
& - \frac{3G}{r^5}\left(r_x r_y \int_V r'_x r'_y dM + r_x r_z \int_V r'_x r'_z dM + r_y r_z \int_V r'_y r'_z dM\right).
\end{aligned} \tag{C.64}$$

This can be simplified by making use of the inertia tensor. The components are given by

$$\begin{aligned}
I_{xx} &= \int_V \left(r'^2_y + r'^2_z\right) dM; \qquad I_{xy} = -\int_V r'_x r'_y dM; \\
I_{yy} &= \int_V \left(r'^2_x + r'^2_z\right) dM; \qquad I_{xz} = -\int_V r'_x r'_z dM; \\
I_{zz} &= \int_V \left(r'^2_x + r'^2_y\right) dM; \qquad I_{yz} = -\int_V r'_y r'_z dM.
\end{aligned} \tag{C.65}$$

Using this results in

$$\begin{aligned}
U_{2,\mathfrak{h}} =& -\frac{G}{r^3}\left(\left(\frac{3r_x^2}{2r^2} - \frac{1}{2}\right)\left(\frac{1}{2}\left(I_{xx} + I_{yy} + I_{zz}\right) - I_{xx}\right)\right. \\
& + \left(\frac{3r_y^2}{2r^2} - \frac{1}{2}\right)\left(\frac{1}{2}\left(I_{xx} + I_{yy} + I_{zz}\right) - I_{yy}\right) \\
& \left. + \left(\frac{3r_z^2}{2r^2} - \frac{1}{2}\right)\left(\frac{1}{2}\left(I_{xx} + I_{yy} + I_{zz}\right) - I_{zz}\right)\right) + \frac{3G}{r^5}\left(r_x r_y I_{xy} + r_x r_z I_{xz} + r_y r_z I_{yz}\right) \\
=& -\frac{G}{r^3}\left(\frac{3}{2r^2}\left(\left(r_x^2 + r_y^2 + r_z^2\right)\left(\frac{1}{2}\left(I_{xx} + I_{yy} + I_{zz}\right)\right) - \left(r_x^2 I_{xx} + r_y^2 I_{yy} + r_z^2 I_{zz}\right)\right)\right. \\
& \left. - \frac{1}{2}\frac{3}{2}\left(I_{xx} + I_{yy} + I_{zz}\right) + \frac{1}{2}\left(I_{xx} + I_{yy} + I_{zz}\right)\right) + \frac{3G}{r^5}\left(r_x r_y I_{xy} + r_x r_z I_{xz} + r_y r_z I_{yz}\right) \\
=& -\frac{G}{r^3}\left(\frac{1}{2}\left(I_{xx} + I_{yy} + I_{zz}\right) - \frac{3}{2}\left(\frac{r_x^2 I_{xx} + r_y^2 I_{yy} + r_z^2 I_{zz}}{r^2}\right)\right) \\
& + \frac{3G}{r^5}\left(r_x r_y I_{xy} + r_x r_z I_{xz} + r_y r_z I_{yz}\right).
\end{aligned} \tag{C.66}$$

The products of inertia, which are seen in the last term, can be cancelled by assuming that the principal axes of inertia are aligned with the coordinate system. Furthermore, by assuming that the primary body is axisymmetric about its axis of rotation (the z-axis), the system is reduced further as $I_{xx} = I_{yy}$ gives

$$U_{2,\mathfrak{h}} = -\frac{G}{r^3}\left(I_{xx} + \frac{1}{2}I_{zz} - \frac{3}{2}\left(\frac{r_x^2 I_{xx} + r_y^2 I_{xx} + r_z^2 I_{zz}}{r^2}\right)\right). \tag{C.67}$$

The position coordinates can be described in spherical coordinates using the geographic coordinate system, equation (2.57)

$$r_x = r\cos\varphi\cos\lambda; \qquad r_y = r\cos\varphi\sin\lambda; \qquad r_z = r\sin\varphi. \tag{C.68}$$

Plugging this in gives

$$\begin{aligned} U_{2,\mathfrak{h}} =& -\frac{G}{r^3}\left(I_{xx} + \frac{1}{2}I_{zz} - \frac{3}{2}\left(\frac{\left(r\cos\varphi\cos\lambda\right)^2 I_{xx} + \left(r\cos\varphi\sin\lambda\right)^2 I_{xx} + \left(r\sin\varphi\right)^2 I_{zz}}{r^2}\right)\right) \\ =& -\frac{G}{r^3}\left(I_{xx} + \frac{1}{2}I_{zz} - \frac{3}{2}\left(\cos^2\varphi I_{xx} + \sin^2\varphi I_{zz}\right)\right) \\ =& -\frac{G}{r^3}\left(\frac{1}{2}\left(I_{zz} - I_{xx}\right) - \frac{3}{2}\sin^2\varphi\left(I_{xx} + I_{zz}\right)\right) \\ =& -\frac{G}{r^3}\left(I_{zz} - I_{xx}\right)\left(\frac{1}{2} - \frac{3}{2}\sin^2\varphi\right). \end{aligned} \tag{C.69}$$

C.6.2 Change to orbital elements U_2

Derivation of equation (2.130) makes use of the relation between latitude right overhead, inclination, and argument of perigee and true anomaly as [51]

$$\sin\varphi = \sin i\sin\left(\omega + \mathrm{f}\right) \quad \Rightarrow \quad \frac{3}{2}\sin^2\varphi - \frac{1}{2} = \frac{3}{2}\sin^2 i\sin^2\left(\omega + \mathrm{f}\right) - \frac{1}{2}. \tag{C.70}$$

Make use of this trigonometric identity

$$\sin^2\vartheta = \frac{1}{2} - \frac{1}{2}\cos\left(2\vartheta\right). \tag{C.71}$$

Which gives

$$\begin{aligned} \frac{3}{2}\sin^2\varphi - \frac{1}{2} =& \frac{3}{2}\sin^2 i\left(\frac{1}{2} - \frac{1}{2}\cos\left(2\left(\omega + \mathrm{f}\right)\right)\right) - \frac{1}{2} \\ =& \frac{3}{4}\sin^2 i - \frac{1}{2} - \frac{3}{4}\sin^2 i\cos\left(2\left(\omega + \mathrm{f}\right)\right). \end{aligned} \tag{C.72}$$

Plug this in the perturbing force function, equation (2.128) to obtain

$$\begin{aligned} \mathscr{R}_{2,\mathfrak{h}} =& -\frac{\mu}{r^3}R_e^2 J_2\left(\frac{3}{2}\sin^2\varphi - \frac{1}{2}\right) \\ =& \frac{\mu}{r^3}R_e^2 J_2\left(\frac{3}{4}\sin^2 i - \frac{1}{2} - \frac{3}{4}\sin^2 i\cos\left(2\left(\omega + \mathrm{f}\right)\right)\right). \end{aligned} \tag{C.73}$$

Then, by grouping some terms together and inserting a/a, the final expression is

$$\mathscr{R}_{2,\mathfrak{h}} = -\frac{\mu}{a}J_2\left(\frac{R_e}{a}\right)^2\left(\left(\frac{a}{r}\right)^3\left(\frac{3}{4}\sin^2 i - \frac{1}{2}\right) - \frac{3}{4}\sin^2 i\left(\frac{a}{r}\right)^3\cos\left(2\left(\omega + \mathrm{f}\right)\right)\right). \tag{C.74}$$

C.6.3 Mean part of $\mathscr{R}_{2,\mathfrak{h}}$

Derivation of equation (2.133) comes down to integrating each term separately and simplifying afterwards. Not necessarily difficult, but the large expression makes it slightly confusing. Doing so gives

$$
\begin{aligned}
\langle \mathscr{R}_{2,\mathfrak{h}} \rangle =& \frac{1}{2\pi} \int_0^{2\pi} \mathscr{R}_{2,\mathfrak{h}} \left(\frac{r}{a}\right)^2 \frac{1}{\sqrt{1-e^2}} d\mathrm{f} \\
=& \frac{1}{2\pi} \int_0^{2\pi} \frac{\mu}{a} J_2 \left(\frac{R_e}{a}\right)^2 \left(\left(\frac{1}{2} - \frac{3}{4}\sin^2 i\right) \left(\frac{a}{r}\right)^3 + \frac{3}{4}\sin^2 i \left(\frac{a}{r}\right)^3 \cos\left(2\left(\omega + \mathrm{f}\right)\right) \right) \\
& \left(\frac{r}{a}\right)^2 \frac{1}{\sqrt{1-e^2}} d\mathrm{f} \\
=& \frac{1}{2\pi} \frac{\mu}{a} J_2 \left(\frac{R_e}{a}\right)^2 \frac{1}{(1-e^2)^{\frac{3}{2}}} \int_0^{2\pi} (1 + e\cos\mathrm{f}) \left(\frac{1}{2} - \frac{3}{4}\sin^2 i\right) \\
& + \frac{3}{4}\sin^2 i \left(1 + e\cos\mathrm{f}\right) \cos\left(2\left(\omega + \mathrm{f}\right)\right) df \\
=& \frac{1}{2\pi} \frac{\mu}{a} J_2 \left(\frac{R_e}{a}\right)^2 \frac{1}{(1-e^2)^{\frac{3}{2}}} \left(\left(\frac{1}{2} - \frac{3}{4}\sin^2 i\right) \left[f + e\sin\mathrm{f}\right]_0^{2\pi} \right. \\
& \left. + \sin^2 i \int_0^{2\pi} (1 + e\cos\mathrm{f}) \left(\cos 2\omega \cos 2\mathrm{f} - \sin 2\omega \sin 2\mathrm{f}\right) d\mathrm{f} \right) \\
=& \frac{1}{2\pi} \frac{\mu}{a} J_2 \left(\frac{R_e}{a}\right)^2 \frac{1}{(1-e^2)^{\frac{3}{2}}} \left(\left(\frac{1}{2} - \frac{3}{4}\sin^2 i\right) 2\pi \right. \\
& + \sin^2 i \left(\cos 2\omega \int_0^{2\pi} \left(\frac{1}{2}e\cos\mathrm{f} + \cos 2\mathrm{f} + \frac{1}{2}e\cos 3\mathrm{f}\right) df \right. \\
& \left. \left. - \sin 2\omega \int_0^{2\pi} \left(\frac{1}{2}e\sin\mathrm{f} + \sin 2\mathrm{f} + \frac{1}{2}e\sin 3\mathrm{f}\right) df \right) \right) \\
=& \frac{1}{2\pi} \frac{\mu}{a} J_2 \left(\frac{R_e}{a}\right)^2 \frac{1}{(1-e^2)^{\frac{3}{2}}} \left(\left(\frac{1}{2} - \frac{3}{4}\sin^2 i\right) 2\pi \right. \\
& + \sin^2 i \left(\cos 2\omega \left[\frac{1}{2}e\sin\mathrm{f} + \frac{1}{2}\sin 2\mathrm{f} + \frac{1}{6}e\sin 3\mathrm{f}\right]_0^{2\pi} \right. \\
& \left. \left. + \sin 2\omega \left[\frac{1}{2}e\cos\mathrm{f} + \frac{1}{2}\cos 2\mathrm{f} + \frac{1}{6}e\cos 3\mathrm{f}\right]_0^{2\pi} \right) \right) \\
=& \frac{\mu}{a} J_2 \left(\frac{R_e}{a}\right)^2 \frac{1}{(1-e^2)^{\frac{3}{2}}} \left(\frac{1}{2} - \frac{3}{4}\sin^2 i\right).
\end{aligned}
\tag{C.75}
$$

To simplify the expression, the following trigonometric identities were applied

$$
\begin{aligned}
\cos\left(\vartheta + \varsigma\right) =& \cos\vartheta\cos\varsigma - \sin\vartheta\sin\varsigma; \\
\cos\vartheta\cos\varsigma =& \frac{1}{2}\left(\cos\left(\vartheta - \varsigma\right) + \cos\left(\vartheta + \varsigma\right)\right); \\
\sin\vartheta\cos\varsigma =& \frac{1}{2}\left(\cos\left(\vartheta + \varsigma\right) + \cos\left(\vartheta - \varsigma\right)\right).
\end{aligned}
\tag{C.76}
$$

C.6.4 Development of $\mathscr{R}_{3,\mathfrak{h}}$

For the third degree, the potential is found by plugging in $n = 3$ in equation (2.127), which gives [51]

$$U_{3,\mathfrak{h}} = \frac{\mu}{r} J_3 \left(\frac{R_e}{r}\right)^3 P_3 \left(\sin\varphi\right). \tag{C.77}$$

The perturbing force function in orbital elements is given by

$$\mathscr{R}_{3,\mathfrak{h}} = -\frac{\mu}{a} J_3 \left(\frac{R_e}{a}\right)^3 \sin i \left(\left(\frac{15}{8}\sin^2 i - \frac{3}{2}\right)\left(\frac{a}{r}\right)^4 \sin\left(\omega + \mathrm{f}\right) - \frac{5}{8}\sin^2 i \left(\frac{a}{r}\right)^4 \sin\left(3\left(\omega + \mathrm{f}\right)\right)\right). \tag{C.78}$$

Taking the average over a whole period after a change of variable with equation (2.132) results in a mean part of

$$\left\langle \mathscr{R}_{3,\mathfrak{h}} \right\rangle = -\frac{3}{8}\frac{\mu}{a} J_3 \left(\frac{R_e}{a}\right)^3 \frac{e}{\left(1-e^2\right)^{\frac{5}{2}}} \left(1 - 5\cos^2 i\right) \sin i \sin\omega. \tag{C.79}$$

The non-zero derivatives of the mean part with respect to the orbital elements are given by

$$\begin{aligned}
\frac{\partial \left\langle \mathscr{R}_{3,\mathfrak{h}} \right\rangle}{\partial a} =& \frac{3}{2}\frac{\mu}{a^2} J_3 \left(\frac{R_e}{a}\right)^3 \frac{e}{\left(1-e^2\right)^{\frac{5}{2}}} \left(1 - 5\cos^2 i\right) \sin i \sin\omega; \\
\frac{\partial \left\langle \mathscr{R}_{3,\mathfrak{h}} \right\rangle}{\partial e} =& -\frac{3}{8}\frac{\mu}{a} J_3 \left(\frac{R_e}{a}\right)^3 \frac{1+4e^2}{\left(1-e^2\right)^{\frac{7}{2}}} \left(1 - 5\cos^2 i\right) \sin i \sin\omega; \\
\frac{\partial \left\langle \mathscr{R}_{3,\mathfrak{h}} \right\rangle}{\partial i} =& -\frac{3}{8}\frac{\mu}{a} J_3 \left(\frac{R_e}{a}\right)^3 \frac{e}{\left(1-e^2\right)^{\frac{5}{2}}} \left(11 - 15\cos^2 i\right) \cos i \sin\omega; \\
\frac{\partial \left\langle \mathscr{R}_{3,\mathfrak{h}} \right\rangle}{\partial \omega} =& -\frac{3}{8}\frac{\mu}{a} J_3 \left(\frac{R_e}{a}\right)^3 \frac{e}{\left(1-e^2\right)^{\frac{5}{2}}} \left(1 - 5\cos^2 i\right) \sin i \cos\omega.
\end{aligned} \tag{C.80}$$

This can once more be used as input for the Lagrange equations (2.112). The non-zero terms are given by

$$\begin{aligned}
\dot{e}_{3,\mathfrak{h}} =& \frac{3}{8} n J_3 \left(\frac{R_e}{a}\right)^3 \frac{1}{\left(1-e^2\right)^2} \left(1 - 5\cos^2 i\right) \sin i \cos\omega; \\
\dot{i}_{3,\mathfrak{h}} =& -\frac{3}{8} n J_3 \left(\frac{R_e}{a}\right)^3 \frac{e}{\left(1-e^2\right)^3} \left(1 - 5\cos^2 i\right) \cos i \cos\omega; \\
\dot{\Omega}_{3,\mathfrak{h}} =& -\frac{3}{8} n J_3 \left(\frac{R_e}{a}\right)^3 \frac{e}{\left(1-e^2\right)^3} \left(11 - 15\cos^2 i\right) \cos i \sin\omega; \\
\dot{\omega}_{3,\mathfrak{h}} =& -\frac{3}{8} n J_3 \left(\frac{R_e}{a}\right)^3 \frac{1}{\left(1-e^2\right)^3} \left(\frac{1+4e^2}{e}\left(1 - 5\cos^2 i\right) \sin i + e\left(11 - 15\cos^2 i\right)\frac{\cos^2 i}{\sin i}\right) \sin\omega; \\
\dot{M}_{e3,\mathfrak{h}} =& -3 n J_3 \left(\frac{R_e}{a}\right)^3 \frac{1}{\left(1-e^2\right)^{\frac{5}{2}}} \left(e + \frac{1}{8}\frac{1+4e^2}{e}\right) \left(1 - 5\cos^2 i\right) \sin i \sin\omega.
\end{aligned} \tag{C.81}$$

C.6.5 Development of $\mathscr{R}_{4,\mathfrak{h}}$

Once more, starting from equation (2.127), now with $n = 4$ [51]

$$U_{4,\mathfrak{h}} = \frac{\mu}{r} J_4 \left(\frac{R_e}{r}\right)^4 P_4 \left(\sin\varphi\right). \tag{C.82}$$

The perturbing force function as a function of orbital elements is

$$\begin{aligned}\mathscr{R}_{4,\mathfrak{h}} = &-\frac{\mu}{a} J_4 \left(\frac{R_e}{a}\right)^4 \left(\left(\frac{3}{8} - \frac{15}{8}\sin^2 i + \frac{105}{64}\sin^4 i\right)\left(\frac{a}{r}\right)^5 \right.\\ &\left. + \left(\frac{15}{8}\sin^2 i - \frac{35}{16}\sin^4 i\right)\left(\frac{a}{r}\right)^5 \cos\left(2\left(\omega + \mathrm{f}\right)\right) + \frac{35}{64}\sin^4 i \left(\frac{a}{r}\right)^5 \cos\left(4\left(\omega + \mathrm{f}\right)\right)\right).\end{aligned} \tag{C.83}$$

The mean part is found to be

$$\begin{aligned}\left\langle \mathscr{R}_{4,\mathfrak{h}} \right\rangle = &-\frac{\mu}{a} J_4 \left(\frac{R_e}{a}\right)^4 \frac{1}{\left(1-e^2\right)^{\frac{7}{2}}} \left(\left(1 + \frac{3}{2}e^2\right)\left(\frac{3}{8} - \frac{15}{8}\sin^2 i + \frac{105}{64}\sin^4 i\right)\right.\\ &\left. + \frac{3}{4}e^2 \left(\frac{15}{8}\sin^2 i - \frac{35}{16}\sin^4 i\right)\cos 2\omega\right).\end{aligned} \tag{C.84}$$

The non-zero derivatives with respect to the orbital elements are given by

$$\begin{aligned}\frac{\partial \left\langle \mathscr{R}_{4,\mathfrak{h}} \right\rangle}{\partial a} = &5\frac{\mu}{a^2} J_4 \left(\frac{R_e}{a}\right)^4 \frac{1}{\left(1-e^2\right)^{\frac{7}{2}}} \left(\left(1 + \frac{3}{2}e^2\right)\left(\frac{3}{8} - \frac{15}{8}\sin^2 i + \frac{105}{64}\sin^4 i\right)\right.\\ &\left. + \frac{3}{4}e^2 \left(\frac{15}{8}\sin^2 i - \frac{35}{16}\sin^4 i\right)\cos 2\omega\right);\\ \frac{\partial \left\langle \mathscr{R}_{4,\mathfrak{h}} \right\rangle}{\partial e} = &-\frac{1}{2}\frac{\mu}{a} J_4 \left(\frac{R_e}{a}\right)^4 \frac{20e + 15e^3}{\left(1-e^2\right)^{\frac{9}{2}}} \left(\frac{3}{8} - \frac{15}{8}\sin^2 i + \frac{105}{64}\sin^4 i\right);\\ \frac{\partial \left\langle \mathscr{R}_{4,\mathfrak{h}} \right\rangle}{\partial i} = &\frac{1}{128}\frac{\mu}{a} J_4 \left(\frac{R_e}{a}\right)^4 \frac{1 + \frac{3}{2}e^2}{\left(1-e^2\right)^{\frac{7}{2}}} \left(105\sin\left(4i\right) + 30\sin\left(2i\right)\right).\end{aligned} \tag{C.85}$$

C.6.6 Development of perturbing acceleration

For $n = 3$, the perturbing acceleration in spherical coordinates is

$$\vec{\Gamma}^S_{3,\mathfrak{h}} = \sqrt{7}\frac{\mu}{r^2}\bar{J}_3 \left(\frac{R_e}{r}\right)^3 \begin{bmatrix} 2\left(5\sin^3\varphi - 3\sin\varphi\right) \\ 0 \\ -\frac{3}{2}\cos\varphi\left(5\sin^2\varphi - 1\right) \end{bmatrix}. \tag{C.86}$$

Same story for $n = 4$.

$$\vec{\Gamma}^S_{4,\mathfrak{h}} = 3\frac{\mu}{r^2}\bar{J}_4 \left(\frac{R_e}{r}\right)^4 \begin{bmatrix} 2\left(35\sin^4\varphi - 30\sin^2\varphi + 3\right) \\ 0 \\ -\frac{5}{2}\cos\varphi\left(7\sin^3\varphi - 3\sin\varphi\right) \end{bmatrix}. \tag{C.87}$$

The rotation matrices to go from spherical to Cartesian coordinates, and later on to an inertial frame, can be applied in the same manner as was shown for $\vec{\Gamma}_{2,\mathfrak{h}}$.

C.6.7 Rewrite $U_\mathfrak{b}$

In order to obtain equation (2.149) from equation (2.148), the law of cosines, seen in equation (C.3), and the definition of the dot product are used. This gives

$$\begin{aligned} U_\mathfrak{b} &= -\mu_3 \left(\frac{1}{\varrho} - \frac{\vec{r} \cdot \vec{r_3}}{r_3^3} \right) \\ &= -\mu_3 \left(\frac{1}{r^2 - 2rr_3 \cos\vartheta + r_3^2} - \frac{r}{r_3^2} \cos\vartheta \right) \\ &= -\frac{\mu_3}{r_3} \left(\frac{r_3}{\sqrt{r^2 - 2rr_3 \cos\vartheta + r_3^2}} - \frac{r}{r_3} \cos\vartheta \right) \\ &= -\frac{\mu_3}{r_3} \left(\frac{1}{\sqrt{\left(\frac{r}{r_3}\right)^2 - 2\frac{r}{r_3} \cos\vartheta + 1}} - \frac{r}{r_3} \cos\vartheta \right). \end{aligned} \tag{C.88}$$

Now, since $r/r_3 < 1$, the first term in the brackets can be rewritten following equation (2.116), which gives

$$U_\mathfrak{b} = -\frac{\mu_3}{r_3} \left(\sum_{n=0}^{\infty} \left(\frac{r}{r_3} \right)^n P_n(\cos\vartheta) - \frac{r}{r_3} \cos\vartheta \right). \tag{C.89}$$

C.6.8 Dot product with orbital elements

The derivation of equation (2.156) makes use of the following trigonometry identities

$$\begin{aligned} \sin(\alpha \pm \beta) &= \sin\alpha \cos\beta \pm \cos\alpha \sin\beta; \\ \cos(\alpha \pm \beta) &= \sin\alpha \sin\beta \mp \cos\alpha \cos\beta. \end{aligned} \tag{C.90}$$

By expanding the brackets and applying the trigonometry identities, the following is obtained

$$\begin{aligned} \cos\vartheta &= (\cos\Omega \cos(\omega + \mathrm{f}) - \sin\Omega \sin(\omega + \mathrm{f}) \cos i) \cos(n_3 t) \\ &\quad + (\sin\Omega \cos(\omega + \mathrm{f}) + \cos\Omega \sin(\omega + \mathrm{f}) \cos i) \sin(n_3 t) \\ &= \cos(\omega + \mathrm{f}) (\cos\Omega \cos(n_3 t) + \sin\Omega \sin(n_3 t)) \\ &\quad + \sin(\omega + \mathrm{f}) (\cos\Omega \sin(n_3 t) - \sin\Omega \cos(n_3 t)) \cos i \\ &= \cos(\omega + \mathrm{f}) \cos(\Omega - n_3 t) + \sin(\omega + \mathrm{f}) \sin(\Omega - n_3 t) \cos i. \end{aligned} \tag{C.91}$$